Drivers and Effects of Plasma Composition Variations in the Solar Corona

Alexandra Teodora Mihailescu

A dissertation submitted in partial fulfillment

of the requirements for the degree of

Doctor of Philosophy

of

University College London.

Department of Space and Climate Physics

University College London

July 18, 2024

I, Alexandra Teodora Mihailescu, confirm that the work presented in this thesis is my own. Where information has been derived from other sources, I confirm that this has been indicated in the work.

Abstract

The plasma composition of the solar corona is characterised by an overabundance of elements with a low first ionization potential (FIP) compared to those with a high FIP. This enhancement of low-FIP elements is believed to take place in the chromosphere and is characterised by the FIP bias parameter. The aim of the research outlined in this thesis is to understand this universal process on large and small spatial scales, long and short timescales, and quiescent and flaring conditions using spectroscopic observations in the extreme ultraviolet range. First, the FIP bias dependence on magnetic activity was investigated in quiescent active regions over large scales and timescales of weeks to months. Results indicate a correlation between FIP bias and magnetic flux density. The active regions in the study display a wide range of FIP bias values which change with the active region evolutionary stage suggesting that sub-active region processes can influence the FIP bias in different ways. Next, the link between plasma composition patterns at sub-active region level and Alfvén wave activity over timescales of a few hours was explored in more detail. Matching spectroscopic observations with predictions from simulations of the FIP effect suggests that the plasma composition pattern observed in a coronal loop depends on the properties of the Alfvén waves driving the enhancement and, particularly, the chromospheric height at which they deposit their energy. Finally, this work was extended to dynamic processes with timescales of seconds to minutes by studying the evolution of plasma composition in an M-class solar flare. The strong heating and associated plasma flows change the plasma composition of the flare loops which, in turn, influences the radiative cooling process of the loops. Observations suggest high/low FIP bias and faster/slower cooling at the top/footpoint

of the loop, in agreement with predictions of the radiative cooling process. The overall conclusion of this thesis is that plasma composition in the solar corona is tightly linked to other processes such as magnetic activity, heating, Alfvén wave activity and radiative cooling.

Impact Statement

The relative abundances of different heavy elements is constant in the solar photosphere, but varies spatially and in time in the solar corona and in the solar wind. This puzzling phenomenon is believed to be driven in the solar upper chromosphere and transition region. This is the same region where processes that heat the solar corona to million of degrees (the coronal heating problem) begin to dominate. There is significant evidence that the variation in plasma composition is tightly linked to heating, wave activity and magnetic activity in the solar atmosphere.

In addition to having the potential to provide insights into the processes that heat the solar corona or drive magnetic activity, plasma composition can also be used as a tool for identifying solar wind sources. This is because once a plasma parcel reaches the corona, the process driving the variations stops and the plasma maintains the same composition if it escapes into the solar wind. The processes driving the abundance variations are also correlated with those driving the acceleration and heating of the solar wind. Therefore, understanding the process that change the plasma composition can provide invaluable insight for understanding how the solar wind is heated and accelerated.

The work in this thesis explores the drivers causing these abundance variations and the effects abundance variations can have on other coronal processes. In particular, the focus is on the impact wave activity and magnetic activity on the plasma composition pattern observed in the solar corona, as well as how this pattern influences the radiative cooling process of plasma in the corona.

UCL Research Paper Declaration Form

Referencing the doctoral candidate's own published work(s) for a research manuscript that has already been published:

1. **What is the title of the manuscript?** What Determines Active Region Coronal Plasma Composition?
2. **Please include a link to or doi for the work:** 10.3847/1538-4357/ac6e40.
3. **Where was the work published?** The Astrophysical Journal.
4. **Who published the work?** The American Astronomical Society.
5. **When was the work published?** 19th July 2022.
6. **List the manuscript's authors in the order they appear on the publication:** T. Mihailescu, D. Baker, L.M. Green, L. van Driel-Gesztelyi, D.M. Long, D.H. Brooks, A.S.H. To.
7. **Was the work peer reviewd?** Yes.
8. **Have you retained the copyright?** Yes.
9. **Was an earlier form of the manuscript uploaded to a preprint server (e.g. medRxiv)? If 'Yes', please give a link or doi.** Yes: https://arxiv.org/abs/2205.05027.

UCL Research Paper Declaration Form

Referencing the doctoral candidate's own published work(s) for a research manuscript that has already been published:

1. **What is the title of the manuscript?** Intriguing Plasma Composition Pattern in a Solar Active Region: a Result of Non-Resonant Alfvén Waves?
2. **Please include a link to or doi for the work:** 10.3847/1538-4357/ad05bf.
3. **Where was the work published?** The Astrophysical Journal.
4. **Who published the work?** The American Astronomical Society.
5. **When was the work published?** 7th December 2023.
6. **List the manuscript's authors in the order they appear on the publication:** T. Mihailescu, D. H. Brooks, J.M. Laming, D. Baker, L. M. Green, A. W. James, D. M. Long, L. van Driel-Gesztelyi, M. Stangalini.
7. **Was the work peer reviewd?** Yes.
8. **Have you retained the copyright?** Yes.
9. **Was an earlier form of the manuscript uploaded to a preprint server (e.g. medRxiv)? If 'Yes', please give a link or doi.** Yes: https://arxiv.org/abs/2310.13677.

List of Publications

1. **T. Mihailescu**, P. R. Young, D. H. Brooks, D. Baker, L. M. Green, D. M. Long, L. van Driel-Gesztelyi (2024). A Study of Plasma Composition Effects on the Radiative Cooling of Flare Loops. *In Prep*.

2. D. Baker, L. van Driel-Gesztelyi, A. W. James, P. Démoulin, A. S. H. To, M. Murabito, D. Long, D. H. Brooks, J. McKevitt, J. M. Laming, L. M. Green, S. L. Yardley, G. Valori, **T. Mihailescu**, S. A. Matthews, H. Kuniyoshi (2024). Searching for Evidence of Solar Subsurface Magnetic Reconnection. *Submitted to The Astrophysical Journal*.

3. **T. Mihailescu**, D. H. Brooks, J.M. Laming, D. Baker, L. M. Green, A. W. James, D. M. Long, L. van Driel-Gesztelyi, M. Stangalini (2023). Intriguing Plasma Composition Pattern in a Solar Active Region: a Result of Non-Resonant Alfvén Waves?. The Astrophysical Journal, 959, 72.

4. D. Baker, P. Démoulin, S.L. Yardley, **T. Mihailescu**, L. van Driel-Gesztelyi, R. D'Amicis, D.M. Long, A.S.H. To, C.J. Owen, T.S. Horbury, D.H. Brooks, D. Perrone, R.J. French, A.W. James, M. Janvier, S. Matthews, M. Stangalini, G. Valori, P. Smith, R. Anzar Cuadrado, H. Peter, U. Schuehle, L. Harra, K. Barczynski, D. Berghmans, A.N. Zhukov, L. Rodriguez, C. Verbeeck (2023). Observational Evidence of S-Web Source of the Slow Solar Wind. The As-

trophysical Journal, 950, 65.

5. S. L. Yardley, C. J. Owen, D. M. Long, D. Baker, D. H. Brooks, V. Polito, L. M. Green, S. Matthews, M. Owens, M. Lockwood, D. Stansby, A. W. James, G. Valori, A. Giunta, M. Janvier, N. Ngampoopun, **T. Mihailescu**, A. S. H. To, L. van Driel-Gesztelyi, P. Démoulin, R. D'Amicis, R. J. French, G. H. H. Suen, A. P. Rouillard, R. F. Pinto, V. Réville, C. J. Watson, A. P. Walsh, A. De Groof, D. R. Williams, I. Zouganelis, D. Müller, D. Berghmans, F. Auchère, L. Harra, U. Schuehle, K. Barczynski, É. Buchlin, R. Aznar Cuadrado, E. Kraaikamp, S. Mandal, S. Parenti, H. Peter, L. Rodriguez, C. Schwanitz, P. Smith, L. Teriaca, C. Verbeeck, A. N. Zhukov, B. De Pontieu, T. Horbury, S. K. Solanki, J. C. del Toro Iniesta, J. Woch, A. Gandorfer, J. Hirzberger, D. Orozco Súarez, T. Appourchaux, D. Calchetti, J. Sinjan, F. Kahil, K. Albert, R. Volkmer, M. Carlsson, A. Fludra, D. Hassler, M. Caldwell, T. Fredvik, T. Grundy, S. Guest, M. Haberreiter, S. Leeks, G. Pelouze, J. Plowman, W. Schmutz, S. Sidher, W. T. Thompson, P. Louarn, and A. Federov (2023). Slow Solar Wind Connection Science during Solar Orbiter's First Close Perihelion Passage. The Astrophysical Journal, 267, 11.

6. S.L. Yardley, L.M. Green, A.W. James, D.S. Stansby, **T. Mihailescu** (2022). The Magnetic Field Environment of Active Region 12673 That Produced the Energetic Particle Events of September 2017. The Astrophysical Journal, 937(2), 57.

7. **T. Mihailescu**, D. Baker, L.M. Green, L. van Driel-Gesztelyi, D.M. Long, D.H. Brooks, A.S.H. To (2022). What Determines Active Region Plasma Composition?. The Astrophysical Journal, 933(2), 245.

8. D. Baker, L.M. Green, D.H. Brooks, P. Démoulin, L. van Driel-Gesztelyi, **T. Mihailescu**, A.S.H. To, D.M. Long, S.L. Yardley, M. Janvier, G. Valori (2022). Evolution of Plasma Composition in an Eruptive Flux Rope. The Astrophysical Journal, 924(1):17.

9. D. Baker, **T. Mihailescu**, P. Démoulin, L.M. Green, L. van Driel-Gesztelyi, G. Valori, D.H. Brooks, D.M. Long, M. Janvier (2021). Upflows Induced by Magnetic Reconnection above an Erupting Flux Rope. Solar Physics, 296(6):103.

Acknowledgements

Throughout my PhD, I've had the incredible luck of being surrounded by kind mentors who taught me so much, inspired me and made science fun. I am so grateful to my supervisor team: Prof. Lucie Green, Dr. Deb Baker, Dr. David Long and Prof. Lidia van Driel-Gesztelyi.

Lucie, thank you for your constant support, guidance, encouragements and for making sure I take breaks during the busiest times to go out and see the Sun in 3D, not just on my screen. It's been a joy to learn so much about the Sun, science and how to communicate science from you.

Deb, thank you for the countless fun chats about FIP and all the cool EIS stuff. Thank you for always being there for me, for making time to chat no matter what I was worried or excited about and for somehow always knowing what piece of advice to give me when I needed it most.

Dave, thank you for teaching me so much about being a disciplined researcher and for the constructive advice that helped me improve my work and grow as a scientist so many times. And thank you for that 6 hours lecture at the beginning of my masters that inspired me to do a project about the Sun!

Lidia, thank you for your kind encouragements, for sharing your boundless knowledge of the Sun, and for teaching me to look at research surprises with excitement and curiosity instead of panic.

To Dr. Peter Young, it's been a privilege to work with you and I am so grateful for everything you taught me, from spectroscopy and flares to how to be a curious and rigorous scientist. Thank you for your support during my visit at Goddard and for always making time to help with my many questions.

To Dr. David Brooks, thank you for the chats, help and advice on all things FIP, for hosting me during my visit at ISAS and teaching me about all the fun EIS stuff (I can say fun because I never had to push the button myself!).

To Dr. Martin Laming, thank you for the interesting discussions and explanations on waves and the ponderomotive force, particularly during my visit at NRL.

I would also like to thank Prof. Lyndsay Fletcher and Prof. Daniel Verscharen for taking the time to read and examine this thesis.

Thank you to all my friends at MSSL for making me feel like home from day one. To Jenny O'K., Andy, Ryan, Jack and Jinge for the warm welcome into G01. To Jenny, for brightening the first day of my PhD in the middle of the pandemic with a 2 hour talk on stealthy CMEs. To Andy, for the many FIP chats and associated debate on where the fractionation *actually* happens, crazy drives to the lab, karaoke sessions and all the fun. To Alex, for your kind and detailed advice that helped me improve my second paper and for cheering me up with our great music project. To Julio for being so kind and encouraging, for the constant supply of good music and funny reels and for almost convincing me to try machine learning. To Camille, for our ability to make everything solar themed if we put our minds to it. To Steph, for always being ready to help or give me advice and for the fun memories of our adventures around Japan.

Jenny F. and Matthijs, I am so glad to have shared this PhD journey with you. Thank you for your friendship, fun board game nights and for infinitely multiplying my knowledge of F1. Jenny, thank you for giving me the pep talk I needed to jump on that zip line, or I would still be up in that tree instead of writing this thesis.

To Miruna and Anna, thank you for always being there for me, encouraging me and for listening so enthusiastically to all my solar fun facts.

Finally, I would like to thank my parents. I would not be who I am without their love and constant support. They deserve far more credit than I can express in words.

Contents

List of Figures

List of Tables

Chapter 1

An Introduction to the Sun

1.1 The Structure of the Sun

The Sun is a G-type main sequence star. Formed approximately 4.6 billion years ago, it is located at the center of the solar system, containing over 99% of its total mass. The structure of the Sun can be broadly divided into the solar interior and the solar atmosphere. Both the interior and the atmosphere are made up of plasma, i.e. an ionised and magnetised gas, but conditions strongly vary in different parts of the Sun's structure. The solar interior has three main components: the core, the radiative zone and the convection zone. The solar atmosphere is divided into the photosphere, chromosphere, transition region and corona. There is also a constant stream of particles traveling away from the Sun and into the solar system, called the solar wind. These layers are described in more detail in the sections below.

1.1.1 The Solar Interior

The Sun's core extends up to approximately 0.25 $R_\odot$ and contains about half of the total mass of the Sun. This region is very dense and very hot (approximately 15 MK). In the core, nuclear fusion of H into He occurs via the proton-proton chain and releases large amounts of energy (e.g. Phillips, 1995).

The layer just outside the core, extending from about 0.25 $R_\odot$ to about 0.67 $R_\odot$, is the radiative zone. In this region, the outward transport of energy generated in the core is dominated by radiation, i.e. by ions emitting photons (mostly in the γ-rays and X-rays) which travel a very short distance before being reabsorbed by other

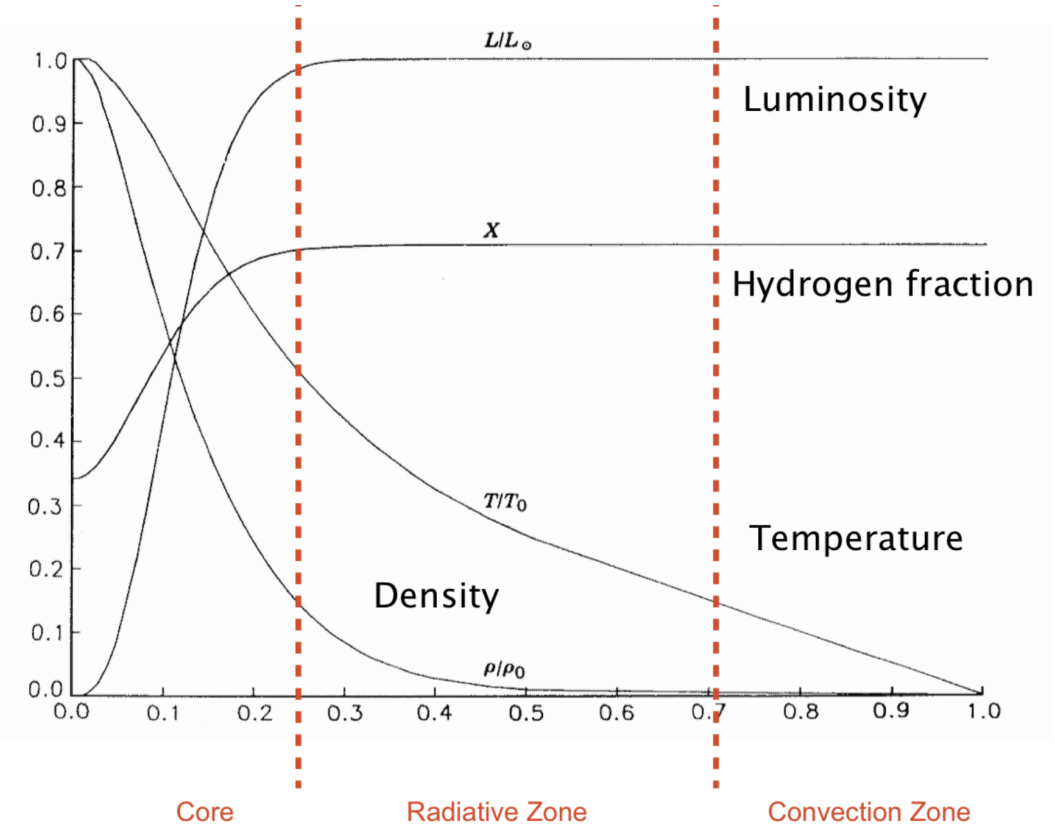

Figure 1.1: Temperature, density, luminosity, and H composition variation in the solar interior. Image from Baker (2011) after Bahcall and Ulrich (1988).

ions (e.g. Antia et al., 2003). Moving away from the core, temperature decreases, from approximately 7 MK to 1-2 MK, and so does density (e.g. Phillips, 1995).

The next layer, extending from about 0.67 $R_\odot$ to 1.0 $R_\odot$, is the convective zone. In this region, the decrease in temperature and associated increase in opacity make it more difficult for radiation to escape, so energy transport via convection dominates (e.g. Antia et al., 2003). Plasma parcels at the bottom of the convection zone expand and move upwards. As they move upwards, these plasma parcels cool down and, when they reach the top of the convection zone, they become cooler and denser than their surroundings, so they sink back to the bottom of the convection zone and the cycle continues. This convection process can be seen in observations as convection granules on the Sun's surface in the visible part of the spectrum. The thin interface layer between the radiative zone and the convective zone is called the tachocline (e.g. Antia et al., 2003). This layer marks the separation between the

rigid rotation of the radiative zone and the differential rotation of the convection zone. This results in strong rotational shear, which is believed to play an important role in the generation of large scale magnetic fields in the solar dynamo.

1.1.2 The Solar Atmosphere

The photosphere is the visible surface of the Sun. It is approximately 100 km thick, and has a blackbody temperature of approximately 5762 K (e.g. Aschwanden, 2004). Since it is located at the top of the convection zone, features such as small scale granulation driven by convective flows from below can be observed in the photosphere (e.g. Antia et al., 2003). Solar magnetic fields also play an important role here. When buoyant magnetic flux tubes from the solar interior rise and emerge through the photosphere, they form regions of high magnetic flux density called sunspots (see Figure 1.3a). Sunspots are made up of a dark central umbra surrounded by a penumbra (e.g. Phillips, 1995). In a sunspot, convection is inhibited by the high magnetic flux density, which reduces the temperature in the sunspot region compared to the rest of the photosphere, making them appear as dark features. Sunspots are typically surrounded by larger brighter features called faculae (see Figure 1.3c).

The chromosphere is the layer just above the photosphere. Moving outwards from the photosphere, density decreases. Temperature, however, first decreases, reaches a minimum approximately 200 km into the chromosphere, and then begins to increase again (e.g. Gabriel and Mason, 1982, see Figure 1.2). The mechanisms responsible for the chromospheric heating which drives the increase in temperature are not yet understood. As height increases in the chromosphere, the plasma β, defined as the ratio between the plasma pressure and the magnetic pressure (e.g. Aschwanden, 2004):

$$\beta = \frac{p_{\text{plasma}}}{p_{\text{magnetic field}}} = \frac{n_e k_B T_e}{B^2/8\pi}, \tag{1.1}$$

begins to decrease. This is caused by the decrease in density and, therefore, decrease in the plasma pressure. The result is that magnetic fields start to dominate the structure in the chromosphere. The plasma in the solar atmosphere is “frozen

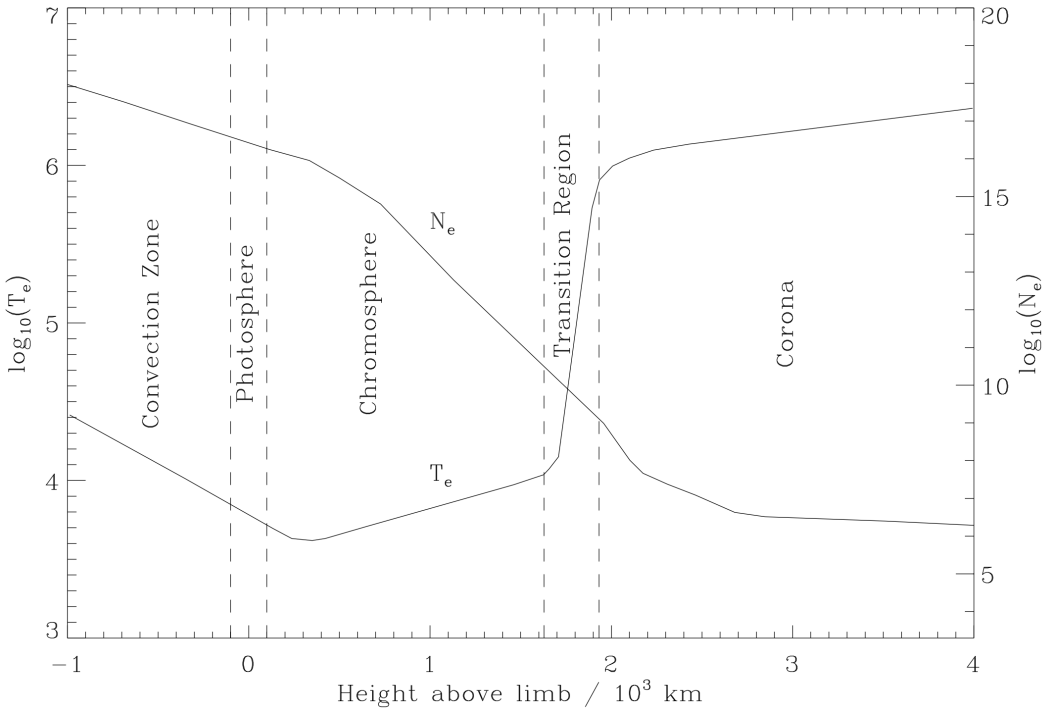

Figure 1.2: Plane parallel model showing the variation in temperature (T_e; K) and density (N_e; cm^{-3}) with height across the different layers of the upper solar interior and the solar atmosphere. Image from Gallagher (2000) after Gabriel and Mason (1982).

in", meaning that plasma and magnetic field move together. In the high plasma β environment of the photosphere, plasma pressure dominates and the magnetic field is moved around by plasma motions. In the chromosphere, however, magnetic fields begin to dominate and move plasma around with them (e.g. Aschwanden, 2004).

At the top of the chromosphere, there is a thin transition region of only about 100 km, where the temperature increases from 10^4 to 10^6 K (see Figure 1.2). The driver behind this sudden temperature increase, known as the coronal heating problem, is unknown, making this one of the biggest mysteries of solar physics (see e.g. Mariska, 1992). There are two main branches of theories that are proposed to explain this phenomenon: dissipation of magnetic stress, referred to as DC heating, and the dissipation of Alfvén waves, referred to as AC heating (Klimchuk, 2006).

The outermost layer of the solar atmosphere is the solar corona. This region extends from approximately 2000 km above the photosphere out into the heliosphere. The corona has much higher temperature (on the order of 1-2 MK, but can go up to

20 MK in the flaring corona), and much lower density (on the order of 7-10 cm^{-3}) than the photosphere and the chromosphere underneath. Similar to the upper part of the chromosphere, the corona is a low plasma β environment (e.g. Aschwanden, 2004), so plasma flows along magnetic field lines, following their motion (see Figure 1.3e-h) and emits the strongest in the EUV and X-ray parts of the spectrum (e.g. Phillips, 2009). Structures with different magnetic field properties and emission patterns can be observed in the corona such as active regions, quiet Sun and coronal holes. Active regions are bright hot regions associated with strong magnetic actvity and the presence of sunspots in the photosphere below (see Section 1.2.1). The quiet Sun is dominated by weaker and smaller scale magnetic activity and quiet Sun plasma typically has lower temperatures than active regions. Coronal holes are regions of open magnetic field lines that connect out into the heliosphere. They typically appear as dark in emission lines that form above approximately 1 MK. An interesting aspect of the plasma composition of the solar corona is that it varies spatially and in time, although the driver of this process is not fully understood.

1.1.3 The Solar Wind

The solar wind is a stream of plasma flowing from the Sun's corona along open magnetic field lines out into the heliosphere. There are two main types of solar wind, primarily based on the properties of the solar wind plasma and its origin on the Sun. The fast solar wind has speeds higher than approximately 500 km/s and originates from coronal holes (e.g. Aschwanden, 2004). The slow solar wind has speeds below 500 km/s and, while some studies suggest it might originate from open magnetic field lines neighbouring solar active regions or the boundaries of coronal holes, its origins are yet not fully understood. Proposed theories regarding the origin of the slow solar wind are discussed in more detail in Section 2.4.4.

1.2 Solar Magnetic Activity

1.2.1 Active Regions

Active regions are the locations of strong magnetic activity driven by the emergence of a magnetic flux tube through the photosphere and its expansion into the

chromosphere and the corona (van Driel-Gesztelyi and Green, 2015). Magnetic flux tubes are generated by the solar dynamo. They originate from the bottom of the convection zone (in the tachocline) and are brought upwards to the surface by magnetic buoyancy (van Driel-Gesztelyi and Green, 2015). Once the flux tube has emerged, the bipolar magnetic configuration of the active region can be observed in a magnetogram (see Figure 1.3b). Regions of concentrated magnetic field usually have one or more associated sunspots, which are visible in white light images (see Figure 1.3a). Bright faculae are also seen in dispersed magnetic fields (see Figure 1.3c). In the corona, the presence of an active region is revealed by plasma emission in the EUV range (see Figure 1.3d-h), but also in a wide range of wavelengths across the EM spectrum, from radio to X-rays or even γ-rays during flares.

The evolution of an active region has two main phases: the emergence phase and the decay phase. In the emergence phase, the magnetic flux tube is rising through the photosphere and expanding into the corona. The photospheric magnetic flux is increasing. Opposite magnetic polarities move away from each other and same polarity magnetic field lines merge to form pores (dark photospheric features), which then merge further forming sunspots (see Figure 1.3a). The active region magnetic field starts reconnecting with the surrounding field soon after the start of the emergence, forming new magnetic connections. Flares are more frequent in the emergence phase, with flare activity peaking when the active region sunspots are at the maximum development, just before the active region enters its decay phase (Waldmeier, 1955; Choudhary et al., 2013).

Active regions enter their decay phase once all the magnetic flux emerged (van Driel-Gesztelyi and Green, 2015), or possibly even before that (e.g. McIntosh, 1981). In the decay phase, sunspots start to be eroded as a result of supergranular buffeting: horizontal plasma flows disperse the eroded field fragments in all directions, the sunspot shrinks and eventually breaks up. The magnetic field becomes progressively more dispersed in both polarities. This phase is marked by a decrease in photospheric magnetic flux density which is also accompanied by a decrease in other plasma parameters such as temperature and emission measure

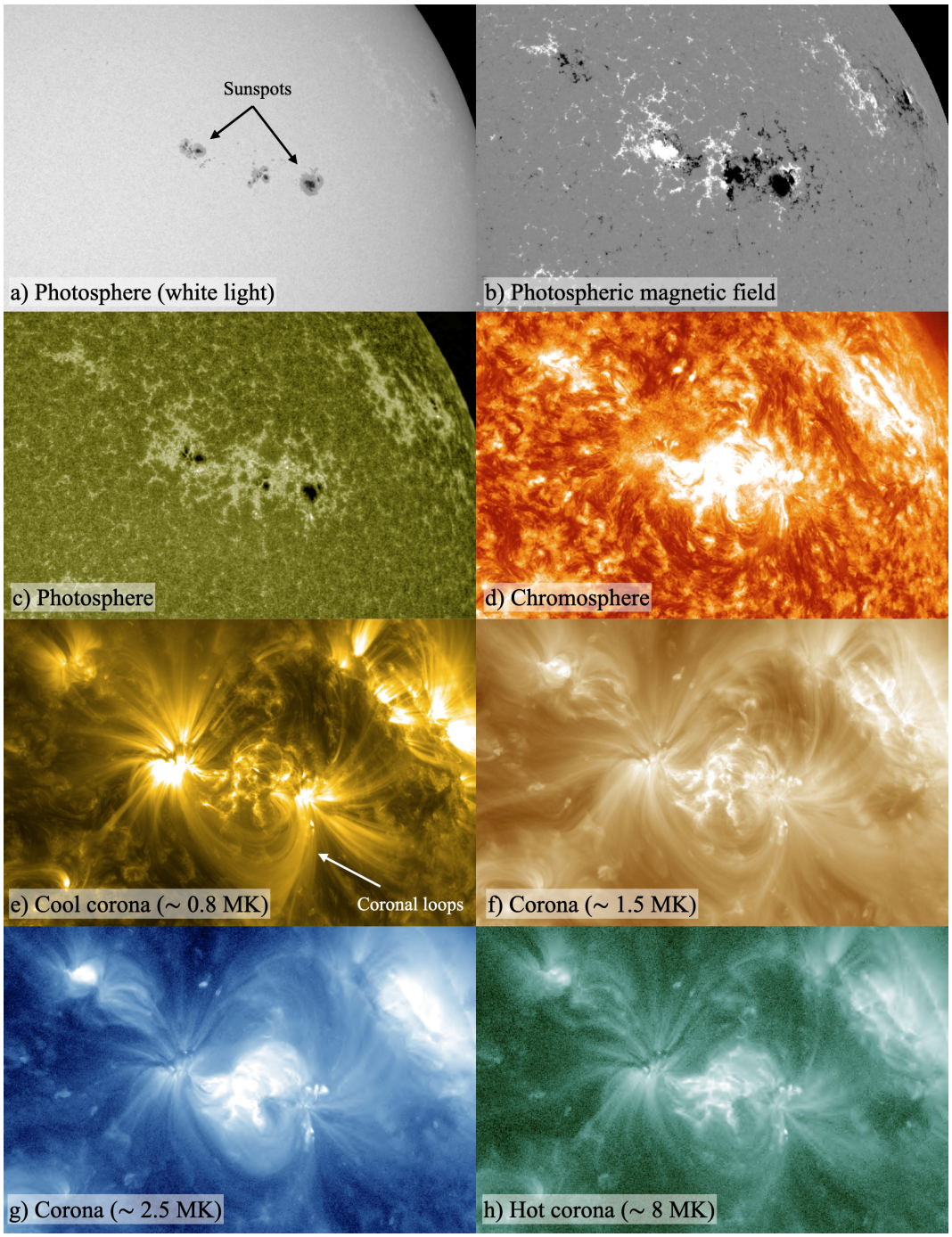

Figure 1.3: Example of active region structure across the different layers of the solar atmosphere: a) photospheric white light emission (HMI continuum); b) photospheric magnetic field from (HMI magnetogram); c) photospheric emission (AIA 1600 Å passband), although note that, while typically assumed to capture the photospheric continuum emission, the AIA 1600 Å channel is likely dominated by emission from chromospheric lines during flares (Simões et al., 2019); d) chromospheric emission (AIA 304 Å passband); e) emission from the cooler ($\sim$ 0.8 MK) coronal plasma (AIA 171 Å passband); f) emission from coronal plasma at $\sim$ 1.5 MK (AIA 193 Å passband); g) emission from coronal plasma at $\sim$ 2.5 MK (AIA 335 Å passband); h) emission from the hot ($\sim$ 8 MK) coronal plasma (AIA 94 Å passband). Image created using the ESA JHelioviewer tool (Müller et al., 2017).

(Driel-Gesztelyi et al., 2003). Small amounts of magnetic flux are carried towards the active region internal polarity inversion line (PIL) where they undergo flux cancellation that can lead to gradually building a flux rope or filament (van Ballegooijen and Martens, 1989) which can erupt. As the active region evolves and the field disperses further, the internal PIL extends as well and can, in some cases, lead to forming long filaments or filament channels that can live in the Sun's atmosphere for multiple rotations. External PILs, i.e. boundaries with neighbouring active regions, show flux cancellation as well, but it may involve less flux.

AR size	**Magnetic flux (Mx)**	**Lifetime**	**Rise/Lifetime**
Large	$5 \times 10^{21} - 3 \times 10^{22}$	weeks-months	3-15 %
Small	$1 \times 10^{20} - 5 \times 10^{21}$	days-weeks	15-27 %
Ephemeral	$3 \times 10^{18} - 1 \times 10^{20}$	hours - 1 day	$\simeq$30%

Table 1.1: Classification of active regions, following the definitions of van Driel-Gesztelyi and Green (2015).

The size of an active region is defined by its total magnetic flux at maximum development. The lifetime of an active region is defined in van Driel-Gesztelyi and Green (2015) as the time period it can be identified in magnetic field observations as a distinct bipole. This is proportional to the total magnetic flux of the active region at its maximum development (Harvey and Zwaan, 1993), so larger active regions are longer lived. The lifetime is also influenced by the active region's interactions with the surrounding field and the level of activity on the Sun at the time. For example, flux emergence and subsequent flux cancellation within the dispersed field of a decaying active region can lead to shifting of the internal PIL of the active region.

The duration of the emergence and decay phases of an active region are asymmetrical (Harvey, 1993): the emergence phase is typically shorter than the decay phase and the ratio between the length of the emergence phase and the lifetime decreases with active region size (see Table 1.1). For ephemeral active regions, which have lifetimes of hours to about 1 day, the length of the decay phase is comparable to the length of the emergence phase. For large active regions, however, which

have a high amount of total magnetic flux, the decay phase is much longer than the emergence phase.

According to Joy's law, bipolar active regions show a systematic deviation from E-W alignment, with the leading polarity being closer to the equator than the following polarity (Hale et al., 1919). There are also asymmetries in the motion and stability of the leading and following polarities. In the emergence phase, the leading polarity converges into a more compact and longer-lived sunspot or sunspot group, while the following polarity may form shorter-lived spots and become dispersed more easily (Hale and Nicholson, 1938). As the flux tube rises through the photosphere, the magnetic tension force is causing the opposite polarities to move away from each other. The leading polarity moves faster in the west direction than the following polarity moves in the east direction, hence the internal PIL is statistically closer to the centre of gravity of the following polarity than the leading (van Driel-Gesztelyi and Petrovay, 1990).

Active regions have a clustering tendency, as they are likely to emerge within or in the immediate vicinity of older active regions. It was found that active regions are 10 to 22 times more likely to emerge within an already existing active regionthan in the quiet Sun (Harvey and Zwaan, 1993). When active regions emerge at the site of an existing active region, they can form 'activity nests'; approximately 50% of active regions are part of an activity nest (Schrijver and Zwaan, 2000). These can be observed for multiple solar rotations; the longest lived activity nest of solar cycle 21 consisted of 29 active regions and persisted for 20 solar rotations (Gaizauskas et al., 1983). New flux emergence within a nest leads to flux cancellation; most of the flux cancellation takes place within the boundary of the activity nest without diffusing out of it. Nesting activity can lead to the formation of large active regions with a high level of complexity.

1.2.2 Solar Flares

Solar flares are powerful events of explosive energy release in the solar corona. They are characterised by strong emission across the entire electromagnetic spectrum, from radio to γ-rays. Flares are a result of magnetic reconnection. When the

Class	X-ray flux [W/m^{-2}]
A	$< 10^{-7}$
B	$10^{-6} - 10^{-7}$
C	$10^{-5} - 10^{-6}$
M	$10^{-4} - 10^{-5}$
X	$< 10^{-7}$

Table 1.2: Classification of solar flare magnitude using GOES soft X-ray flux.

magnetic energy in a structure increases, for example as a result of coronal loop footpoint motions or flux emergence, magnetic diffusion can begin to dominate on small scales. This enables the magnetic field to reconfigure itself back into a lower energy state via reconnection. The previously stored magnetic energy is released leading to heating, particle acceleration, electromagnetic radiation and waves. The amount of energy released varies from one flare to another. The main way of classifying flares by the energy they release is via the soft X-ray emission they produce at $1 - 8$ Å, as measured by GOES (see Section 4.4). Flare magnitudes definitions are given in Table 1.2: they decrease on a base 10 logarithmic scale from X (largest type of solar flare), M, C, B to A (smallest type of solar flare). Solar flares, particularly the larger X-class or M-class ones, can be associated with eruptions of highly magnetised plasma, called coronal mass ejections (CMEs), as well as with the acceleration of solar energetic particles (SEPs).

The timeline of a solar flare is broadly divided in three main phases, characterised by emission at different wavelengths. In the preflare phase, the plasma around the reconnection region starts to heat up and emit in the EUV and soft X-rays (e.g. Benz, 2008). Most of the magnetic energy is released in the impulsive phase, which leads to strong heating as well as acceleration of electrons and ions. This phase lasts for tens of seconds to tens of minutes (e.g. Fletcher et al., 2011) and is characterised by a sharp increase in soft X-rays emission, the appearance of hard X-ray emission from the chromospheric footpoints of flare loops (hard X-ray emission is also produced in the corona, but it is much weaker), a peak in EUV emission as well as an increase in microwaves emission (e.g. Benz, 2008). In the decay phase, the plasma cools down, marked by the brightening of progressively

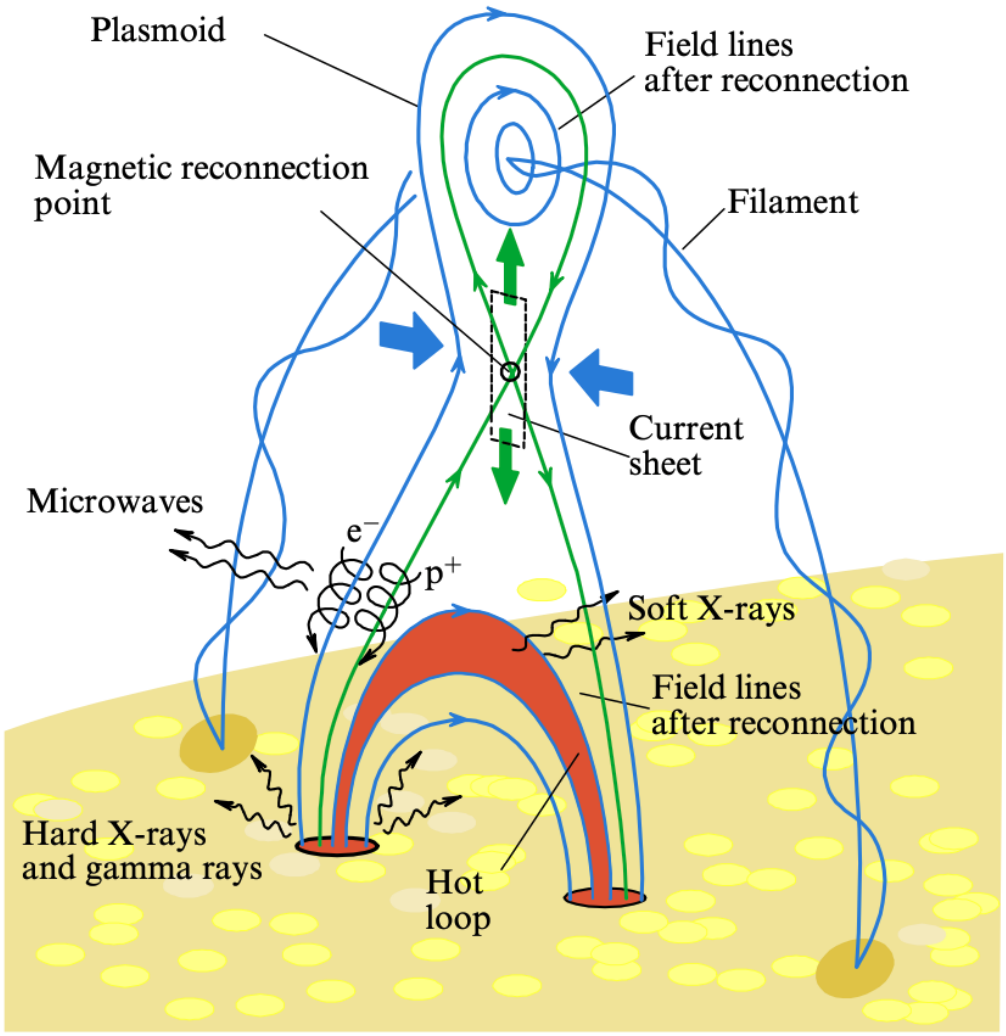

Figure 1.4: A simple schematic of the standard flare model. Image from Lysenko et al. (2020) after Shibata et al. (1995).

cooler EUV lines. The hard X-ray emission stops after the end of the impulsive phase and the soft X-ray emission decreases slowly over minutes to hours.

In the eruptive standard flare model (illustrated in Figure 1.4), flares are produced by the eruption of a filament or flux rope (Shibata et al., 1995). Initially, the flux rope sits in the solar atmosphere underneath an overlying magnetic field arcade. As the flux rope is destabilised and starts to rise, oppositely oriented magnetic field lines making up the arcade are drawn towards each other (see blue arrows in Figure 1.4). Under certain conditions, diffusion can start to dominate over small scales (where the magnetic Reynolds number, R_m, is sufficiently small) between these op-

positely oriented field lines, creating a current sheet where magnetic reconnection can take place.

Magnetic reconnection separates the initial arcade into two structures, one below and one above. Above the reconnection region, newly reconnected field lines form a plasmoid feature wrapped around the flux rope. As reconnection goes on, more and more of the overlying arcade is removed and eventually the flux rope erupts as a CME. Beneath the reconnection region, the newly reconnected field lines move back down towards the Sun, forming the flare loops.

Electrons and ions accelerated as a result of the reconnection travel down to the chromospheric footpoints of the flare loops.In this process, electrons emit radiation in the microwaves. When they reach the loop footpoints, they are decelerated by the increasingly higher density of the chromosphere and lose their energy via Coulomb collisions. This energy deposition at the chromospheric footpoints has two effects: 1) it heats up the plasma to millions of degrees and 2) it produces emission in the hard X-rays via the Bremsstrahlung process (e.g. Krucker et al., 2008, see Section 3.2.3.2). The pressure increases, causing the plasma to expand along the magnetic field line. The upwards expansion at speeds in the order of 100 km s^{-1} fills the coronal loop with chromospheric plasma, and, to conserve momentum, the plasma in the cooler and denser layers below moves downwards, causing chromospheric condensation. The energy transfer from the reconnection site to the chromosphere can happen via thermal conduction, leading to gentle evaporation typically observed in the preflare and decay phase, or via free-streaming non-thermal particles, leading to explosive evaporation observed in the impulsive phase (Fisher et al., 1985a,b,c). The main difference between the two types of evaporation is that the velocities observed are higher in the explosive evaporation. The evaporation velocity is directly related to the temperature to which the plasma was heated (Milligan and Dennis, 2009; Young et al., 2013) and it also varies with time, increasing quickly after the peak of the flare and then decreasing back to zero after the heating stops (Brosius, 2013). Another, more recently proposed mechanism of energy transfer from the reconnection site in the corona to the chromospheric part of the flare loops is via

Alfvénic wave heating (e.g. Reep and Russell, 2016; Reep et al., 2018). As heating decreases when the flare enters its decay phase, chromospheric evaporation slows down and the flare loops cool, becoming visible in the EUV (e.g. Fletcher et al., 2011).

1.3 Thesis Outline

The work outlined in this thesis explores the variations in elemental abundances observed in the solar corona in relation with various aspects of the observed magnetic activity specific to active regions and solar flares. An overview of previous observations of variation of plasma composition in the solar corona is provided in Chapter 2, with different models proposed to explain this phenomenon being discussed. Measurements of the relative abundances of different elements in the solar corona are obtained from complex spectroscopic analysis of spectral data. An overview of how this emission is formed in the coronal plasma environment and how it is used for abundance measurements is provided in Chapter 3. The various instruments used for the work in this thesis are described in Chapter 4. The work presented in this thesis explores the link between coronal elemental abundances and active region evolution in Chapter 5, wave activity in Chapter 6 and radiative loop cooling in Chapter 7. Finally, the main conclusions and possible directions for future work are presented in Chapter 8.

Chapter 2

Solar Plasma Composition

The chemical composition of the Sun consists of approximately 71% H, 27% He and 2% heavier elements by mass fractions (e.g. Anders and Grevesse, 1989). The heavy elements are not produced in the core of the Sun, since the Sun is a main sequence star and, more importantly, is not massive enough to produce them via fusion. These heavy elements likely originate from supernovae remnants and were present in the solar nebula before the Sun formed, making the Sun a second generation star.

2.1 Solar Photospheric Abundances

The relative abundances of different elements are typically measured from spectroscopic observations of the solar photosphere (initiated by Payne, 1925; Russell, 1929) and/or mass spectroscopy of primitive meteorites (starting with the influential work of e.g. Goldschmidt, 1922, 1938). The two methods are highly complementary: for some elements, more precise composition measurements are obtained from the photospheric spectroscopic method (if the element has sufficiently strong emission lines in the visible part of the spectrum), while for others from meteorite observations (for noble gases or if the element has weak/no emission lines in the visible part of the spectrum). It is common to combine estimates using these two methods to obtain a complete solar abundance set. In addition, abundances of noble gases are also determined from coronal abundances (e.g. Feldman and Widing, 1990; Young, 2005). Finally, abundance estimations can also be made from mod-

Element	FIP (eV)	Photospheric Abundance	
		Asplund et al. (2009)	Scott et al. (2015b,a)
K	4.3	5.03 ± 0.09	5.04 ± 0.05
Al	6.0	6.45 ± 0.03	6.43 ± 0.04
Ca	6.1	6.34 ± 0.04	6.32 ± 0.03
Ni	7.6	6.22 ± 0.04	6.20 ± 0.04
Mg	7.6	7.60 ± 0.04	7.59 ± 0.04
Fe	7.9	7.50 ± 0.04	7.47 ± 0.04
Si	8.2	7.51 ± 0.03	7.51 ± 0.03
S	10.4	7.12 ± 0.03	7.12 ± 0.03
P	10.5	5.41 ± 0.03	5.41 ± 0.03
C	11.3	8.43 ± 0.05	-
H	13.6	12.00	-
O	13.6	8.69 ± 0.05	-
N	14.5	7.83 ± 0.05	-
Ar	15.8	6.40 ± 0.13	-
Ne	21.6	7.93 ± 0.10	-
He	24.6	10.93 ± 0.01	-

Table 2.1: Properties of the main elements relevant for the work presented in this thesis: fist ionization potential from the NIST Atomic Spectra Database[1] (Kramida et al., 2023), photospheric abundances measured by Asplund et al. (2009) and, where available, updated photospheric abundances by Scott et al. (2015b,a). Abundances are given in the usual logarithmic scale relative to H ($A_X = \log(N_X/N_H) + 12.00$).

elling the solar interior and testing what abundance values provide best agreement with helioseismic observations. Currently the He abundance is the only one that is determined in this way (Basu and Antia, 2004). Abundance sets have undergone various revisions over the last few decades. Taking Anders and Grevesse (1989) as a starting point, the main recommended abundance sets include Grevesse and Sauval (1998), Grevesse et al. (2007), Asplund et al. (2009), Caffau et al. (2011), Scott et al. (2015b,a), and, most recently, Asplund et al. (2021). The relative photospheric abundances considered for the elements relevant for the work presented in this thesis are given in Table 2.1.

[1] Available online at: https://physics.nist.gov/PhysRefData/ASD/ionEnergy.html

2.2 Plasma Composition Variations in the Solar Corona

While the composition of the photosphere is relatively well known and approximately constant (Asplund et al., 2009; Scott et al., 2015b,a), the composition of the corona varies with different magnetic structures and in time. The elemental abundance variation in the corona and the solar wind strongly depends on the first ionisation potential (FIP) of the element (Meyer, 1985a,b; Feldman et al., 1992) and not on other parameters such as mass or charge (Meyer, 1991). Elements with a low FIP (<10 eV) such as Si, Fe, Ca, are enhanced in the corona, compared to high-FIP (>10 eV) elements such as S, Ar, O, which maintain their photospheric abundances (see e.g. Widing and Feldman, 1995). Studies and models suggest that this is due to a preferential transport of low-FIP elements from the chromosphere to the corona. This is called the FIP effect. The degree of enhancement of an element in the corona is given by the FIP bias parameter:

$$\mathrm{FIP_{bias}} = \frac{\text{coronal elemental abundance}}{\text{photospheric elemental abundance}}. \tag{2.1}$$

A detailed explanation of the spectroscopic methods for estimating the FIP bias in the solar corona is provided in Section 3.3.7. Typical FIP bias values vary for different coronal structures. Coronal hole plasma has a FIP bias close to 1, i.e. photospheric composition (Feldman and Widing, 1993; Brooks and Warren, 2011). In the quiet Sun, slightly increased values are observed with the FIP bias going up to 1.5-2 (Feldman and Widing, 1993). Active regions show higher FIP bias: the first composition studies using Skylab spectroheliogram measurements registered values of up to 7-8 (eg. Widing and Feldman, 2001), while more recent studies using *Hinode* EIS data found values of 2-4 (Baker et al., 2013, 2015; Brooks et al., 2015; Baker et al., 2018). An extensive overview of typical FIP bias values found in various coronal structures is provided by Del Zanna and Mason (2018).

The presence of this variability is also supported by in-situ measurements of the chemical composition of the solar wind, which also show a variable composition

(von Steiger and Schwadron, 2000). The solar wind shows an inverse correlation between speed and FIP bias (Geiss et al., 1995), with typical FIP bias values of 1 for the fast solar wind and higher values of up to 3-4 for the slow solar wind (Meyer, 1985a,b; Gloeckler and Geiss, 1989). There is growing consensus that the elemental composition is likely the only plasma characteristic that does not change as the solar wind propagates into the heliosphere, unlike other parameters such as density, particle distributions etc. This is because the FIP effect is believed to take place in the chromosphere (see Section 2.3) and not affect the composition of a plasma once it leaves the transition region. Hence, it can be used as a tracer of solar wind source regions (e.g. Brooks et al., 2015; Fu et al., 2017). It is widely accepted that the fast solar wind originates from coronal holes, and the lack/low level of FIP effect observed both remotely in coronal holes and in situ in the fast solar wind is in agreement with this. The sources of slow solar wind, however, are still not yet fully understood. Given that active region FIP bias levels are similar to those observed in the slow solar wind, active region outflows are considered likely potential source regions of the slow solar wind (e.g. Brooks and Warren, 2011; Brooks et al., 2015).

The chemical composition of a given part of the Sun's corona (expressed as the FIP bias) is the result of three main processes (see also Figure 2.1):

1. **The FIP effect**: this is the main process that generates the low-FIP enhancements in the first place and there is general agreement among theoretical models that this takes place in the chromosphere (see Section 2.3). Ionized low-FIP elements are preferentially accelerated upwards at the chromospheric footpoints of coronal loops, resulting in an abundance change at the top of the chromosphere/transition region.

2. **Transport mechanisms**: plasma with changed abundance must then be transported from the top of the chromosphere to the corona to change the coronal abundance. The flux and speed of this upward transport, which varies depending on coronal conditions, dictates the supply of plasma with changed abundance to the corona. This influences the final FIP bias value of the coronal region, as well as the time taken to reach it; the newly transported plasma

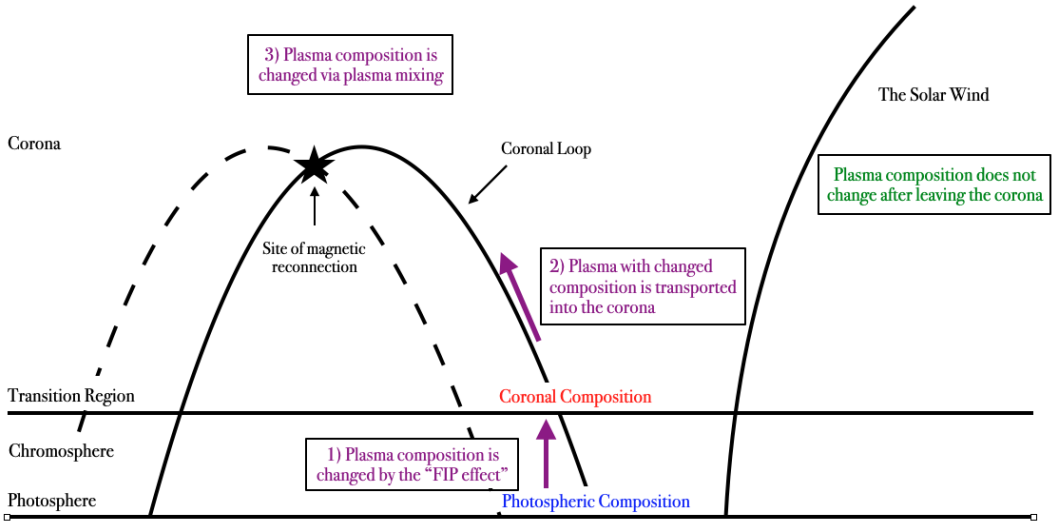

Figure 2.1: Schematic illustrating the main drivers that contribute to plasma composition changes in the solar corona.

mixes with the plasma that was already there, so it takes some time until the abundance of the new plasma dominates. In solar flares, the upwards transport is likely due to chromospheric evaporation (Warren, 2014) and changes the coronal plasma composition within minutes. The upwards transport appears to be much slower in quiescent conditions. The FIP bias in emerging active regions was found to increase almost linearly with time over a few days days (Widing and Feldman, 2001). It is difficult, however, to disentangle what takes longer in this scenario: for the active region to reach the right conditions for the FIP effect to start, for the plasma to be transported upwards or for the fractionated plasma to mix with the plasma already present in the corona.

3. **Plasma mixing**: coronal plasma composition can also be changed as a result of magnetic reconnection in the corona. If magnetic field lines carrying plasma with different composition reconnect, the plasma along these loops will mix, resulting in a mixed FIP bias along the post-reconnection magnetic field lines. This process is independent of the FIP effect itself.

In addition, the FIP bias in a given location can vary depending on the spectroscopic diagnostic used to measure it. Elements are typically divided into low-FIP and high-FIP, but the intensity of the FIP effect varies (for low-FIP elements) with

the FIP of the element as well (Laming, 2015; Dahlburg et al., 2016). Low-FIP elements that have similar FIP values show similar FIP bias values in the corona (e.g. Dennis et al., 2015; Ko et al., 2016), but those with a large separation in FIP show different FIP bias values (e.g. Sylwester et al., 2014; To et al., 2021). This aspect is investigated further in Chapter 6. Other factors, such as the uncertainty in the photospheric abundances of the elements involved (see Section 2.1) or the temperature formation of the lines involved (see Section 3.3.7) can also lead to different diagnostics indicating different values for the FIP bias. All the factors listed above could explain, for example, the apparently very different values obtained in active regions using the Mg/Ne ratio in Skylab spectroheliogram measurements (eg. Widing and Feldman, 2001) and the Si/S one in *Hinode* EIS observations (e.g. Baker et al., 2013). For this reason, the diagnostic used and the plasma temperature it captures are both indicated, alongside with the FIP bias value obtained, for the measurements discussed in this chapter.

2.3 The FIP Effect

2.3.1 Early Models

Various processes have been proposed to be responsible for the FIP effect, such as diffusion or inefficient Coulomb drag (e.g. von Steiger and Geiss, 1989; Marsch et al., 1995; Pucci et al., 2010; Bø et al., 2013), thermoelectric driving (Antiochos, 1994), chromospheric reconnection (Arge and Mullan, 1998), ion cyclotron wave heating (Schwadron et al., 1999) or Alfvén ionization (Diver et al., 2005). Among the many candidates, a collisionless wave–particle mechanism based on the ponderomotive force (Laming, 2004, 2015) appears to be able to describe this phenomenon more realistically than previously suggested mechanisms.

2.3.2 The Ponderomotive Force Model

The ponderomotive force model (Laming, 2004, 2015, 2017; Laming et al., 2019; Laming, 2021) suggests that the preferential upwards transport of low-FIP elements in the chromosphere, also called the fractionation process, is driven via ponderomotive forces that arise as a consequence of the interaction between magneto-

hydrodynamic waves and the plasma environment of the solar chromosphere and transition region.

2.3.2.1 The Ponderomotive Force

The ponderomotive force is a non-linear electromagnetic force that acts on plasma particles in the presence of an oscillating electromagnetic field. It originates from a second order term incorporating the $\rho\delta\mathbf{v}\cdot\nabla\delta\mathbf{v}$ and $\delta\mathbf{J}\times\delta\mathbf{B}/c$ terms in the MHD momentum equation (Rakowski and Laming, 2012). It is essentially generated by the interaction between Alfvén waves and particles through the refractive index of the plasma. Here, the focus is on the time averaged ponderomotive force, since this is the one that drives the fractionation process. The ponderomotive force on a particle i (see Laming, 2009, 2015, and references therein for full derivation) is given by:

$$F_i(z) = \frac{q_i^2}{4m_i}\frac{d}{dz}\left[\frac{\delta E_P(z)^2}{(\Omega_i^2-\omega^2)}\right], \tag{2.2}$$

where q_i and m_i are the charge and mass of the particle, δE_p is the linear perturbation of the wave peak transverse electric field, Ω_i is the particle cyclotron frequency, ω is the Alfvén wave frequency, and z is the position along the loop. The particle cyclotron frequency is given by:

$$\Omega_i = \frac{q_i B(z)}{m_i}. \tag{2.3}$$

Note that the ponderomotive force is proportional to the square of the electric charge of the particle. Therefore, the direction of the force does not depend on whether the particle is positively or negatively charged, so both ions and electrons are moved in the same direction. Substituting Eqn. 2.3 into Eqn. 2.2 and taking the low-frequency limit, $\omega \ll \Omega_i$ (an appropriate approximation for Alfvén waves in the solar atmosphere), the ponderomotive force becomes :

$$F_i(z) = \frac{m_i}{4}\frac{d}{dz}\left[\frac{\delta E_p(z)^2}{B(z)^2}\right]. \tag{2.4}$$

Note that, in this low-frequency limit, the ponderomotive acceleration, $a_i = F_i/m_i$, is independent of particle mass. This is in line with the mass-independent fractionation observed on the Sun. It is also independent of particle charge, so long as the particle is charged. Since the perturbation of the wave transverse electric field is given by:

$$\delta E_p(z) = \delta v_p B(z), \tag{2.5}$$

where δv_p is the perturbation of the flow velocity, Eqn 2.4 can be rewritten as:

$$F_i(z) = \frac{m_i}{4}\frac{d}{dz}\delta v_p^2. \tag{2.6}$$

The perturbation of the flow velocity, δv_p, varies as a response to varying density of the ambient plasma. Therefore, the ponderomotive force is stronger in regions where the density gradient is stronger. In the solar atmosphere, this force arises in the chromosphere and the transition region as a consequence of the change in the wave direction when Alfvén waves refract in the high density gradient of the transition region and the chromosphere.

2.3.2.2 The Chromospheric Environment

The chromospheric vertical density structure can be broadly approximated to be exponential with a hydrostatic scale height of approximately 200 km (e.g. Hollweg, 1984). In fact, the density gradient is even higher in the upper the chromosphere. Moving upwards from the photosphere, the chromosphere is heated via mechanisms that are not fully understood. As a result, H starts to become ionized at approximately 1000-1500 km above the photosphere, reaching 50% ionization at 2000 km (Avrett and Loeser, 2008). The H radiative cooling, which is an important cooling process in the chromosphere, becomes increasingly more inhibited as height increases. This causes the temperature to rise and, therefore the density to decrease. As a result, the upper chromosphere has a steeper density gradient than the typical hydrostatic scale height. This is why the region where H becomes ionised is the region where the FIP effect is most likely to occur.

Ionization balance for H can be used to derive electron density (Avrett and Loeser, 2008). This is then used to calculate ionization balance for any elements of interest assuming collisional processes (such as ionization, radiative and dielectronic recombination; see Mazzotta et al., 1998). In the resulting chromospheric model, low-FIP elements have very high ionization fractions (>99%; see Laming, 2015, and references therein), while high-FIP elements ionization fractions are lower, i.e. more of the high-FIP elements are neutral in the chromosphere. It is for this reason that a higher fraction of the low-FIP elements experience the ponderomotive force and are preferentially transported upwards. Note that the described chromospheric model is a steady state model and does not treat dynamic events such as, for example, the effects of shock waves on H ionization and, therefore, on the ionization balance of the environment. The model also assumes that the chromosphere is initially fully mixed, i.e. that sufficient turbulence exists to inhibit any gravitational settling of other forms of diffusion that might occur and that there is no initial fractionation.

2.3.2.3 The Fractionation Process

The fractionation process is driven by the complex interaction between Alfvén waves and the chromospheric and transition region plasma. To simulate this, the model treats the parallel propagation of Alfvén waves along a closed loop (starting from the linearized MHD momentum and induction equations) to produce a profile of the ponderomotive acceleration across the whole loop. It covers the wave propagation in the corona from one loop footpoint to another and the interaction between the wave and the chromospheric environment at each footpoint (see Figure 2.2).

In the coronal part of the loop, the behaviour of a resonant Alfvén wave is similar to that of a standing wave. Here, resonance means that the wave travel time from one loop footpoint to the other is an integer number of wave half-periods. In the absence of significant density gradients in the corona, the coronal ponderomotive acceleration is approximately of $0-400$ cm s^{-2} (Laming, 2015), i.e. significantly lower than the solar gravitational acceleration of $g_{\odot} = 2.7 \times 10^4$ cm s $^{-2}$.

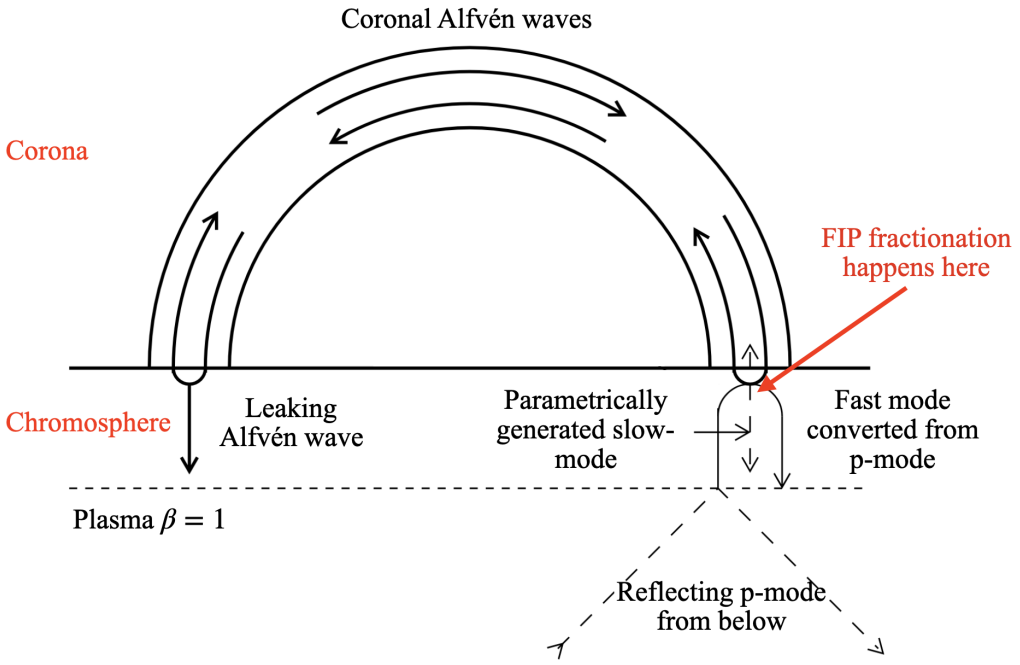

Figure 2.2: Schematic showing the fractionation process in a closed loop as a result of Alfvén wave activity, according to the ponderomotive force model. Coronal Alfvén waves (black thick lines) bounce between footpoints with a probability of being transmitted (leaking) into the chromosphere at each bounce. Alfvén waves reflecting at one footpoint can generate slow-mode (or p-mode) waves (straight dashed line) via a parametric process. Acoustic p-mode waves (straight dashed line below the $\beta = 1$ layer) originating from the solar envelope can either reflect back downwards or mode convert into fast mode waves (thin line) and reflect back downwards. All footpoint wave processes can happen at both footpoints, but here are split between the two for clarity. Adapted from Laming (2015).

In the chromospheric part of the loop, the ponderomotive acceleration is larger due to the steep density gradients. Here, the ponderomotive force acts on the ions preferentially transporting them in the direction of high wave energy density, particularly when the energy and momentum of the wave are high (in the $\omega \ll \Omega_i$ limit, and assuming the wave pressure dominates over the thermal pressure of the ionized component of the plasma; Laming, 2009, 2015). Strong coronal waves, leading to a high energy density in the corona, drive a strong FIP effect, as chromospheric ions are attracted upwards. Conversely, weak coronal waves and/or strong waves originating from below the chromosphere, leading to a higher energy density below the chromosphere, may lead to an inverse FIP effect, as chromospheric ions are attracted downwards. Note that the ionised fraction of high-FIP elements also ex-

perience the ponderomotive force, but this ionization fraction is significantly lower than the ionization fraction of low-FIP elements, so the upwards transport of high-FIP elements via the ponderomotive force is negligible compared to that of low-FIP elements. Theoretically, the enhancement of an element in a location in the chromosphere results in a depletion of that element in the layer below. However, since the density gradient is so high in this part of the solar atmosphere, this depletion is considered negligible relative to the density in the layer below.

Not all low-FIP elements show the same enhancement level: typically, the lower their FIP, the higher their ionization fraction, which leads to a stronger FIP effect. Once the fractionated plasma reaches the corona, the ponderomotive force becomes very small. In addition, all elements are ionised in the corona, so the small ponderomotive force (if present) no longer acts to separate low-FIP from high-FIP elements. Therefore, the fractionation process stops at transition region level. From here, fractionated chromospheric plasma is transported into the corona via a steady upward flow. This flow arises as the chromospheric response to heat being conducted downwards from the corona, driving the expansion of chomospheric plasma upwards along the loop. Typical speeds for this type of upflows in the chromosphere are approximately one to a few km s^{-1} (e.g. Bray et al., 1991; Imada and Zweibel, 2012). This indicates that it takes some time, likely hours to days (as suggested by Widing and Feldman, 2001), for the fractionated plasma to reach the corona, where it can be observed as enhanced relative abundances of low-FIP elements compared to the photosphere.

The fractionation pattern obtained, i.e. the relative level of enhancement of the various low-FIP elements, depends on the frequency of the wave driver. If the wave driver is at resonance with the coronal loop cavity, fractionation takes place in a small region at the top of the chromosphere and in the transition region. An important aspect of the fractionation process is that the propagation of the driver Alfvén wave through the lower atmosphere leads to parametrically generated slow-mode waves. In the resonant case, these parametrically generated slow-mode waves are significant in the region where the strongest fractionation happens. If the wave

driver is away from resonance, fractionation occurs over a wider layer of the chromosphere, as Alfvén waves are able to reach deeper into the chromosphere before being reflected upwards. This results in a different behaviour of the Alfvén waves and a few differences in fractionation pattern obtained, such as S being fractionated more (Rakowski and Laming, 2012). In addition, slow mode waves are generated more strongly deeper in the chromosphere, so, in this case, they play a more important role in amplifying the fractionation process. The strength of the fractionation process primarily depends on the amplitude of the wave driver: the larger the wave amplitude, the stronger the fractionation.

2.3.2.4 Observational Evidence

Detailed FIP bias observations in an active region found the strongest FIP bias at loop footpoints, and mild FIP bias along the active region loops (Baker et al., 2013), supporting this scenario of fractionated plasma being supplied to the corona via the chromospheric footpoints. Recent work by Baker et al. (2021b); Stangalini et al. (2021); Murabito et al. (2021) found magnetic fluctuations in the chromosphere being magnetically connected to regions of high FIP bias in the corona which also supports this theoretical model.

2.3.3 Ponderomotive Force Simulations

Numerical simulations by Dahlburg et al. (2016), using a 3D MHD model of the solar corona, support the presence of the ponderomotive acceleration at the chromospheric footpoints of solar coronal loops. This acceleration occurs as a by-product of wave-driven coronal heating and has the appropriate magnitude and direction to drive the observed FIP effect. In the simulations, the calculated Alfvén speed is comparable to the electron thermal speed. This makes it likely that, following the energy release driven by the reconnection event in the corona, Alfvén waves arrive at the chromospheric footpoints and drive fractionation before heat conducted down can drive a significant upflow. The likely drivers of this force are Alfvén or fast-mode waves. Unlike slow-mode waves, which are communicated through particle collisions, Alfvén or fast-mode waves are communicated through

electric and magnetic fields. Therefore, the ponderomotive force they drive is able to cleanly separate ions from neutrals. Simulation results show that the ponderomotive force is strongly intermittent, as would be expected if driven by waves released as a consequence of reconnection.

Recent work of Martínez-Sykora et al. (2023) extends the study of Dahlburg et al. (2016) by studying ponderomotive force properties in realistic 2.5D radiative MHD simulations, including nonequilibrium ionization effects, ion–neutral interaction effects, and a more accurate description of chromospheric radiative losses. Results show that nonequilibrium effects have a strong impact on the chromospheric region where fractionation occurs and should, therefore, be considered when modelling the FIP effect. A big difference between these results and the theory proposed by Laming (2017) is the direction of Alfvén wave propagation. These simulations suggest that the waves should propagate from the chromosphere to the corona, while Laming (2015, 2017) propose that the waves must have a coronal origin and, therefore propagate from the corona down to the chromosphere.

More recent numerical simulations by Réville et al. (2021) using a shell turbulence model investigated the effect of turbulence on the FIP fractionation in different configurations, with a particular focus on the potential of waves propagating along open field lines being able to drive fractionation. Results show that, under the assumption that turbulence is the main driver of coronal heating and solar wind acceleration, a ponderomotive force can appear in the chromosphere and the transition region. If energy is injected at scales of super granules, the force can be strong enough to create the FIP effect. However, that is not the case for smaller scales such as granules, for example. They also find that wave resonance (proposed by Laming, 2004, 2015, to be essential for driving a fractionation level comparable to observations) is not needed to obtain significant FIP bias values in either closed loops or open field regions. While apparently in opposition with the work of Laming (2004, 2015), this result is not entirely surprising since it has previously been proposed that ponderomotive forces can appear in open field regions and be responsible for

providing the additional acceleration that creates the fast solar wind (see e.g. Leer et al., 1982).

2.4 Plasma Composition and Magnetic Activity

2.4.1 Active Regions

The strongest FIP effect is observed in active regions. FIP bias also varies throughout the active region's evolution and is modulated by different processes during the emergence and decay phases. Emerging magnetic flux was found to carry plasma with photospheric composition, i.e. FIP bias of approximately 1 (Mg VI/Ne VI ratio, $\log(\mathrm{T[K]}) \approx 5.6 - 5.7$; Young and Mason, 1997; Widing and Feldman, 2001). The FIP bias then increases as the active region goes through its emergence (Widing and Feldman, 2001) and early decay phases (Si X/S X ratio, $\log(\mathrm{T[K]}) \approx 6.2$; Baker et al., 2018), suggesting that the higher level of magnetic activity observed during the emergence phase is linked to the processes that drive the FIP effect.

After an active region enters its decay phase, the FIP bias starts to decrease (Si X/S X ratio, $\log(\mathrm{T[K]}) \approx 6.2$, Baker et al., 2015; Ko et al., 2016) until it reaches the FIP bias of the surrounding quiet Sun (Si X/S X and Fe XII/S X ratios, $\log(\mathrm{T[K]}) \approx 6.2$, Ko et al., 2016). The FIP bias decrease could be attributed to a combination of two main factors: a decrease in the fractionation process as the active region activity level drops and plasma mixing due to reconnection with surrounding structures. As the active region magnetic field disperses and reconnects with nearby structures, active region plasma will mix with the plasma in these structures. Therefore, the magnetic structures present in the area surrounding the dispersing AR will influence its composition, especially at the edges. In particular, in the active region studied by Baker et al. (2015), small bipoles emerged within and around the boundary of supergranular cells, as the magnetic field got progressively more dispersed. The small newly emerged loops contain photospheric plasma and their reconnection with older active region loops brings this photospheric material upwards into the corona, leading to plasma mixing and an overall FIP bias decrease.

A similar study (using a similar FIP bias diagnostic) followed the decay phase of another large active region, also finding that FIP bias values decrease in the decay phase and eventually settle around the FIP bias value of 1.5, corresponding to the FIP bias value of the surrounding quiet Sun (Ko et al., 2016).

Plasma composition also shows interesting substructure within an active region. FIP bias appears to be high at active region loop footpoints (Si X/S X ratio, $\log(\mathrm{T[K]}) \approx 6.2$; Baker et al., 2013), indicating that this is where the fractionation process takes place. Traces of high FIP bias are observed along some of the AR loops, indicating plasma being transported into the corona and starting to mix along the loops (Baker et al., 2013). The core loops of quiescent active regions show a relatively consistent FIP bias of about 3 (enhancement of Fe, $\log(\mathrm{T[K]}) \approx 6.5$; Del Zanna, 2013a; Del Zanna and Mason, 2014). Significant enhancements in the FIP bias are also found in outflows located at active region boundaries and in large and cool fan loops (Si X/S X ratio, $\log(\mathrm{T[K]}) \approx 6.2$; Testa et al., 2023). The FIP bias over areas near sunspots is typically photospheric or between photospheric and coronal (Ca XIV/Ar XIV ratio, $\log(\mathrm{T[K]}) \approx 6.6 - 6.7$; Doschek and Warren, 2017), and can be influenced by the length and magnetic connectivity of the loops rooted in the sunspot (Baker et al., 2021a).

2.4.2 Solar Flares

The plasma composition behaviour in solar flares is not yet fully understood, with some studies finding coronal composition, others finding photospheric composition and, in a few instances even an inverse FIP (IFIP) effect is observed.

In the EUV, flare observations using full-Sun spectra from the SDO EUV Variability Experiment (EVE) found that the average FIP bias, dominated by the flare emission, shows reduced Ca (Del Zanna and Woods, 2013) and Fe (Del Zanna and Woods, 2013; Warren et al., 2014). In addition, the Fe abundance was found to evolve from quiet Sun values in the preflare phase to photospheric values around the peak of the X-ray flux, and returns to its original value over the course of a few hours (Warren et al., 2014). This study used ratios of hot Fe emission lines to continuum emission (essentially providing a proxi for the Fe/H abundance) to obtain this

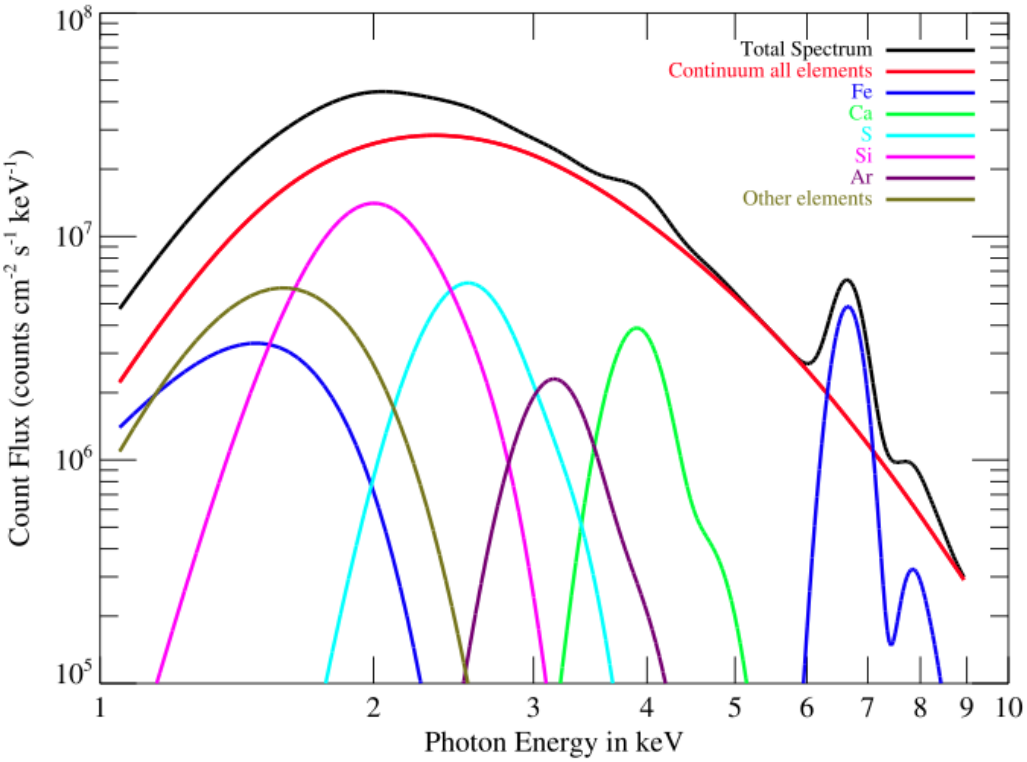

Figure 2.3: Example of solar soft X-ray spectrum from the Solar Assembly for X-rays (SAX) instrument on the Mercury MESSENGER spacecraft. The total X-ray spectrum (black) is dominated by the thermal continuum emission (red), but also contains a few emission lines. Image from Dennis et al. (2015).

result, in contrast to most EUV plasma composition studies which use ratios of EUV emission lines (see Section 3.3.7). A decrease in FIP bias seems logical: in flares, plasma is rapidly expelled from the chromosphere via chromospheric evaporation at speeds of up to 200 km s^{-1} (e.g. Brosius, 2013), i.e. significantly faster than the steady upflow speeds of a few km s^{-1} typical to quiescent conditions (e.g. Imada and Zweibel, 2012). This means that it is likely that plasma is expelled from the chromosphere before the FIP effect can occur, hence its photospheric composition. However, other studies using the *Hinode* EIS Ca XIV/Ar XIV found plasma with close to photospheric composition only around the flare loop footpoints (Doschek et al., 2018), while the bright flare loops show coronal composition in flares of different magnitudes, from X-class (Doschek et al., 2015, 2018), to M-class (see Chapter 7) to much smaller flares (To et al., 2021). This appears to be in contradiction with the results of Warren et al. (2014).

In the X-rays, relative abundances of various elements can be calculated from the strength of X-ray emission lines relative to the continuum emission (for an X-ray spectrum example, see Figure 2.3). Dennis et al. (2015) analysed the abundance enhancement compared to photospheric values of a series of elements in a large dataset of 526 large flares detected by the MESSENGER Solar Assembly for X-rays (SAX). They found, on average, significant enhancements of about 4 in Ca, very mild enhancement between 1 and 2 (close to photospheric values) in Fe, Si and S and, surprisingly, some enhancement of 2 to 3 in Ar. The Ar enhancement is interesting, however, one must be careful when interpreting this since the photospheric Ar abundance is not actually known (see e.g. Lodders, 2008). The close to photospheric values in Fe and Si are in agreement with the results of Warren et al. (2014). However, the relatively strong enhancement in Ca suggests that it is possible that, in flaring conditions, fractionation occurs for elements with a FIP lower than about 7 eV rather than 10 eV. Similarly low values for the Si enhancement were found in RESIK observations of an M-class flare (Sylwester et al., 2014), supporting the idea of a lower threshold. However, RHESSI results from 20 flares find a significant Fe enhancement of about 3 (Phillips and Dennis, 2012) and a similar value was measured in a C-class flare observed by the X-ray Solar Monitor (XSM) on the Indian lunar space mission Chandrayaan-1 (Narendranath et al., 2014). These results, mainly focusing on relatively large flares, are summarised in Figure 2.4. Observations of smaller A and B class flares with Chandrayaan-2 XSM show a clear decrease in the abundances of Mg, Al, Si and S to photospheric values during the flare impulsive phase which can be explained by chromospheric evaporation of plasma with photospheric abundances (Mondal et al., 2021; Nama et al., 2023). In the case of Mg, Si and S, the photospheric values are in agreement with those in larger flares (Dennis et al., 2015; Sylwester et al., 2014). However, the lack of enhancement in Al (very low FIP) is in contradiction with the idea of a 7 eV threshold for fractionation. They also observe a very quick recovery to pre-flare values which is difficult to explain. Again, there seems to be a discrepancy between the results observed in large flares and the ones observed in small flares. This is even more

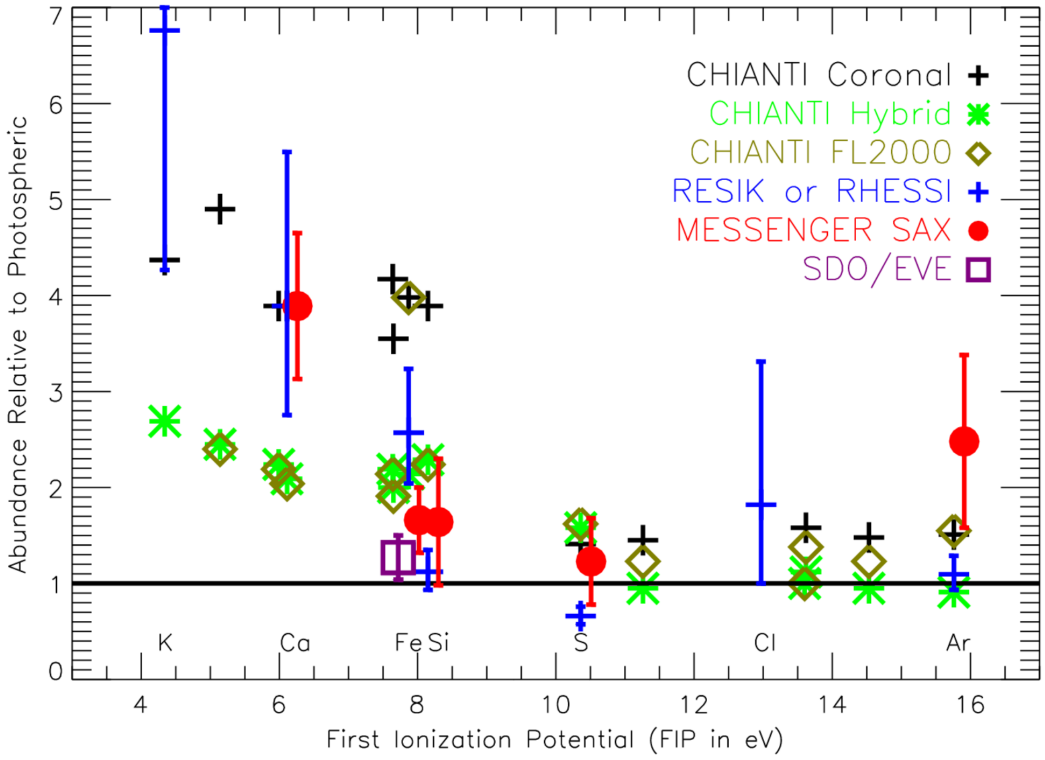

Figure 2.4: Summary of measured FIP bias values during flares as a function of FIP in a series of early studies. Blue plus signs: RESIK results for K, Ca, Si, S, and Ar in an M1.0-class flare Sylwester et al. (2014) and RHESSI result for Fe in a dataset of 20 flares (Phillips and Dennis, 2012). Red circles: MESSENGER SAX results for Fe, Ca, Si, S, and Ar in a dataset of 526 large flares (Dennis et al., 2015). Purple square: SDO EVE result for Fe in 21 flares (Warren et al., 2014). The black crosses and green asterisks show CHIANTI coronal abundances (Asplund et al., 2009) and hybrid abundances (Fludra and Schmelz, 1999) for reference. Image from Dennis et al. (2015).

surprising considering the fact that stronger heating in larger flares is likely to cause stronger chromospheric evaporation and bring upwards more photospheric plasma. So, one would expect this change in plasma composition to photospheric values to be stronger in larger flares, rather than the other way around.

All these flare observations are very different, so one must be careful when comparing them and trying to reconcile the results. A few points to take into account are:

1. Where does the emission come from? This is particularly important for the full-Sun observations, where the FIP bias measurement is integrated over the whole coronal structure. The emission from different parts of a flare loop

varies in strength in different lines. For example, soft X-ray signatures are dominated by coronal emission throughout most of a flare, but there is also soft X-ray emission from the loop footpoints during the impulsive phase of the flare (e.g. Hudson et al., 1994). EUV signatures are dominated by emission originating from the loop footpoints and ribbons in the impulsive phase and from the loop apex in the later stages as it takes time for the flare loops to develop. Doschek et al. (2018) found evidence of FIP bias varying along the loop, from the apex to the footpoints. This suggests that the part of the loop with the strongest emission in a particular line will also dominate the observed FIP bias.

2. Is the emission in different lines forming at the same time or phase of the flare evolution? Flare loop plasma cools down relatively fast (often over a few minutes, but up to a few hours in long duration flares), so they brighten in hot lines first and in successively cooler lines as they become cooler. This means that the hotter lines (analysed by e.g. Warren et al., 2014, and in the X-ray studies mentioned above) will capture the plasma composition earlier in the flare evolution than the cooler Ca XIV and Ar XIV lines (analysed by e.g. Doschek et al., 2015; Doschek and Warren, 2016, 2017; To et al., 2021). Since there is evidence that the plasma composition changes rapidly over a few minutes in flare loops (Warren et al., 2014; Mondal et al., 2021; Nama et al., 2023), it could be that different observations just capture it at different times.

3. Are the observations capturing the same structure? It is still possible that emission in the cooler and hotter lines originates from different structures along the lines of sight, even if the observations are co-temporal and appear to be co-spatial.

A striking aspect of plasma composition in flare observations is that, in a few instances, an IFIP effect was observed around the footpoint of the flare loops (Doschek et al., 2015; Doschek and Warren, 2016, 2017). In the IFIP case, low-FIP

elements are under-abundant in the corona compared to high-FIP elements. It is not certain whether this effect is given by a depletion of low-FIP elements or an enhancement of high-FIP elements (Doschek et al., 2015), but the low-FIP elements depletion scenario appears to be more likely (Doschek and Warren, 2016; Brooks, 2018). This scenario is also supported by the ponderomotive force model (Laming, 2004, 2015). According to the model, such an effect can happen if the ponderomotive force points downwards towards the Sun's surface instead of upwards towards the corona. The IFIP effect has only been observed during flares and around strong complex sunspot regions. This suggests there are two important conditions that must be met to observe it:

1. The ponderomotive force must be pointing downwards. To obtain a downwards ponderomotive force, the chromospheric wave energy density below the fractionation region must be higher than the wave energy density in the corona. This could be achieved if the wave driver is an upward propagating fast mode wave originating from below the chromosphere. Such waves can be excited in regions of strong magnetic fields (i.e. sunspots), with some studies suggesting they could be a result of subphotospheric or photospheric (high plasma β) reconnection (Baker et al., 2019, 2020). When these upward travelling fast mode waves refract and reflect back down, they apply a downward ponderomotive force on low-FIP elements (equivalent to but oppositely oriented to the effect of resonant waves described in Section 2.3.2), causing a depletion of low-FIP elements (Laming, 2021). The IFIP effect created by these fast mode waves is in competition with the FIP effect created by resonant waves and, if it is stronger, then the overall effect is a depletion of low-FIP elements at chromospheric level.

2. The IFIP plasma must be rapidly transported to the corona. Chromospheric evaporation during flares provides a pathway for IFIP plasma to be transported to the corona fast enough and in a large enough volume to immediately dominate the plasma composition there, making it detectable in observations. It is likely that the IFIP effect driven by fast mode waves is short-lived (other-

wise it should be detected more often). Assuming that initially the corona has plasma with coronal abundances, if the IFIP plasma is transported upwards via say diffusion then, by the time it mixed with the FIP plasma present in the corona, all the IFIP signatures will be gone. So, transport via chromospheric evaporation provided only in flaring conditions is vital for detecting IFIP signatures.

In summary, detecting IFIP plasma in the solar corona may require the presence of complex magnetic activity driving the downwards ponderomotive force (this is not always the case in flares, which could explain why it is not observed in all flares) and relatively strong flaring, along with the associated chromospheric evaporation, to transport the IFIP plasma into the corona (which could explain why IFIP is only observed in flares). It is not excluded that the photospheric composition observed at the footpoints of flare loops is also a result of an IFIP effect caused by fast mode waves. If the IFIP effect of these fast mode waves is not quite strong enough to change the footpoint plasma composition to IFIP, it could still be strong enough to balance out the FIP effect driven by resonant waves, such that the overall observed plasma composition is photospheric. It is important to keep in mind that the ionization state of the chromospheric plasma is changed drastically as a result of the energy deposition in the chromosphere during a flare and it can even deviate from ionization balance, which is likely to have a significant impact on the fractionation process. This aspect is not accounted for in the model.

The IFIP effect was also observed in situ in the solar wind in three different events (Brooks et al., 2022a). The sources of solar wind in these three cases are all active regions. One of these active regions was similar to the ones where the IFIP effect was observed in spectroscopic observations: complex magnetic configuration with significant flaring. However, the second was an emerging active regions and the third was an active region with a very large leading sunspot with a light bridge. This suggests that IFIP might occasionally be produced in other types of active regions as well.

The plasma composition pattern and evolution observed in solar flares have the potential to provide insights into the flare dynamics. The composition of the plasma transported upwards during a flare via chromospheric evaporation is directly linked to the depth in the chromosphere at which energy is deposited during the flare. The latter is given by the energy of the electron beam accelerated as a result of magnetic reconnection. It is likely that the evolution of the plasma composition in the flare loop, particularly at the flare loop footpoints, can be used to estimate the height of the energy deposition in the chromosphere, and, therefore, place constraints on the electron beam energy.

2.4.3 Magnetic Topology and Magnetic Flux Rope Formation

Plasma composition has been observed to vary depending on the magnetic topology of a structure. A magnetic flux rope is a structure characterised by twisted magnetic field, which stores free magnetic energy that can be released as a coronal mass ejection (CME). These structures form via reconnection of magnetic field lines. The height in the solar atmosphere where this reconnection happens influences the plasma composition of the structure. Reconnection in the lower atmosphere, which manifests itself as photospheric flux cancellation, can lead to the formation of a low-lying flux rope (van Ballegooijen and Martens, 1989). In this case, field lines in the underside of the flux rope have a bald patch (BP) topology, i.e. they are tangent to the photosphere (Green and Kliem, 2009). This provides a pathway for plasma with photospheric composition to be injected into the loops forming the flux rope (Fletcher et al., 2001; Baker et al., 2022, 2013). Plasma composition has been found to remain predominantly photospheric following eruptions and failed eruptions (Baker et al., 2015, 2022). In constrast, if the flux rope forms via reconnection in the corona, it retains its coronal composition (e.g. James et al., 2017). This highlights the potential of plasma composition observations in providing insight about the magnetic topology of a structure. It is important to note that the changes in plasma composition driven during the flux rope formation process are likely only due to plasma mixing as a result of magnetic reconnection between coronal loops (see Figure 2.1) rather than the FIP effect.

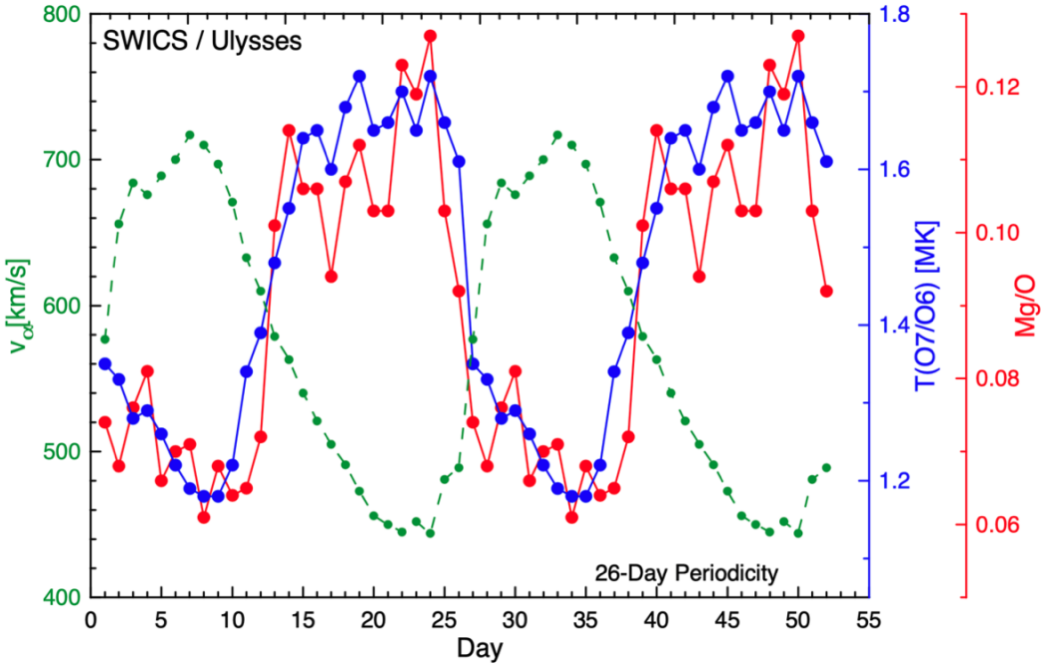

Figure 2.5: Variation of solar wind parameters: speed (green), freezing in temperature from O^7 to O^6 ratio(blue) and Mg/O ratio as a proxi for the FIP bias (red). Image from Krasnoselskikh et al. (2022) after Geiss et al. (1995).

2.4.4 Solar Wind Heating and Acceleration

The plasma composition of the solar wind was found to be correlated to the solar wind temperature and inversely correlated with the solar wind speed (Geiss et al., 1995, see Figure 2.5). This suggests that the processes that drive changes in the elemental composition could be linked to those responsible for the heating and acceleration of the solar wind.

In wave driven models, solar wind heating and acceleration are believed to be driven by wave activity and turbulence and depend on the expansion factor of the magnetic field, i.e. how fast it decreases with height (Abbo et al., 2016). Photospheric motions can drive wave-like fluctuations that propagate along magnetic field lines into the corona. When these waves partially reflect back towards the photospheric footpoints of the loop, they can develop strong turbulence and/or dissipate their energy over a range of heights, leading to heating and particle acceleration. This is very similar to the drivers proposed by Laming (2004, 2015) to be responsible for the plasma composition changes (see Section 2.3.2). Assuming the heating

rate depends on the magnetic field strength, the expansion factor is inversely correlated to the wind speed (Abbo et al., 2016). If the expansion factor is large, i.e. a rapid decrease of magnetic field strength with height, heating is concentrated at the base of the corona. A large amount of the available energy is then conducted into the transition region, where it increases the mass flux, but reduces the energy available higher up for accelerating particles, thus reducing the wind speed. Energy being deposited at transition region and chromospheric levels drives a stronger FIP effect, as observed in the slow solar wind plasma composition (see Figure 2.5). If, however, the expansion factor is low, the available energy will be deposited over a larger portion of the field line, resulting in stronger particle acceleration but weaker FIP effect, as observed in the fast solar wind plasma composition (see Figure 2.5). In this case, less energy is deposited into the transition region so the mass flux is lower. In summary, the difference between the fast and slow solar wind is mainly given by the expansion factor of magnetic field lines at the source region and the way it affects the height of the wave energy deposition in the solar atmosphere.

Of course, a question remains about the origin of this common wave driver (for both solar wind acceleration and plasma fractionation) and the necessity for it to be amplified via some sort of resonance. The original ponderomotive force model (Laming, 2004, 2015) concludes that the wave driver for the fractionation process must be amplified by resonance to create the level of FIP bias observed in the corona and the slow solar wind. Since resonance can only be reached in closed loops, not open field lines, it was originally suggested that fractionation cannot take place in open field. However, recent simulations by Réville et al. (2021) show that resonances are not needed to obtain a FIP bias in coronal loops and open slow wind source regions. This aspect is also investigated in Chapter 6 of this thesis.

There is a second group of solar wind acceleration models, which involve interchange reconnection between closed loops and open field lines that connect into the solar wind. Some studies suggest that interchange reconnection is an alternative pathway for plasma with coronal composition to escape from closed loops into the solar wind. The results of Réville et al. (2021) question the necessity of interchange

reconnection to explain the presence of a FIP bias in the solar wind plasma composition. Since, following their results, fractionation can happen in open field lines as well, there is no need for fractionated plasma to be transported from a closed field region into the open field. Nevertheless, coronal holes have small-scale included polarities, which form closed loops with the majority polarity and undergo interchange reconnection with their open field lines, resulting in small-scale jet activity. This could provide a pathway for interchange reconnection to contribute to the coronal hole composition.

Another interesting aspect of solar wind plasma composition is that S, P and C, which have a FIP just above the 10 eV threshold (see Table 2.1), appear to show some enhancement (e.g. Reames, 2018). This was originally unexpected as these were considered high-FIP elements since they do not typically show any enhancements in closed loops. S, P and C were found to have mild enhancements in slow solar wind (e.g. Bochsler, 2009), fast solar wind (e.g. Bochsler, 2009) and corotating interaction regions (e.g. Reames, 2018), but their enhancements were lower than those of elements with significantly lower FIP. For this reason, S, P and C are sometimes referred to as intermediate FIP elements. In contrast, intermediate FIP elements show no enhancement in solar energetic particles (e.g. Reames, 2018) which suggests they originate from and are accelerated in closed loops. Laming et al. (2019) proposes that the enhancement of intermediate FIP elements is a result of fractionation being driven by nonresonant waves and taking place lower in the chromosphere, where H is neutral. This type of 'solar wind-like' fractionation is studied in detail in Chapter 6.

Chapter 3

Solar Spectroscopy

3.1 Fundamentals of Solar Radiation

Plasma in the solar atmosphere emits thermal radiation at temperatures ranging from about 5,800 K in the photosphere (or even lower in the cool sunspot umbrae regions) to about 10 MK in the corona (or even higher in flaring regions). The thermal emission from the photosphere is mainly black-body radiation that peaks in the visible part of the spectrum, while thermal emission from the corona falls mainly in the wavelength domain of EUV and soft X-rays (see Figure 3.1). Generally, quiet Sun regions emit in the temperature range of 1-3 MK, i.e. cooler EUV lines, active regions in the range of 2-8 MK, i.e. hotter EUV lines and soft X-rays, and flares in the range of 10-40 MK, i.e. very hot EUV lines and soft X-rays. Flaring regions also emit in the hard X-rays, although this is nonthermal emission. This chapter focuses on EUV emission from the solar corona and how it can be used for plasma diagnostics.

3.1.1 Atomic Processes and Mechanisms

Since the corona is fully ionised, the coronal plasma population is divided into ions and electrons that move along magnetic field lines. Ions and electrons interact with each other and with electromagnetic radiation in a wide range of ways depending mainly on the temperature and density of the plasma. These interactions often involve capturing or producing a photon, resulting in absorption or emission of radiation. Typically, each absorption mechanism has an associated emission mech-

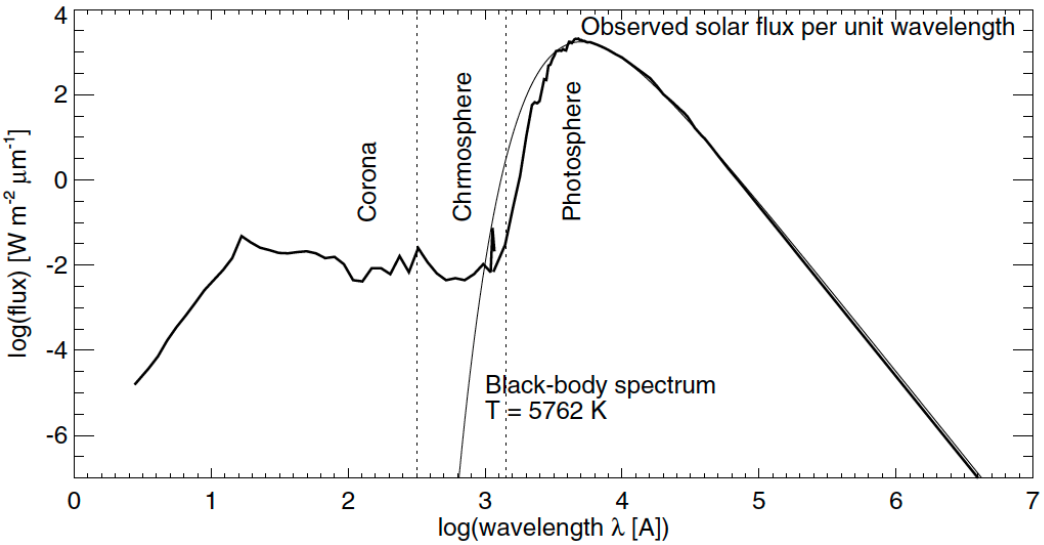

Figure 3.1: The observed solar flux per unit wavelength (thick curve) with a black body spectrum, of temperature 5762 K. Image from Aschwanden (2004).

anism. The main atomic processes that contribute to the continuum and line emission of the solar corona in soft X-rays and EUV are described below and shown schematically in Figure 3.2. These processes can be categorised into bound-bound transitions, bound-free or free-bound transitions, and free-free transitions.

In bound-bound transitions, the ion electronic configuration is changed by interaction with either electromagnetic radiation or free electrons and ions. The involved electron remains attached (bound) to the ion both before and after the change. These processes change the excitation level of the ion, but not its ionization state:

- **Induced absorption**: when an incoming photon has the right frequency, it can be absorbed by an ion and excite one of the ion's electrons into a higher energy level. The transition rate for this process is given by:

$$R_{\text{induced absorption}} = U_\lambda B_{ij} N_i(X^{+m}), \qquad (\text{s}^{-1}\ \text{cm}^{-3}) \tag{3.1}$$

where U_λ [erg cm^{-4}] is the energy density per unit wavelength of the radiation field, B_{ij} [erg^{-1} cm^4 s^{-1}] is the Einstein absorption coefficient and $N_i(X^{+m})$ [cm^{-3}] is the population of element X ionised m times that is in the lower

excitation level i. Note that the units of B_{ij} vary depending on whether the energy density is defined per unit wavelength or per unit frequency.

- **Stimulated emission**: an incoming photon can also stimulate an electron in an excited ion to move from a higher energy state j to a lower energy state i, emitting a photon as a result. The transition rate for this process is given by:

$$R_{\text{stimulated emission}} = -U_\lambda B_{ji} N_j(X^{+m}), \qquad (\text{s}^{-1}\ \text{cm}^{-3}) \qquad (3.2)$$

where B_{ji} is the Einstein stimulated emission coefficient and $N_j(X^{+m})$ is the population of element X ionised m times that is in the upper excitation level j.

- **Spontaneous emission**: similar to stimulated emission, except no incoming photon is needed. The excited electron spontaneously moves from the higher to the lower energy state emitting a photon. The transition rate for this process is given by:

$$R_{\text{spontaneous emission}} = -A_{ji} N_j(X^{+m}), \qquad (\text{s}^{-1}\ \text{cm}^{-3}) \qquad (3.3)$$

where A_{ji} is the Einstein spontaneous emission coefficient.

- **Collisional excitation**: an incoming free electron (or ion) collides with the bound electron and causes it to move to a higher energy state. No radiation is emitted/absorbed in this process.

- **Collisional de-excitation**: an incoming free electron (or ion) collides with the bound electron and causes it to move to a lower energy state. No radiation is emitted/absorbed in this process.

In bound-free or free-bound transitions, the ionization state of the ion is changed by interaction with either electromagnetic radiation or free electrons. The involved electron goes from being bound to being free or vice versa:

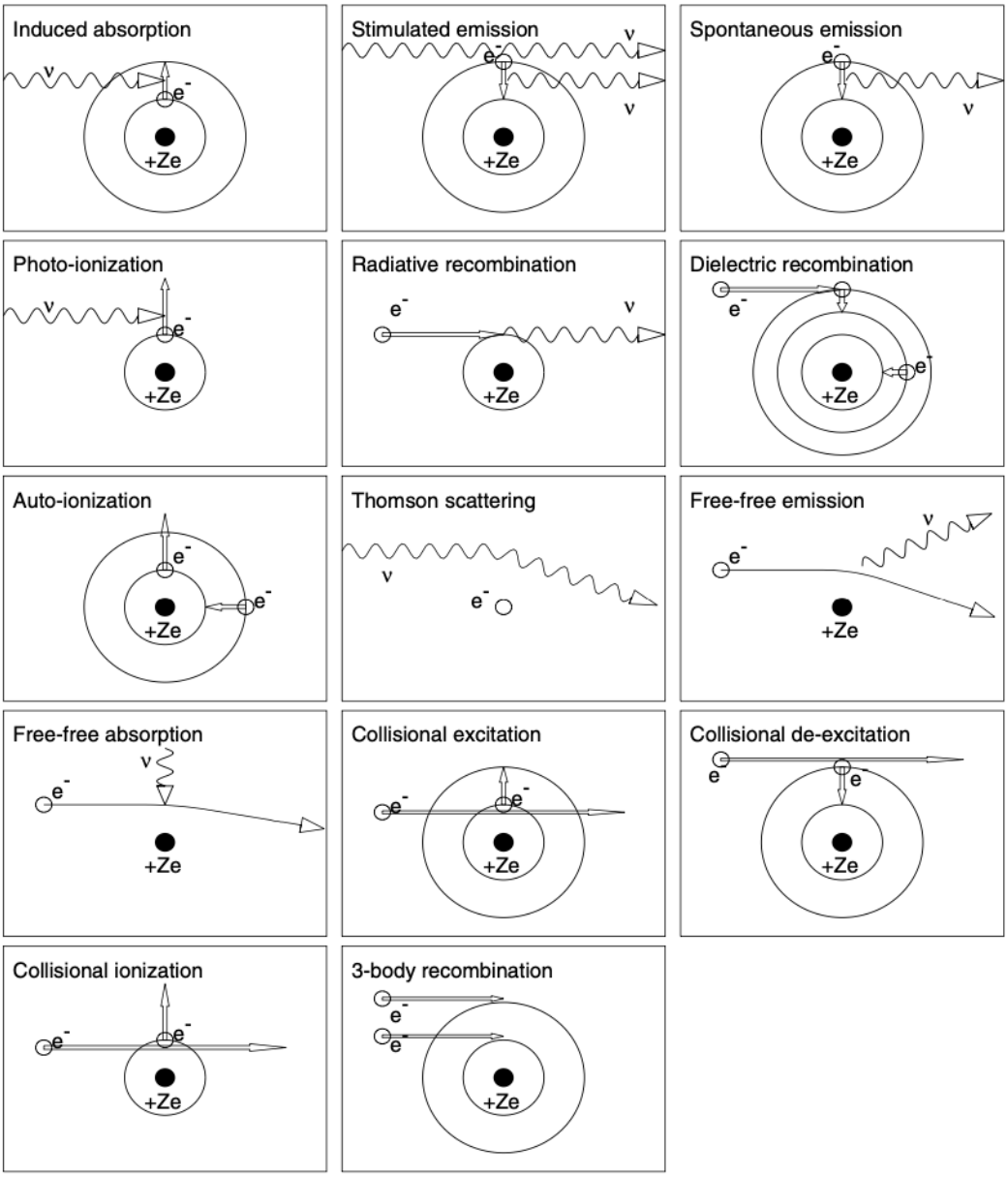

Figure 3.2: Diagrams of the main atomic processes (absorption, emission, ionization, recombination, excitation and de-excitation) responsible for the EUV and soft X-ray emission in the solar corona. Atoms and ions are marked with filled dots, electrons with open dots, electron orbits with circles, electron transitions with arrows, and photons with a wiggly arrow. Time is proceeding from left to right. Image from Aschwanden (2004).

- **Photo-ionization**: if the incoming photon's energy is higher than the ionization potential of the ion, the bound electron is removed and the ion moves into a higher ionization state.

- **Auto-ionization**: similar to photo-ionization, except no incoming photon is needed. This process requires, however, that the ion is initially in a doubly excited state and, when the electron from the lower energy state is removed, the electron from the higher energy state moves down to the emptied lower state to stabilise the ion.

- **Radiative recombination**: a free electron is captured, moving the ion into a lower ionization state and emitting a photon.

- **Dielectronic recombination**: a free electron is captured, resulting in a doubly excited state: the originally free electron occupies an excited state and one of the bound electrons moves to a higher energy state.

- **Collisional ionization**: an incoming free electron (or ion) collides with the bound electron and removes the electron from the ion, leaving it in a higher ionization state. No radiation is emitted/absorbed in this process.

- **Three-body recombination**: similar to dielectronic recombination, except two incoming electrons are involved.

In free-free transitions, the electron is free both before and after the change. The atomic structure is not changed, so the ion maintains both its ionization state and excitation level:

- **Free-free emission** or Bremsstrahlung: electrons are scattered off an ion, emitting a photon whose frequency is proportional to the kinetic energy difference of the free electron.

- **Free-free absorption**: electrons are scattered off an ion, absorbing a photon whose frequency is proportional to the kinetic energy difference of the free electron.

In addition to processes that involve ions, the free electrons can interact with electromagnetic radiation via **Thomson scattering**. Photons are scattered off free electrons. Typically the photon changes its direction but not frequency.

3.1.2 Ionization Equilibrium

The relative abundance of each ionization state and excitation level can be calculated by solving the complex set of equations that drive all the atomic processes listed in Section 3.1.1. However, this system has more unknowns than equations, so additional constraints must be included. If the system is in ionization equilibrium, the relative abundance of each ionization state and excitation level is constant.

The relative abundance of an ionization state m for an element X, $N(X^{+m})/N(X)$ is dictated by the interplay between bound-free interactions. In ionization equilibrium, the rate of ionization is equal to the rate of recombination. Similarly, the relative abundance of an excitation level j, $N_j(X^{+m})/N(X^{+m})$ is dictated by the interplay between bound-bound interactions. In ionization equilibrium, the rate of absorption is equal to the rate of emission for all transitions. The dominating processes in each case depend on the properties of the plasma.

An additional important assumption in this type of calculation is that the processes that change the energy levels of the ion (excitation and de-excitation) can be decoupled from those that change its ionization state (ionization and recombination). For the plasma conditions in the solar atmosphere, this is usually a reasonable assumption, since the time scales for ionization and recombination are usually significantly longer than those for excitation and de-excitation (Phillips, 2009).

3.2 Radiation Spectrum of the Solar Corona

The X-ray and EUV radiation spectrum in the solar corona consists of emission lines produced by bound-bound (primarily spontaneous emission) transitions and continuum emission produced by free-bound (radiative recombination) and free-free (Bremsstrahlung) transitions.

3.2.1 The Coronal Approximation

Modelling emission in the solar atmosphere using atomic models such as CHIANTI (Dere et al., 1997; Del Zanna et al., 2021) relies on the assumption of ionization equilibrium. This is because the strength of a particular emission line depends on the fractional abundance of the ion that produces it.

In coronal conditions, a few simplifying assumptions are made for ionization equilibrium calculations. Firstly, the relative abundance of ionization levels is dominated by ion-electron interactions. Ionization and recombination processes usually occur only between adjacent stages of ionization. The dominating ionization processes are collisional ionization and auto-ionization, while the dominating recombination processes are radiative recombination and dielectronic recombination. Other ionization and recombination processes, such as photoionization or three-body recombination, are typically ignored in coronal conditions, mostly because of the low density and of the lack of radiation fields sufficiently strong to compete with collisional processes in ionizing ions (Phillips, 2009). However, photoionization could become important for transition region ions (e.g. Dzifčáková and Dudík, 2017). Similarly, the relative abundance of excitation levels within an ion is dominated by collisional excitation and spontaneous emission. Other excitation and de-excitation processes such as radiative excitation and collisional de-excitation are ignored.

An example of ionization equilibrium ion fraction calculations for Fe is shown in Figures 3.3 and 3.4. The relative abundance of different ions changes with temperature: the higher the temperature, the higher the population of ions at higher ionization states. Ionization equilibrium is assumed for all the calculations presented in this thesis. It is important to note that coronal plasma might occasionally deviate from ionization equilibrium, particularly in low density regions or regions of explosive energy release like solar flares (e.g. Kato et al., 2000). However, this aspect is not covered in this thesis.

3.2.2 Emission Lines

Bound-bound transitions lead to emission at discrete wavelengths. Typically, for heavy elements, spontaneous emission produced by an electron moving from

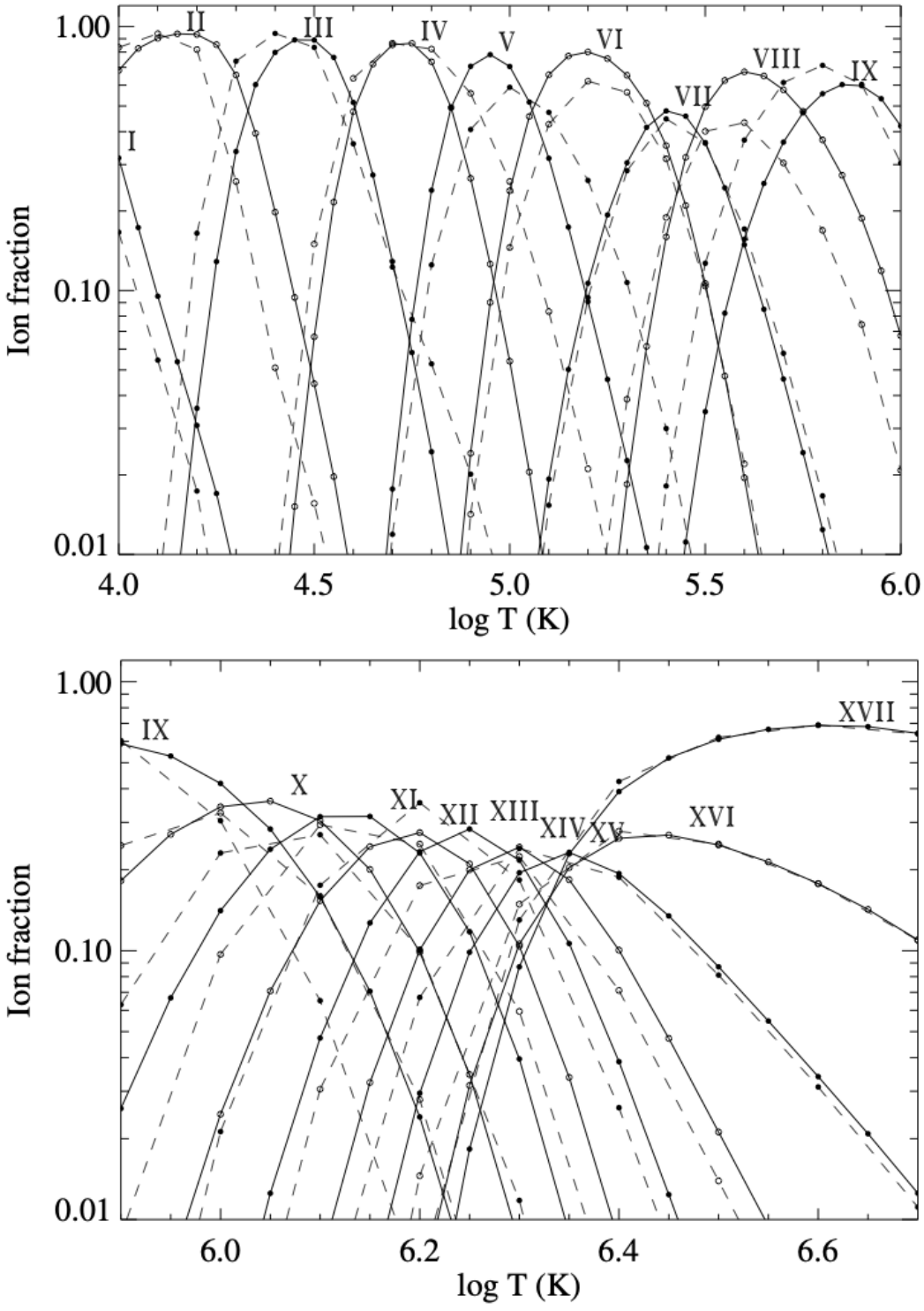

Figure 3.3: Ionization equilibrium ion fractions as a function of temperature for Fe I-XVII. Dashed lines show calculations by Mazzotta et al. (1998) and solid lines show updated calculations by Dere et al. (2009). Images from Dere et al. (2009).

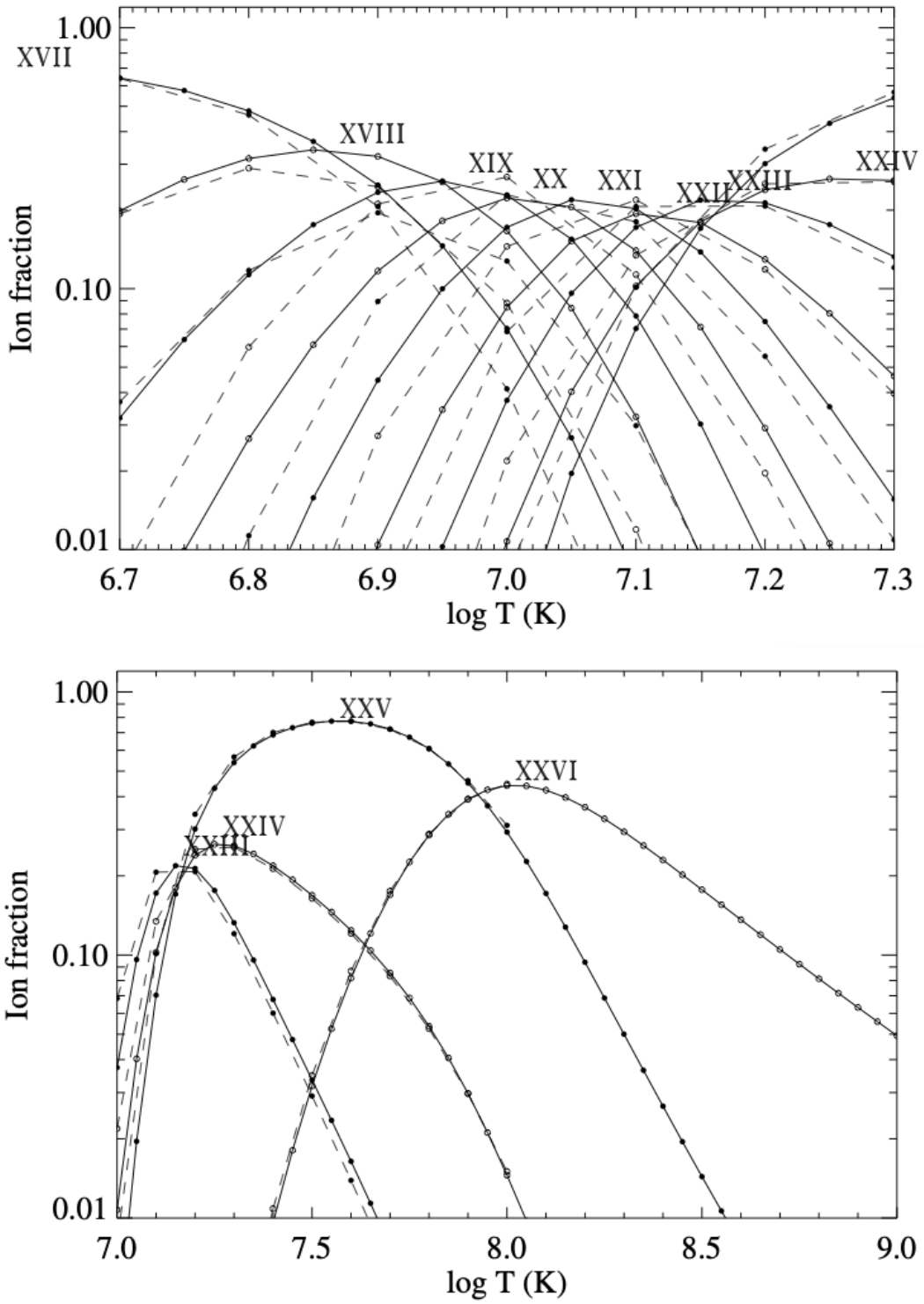

Figure 3.4: Ionization equilibrium ion fractions as a function of temperature for Fe XVIII-XXVI. Dashed lines show calculations by Mazzotta et al. (1998) and solid lines show updated calculations by Dere et al. (2009). Images from Dere et al. (2009).

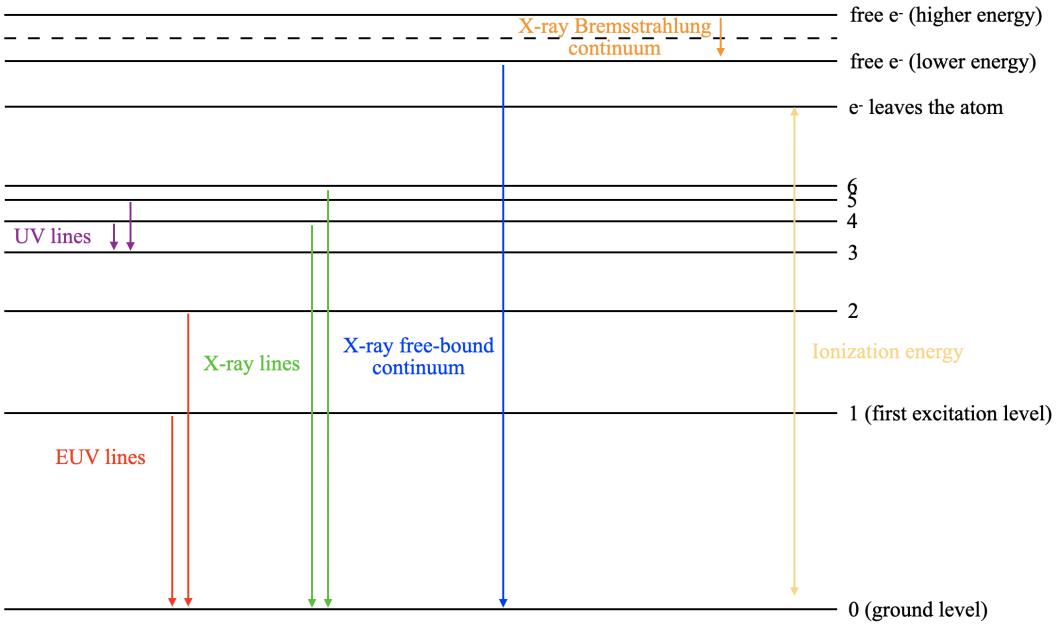

Figure 3.5: Illustrative schematic of the main atomic transitions and processes within a heavy ion that produce UV lines (purple), EUV lines (red), soft X-ray lines (green), free-bound soft X-ray continuum emission (blue) and Bremsstrahlung soft and hard X-ray continuum emission (orange) in the solar corona. The ionization energy (yellow) corresponds to the energy required for the electron to leave the atom. The dashed black line indicates that the energy separation between the two free electrons is larger than the schematic suggests. The wavelength regimes indicated give a good representation for a highly ionised heavy ion. Emission will be at lower energies for lower ionisation states.

one of the first excited states to the ground state leads to emission in the EUV. The energy separation between the first excited states is relatively large, so EUV lines from the same ion are well separated. If the electron is moving from one of the higher energy states to the ground state, the energy gap is larger, so the wavelength of the emitted photon is lower, leading to emission in the soft X-ray range. Energy separation between adjacent energy states decreases at higher energy states, which leads to X-ray emission lines being more tightly packed together and harder to disentangle than EUV lines. If the electron is moving between two excited states, the energy gap is smaller, so the wavelength of the emitted photon is higher, leading to emission in the UV range. These lines are typically faint or hard to detect. Figure 3.5 schematically illustrates these transitions.

3.2.2.1 "Forbidden lines"

Some emission lines observed in the solar atmosphere are called "forbidden lines". They involve the de-excitation of metastable energy levels within an atom. According to quantum mechanical rules, these transitions are highly unlikely to occur spontaneously, hence the name "forbidden". However, in the very high temperature but very low density environment of the corona, the rates of these transitions are high enough for the emission lines to be detected. Such an example is the Fe XIV 5303 Å in the visible part of the spectrum. In laboratory plasmas the collisional de-excitation timescale is very short, i.e. the metastable energy level becomes depopulated via collisional de-excitation before spontaneous emission can happen, so this line would never be observed. In the corona, however, the collisional de-excitation timescale is significantly longer as a result of the low density and high temperature, so the line can be observed (Aschwanden, 2004). As a consequence of the low transition rate, these lines have low intensity, so they can typically only be observed off limb, i.e. against a dark background, but not on the solar disk as the emission from other lines is much stronger.

3.2.3 Continuum Emission

3.2.3.1 Free-Bound Continuum Emission

Free-bound continuum emission in the soft X-ray range is produced by ions capturing a free electron via radiative recombination. The energy of the emitted photon is equal to the difference between the kinetic energy of the incoming free electron and the ionization potential of the ion (the energy required to remove the electron from the ion). The incoming free electrons have a non-discrete range of kinetic energies which results in continuum emission, rather than discrete emission lines. For a Maxwellian electron velocity distribution, the free-bound continuum emission is characterized by discontinuities at the ionization thresholds (e.g. Del Zanna and Mason, 2018). For a plasma with a temperature of 10 MK, most of the free-bound emission is in the soft X-rays wavelength range.

3.2.3.2 Bremsstrahlung Emission

Bremsstrahlung radiation is produced by electrons that are scattered by ions. These electrons lose some of their kinetic energy via collisions with ions and produce a photon as a result. There are two main types of Bremsstrahlung emission (Aschwanden, 2004): thermal and non-thermal. Thermal Bremsstrahlung is produced by electrons which have the same temperature as the ambient plasma. This mechanism produces emission in the soft X-rays. Non-thermal Bremsstrahlung is produced by electrons which have been accelerated to much higher energies (are non-thermal) before they hit the thermal plasma. This typically happens in solar flares, when electrons accelerated via flare processes precipitate to the chromospheric footpoints of flare loops. These electrons produce emission in the hard X-rays both in the corona (thin-target Bremsstrahlung) and at the chromospheric footpoints (thick-target Bremsstrahlung). The coronal hard X-ray emission is significantly fainter than the chromospheric one and can typically only be observed in footpoint-occulted flares.

3.2.3.3 Thomson Scattering

Thomson scattering is the scattering of photons off free electrons. No radiation is actually produced in this process because the incoming photon changes momentum but conserves its energy. Nonetheless, this is an important process in the solar corona because it enables us to observe coronal structures in coronagraph data or during solar eclipses (the so-called K-corona). In the absence of Thomson scattering, photons would travel radially and not be detected at Earth when the solar disk is occulted. In addition, the scattering rate is proportional to electron density, providing a method for electron density calculations in the solar corona.

3.3 EUV Spectroscopic Diagnostics in the Solar Corona

Under the assumption of ionization equilibrium, the radiance (sometimes called intensity) of a spectral line of wavelength λ_{ji} is directly related to its bound-

bound emissivity as follows:

$$I(\lambda_{ji}) = \frac{h\nu_{ji}}{4\pi} \int N_j(X^{+m}) A_{ji} ds, \qquad (\text{erg cm}^{-1}\ \text{s}^{-1}\ \text{sr}^{-1}) \tag{3.4}$$

where h is Planck's constant, i and j are the lower and upper levels of the ion X^{+m}, ν_{ji} is the frequency of the emitted photon ($\nu_{ji} = c/\lambda_{ji}$), $N_j(X^{+m})$ is the population density in the upper level j of element X that is ionised m times, A_{ji} is the Einstein A coefficient (the spontaneous decay rate between upper level j and lower level i) and s is the line of sight coordinate. The quantity

$$P_{ji} = h\nu_{ji} N_j(X^{+m}) A_{ji} \qquad (\text{erg cm}^{-3}\ \text{s}^{-1}) \tag{3.5}$$

is the spectral line emissivity per unit volume (power), so Eqn. 3.4 can be rewritten as:

$$\boxed{I(\lambda_{ji}) = \frac{1}{4\pi} \int P_{ji} ds.} \tag{3.6}$$

Alternatively, $N_j(X^{+m})$ can be expressed as:

$$N_j(X^{+m}) = \frac{Nj(X^{+m})}{N(X^{+m})} \times \frac{N(X^{+m})}{N(X)} \times \frac{N(X)}{N(H)} \times \frac{N(H)}{N_e} \times N_e, \tag{3.7}$$

where

- $\frac{Nj(X^{+m})}{N(X^{+m})}$ is the fraction of ion X^{+m} population that is in the j excitation level,
- $\frac{N(X^{+m})}{N(X)}$ is the fraction of element X population that is in the m ionization state,
- $\frac{N(X)}{N(H)} = Ab(X)$ is the abundance of element X relative to hydrogen,
- $\frac{N(H)}{N_e}$ is the abundance of hydrogen relative to electron density,
- N_e is the electron number density.

The first two terms are dependent on the temperature and density of the ambient electrons, while the third and fourth are a function of the elemental abundance of the emitting plasma. This makes it convenient to define a second quantity, the contribution function of a spectral line (see examples in Figure 3.6). Depending on the

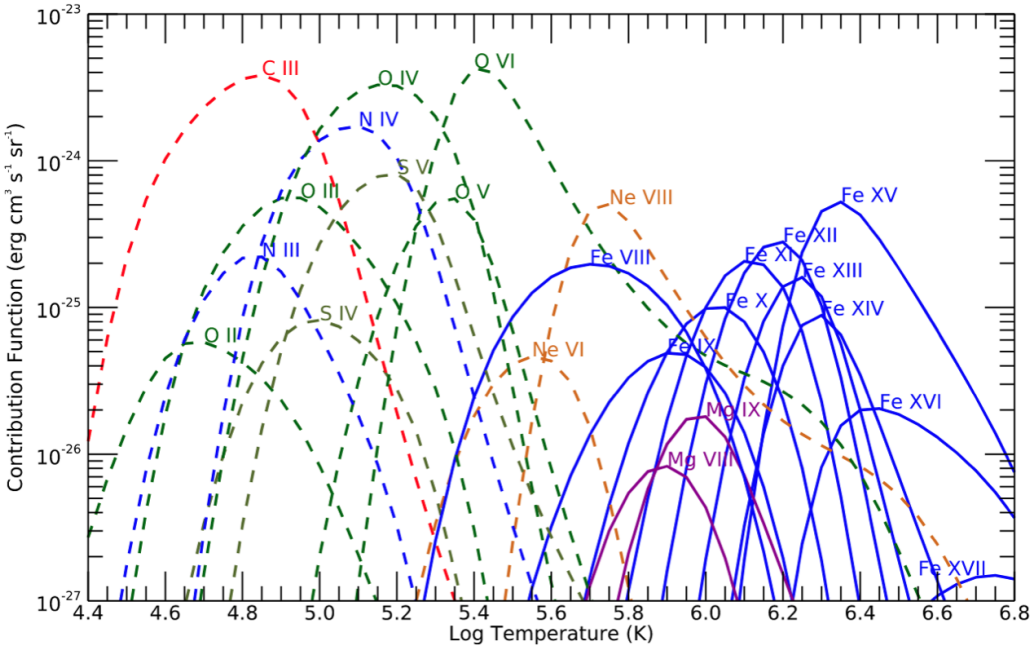

Figure 3.6: Examples of contribution functions for many important EUV emission lines in the solar atmosphere. Image from Brooks et al. (2022b).

exact definition, which varies slightly in the literature, the contribution function can either include the abundance factor $Ab(X)$:

$$G(N_e,T,\lambda_{ji}) = Ab(X)A_{ji}\frac{h\nu_{ji}}{4\pi}\frac{Nj(X^{+m})}{N(X^{+m})}\frac{N(X^{+m})}{N(X)}\frac{1}{N_e}, \qquad (\text{erg cm}^3\ \text{s}^{-1}\ \text{sr}^{-1}) \quad (3.8)$$

or not include it:

$$C(N_e,T,\lambda_{ji}) = A_{ji}\frac{h\nu_{ji}}{4\pi}\frac{Nj(X^{+m})}{N(X^{+m})}\frac{N(X^{+m})}{N(X)}\frac{1}{N_e}. \qquad (\text{erg cm}^3\ \text{s}^{-1}\ \text{sr}^{-1}) \quad (3.9)$$

Here, the notation of Del Zanna and Mason (2018) is used to distinguish between the two definitions. Either way, the contribution function contains all the atomic physics parameters relevant for a given transition. For most emission lines, this has a narrow peak in temperature, so it effectively confines the emission to a fixed temperature range. Eqn. 3.4 can then be rewritten as:

$$I(\lambda_{ji}) = \int Ab(X)C(N_e,T,\lambda_{ji})N_eN_Hds. \quad (3.10)$$

Under the assumption that H and He are fully ionised at coronal temperatures, the N_H/N_e ratio only depends on the He relative abundance (e.g. Del Zanna and Mason, 2018). The broadly agreed value is $N_H/N_e = 0.83$ (based on abundance calculations by Meyer, 1985b), so:

$$\boxed{I(\lambda_{ji}) = 0.83 \int Ab(X)C(N_e,T,\lambda_{ji})N_e^2 ds.} \tag{3.11}$$

The above radiance calculations are for one transition in one atom.The total emission from a volume of plasma on the Sun is, therefore, given by the sum of all the individual atom radiances. Under the assumption that the volume of plasma considered emits symmetrically in all directions, the total photon flux observed at Earth, i.e. the total irradiance of a spectral line, is given by:

$$F(\lambda_{ji}) = \frac{1}{4\pi d^2} \int P_{ji} dV, \qquad (\text{erg cm}^{-2}\ \text{s}^{-1}) \tag{3.12}$$

where d is the distance between the Earth and the Sun and dV is the volume element. The volume integrated over is the line of sight plasma column in the corona. Under the assumption that the electron density N_e is a function of the electron temperature T only, a differential emission measure (DEM) can be defined as a quantitative expression of the multi-temperature distribution of the plasma in the corona (Withbroe, 1978):

$$\int DEM(T)dT = \int N_e N_H ds = \int 0.83 N_e^2 ds, \tag{3.13}$$

i.e.

$$DEM(T) = N_e N_H \frac{ds}{dT} = 0.83 N_e^2 \frac{ds}{dT}. \qquad (\text{cm}^{-5}\ \text{K}^{-1}) \tag{3.14}$$

Therefore, the total irradiance of a spectral line can be written as:

$$\boxed{F(\lambda_{ji}) = \int Ab(X)C(N_e,T,\lambda_{ji})DEM(T)dT.} \tag{3.15}$$

The above derivations are based on those presented by e.g. Aschwanden (2004); Del Zanna and Mason (2018). Note that the term "intensity" is used somewhat

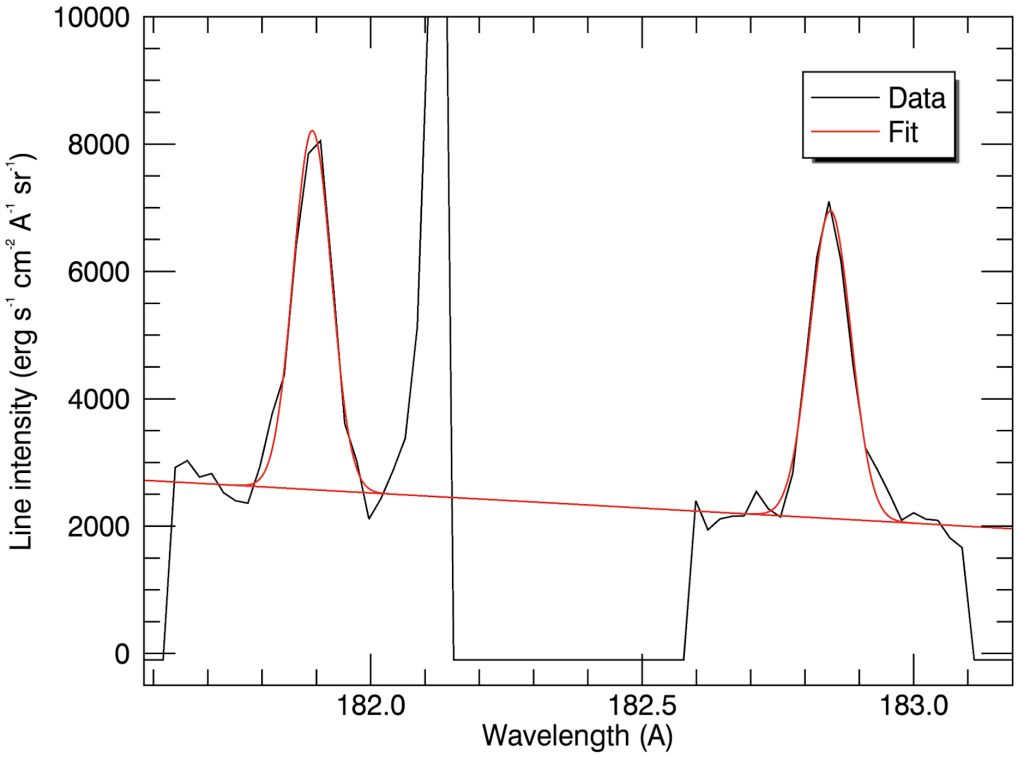

Figure 3.7: Example of an Ca XV 181.902 Å and Ca XV 182.863 Å spectrum (black) with a single Gaussian fit (red) for each line.

interchangeably in the literature to refer to both radiance (Eqn. 3.11) and total irradiance (Eqn. 3.15). In this thesis, it is exclusively used to refer to total irradiance.

3.3.1 Spectral Line Intensity

In observations, the intensity of a spectral line (the total irradiance) is defined as the number of photons that can confidently be attributed to a given transition and is calculated as the area under the Gaussian fit to the emission curve (see example in Figure 3.7). If the emission is clearly separated from emission from other lines, a single Gaussian can be used. If, however, the emission line is formed in a region where there is significant emission from other lines, i.e. if the line is blended, then two or more Gaussians might be needed to extract the intensity of each of the lines.

In practice, single Gaussian functions are routinely used to automatically fit spectral data. However, once the fits are produced, there are a few aspects that must be checked to validate the results:

- Blends: there are a few methods to identify potential line blends. The first step is to check if there are any identified blends that have a non-negligible atomic transition probability using, for example, the CHIANTI database (Dere et al., 1997). Another method is to compare the fits with those of an emission line produced by a different transition within the same ion (assuming their intensity ratio is not density sensitive; see Section 3.3.4). If the ratios of the two intensities, widths (see Section 3.3.3) or shifts from the theoretical wavelength of the line (see Section 3.3.2) vary spatially then it is likely a blending issue is involved. A technique to avoid blending issues is to constrain the parameters of the Gaussian fit such that the centroid or width of the line are tied to those of another line that is known to not have blending issues.

- Background: in the EUV part of the spectrum analysed in this thesis, the background is typically assumed to be linear in wavelength. If the spectral window is narrow, then a constant background is typically an appropriate assumption. If the window is wider (see e.g. Figure 3.7), allowing the background to have a slight tilt improves the background fit quality. In addition, it is important to identify other lines are present in the spectral window used for the fit and not include them in the background fit as they would artificially increase the background level.

- Signal to noise ratio: the main contributors that lead to a low signal to noise ratio are 1) the atomic transition that produces the emission line has a low probability and 2) the plasma temperature is significantly different from the formation temperature of the emission line analysed. One technique to improve the signal to noise ratio for a spectral line is to spatially bin the data but, of course, this comes at the cost of sacrificing spatial resolution.

- Non-Gaussianity: there is evidence suggesting that in complex flaring conditions where plasma might deviate from ionization equilibrium, a kappa line profile might be more appropriate (Jeffrey et al., 2016) than a Gaussian one. This aspect, however, is not covered in this thesis.

3.3.2 Plasma Flow Velocities

As described in Section 3.1, each transition results in emission at a specific wavelength. However, plasma motions in the line of sight direction result in changes of the observed wavelength according to the Doppler effect. The Doppler effect occurs when there is relative motion between the source of a wave and the observer: if the source is moving towards (away from) the observer, the observed wavelength will increase (decrease). The change in wavelength due to the relative motion is given by:

$$\frac{\lambda - \lambda_0}{\lambda_0} = \frac{v}{c}, \tag{3.16}$$

where λ is the observed wavelength, λ_0 is the rest wavelength, v is the relative speed along the line of sight and c is the speed of light.

In spectra, this effect is observed as a shift in the centroid of the emission line. Plasma motions away from (towards) the Sun lead to blue (red) shifts of the line centroids and, if the rest wavelength is known, the plasma speed can be measured using Eqn. 3.16. Note that this method can only be used to gain insight into the line of sight (or line of sight component of the) bulk plasma motions. Any motions perpendicular to the line of sight direction cannot be detected in this way.

The theoretical rest wavelength of a given emission line can be calculated using atomic physics data from the CHIANTI database (Dere et al., 1997). If using theoretical values, one must be careful that any instrumental effects that could result in wavelength shifts are also taken into account. Observationally, the rest wavelength can be determined by calculating the average centroid value over an area of the Sun where no significant line of sight plasma motions are expected (e.g. quiet Sun or limb). This method is reliable because, while the rest wavelength is not yet known, it is easy to identify areas that show a significant wavelength shift compared to the surroundings (indicative of a significant line of sight plasma motion at that location) and exclude it from the calculations. In addition, in this way, systematic instrumental effects that lead to wavelength shifts can be accounted for as well.

3.3.3 Line Broadening

Observed spectral lines have a non-zero width. The main contribution to the broadening of an emission line is caused by thermal motions within the plasma (Phillips, 2009). The thermal speed v_t (most probable speed) of a plasma at a particular temperature is given by:

$$v_t = \sqrt{\frac{2k_BT}{m_i}}, \tag{3.17}$$

where T is the plasma temperature, m_i is the ion mass and k_B is the Boltzmann constant. Particles within the plasma move in random directions at speeds that have a Maxwell-Boltzmann distribution peaking at v_t. This results in plasma motions at different speeds along the line of sight and their associated Doppler shifts. The superposition of all these small Doppler shifts gives the thermal broadening of the emission line:

$$\Delta\lambda = \lambda_0\sqrt{4\ln 2\frac{2k_BT}{m_i}}. \tag{3.18}$$

Note that this motion within the plasma is different from the bulk plasma motion discussed in Section 3.3.2. In addition, instrumental effects caused by the finite resolution of the detector also contribute to line broadening. It was observed, however, that observed spectral lines (the full width half maximum of the spectral line Gaussian fit) are sometimes broader than thermal broadening and instrumental effects could explain (Harra and Mason, 2004). The excess was broadly defined as non-thermal line broadening:

$$\Delta\lambda^2_{\text{observed}} = \Delta\lambda^2_{\text{thermal}} + \Delta\lambda^2_{\text{instrumental}} + \Delta\lambda^2_{\text{non-thermal}}. \tag{3.19}$$

The source of this excess broadening has been proposed to be due to a variety of reasons, including plasma turbulence, wave activity or unresolved Doppler shifts. Of course, line widths can also be artificially increased by line blends as well, but the likelihood of this happening can be confidently estimated from atomic physics data.

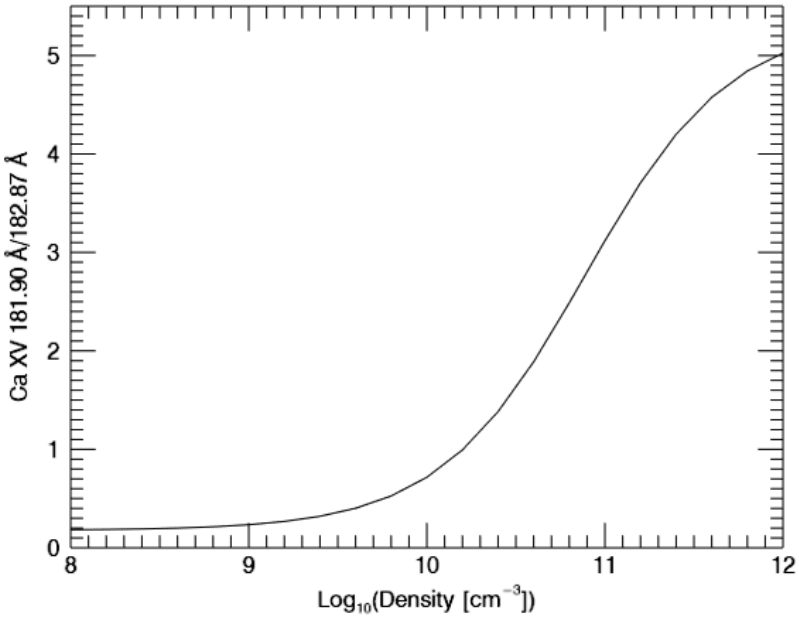

Figure 3.8: Predicted variation of the Ca XV 181.90 Å / 182.87 Å ratio with density, computed using the CHIANTI database (Dere et al., 1997) Version 10.1 (Del Zanna et al., 2021).

3.3.4 Density

Electron density can be measured using a pair of emission lines from a single ion for which the ratio of emissivities is density sensitive. This requires the existence of metastable levels within the ion (for details see e.g. Mariska, 1992). It is important to also check that the line ratio has no temperature dependence. An example of such a line pair (used for density calculations in Chapter 7) is Ca XV 181.90 Å / 182.87 Å and the theoretical dependence of the line ratio on density is shown in Figure 3.8. To calculate the electron density, the observed spectral line ratio must be compared against the theoretical curve.

3.3.5 Temperature

Electron temperature can be measured using a pair of emission lines from consecutive ions of a given element. The relative population at different ionization states is temperature dependent. It is important to check that the line ratio has no density dependence. An example of such a pair (used for temperature calculations in Chapter 7) is Fe XV 284.163 Å / Fe XVI 262.976 Å and the line ratio with tem-

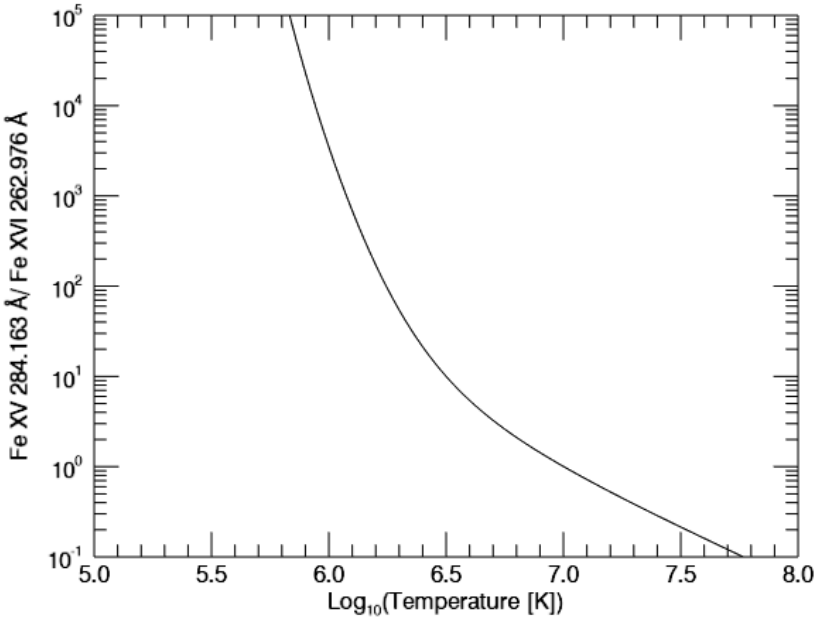

Figure 3.9: Predicted variation of the Fe XV 284.163 Å / Fe XVI 262.976 Å ratio with density, computed using the CHIANTI database (Dere et al., 1997) Version 10.1 (Del Zanna et al., 2021).

perature is shown in Figure 3.9. To calculate the electron temperature, the observed spectral line ratio must be compared against the theoretical curve.

3.3.6 Differential Emission Measure

The DEM, defined in Eqn. 3.13, is an indication of the amount of plasma along the line of sight that emits radiation at a given temperature T. Since the intensity of a spectral line is related to the DEM via:

$$I(\lambda) = \int Ab(X)C(N_e, T, \lambda)DEM(T)dT, \tag{3.20}$$

the DEM can be retrieved via an inversion method from a series of spectral line intensity measurements. There are currently three types of commonly implemented methods for calculating DEMs (see Young, 2023a): Gaussian DEMs, multi-linear DEMs and Markov-Chain Monte Carlo method (MCMC) DEMs. Gaussian and multi-linear DEMs assume a functional form for the DEM. MCMC DEMs do not, but they do assume a smooth DEM curve. Commonly used methods for obtaining the types of DEMs listed above are to either forward fit a chosen model (for the

Gaussian or multi-linear DEMs) or to use a Bayesian approach (for the MCMC DEMs; Kashyap and Drake, 1998). The advantages and disadvantages of these methods are discussed extensively by Del Zanna and Mason (2018).

After the inversion is performed and the DEM function is calculated, the inferred intensity of a given spectral line can be calculated using Eqn. **??**equation $\mathrm{I}_{\mathrm{inferred}}(\lambda) = \int Ab(X)C(N_e,T,\lambda)DEM_{\mathrm{inferred}}(T)dT$. This can be done for any spectral line, not only those included in the DEM analysis. To quantify the deviation of the calculated DEM, $DEM_{\mathrm{inferred}}(T)$, from the true DEM of the plasma, $DEM(T)$, a χ^2 quantity can be calculated as:

$$\chi^2 = \sum_{\text{all DEM lines}} \left(\frac{I_{\mathrm{inferred}} - I_{\mathrm{observed}}}{\sigma_{\mathrm{I_{observed}}}} \right)^2, \tag{3.21}$$

where I_{inferred} is the inferred spectral line intensity, I_{observed} is the observed spectral line intensity and $\sigma_{\mathrm{I_{observed}}}$ is the error in the observed intensity. The sum is over all the lines included in the DEM calculation. As a check that the calculated DEM is reasonably close to the true DEM, the values of the χ^2 should not be higher than the number of lines used in the DEM calculation. This ensures that the differences between the observed and inferred intensities are approximately within the observed errors.E:S/spectral line intensity:

$$I_{\mathrm{inferred}}(\lambda) = \int Ab(X)C(N_e,T,\lambda)DEM_{\mathrm{inferred}}(T)dT. \tag{3.22}$$

This can be done for any spectral line, not only those included in the DEM analysis. To quantify the deviation of the calculated DEM, $DEM_{\mathrm{inferred}}(T)$, from the true DEM of the plasma, $DEM(T)$, a χ^2 quantity can be calculated as:

$$\chi^2 = \sum_{\text{all DEM lines}} \left(\frac{I_{\mathrm{inferred}} - I_{\mathrm{observed}}}{\sigma_{\mathrm{I_{observed}}}} \right)^2, \tag{3.23}$$

where I_{inferred} is the inferred spectral line intensity, I_{observed} is the observed spectral line intensity and $\sigma_{\mathrm{I_{observed}}}$ is the error in the observed intensity. The sum is over all the lines included in the DEM calculation. As a check that the calculated DEM is

reasonably close to the true DEM, the values of the χ^2 should not be higher than the number of lines used in the DEM calculation. This ensures that the differences between the observed and inferred intensities are approximately within the observed errors.e the DEM is known, it is possible to calculate a total emission measure (EM) by integrating the DEM over the whole temperature range:

$$EM \equiv \int_h N_e N_H dh = \int_T DEM(T) dT. \qquad (\mathrm{cm}^{-5}) \qquad (3.24)$$

Another helpful product that can be obtained from the DEM is the effective temperature of a given emission line. This is defined as the weighted average of the temperature:

$$T_{\mathrm{eff}} = \frac{\int G(N_e, T, \lambda) DEM(T) T dT}{\int G(N_e, T, \lambda) DEM(T) dT}, \qquad (3.25)$$

and gives an indication of the temperature range where most of the line emission comes from. Note that this can often be different from T_{max}, which is the temperature corresponding to the peak of the contribution function $G(N_e, T, \lambda)$. In this thesis, the MCMC method is used in reconstructing the DEM from high resolution spectral data for the FIP bias calculations presented in Chapters 5 and 6 (see also Section 3.3.6).

Another method is to use regularised inversions which was shown to recover a DEM similar to that found via a MCMC method but in considerably less computational time (Hannah and Kontar, 2012). The regularised inversion method can be applied to high resolution spectral data (such as *Hinode* EIS), but can also be extended to broadband imaging data (such as SDO AIA). In this thesis, the regularised inversion method is used for computing the temperature distribution using broadband imager data in Chapter 6.

3.3.7 Plasma Composition

The total irradiance of a spectral line is proportional to the abundance of the element it corresponds to. This provides an opportunity to use spectral line intensity observations for coronal plasma composition measurements (see Section 2.2). Pottasch (1963) developed the first method to calculate an approximate emission mea-

sure and investigate elemental abundance using full-Sun EUV observations. Further methods have been developed by Jordan and Wilson (1971) and Widing and Feldman (1989), with the latter being used extensively for abundance measurements. Currently, a variety of methods for estimating the FIP bias can be found in the literature. An overview of the different methods of deriving chemical abundances using EUV spectroscopy is given by Del Zanna and Mason (2018). The methods used for the work in this thesis are described below.

If the total irradiances of the two lines are given by:

$$F(\lambda_{ji}) = Ab(X) \int C(N_e, T, \lambda_{ji}) DEM(T) dT, \tag{3.26}$$

and

$$F(\lambda_{lm}) = Ab(Y) \int C(N_e, T, \lambda_{lm}) DEM(T) dT, \tag{3.27}$$

then the relative abundance of the two elements in the corona is given by:

$$\frac{Ab(X)}{Ab(Y)} = \frac{F(\lambda_{ji})}{F(\lambda_{lm})} \times \frac{\int C(N_e, T, \lambda_{lm}) DEM(T) dT}{\int C(N_e, T, \lambda_{ji}) DEM(T) dT.} \tag{3.28}$$

The FIP bias, i.e. the relative abundance of the two elements in the corona compared to the photosphere, is then:

$$FIP_{bias} = \left(\frac{Ab(X)}{Ab(Y)}\right)_{\text{corona}} / \left(\frac{Ab(X)}{Ab(Y)}\right)_{\text{photosphere}}, \tag{3.29}$$

where the photospheric relative abundance is essentially a normalisation factor since the photospheric abundances do not change (see Chapter 2). Different methods for deriving the FIP bias can be found in the literature, and they include various ways of estimating the second term in Eqn. 3.28 depending on the number of lines available, the region studies etc. Note that the absolute abundances of some elements in the photosphere have not been measured directly (e.g. Ar; Lodders, 2008) and, therefore, have high uncertainties. For this reason, some studies prefer to only use the relative abundance of two elements (Eqn. 3.28) and not normalise by the

photospheric relative abundance, i.e. use Eqn 3.29, to avoid additional sources of uncertainty.

3.3.7.1 Spectral Line Ratios

This method involves making the approximation that the second term in Eqn. 3.28 is approximately 1, i.e. assuming that the contribution functions of the two spectral lines are identical. This reduces the FIP bias expression to the ratio of intensities of the emission lines involved:

$$FIP_{bias} = \frac{F(\lambda_{ji})}{F(\lambda_{lm})} / \left(\frac{Ab(X)}{Ab(Y)}\right)_{\text{photosphere}}. \tag{3.30}$$

In reality, no two contribution functions are identical. This means that the emission lines ratio is sensitive to temperature and density variations in addition to the plasma composition variations (see Figure 3.10). These introduce uncertainties to the FIP bias measurement which are difficult to estimate. To minimise these uncertainties, emission lines must be chosen carefully such that they have very similar contribution functions, i.e. a relatively constant contribution function ratio, at least over the expected temperature range of the plasma that is being observed (examples of such line pairs in the *Hinode* EIS spectral range are provided by Feldman et al., 2009). If the required emission lines are available, an additional level of confidence can be provided by analysing the temperature (see e.g. Doschek et al., 2018; Baker et al., 2022) or DEM distribution (see e.g. To et al., 2021) variations in the regions under study. If changes in the measured FIP bias are not associated with changes in the temperature/DEM distribution, then it is more likely that they are real composition variations. Density effects are typically much weaker than temperature effects.

This method has the advantages of being easy to apply and computationally inexpensive. It also does not require an extensive list of emission lines, which means it can also be applied to *Hinode* EIS studies that were not designed specifically for plasma composition measurements. The disadvantage is larger errors on the FIP bias measurements due to temperature and density effects . This method is used for plasma composition measurements presented in Chapter 6.

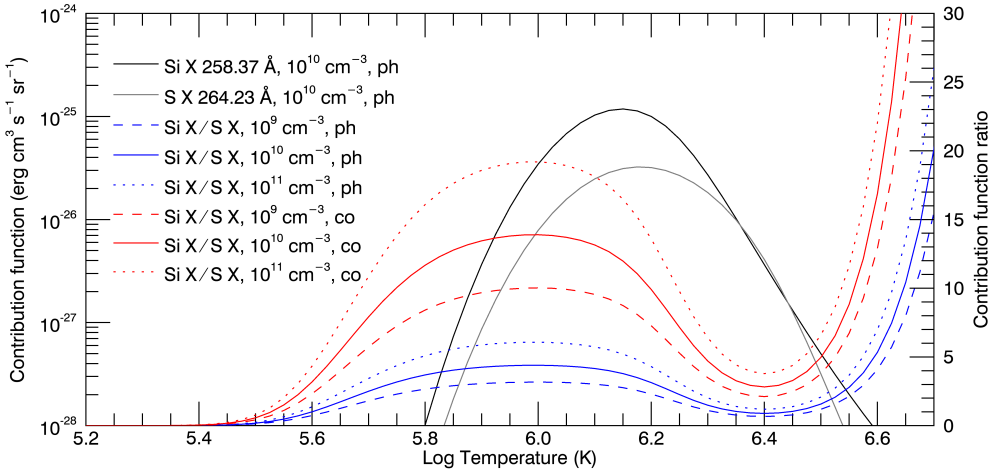

Figure 3.10: Contribution functions, $G(N_e, T, \lambda_{ij})$, at a density of 10^{10} cm^{-3} and assuming photospheric composition (sun_photospheric_2021_asplund) for Si x 258.37 Å (black) and S x 264.23 Å (gray). Ratio of the Si x 258.37 Å and S x 264.23 Å contribution functions for a selection of electron density values indicated in the legend assuming photospheric (sun_photospheric_2021_asplund; blue) and coronal (sun_coronal_2021_chianti; red) composition. Computed with CHIANTI (Dere et al., 1997) Version 10.1 (Del Zanna et al., 2021).

3.3.7.2 Isothermal Approximation

This method involves approximating the second term in Eqn. 3.28 by assuming the bulk of the plasma is isothermal. This means assuming that the DEM distribution has contribution from plasma at a single temperature, that all the plasma along the line of sight has a single temperature, so the second term in Eqn. 3.28 is approximated by the ratio of contribution functions. This, therefore, reduces the FIP bias expression to:

$$FIP_{bias} = \frac{F(\lambda_{ji})}{F(\lambda_{lm})} \times \frac{C(N_e, T_{\rm plasma}, \lambda_{lm})}{C(N_e, T_{\rm plasma}, \lambda_{ji})} \Big/ \left(\frac{Ab(X)}{Ab(Y)}\right)_{\rm photosphere}, \tag{3.31}$$

where $T_{\rm plasma}$ is the bulk plasma temperature, calculated as detailed in Section 3.3.5. Electron density can also be calculated as detailed in Section 3.3.4 and used for the contribution function ratio calculation.

This method provides a more accurate FIP bias estimation than the one given by Eqn. 3.30, as it accounts (to a first order approximation) for the effects of temper-

ature variations on the spectral line ratio. Coronal plasma is, however, multi-thermal and, in the absence of a DEM analysis, it is difficult to estimate the plasma population at temperatures away from the average (measured) temperature and the effect it has on the spectral line ratio.

This method has the advantage of being more accurate than the spectral line ratio one, in addition to being easy to apply and computationally inexpensive. The disadvantage is that uncertainties are still hard to estimate. And, of course, it has the additional requirement that observations of emission lines which can be used for the temperature diagnostic and have similar formation temperatures as the ones involved in the FIP bias diagnostic must be available. This method is used for plasma composition measurements presented in Chapter 7.

3.3.7.3 Differential Emission Measure Analysis

This method involves calculating the second term in Eqn. 3.28 by performing a DEM analysis (see Section 3.3.6) to account for temperature effects and, if lines are available, a density analysis (see Section 3.3.4) to account for density effects. There are various applications of this method, but the general idea of the version used in this thesis (also by e.g. Brooks and Warren, 2011; Baker et al., 2013; Brooks et al., 2015) is presented below.

The emission lines needed are: a pair of low-FIP (X) and high-FIP (Y) elements, a series of emission lines from the same ion (Z) for the DEM analysis and a line pair that is density sensitive. The density is measured as described in Section 3.3.4 and used to compute the contribution function (assuming photospheric abundances) as a function of temperature for the spectral lines involved in the DEM analysis. The DEM is computed using a series of emission lines from a low-FIP element, such that the calculated DEM is sensitive to the FIP effect. Ideally, all the lines used for the DEM belong to the same element such that they are equally affected by the FIP effect. However, in case not enough lines are available from the same element, multiple low-FIP elements can be used. The *Hinode* EIS spectrum includes a range of strong Fe lines with good temperature coverage which are typically used for the DEM analysis. The DEM distribution is reconstructed by in-

version of the observed spectral line intensities as described in Section 3.3.6. In this thesis an MCMC approach is used for the DEM calculation following the method of Brooks and Warren (2011); Baker et al. (2013); Brooks et al. (2015), although other methods exist as well (see Section 3.3.6). Since Z is a low-FIP element, the computed DEM will be higher than the DEM of a high-FIP element Y by a factor of the FIP bias, i.e.

$$DEM_{\text{inferred from Z}} = \text{FIP}_{\text{bias}} DEM_{\text{Y}}. \tag{3.32}$$

This means that, if the inferred DEM is used to compute the intensity of the high-FIP element Y (note that that high-FIP element Y was not used in the DEM calculation), it will overestimate it by a factor of the FIP bias:

$$\begin{aligned} \text{I}_{\text{inferred}}(\lambda, Y) &= \int G(N_e, T, \lambda) DEM_{\text{inferred}}(T) dT && (3.33)\\ &= \int G(N_e, T, \lambda) \text{FIP}_{\text{bias}} DEM_{\text{Y}} dT && (3.34)\\ &= \text{FIP}_{\text{bias}} \int G(N_e, T, \lambda) DEM_{\text{Y}} dT && (3.35)\\ &= \text{FIP}_{\text{bias}} \text{I}_{\text{observed}}(\lambda, Y). && (3.36) \end{aligned}$$

Therefore, the FIP bias is given by the ratio between the inferred and the observed line intensities of the high-FIP element:

$$\text{FIP}_{\text{bias}} = \frac{I_{\text{inferred}}(\lambda_{lm}, Y)}{I_{\text{observed}}(\lambda_{lm}, Y)}. \tag{3.37}$$

If the low-FIP element used for the FIP bias diagnostic (X) is not the same as the one used for the DEM analysis (Z), an additional step can be added where the DEM curve is scaled up or down (if necessary) such that the predicted intensity of the element X matches its observed intensity. In case X and Z have a significant separation in ionization potential they might show slightly different FIP bias values in the corona. Therefore, this step ensures that the inferred DEM accurately reflects the FIP bias of element X.

The main advantage of this method is that the temperature and density effects are accounted for. In addition, uncertainties can be quantified and errors can be

associated with the FIP bias measurement. The main challenge is that a DEM analysis requires an extended list of emission lines (typically Fe lines for the *Hinode* EIS spectrum) that cover the temperature range of the plasma composition diagnostic used. Not all EIS studies include an appropriate list of Fe lines and, for higher temperature diagnostics such as the Ca XIV 193.87 Å /Ar XIV 194.40 Å diagnostic, constraining the DEM can be challenging even if all the available *Hinode* EIS lines are present in the study. Another downside is that it is also computationally expensive. This method is used for plasma composition measurements presented in Chapter 5 and 6 (in Chapter 6, it is used alongside the spectral line ratios method).

Chapter 4

Instrumentation

A series of instruments and data products were used throughout this thesis to characterize the plasma composition of the selected target and explore how it is linked to other processes taking place in the solar atmosphere. This chapter provides an overview of these instruments.

4.1 Hinode

Hinode, or Sunrise, (called Solar-B until launch; Kosugi et al., 2007) was launched on 23 September 2006 (Japan time). It is a JAXA-led mission, with significant contributions from NASA and ESA. *Hinode* orbits the Earth in a Sun-synchronous polar orbit with a period of 98 minutes. It provides virtually continuous observations for nine months at a time. During the three months of summer in the northern hemisphere, *Hinode* experiences an 'eclipse season', where it orbits behind (and is therefore eclipsed by) the Earth for a maximum of 10 minutes in every orbit.

Hinode's main scientific aims include understanding the mechanisms responsible for coronal heating, drivers of transient phenomena such as flares and CMEs and energy transfer from the photosphere to the corona. The payload consists of three instruments providing remote solar observations at visible, EUV and X-ray wavelengths. The Solar Optical Telescope (SOT; Tsuneta et al., 2008) takes observations in the visible to study photospheric dynamics and magnetic field evolution. The EUV Imaging Spectrometer (EIS; Culhane et al., 2007) studies coronal dynam-

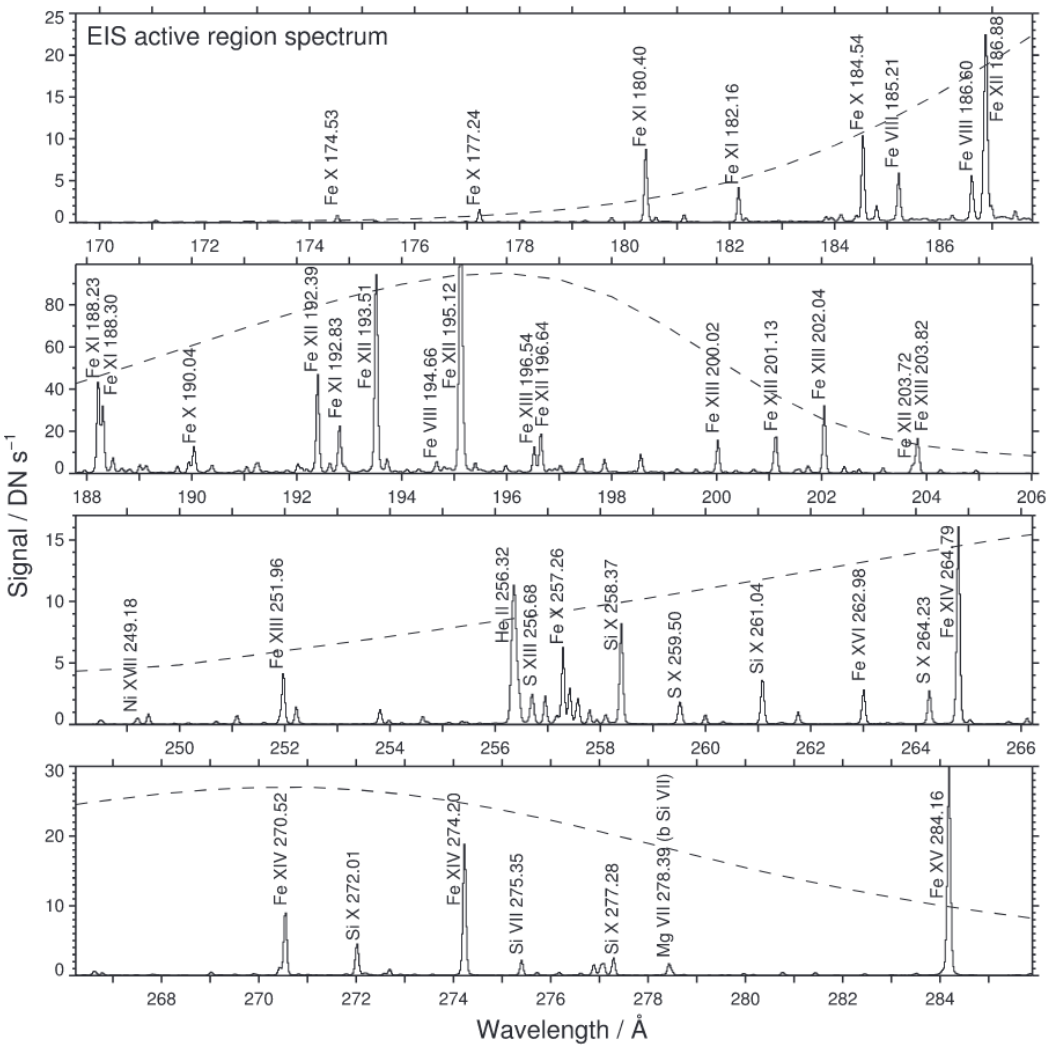

Figure 4.1: An example of an EIS active region spectrum with identifications for the main emission lines. Dashed lines show the effective area of the instrument, which peaks at 0.31 cm^2 on the short wavelength detector and 0.11 cm^2 on the long wavelength detector. Image from Young et al. (2007).

ics in the EUV. The X-Ray Telescope (XRT; Golub et al., 2007) takes observations in the X-rays, covering the temperature range 1-30 MK, to study coronal dynamics, particularly in active regions and solar flares.

4.1.1 The EUV Imaging Spectrometer (EIS)

The EUV Imaging Spectrometer (EIS; Culhane et al., 2007) provides high resolution spectral observations of the solar corona and transition region in two wavelength ranges, 170 - 210 Å (short wavelength band) and 250 - 290 Å (long wavelength band). The strongest lines observed in the EIS spectrum in an active region

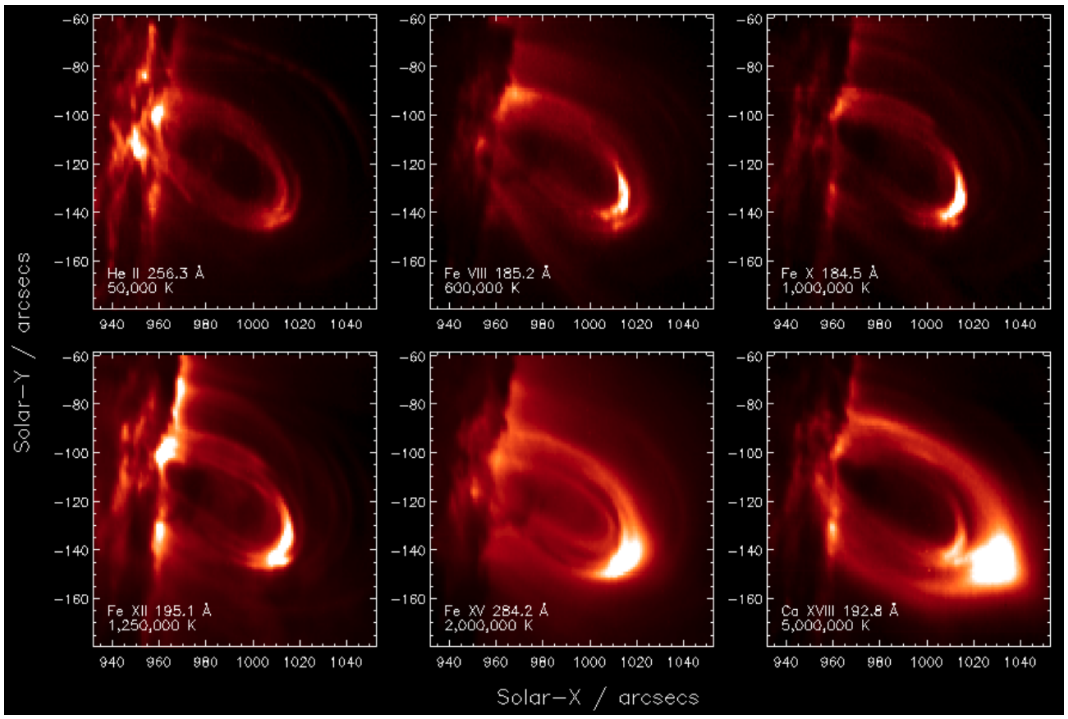

Figure 4.2: A system of coronal loops observed by *Hinode* EIS at the West limb on 17 December 2006 in a series of emission lines. Each of the lines is formed at a different temperature, and thus captures emission from plasma at different temperatures. Image produced by Dr. Peter Young [1].

are shown in Figure 4.1. EIS simultaneously observes a series of emission lines covering temperatures from 0.05 MK (He II) to as high as 16 MK (Fe XXIV) and providing temperature slices through the Sun's atmosphere (see Figure 4.2). EIS data and a series of data products are used extensively throughout this thesis.

4.1.1.1 Instrument Overview

EIS is a normal incidence multilayer-coated imaging spectrometer. The optical layout of the instrument is shown in Figure 4.3. Light emitted at the Sun enters the instrument through a thin 1500 Å Al filter (right hand side of Figure 4.3) which stops visible radiation from passing through. Radiation is then reflected off a primary mirror and focused onto a slit. After passing through the slit, it is dispersed by a diffraction grating onto the two CCD detectors.

The slit exchange mechanism (see Figure 4.3) can be used to choose between a 1″ slit, 2″ slit, 40″ slot or 266″ slot for each observation. Slit observations have

[1] Available at: https://pyoung.org/Hinode/gallery/flare_dec17.html.

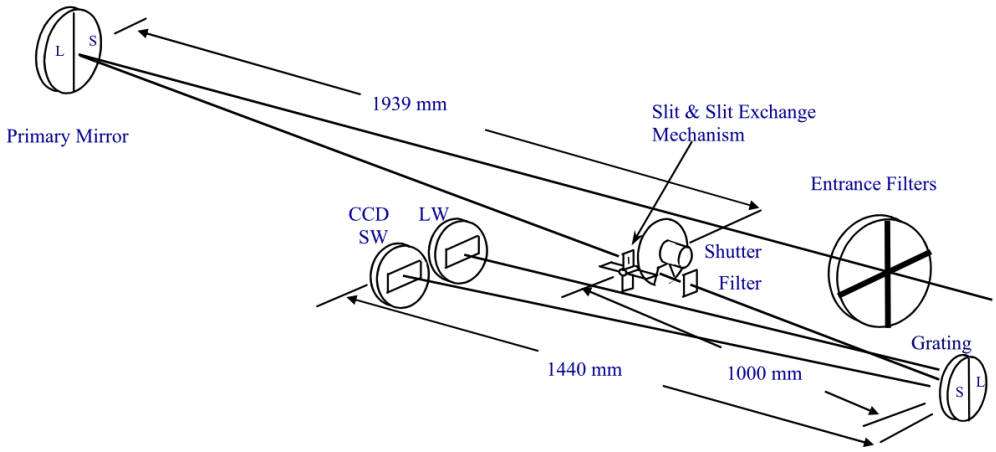

Figure 4.3: *Hinode* EIS optical layout, with labeled components. S/SW and L/LW refer to parts of the instrument that correspond to the short and long wavelength detectors. Image from Culhane et al. (2007).

high spectral resolution but it takes longer to produce a scan. Slot observations of a similar target are much faster, but this comes at the expense of reduced spectral resolution. Slot images can be interpreted as a superposition of simultaneous narrow slit spectra from adjacent solar positions. Under some assumptions, it is possible to deconvolve the narrow slit spectra hidden under the 40″ slot images (Ugarte-Urra et al., 2009). The analysis in this thesis uses slit observations.

EIS can perform two types of scans: raster scans and sit-and-stare scans. For raster scans, the location of the slit changes after each reading (moving from right to left), providing spatial information of the selected target. Rastering over a target can take tens of minutes to hours (depending on field of view and exposure time). This means that temporal information is sacrificed for spatial information. In addition, each slit scan takes place at a different time, so the rightmost part of the raster scan is observed earlier than the leftmost one. This type of scan is appropriate for scanning targets that are not expected to evolve significantly over the time of the scan. For sit-and-stare scans, the slit does not move, providing high cadence observations, but sacrificing spatial resolution. In this thesis, raster scans are used to study active region evolution (see Chapters 5 and 6) and sit-and-stare scans are used to study flare dynamics (see Chapter 7).

4.1.1.2 Known Instrumental Effects

There are a number of known instrumental effects that must be taken into account when working with EIS data. EIS instrumental effects and software to correct them are well documented in a series of EIS Software Notes[2]. The most important effects for the work included in this thesis are detailed below.

Spectrum tilt: Images obtained from different EIS emission lines are offset from each other in the Y direction. The spectrum tilt, T, is defined as:

$$T = \frac{Y_2 - Y_1}{\lambda_2 - \lambda_1}, \qquad \text{(pixels/Å)} \tag{4.1}$$

where Y is the Y-pixel position of an observed solar feature on the detector and λ is the wavelength at which the feature is observed. There are two instrumental effects that contribute to this: a tilt of the diffraction grating relative to the CCD axes (notation: $T_{\rm SW}$ and $T_{\rm LW}$ for the short and long wavelength detectors respectively), and a spatial offset in the Y direction between the two EIS CCDs (notation: Δ). The Y-offset of a given line is measured relative to the He II 256.32 Å line as:

$$Y = \begin{cases} T_{\rm SW}(\lambda - 185.21) + \Delta & \text{(pixels/Å)} \quad \text{for the SW channel,} \\ T_{\rm LW}(\lambda - 256.32) & \text{(pixels/Å)} \quad \text{for the LW channel.} \end{cases} \tag{4.2}$$

The grating tilt was calculated by Young et al. (2009), Del Zanna and Ishikawa (2009) and S. Kamio & H. Hara (unpublished work). Young et al. (2009) found a value of $T_{\rm SW} = -0.0792$ pixel/Å by analysing emission observed in Fe VIII and Fe XII on the SW channel. Del Zanna and Ishikawa (2009) found values of $T_{\rm SW} = -0.0802$ pixel/Å and $T_{\rm LW} = -0.0804$ pixel/Å by cross-correlating intensities from lines at different wavelengths. S. Kamio & H. Hara (unpublished work) found values of $T_{\rm SW} = -0.0872$ pixel/Å and $T_{\rm LW} = -0.0768$ pixel/Å using observations of the Mercury transit on 8 November 2006. While these values are slightly different, the resulting differences are below the size of one pixel. The IDL Solarsoft routine used for this correction, eis_ccd_offset, assumes the value of Young et al. (2009) for

[2] Available at: https://solarb.mssl.ucl.ac.uk/SolarB/eis_docs/EIS_Software_Notes.html

both detectors. The spatial offset between the two detectors was calculated by P. R. Young (unpublished work) and S. Kamio & H. Hara (unpublished work). The two studies are in agreement, finding an offset of 18.5 pixels between features observed in the Si VII 275.37 Å (LW detector) and Fe VIII 185.21 Å (SW detector) lines. Assuming a diffraction grating tilt of $T_{\mathrm{SW\,\&\,LW}} = -0.0792$ pixel/Å, an offset of 7.1 pixels is due to the grating tilt, leaving a physical offset of $\Delta = 11.4$ pixels between the two CCD detectors. This instrumental effect is discussed in EIS Software Note No. 3. This effect is wavelength dependent, and, therefore, it is particularly important to account for it when using spectroscopic diagnostics which use multiple emission lines such as FIP bias, density, temperature or DEM, all of which are used in this thesis.

Spectrum drift: The centroid of any given emission line on the EIS detector oscillates with a period of 98 minutes (*Hinode*'s orbital period) due to thermal effects on the detector. Throughout its orbit, *Hinode* maintains its pointing towards the Sun. It also does not rotate, so the illumination from Earth that reaches each side of the spacecraft varies with time. Particularly for EIS, this means that there are parts of the orbit where it is directly illuminated by the Earth and parts where it is shadowed by SOT. This results in a variation in the temperature of the instrument, which affects the EIS grating, resulting in a small rotation of the grating position. The location of emission lines moves on the CCD as a result, creating artificial Doppler shifts. As illustrated in Figure 4.4, these dominate the Doppler shifts due to real plasma motions on the Sun, so this effect must be corrected before using the data. Details about the spectrum drift and how to correct for it are provided by Kamio et al. (2010) and EIS Software Note No. 5.

Slit tilt: The EIS narrow slits ($1''$ and $2''$) are tilted relative to the CCD axes. In addition, the slits also have a small curvature. As a result, the measured line centroids vary systematically with Y-position. This introduces another artificial velocity shift (note this is completely different from the spectrum shift effect), as lines are increasingly more blue-shifted towards the top of the CCD. This effect is stronger for the $2''$ slit because the tilt of the $2''$ slit is larger than that of the $1''$ slit.

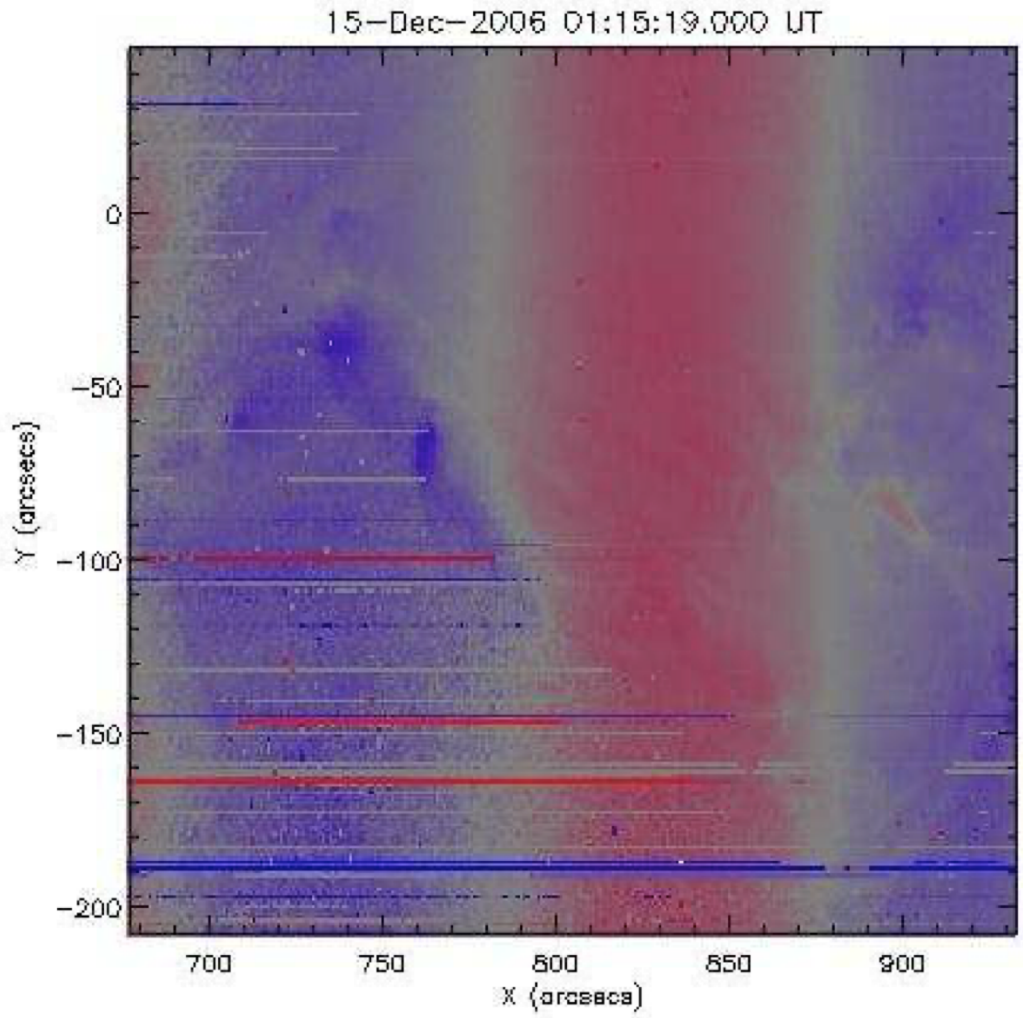

Figure 4.4: A velocity map derived from an EIS raster. EIS rasters from right-to-left, and the vertical bands of blue and red correspond to the spectrum drift during the raster. Image from EIS Software Note No. 5.

The slit tilt and curvature were estimated from EIS observations in strong emission lines (Kamio et al., 2010). More details on this effect can be found in EIS Software Note No. 4.

Point-spread function (PSF): EIS has an asymmetric PSF, which results in a spatial Y offset between regions of strong blueshifts/redshifts and regions of high intensity. This is another type of artificial velocity shift, but it is, again, completely different from the spectrum shift and slit tilt effects. The EIS PSF has an elliptical shape and is tilted relative to the Solar-Y and wavelength axes (see Figure 4.5). When a bright point is imaged, the photon counts on the detector follow the shape

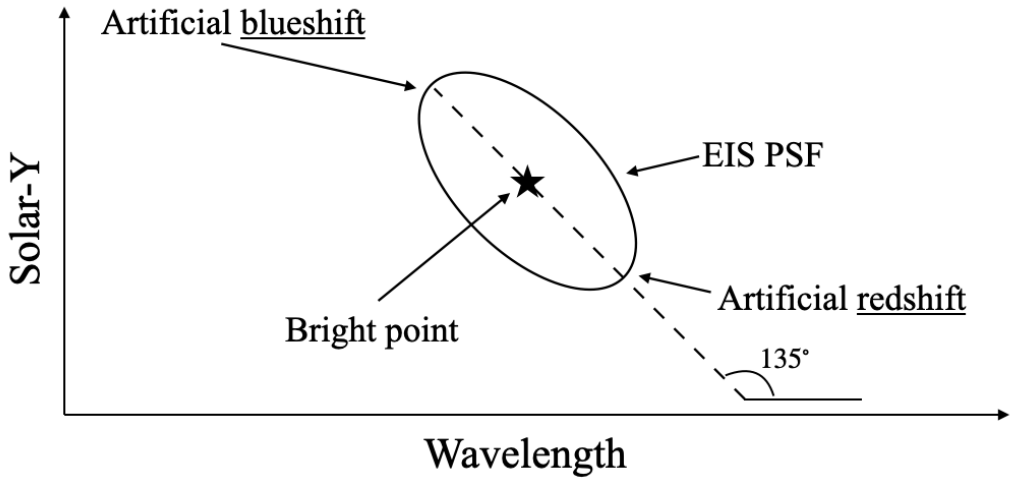

Figure 4.5: Schematic of the EIS PSF (solid line ellipse) of a bright point (marked by a star). The main axis of the ellipse is tilted at an angle of 135° relative to the wavelength axis. Adapted from EIS Wiki [3].

of this ellipse. This results in a blueshift in the north side of the bright point and a redshift in the south side. If the PSF was rotated by 90°, we would see the opposite effect and, if the ellipse was aligned with either the Solar-Y or the wavelength axes, we would not see an asymmetric effect at all. If the intensity gradient is decreasing from north to south, the centroid of the emission line is redshifted and if it is increasing the centroid of the emission line is blueshifted (Young et al., 2012). Typically, this effect is small, but it becomes significant in regions with a strong intensity gradient along the slit. This is particularly important at the solar limb, where coronal lines are stronger due to limb brightening (e.g. Tian et al., 2010). This effect is described in detail by Young et al. (2012) and in EIS Software Note No. 8.

Instrumental width: The widths of emission lines captured by EIS (see Section 3.3.3) are dominated by an instrumental component. This instrumental width is different for the two detectors and also for the 1″ and 2″ slits. Early post-launch calculations estimated widths of 54 mÅ for the SW band and 55 mÅ for the LW band (Brown et al., 2008). The instrumental width was soon after discovered to also vary with Y-pixel position on the CCD detector. It varies from approximately 60 mÅ at the bottom of the CCD to 75 mÅ at the top for the 1″ slit and is approximately 7

[3] Available at: https://vsolar.mssl.ucl.ac.uk/JSPWiki/, with original image available in the Spatial offset of velocity features relative to intensity features section.

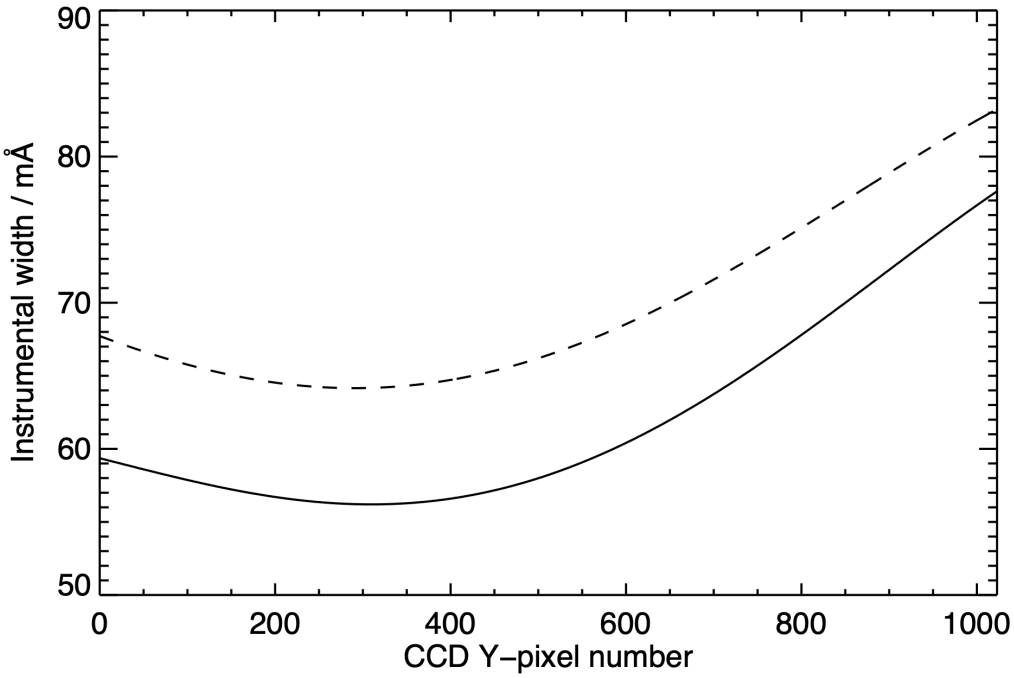

Figure 4.6: *Hinode* EIS instrumental width variation with CCD Y-pixel location for the 1″ (solid line) and 2″ (dashed line) slits. Image from EIS Software Note No. 7.

mÅ higher for the 2″ slit (see Figure 4.6). This effect is detailed in EIS Software Note No. 7 and is routinely corrected using the Solarsoft eis_slit_width routine.

Detector sensitivity and degradation: The detector sensitivity varies with wavelength on both detectors. In addition, the relative degradation of the two detectors is not known. A few calibration studies focused on accounting for these effects, in particular Del Zanna (2013b), Warren et al. (2014) and, more recently, Del Zanna et al. (2023). This aspect is particularly important for any calculations that involve multiple emission lines and it is the reason why quantities such as density, temperature or FIP bias are only calculated using ratios of emission lines from the same detector. Where possible, it is preferred that the lines involved in the ratios are close in wavelength to minimise the effects of detector sensitivity variation with wavelength.

Hot and warm pixels: the EIS detectors have a few hot pixels and a relatively large and increasing number of warm pixels. These are locations where the solar signal is affected by issues with the detector electronics and must be flagged before carrying out data analysis. Hot pixels are pixels on the CCD which have higher than

normal rates of charge leakage, likely due to defects in certain parts of the detector or caused by radiation damage (in particular the South Atlantic Anomaly, which *Hinode* passes through during every orbit). Warm pixels are similar to hot pixels, but they have lower signal levels and, unlike hot pixels, they are harder to identify in the data. The properties of these hot and warm pixels are discussed in EIS Software Note No. 6 and suggestions on how to handle them in data analysis are discussed in EIS Software Note No. 13.

4.1.1.3 Data products

Hinode EIS data can be used to derive a variety of spectroscopic diagnostics, including all of those listed in Section 3.3. Intensity, Doppler velocity and nonthermal velocity can be measured for each line on the extensive emission lines list on the EIS spectrum. Density, temperature and FIP bias can also be measured using pairs of emission lines. In addition, the EIS spectrum includes a wide range of Fe lines which can be used to derive the EM and DEM distribution (see Section 3.3.6).

The *Hinode* EIS spectral range includes line pairs that can be used as plasma composition diagnostics at different plasma temperatures. In addition, calculations of the DEM distribution can be used to account for temperature effects in the line ratio (see Section 3.3.7). A few examples of the EIS plasma composition diagnostics used in the literature include: Si x 258.375 Å/S x 264.233 Å ($\log(T[\mathrm{K}]) \approx 6.2$; e.g. Brooks and Warren, 2011; Baker et al., 2013), Fe XII 195.12 Å/S x 264.23 Å ($\log(T[\mathrm{K}]) \approx 6.2$; e.g. Ko et al., 2016), Fe XVI 262.98 Å/S XIII 256.69 Å ($\log(T[\mathrm{K}]) \approx 6.4$; e.g. Baker et al., 2022), Ca XIV 193.87 Å /Ar XIV 194.40 Å ($\log(T[\mathrm{K}]) \approx 6.6$; e.g. Doschek et al., 2018; To et al., 2021). A list of additional plasma composition diagnostics that could be derived from *Hinode* EIS data are explored by Feldman et al. (2009).

4.2 The Solar Dynamics Observatory (SDO)

The *Solar Dynamics Observatory* (SDO; Pesnell et al., 2012), the first mission to be part of NASA's Living With a Star (LWS) Program, was launched on 11 February 2010. The spacecraft is placed in a geosynchronous orbit above its ground

station in New Mexico, which enables it to take continuous observations of the Sun. SDO's payload consists of three instruments. The Atmospheric Imaging Assembly (AIA; Lemen et al., 2012) observes the evolution of the solar atmosphere at various temperatures. The Helioseismic and Magnetic Imager (HMI; Scherrer et al., 2012) monitors the evolution of the photospheric white light emission and magnetic field. The EUV Variability Experiment (EVE; Woods et al., 2012) measures the full-Sun integrated EUV irradiance with unprecedented spectral resolution.

4.2.1 The Atmospheric Imaging Assembly (AIA)

The Atmospheric Imaging Assembly (AIA; Lemen et al., 2012) is a broadband imager that produces full-Sun observations of the various layers of the solar atmosphere in ten wavelength bands (see Table 4.1) with a cadence of 12 s. One of these passbands (4500 Å) observes in the optical part of the spectrum, capturing continuum emission from the photosphere. Two of these passbands (1700 Å and 1600 Å) observe emission in the ultraviolet (UV) part of the spectrum. While the 1600 Å and 1700 Å channels are typically believed to be dominated by photospheric continuum emission, results of Simões et al. (2019) suggest that this is only the case in plage regions while in flaring regions the flare excess emission is of chromospheric origin. The other seven passbands (304 Å, 171 Å, 193 Å, 211 Å, 335 Å, 94 Å and 131 Å) cover strong emission lines formed in the EUV part of the spectrum. Each passband is centered on lines that form at different temperatures, maximizing the temperature coverage of the instrument. The 304 Å passband is dominated by the He II line and observes the chromosphere and transition region. The 171 Å, 193 Å, 211 Å, 335 Å, 94 Å and 131 Å passbands are dominated by different Fe lines and observe the corona at different temperatures. Figure 4.7 shows the temperature response of the coronal passbands. It is important to note that, while each filter has a primary contribution from one or two lines, AIA is a broadband instrument, so emission from other lines is captured as well. This can introduce uncertainty about what plasma population is dominating in an observation. AIA data are used throughout this thesis.

Channel	Primary ion(s)	Region of the atmosphere	Char. log(T[K])
4500 Å	continuum	photosphere	3.7
1700 Å	continuum	temperature minimum, photosphere	3.7
304 Å	He II	chromosphere, transition region	4.7
1600 Å	C IV + cont.	transition region, upper photosphere	5.0
171 Å	Fe IX	quiet corona, upper transition region	5.8
193 Å	Fe XII, Fe XXIV	quiet corona and hot flare plasma	6.2, 7.3
211 Å	Fe XIV	active region corona	6.3
335 Å	Fe XVI	active region corona	6.4
94 Å	Fe XVIII	flaring corona	6.8
131 Å	Fe VIII, Fe XXI	transition region, flaring corona	5.6, 7.0

Table 4.1: Primary emission contribution(s) and temperature range covered by each SDO AIA passband. Table from Lemen et al. (2012).

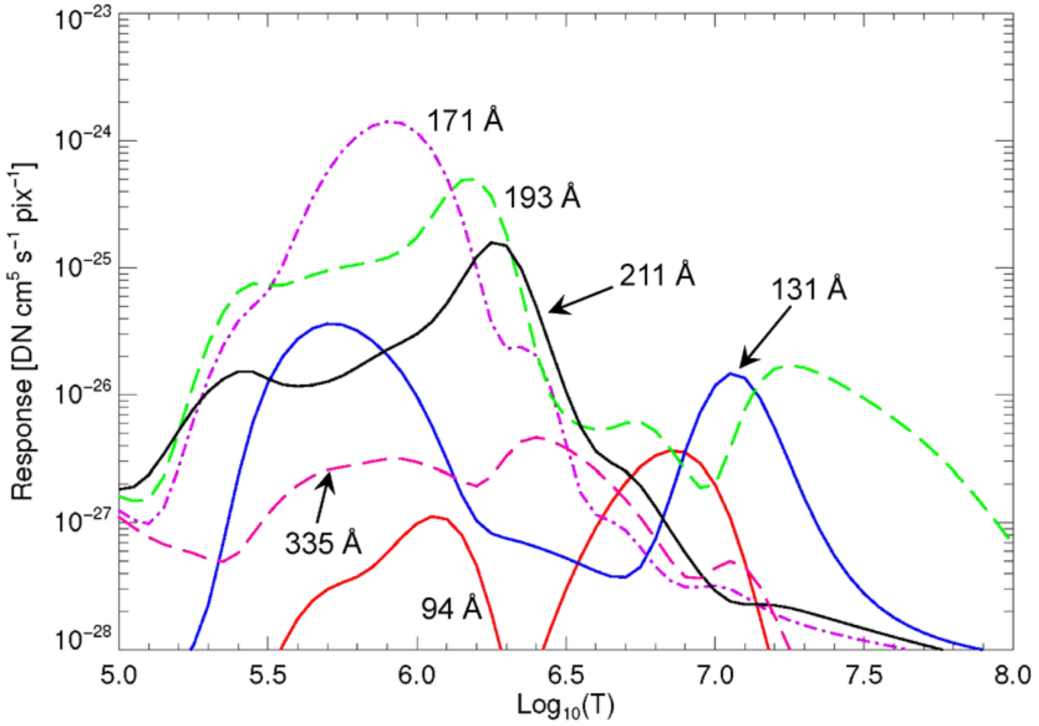

Figure 4.7: Temperature response functions for the six AIA channels dominated by coronal Fe emission. The functions are calculated from the AIA effective area functions (Boerner et al., 2012) and using atomic data from the CHIANTI database (Dere et al., 1997). Image from Lemen et al. (2012).

4.2.2 The Helioseismic and Magnetic Imager (HMI)

The Helioseismic and Magnetic Imager (HMI; Scherrer et al., 2012) is a narrow-band instrument that produces full-Sun high-cadence observations of the solar photosphere. It observes the 4 Stokes polarisation states (I, Q, U, V) at 6 wavelengths across the Fe I 6173 Å absorption line as well as the continuum emission near the Fe I 6173 Å spectral line. These observations are then used to measure continuum intensity, Doppler velocity and line-of-sight magnetic flux in the photosphere with a cadence of 45 s and photospheric vector magnetic field with a cadence of 12 minutes.

The photospheric magnetic field strength can be estimated using knowledge of the Zeeman effect. The Zeeman effect is the effect of splitting of a spectral line into several components in the presence of a static magnetic field: one at higher wavelength, one at lower wavelength and one unchanged. The degree of splitting is related to, and, therefore, can be used to measure, the strength of the magnetic field. These shifted components also have different polarisation states, one is right-hand circularly polarised and the other left-hand circularly polarised. The unshifted component is linearly polarised. HMI obtains 24 filtergrams (six wavelengths and four Stokes parameters) which can be used to determine the line of sight and, using an inversion process, the vector magnetic field. Photospheric plasma flows can also be investigated using the Doppler effect of spectral lines (using the principle outlined in Section 3.3.2). HMI magnetic field data are used in Chapters 5 and 6.

4.3 The Solar Terrestrial Relations Observatory (STEREO)

The *Solar TErrestrial RElations Observatory* (STEREO; Kaiser et al., 2008) mission was launched in October 2006. It consists of two identical satellites, STEREO-A and STEREO-B, placed in heliocentric orbits at a distance of approximately 1 AU from the Sun. STEREO-A is slightly closer to the Sun than Earth, orbits the Sun slightly faster than Earth and is, therefore, orbiting ahead of Earth. STEREO-B is slightly further away from the Sun than Earth, orbits the Sun slightly

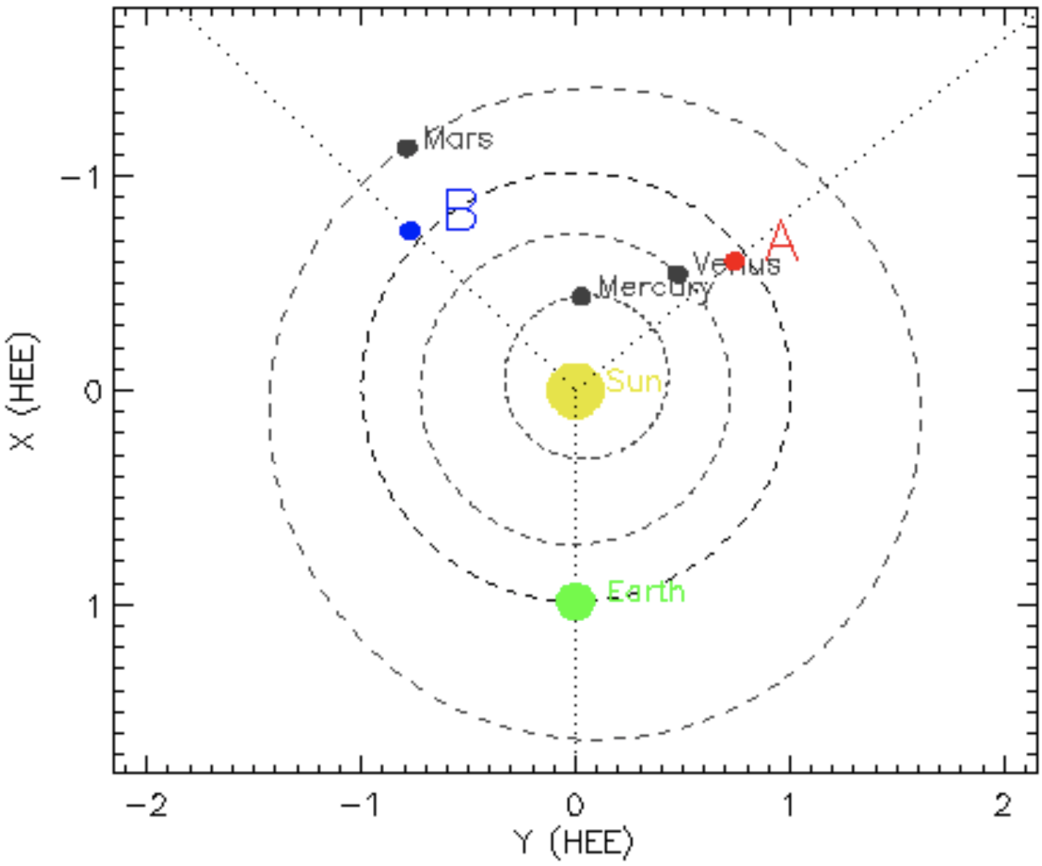

Figure 4.8: Locations of the STEREO-A and STEREO-B spacecraft relative to Earth on the 16th January 2013. Image created using the 'Where is STEREO?' tool [4].

slower than Earth and is, therefore, orbiting behind Earth. The angular separation between STEREO-A/STEREO-B and Earth increases by approximately 22° every year, enabling them to provide a stereoscopic view of the Sun as this separation angle increases. An example of the STEREO spacecraft and SDO being located ideally to image the whole Sun is shown in Figure 4.8 (SDO and *Hinode* are essentially located at Earth). Contact with STEREO-B was lost on 1 October 2014, but STEREO-A remained functional. Each STEREO satellite has a total of 16 instruments on board, providing both remote sensing and in situ observations.

4.3.1 The Extreme Ultraviolet Imager (EUVI)

The Extreme Ultraviolet Imager (EUVI; Wuelser et al., 2004) is part of the Sun Earth Connection Coronal and Heliospheric Investigation (SECCHI; Howard et al.,

[4] Available at: https://stereo-ssc.nascom.nasa.gov/cgi-bin/make_where_gif.

2008) instrument suite. It is a broadband imager that observes the chromosphere and the low corona in four passbands: 171 Å, 195 Å, 284 Å and 304 Å, covering a temperature range from 50,000 K to 20 MK. EUVI produces full-Sun images with a resolution of 1.6 arcsec per pixel and initial passband dependent cadence of 75-300 s for the 171 Å channel, 300-600 s for the 195 Å and 304 Å channels and 1200 s for the 284 Å channel. Later in the mission, as the spacecraft separation increased and, as a consequence, the bandwidth decreased, the cadence was reduced to 300 s in the 195 Å passband, 600 s in the 304 Å passband and approximately 4 hours for the 171 Å and 284 Å passbands. Data from STEREO-A EUVI and STEREO-B EUVI are used in Chapter 5.

4.4 Geostationary Operational Environmental Satellites (GOES)

The *Geostationary Operational Environmental Satellites* (GOES) suite is a network of satellites that continuously monitors atmospheric conditions and solar activity. They have two main goals: 1) to make timely weather forecasts and understand long-term climate conditions, and 2) to make accurate space weather predictions.

4.4.1 X-ray Sensor (XRS)

Each GOES satellite has two X-ray Sensors (XRS) which measure solar X-ray fluxes in two passbands: 0.5-4.0 Å (short channel) and 1.0-8.0 Å (long channel). The peak X-ray flux registered in the long channel passband during a solar flare is used to classify the magnitude of the solar flare (see Table 1.2 in Section 1.2.2). Data from GOES XRS are used briefly throughout this thesis to classify flare classes.

Chapter 5

Global Plasma Composition Patterns in Quiescent Active Regions: Links to Evolutionary Stage

This chapter contains results published in The Astrophysical Journal (Mihailescu et al., 2022). This work was carried out under the supervision of Prof. Lucie Green, Dr. Deborah Baker, Dr. David Long and Prof. Lidia van Driel-Gesztelyi. The FIP bias calculations were performed by Dr. David Brooks (George Mason University). The results of this work were presented in two contributed talks at the COSPAR Scientific Assembly (Athens, Greece) in July 2022 and the *Hinode* 15/IRIS 12 Meeting (Prague, Czech Republic) in September 2022 and a virtual seminar at the Astronomical Institute of the Romanian Academy (Bucharest, Romania) in November 2022.

5.1 Introduction

Plasma composition is highly variable in active regions, both spatially and in time. As detailed in Section 2.4.1, the plasma composition in the early stages of an active region's emergence phase is photospheric (Widing and Feldman, 2001). This makes sense, since magnetic flux tubes are emerging from below the photosphere and expanding into the corona, bringing upwards plasma with photospheric composition. As flux emergence progresses, the FIP bias increases with time in both large

active regions (Widing and Feldman, 2001) and small emerging flux regions (Baker et al., 2018). Once the active region enters its decay phase, it is dominated by a global decrease in the FIP bias (Baker et al., 2015; Ko et al., 2016) until it reaches values comparable with those of the surrounding quiet Sun (Ko et al., 2016). Baker et al. (2018) proposed that the FIP bias increase in the emergence phase is driven by the fractionation process (Laming, 2004, 2015) and transport of fractionated plasma from the chromosphere into the corona. In contrast, the FIP bias decrease in the late decay phase is driven by plasma mixing as a result of magnetic reconnection between active region loops and small emerging bipoles that bring up photospheric plasma in the dispersing field of the active region.

As well as temporal variation, active regions show spatial variation in FIP bias. The highest FIP bias values are observed at active region loop footpoints (Baker et al., 2013), indicating that this is where the fractionation process takes place (as proposed by Laming, 2004). Traces of high FIP bias are observed along some of the active region loops, indicating plasma starting to mix along loops (Baker et al., 2013). Flux cancellation along the active region main polarity inversion line (PIL), and the associated flux rope formation can lead to lower FIP bias levels (Baker et al., 2013, 2022). The FIP effect was found to partially shut down in regions above strong sunspots, with observations showing plasma with photospheric or close to photospheric composition (Doschek and Warren, 2017; Baker et al., 2021b).

The case studies outlined above found trends and patterns in how FIP bias evolves and is distributed within active regions. In the work presented in this chapter, active region plasma composition trends are explored in a large dataset of 28 active regions from 3 full Sun *Hinode* EIS scans to understand the effects of age, magnetic flux, magnetic configuration and evolutionary stage on the observed FIP bias variations. The dataset contains active regions of all evolutionary stages, from emergence to decay, including very dispersed active regions that are in a more developed stage than the ones analysed in previous studies. This provides an opportunity to investigate whether there is a link between plasma composition and active region characteristics such as age, evolutionary stage and magnetic field configu-

ration in a larger dataset than before. Individual case studies are also investigated to understand how particular aspects of an active region can influence its plasma composition in the corona.

5.2 Observations

The dataset used for this study comprises three full Sun EIS scans taken on 16-18 January 2013, 1-3 April 2015 and 18-20 October 2015. In total, these scans cover 28 active regions and the *Hinode* EIS spectroscopic observations can be analysed to obtain composition measurements at the time of each scan. The active regions are shown in Figure 5.1 and their general characteristics are given in Table 5.1. Details on all the active regions in the study are shown in Figures 5.2-5.11.

5.2.1 Photospheric Magnetic Field and Coronal EUV Observations

Photospheric line of sight magnetic field data from SDO HMI were used alongside coronal EUV images from SDO AIA and STEREO EUVI to explore the history of each active region and determine its approximate age and complexity at the time of its corresponding EIS scan. Each active region was tracked back in time to the moment when its first signs of flux emergence are observed. In photospheric magnetic field observations, the considered signs of flux emergence were the appearance of pairs of positive and negative magnetic field fragments that move away from each other. In the EUV, flux emergence signatures considered were the appearance of bright loops that expand as a result of the photospheric footpoints moving away from each other.

Where the flux emergence was captured in observations, either by SDO or STEREO, the time of emergence was defined as the time when the first flux emergence signature is observed. This likely results in an uncertainty of a few minutes or hours on the active region age. Where the emergence happened in an area that was not being observed by either spacecraft, a minimum and maximum age were determined instead. The minimum (maximum) age was given by the first available observation of the active region (last available observation before the data gap).

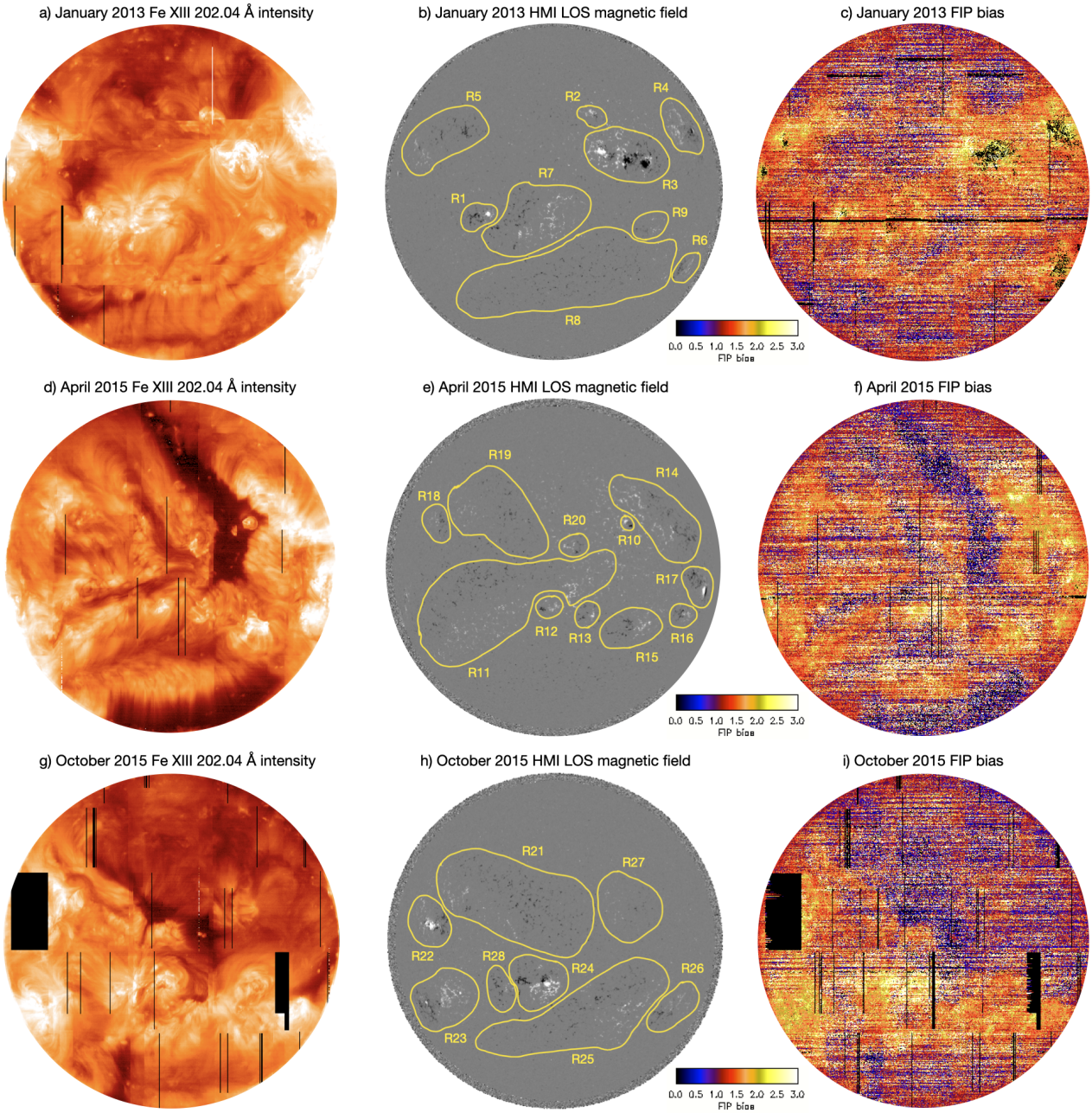

Figure 5.1: Full Sun maps contructed from: a, d, g) *Hinode* EIS Fe XIII 202.04 Å intensity; b, e, h) HMI line of sight photospheric magnetic field strength with overlaid active region contours (in yellow); c, f, i) *Hinode* EIS Si/S FIP bias. The black boxes present in the FIP bias and Fe XIII 202.04 Å intensity maps represent gaps in the EIS data. Individual active region contours overlaid on *Hinode* EIS Fe XIII 202.04 Å intensity, HMI line of sight photospheric magnetic field strength and *Hinode* EIS FIP bias maps are shown in Figures 5.2–5.11.

Table 5.1: General characteristics of active regions presented in Figure 5.1.

Region	NOAA number	Type	Age (days)	Evolutionary stage	Total magnetic flux ($\times 10^{20}$ Mx)	Mean magnetic flux density (G)	Median FIP bias	Skewness coefficient	Spread	Percentage FIP bias > 4
R1	11658	Simple	5	Spots	59 ± 0.07	200 ± 0.2	1.9	0.12	0.6	0.1
R2	11656	Simple	11	Decayed	15 ± 0.04	145 ± 0.4	1.7	0.15	0.5	0.6
R3	11654	Nest	11 (63)	Spots	364 ± 0.17	222 ± 0.1	1.9	0.21	0.6	0.9
R4	11652	Simple	13-26	Spots	59 ± 0.10	103 ± 0.2	1.9	0.15	0.5	0.0
R5	N/A	Simple	39	Dispersed	52 ± 0.09	100 ± 0.2	1.7	0.19	0.6	0.7
R6	11650	Simple	13-26	Decayed	16 ± 0.06	83 ± 0.3	1.7	0.15	0.4	0.2
R7	N/A	Simple	53	Dispersed	123 ± 0.13	120 ± 0.1	1.6	0.18	0.6	0.5
R8	N/A	Nest	189 (244)	Filament channel	70 ± 0.12	81 ± 0.1	1.5	0.25	0.8	1.0
R9	11657	Simple	13-24	Decayed	10 ± 0.04	87 ± 0.4	1.6	0.18	0.6	0.1
R10	12317	Simple	0.5	Emerging	19 ± 0.04	233 ± 0.5	1.7	0.16	0.7	0.7
R11	N/A	Nest	120 (214)	Filament channel	197 ± 0.18	95 ± 0.1	1.6	0.25	0.8	2.0
R12	12316	Simple	6-21	Decayed	20 ± 0.05	147 ± 0.4	2.0	0.27	0.8	3.0
R13	12314	Simple	8-20	Decayed	14 ± 0.04	141 ± 0.4	1.7	0.19	0.6	0.5
R14	12310	Nest	8-25 (86)	Dispersed	95 ± 0.12	106 ± 0.1	1.8	0.16	0.5	0.3
R15	N/A	Simple	24	Decayed	41 ± 0.08	119 ± 0.2	1.8	0.19	0.7	2.0
R16	12315	Simple	11-19	Decayed	18 ± 0.05	113 ± 0.3	1.8	0.10	0.5	0.1
R17	12305	Simple	12-19	Spots	64 ± 0.05	169 ± 0.2	1.9	0.21	0.5	0.5
R18	N/A	Simple	3-17	Decayed	13 ± 0.04	99 ± 0.4	1.7	0.13	0.5	0.4
R19	N/A	Nest	58-76 (111)	Filament channel	39 ± 0.09	84 ± 0.2	1.5	0.23	0.8	2.0
R20	N/A	Simple	7-20	Decayed	15 ± 0.05	125 ± 0.4	1.6	0.29	0.8	2.0
R21	N/A	Nest	29 (183)	Filament channel	143 ± 0.16	97 ± 0.1	1.5	0.25	1.0	4.0
R22	12436	Simple	30-44	Spots	100 ± 0.10	166 ± 0.2	1.9	0.08	0.6	0.4
R23	N/A	Simple	27	Spots	107 ± 0.10	115 ± 0.1	1.9	0.10	0.4	1.0
R24	12434	Simple	27	Spots	188 ± 0.12	213 ± 0.1	2.2	0.23	1.0	4.0
R25	N/A	Simple	63-79	Dispersed	107 ± 0.13	104 ± 0.1	1.7	0.23	0.7	1.0
R26	N/A	Simple	38-51	Dispersed	28 ± 0.07	97 ± 0.2	1.7	0.09	0.4	0.1
R27	N/A	Simple	35	Dispersed	13 ± 0.05	79 ± 0.3	1.4	0.34	0.9	2.0
R28	N/A	Simple	21-25	Decayed	21 ± 0.06	119 ± 0.3	1.9	0.24	0.6	1.0

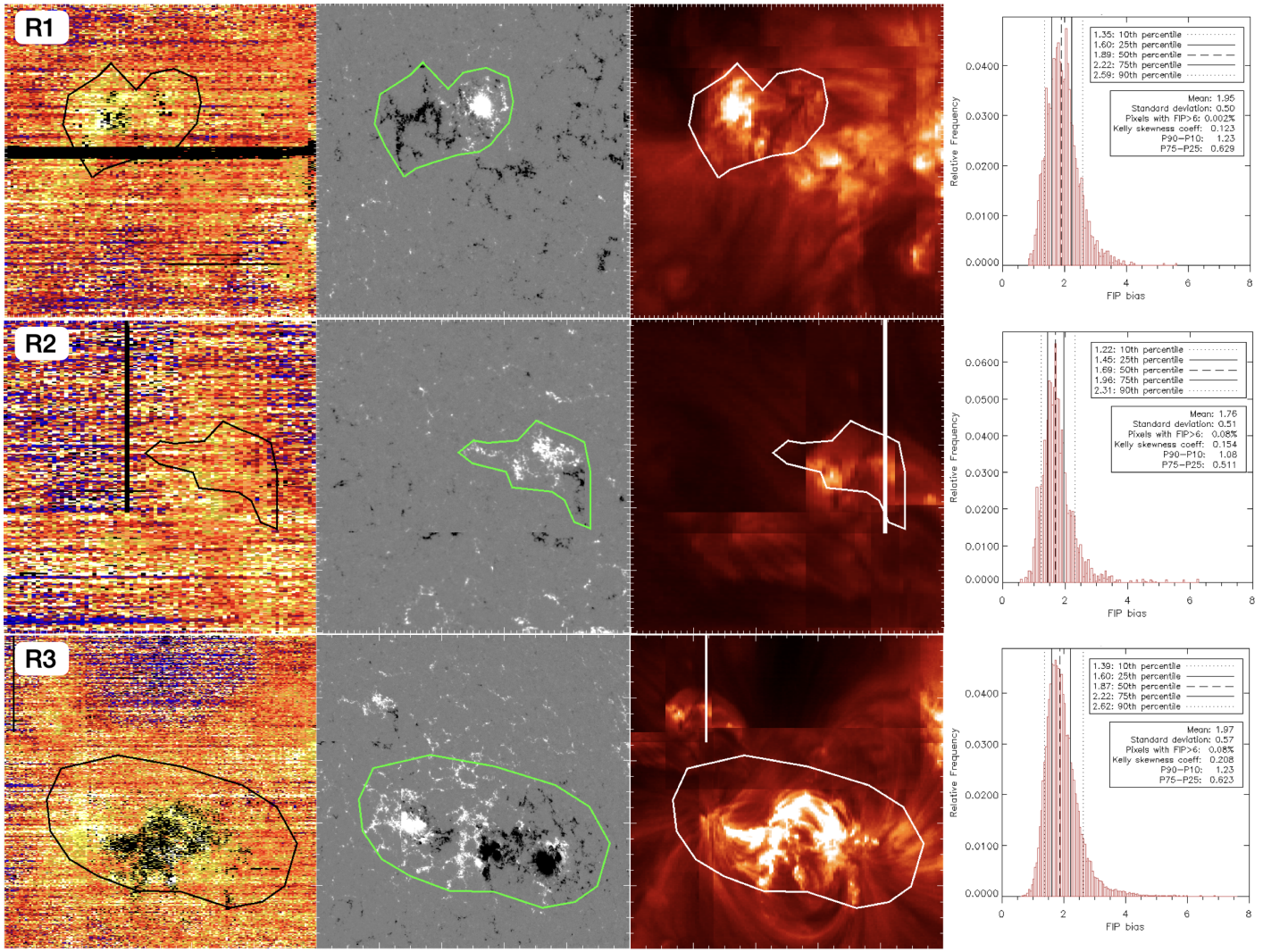

Figure 5.2: FIP bias distributions in the selected active region contours (R1-R3) indicating the magnetic field boundaries of the active regions. From left to right: *Hinode* EIS Si/S FIP bias, HMI line of sight magnetic field strength, *Hinode* EIS Fe XIII 202.04 Å intensity, and FIP bias distribution within the active region contour (shown in black, green and white, respectively).

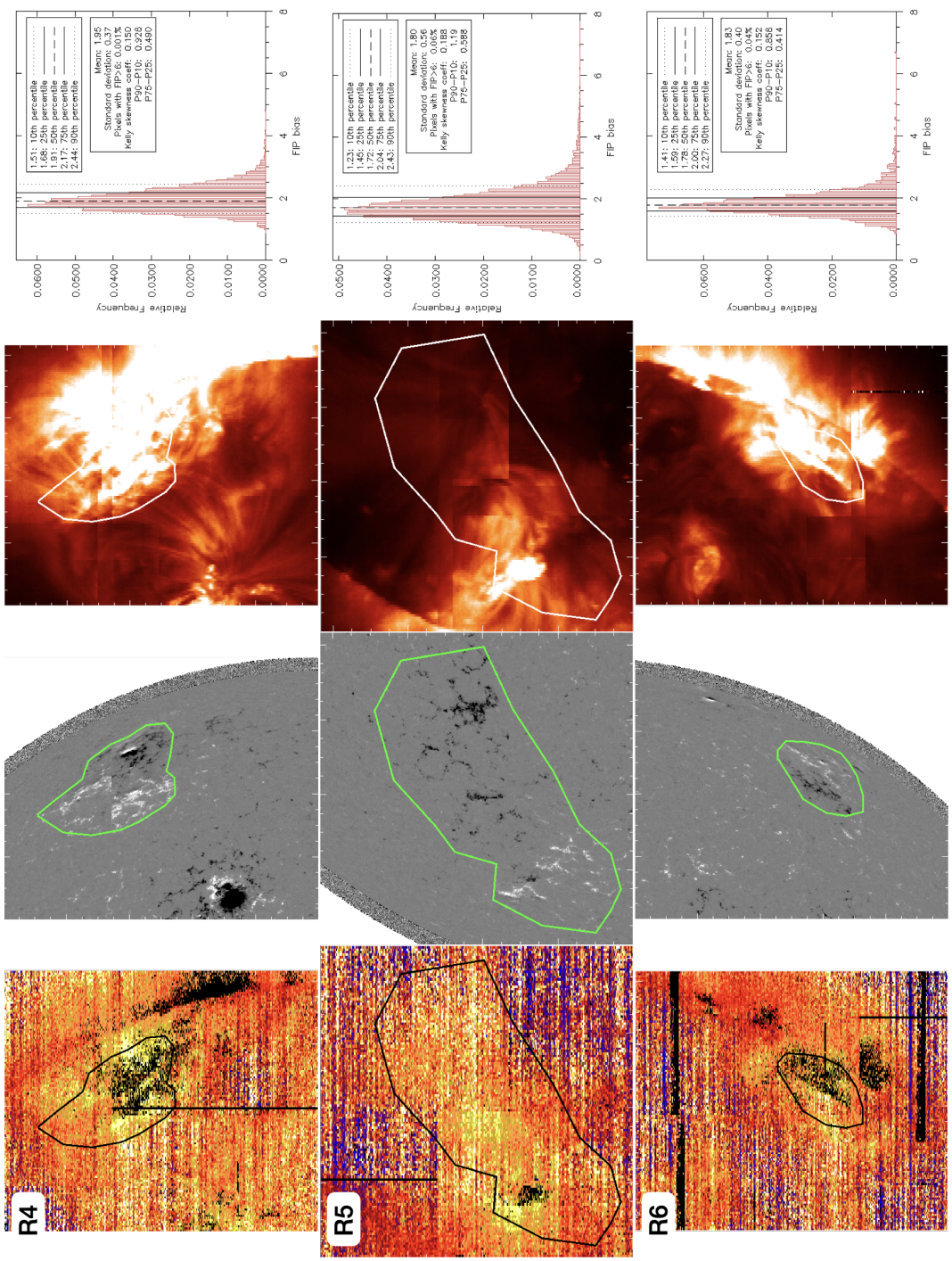

Figure 5.3: FIP bias distributions in the selected active region contours (R4-R6) indicating the magnetic field boundaries of the active regions. From left to right: *Hinode* EIS Si/S FIP bias, HMI line of sight magnetic field strength, *Hinode* EIS Fe XIII 202.04 Å intensity, and FIP bias distribution within the active region contour (shown in black, green and white, respectively).

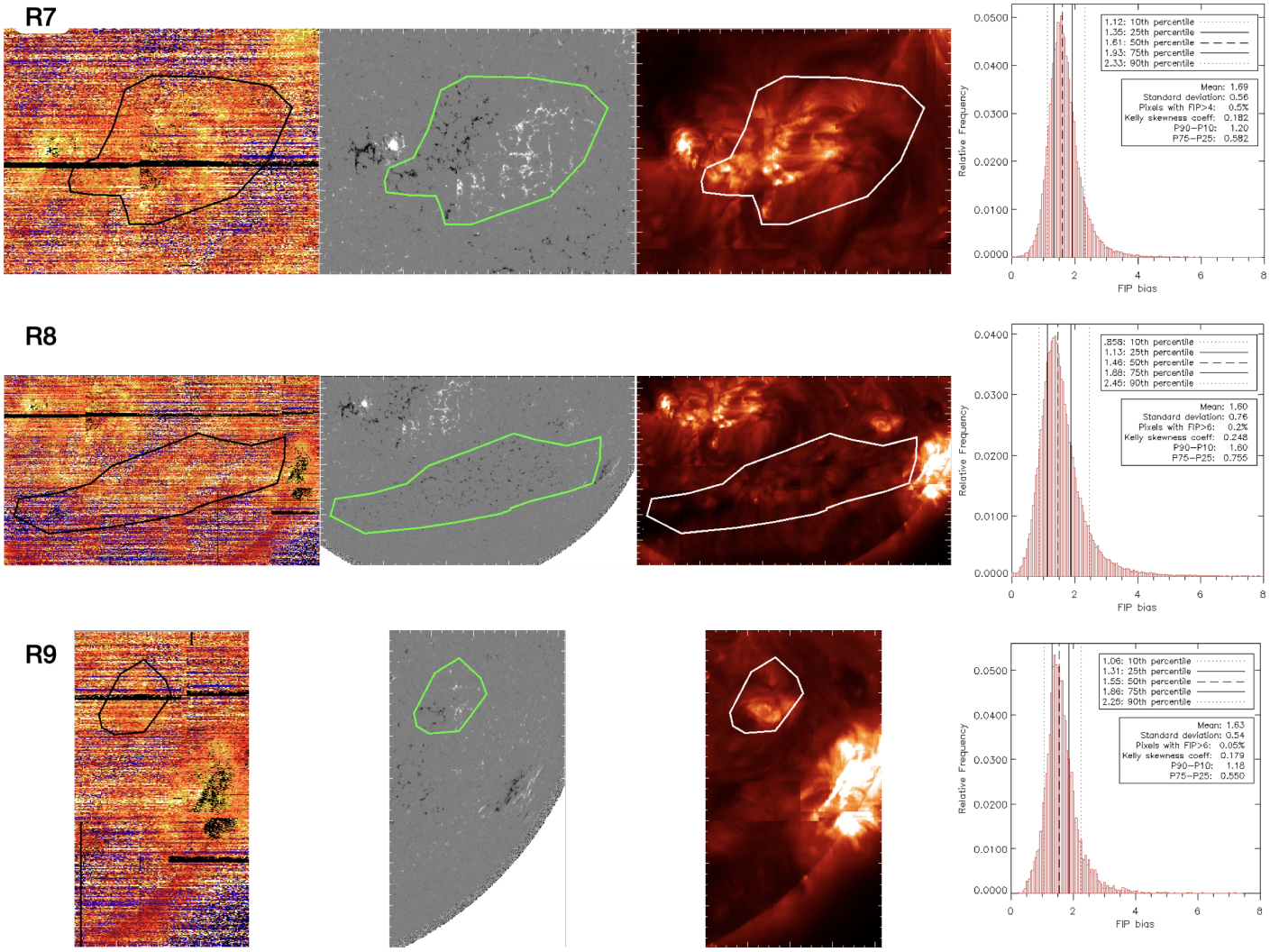

Figure 5.4: FIP bias distributions in the selected active region contours (R7-R9) indicating the magnetic field boundaries of the active regions. From left to right: *Hinode* EIS Si/S FIP bias, HMI line of sight magnetic field strength, *Hinode* EIS Fe XIII 202.04 Å intensity, and FIP bias distribution within the active region contour (shown in black, green and white, respectively).

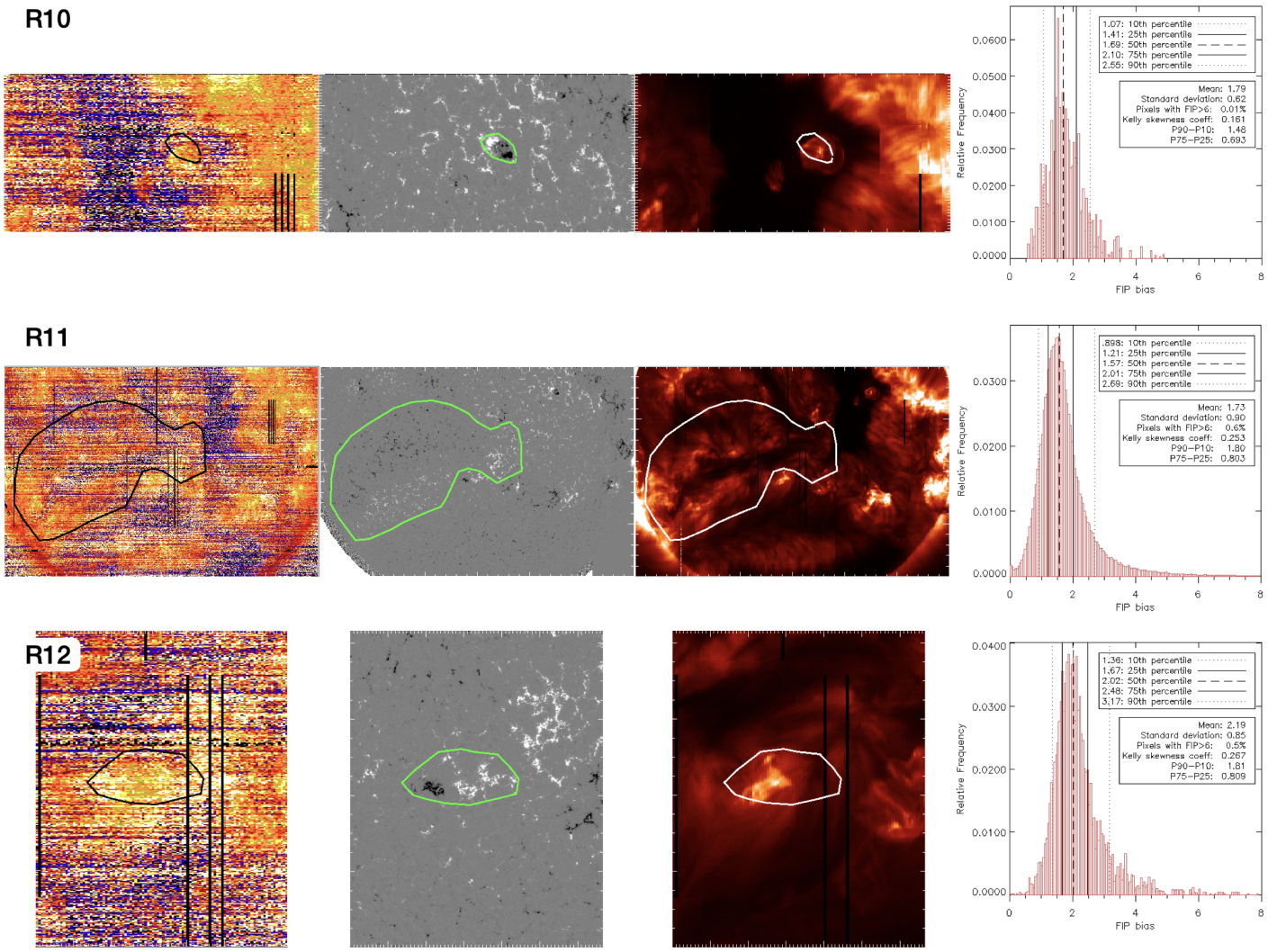

Figure 5.5: FIP bias distributions in the selected active region contours (R10-R12) indicating the magnetic field boundaries of the active regions. From left to right: *Hinode* EIS Si/S FIP bias, HMI line of sight magnetic field strength, *Hinode* EIS Fe XIII 202.04 Å intensity, and FIP bias distribution within the active region contour (shown in black, green and white, respectively).

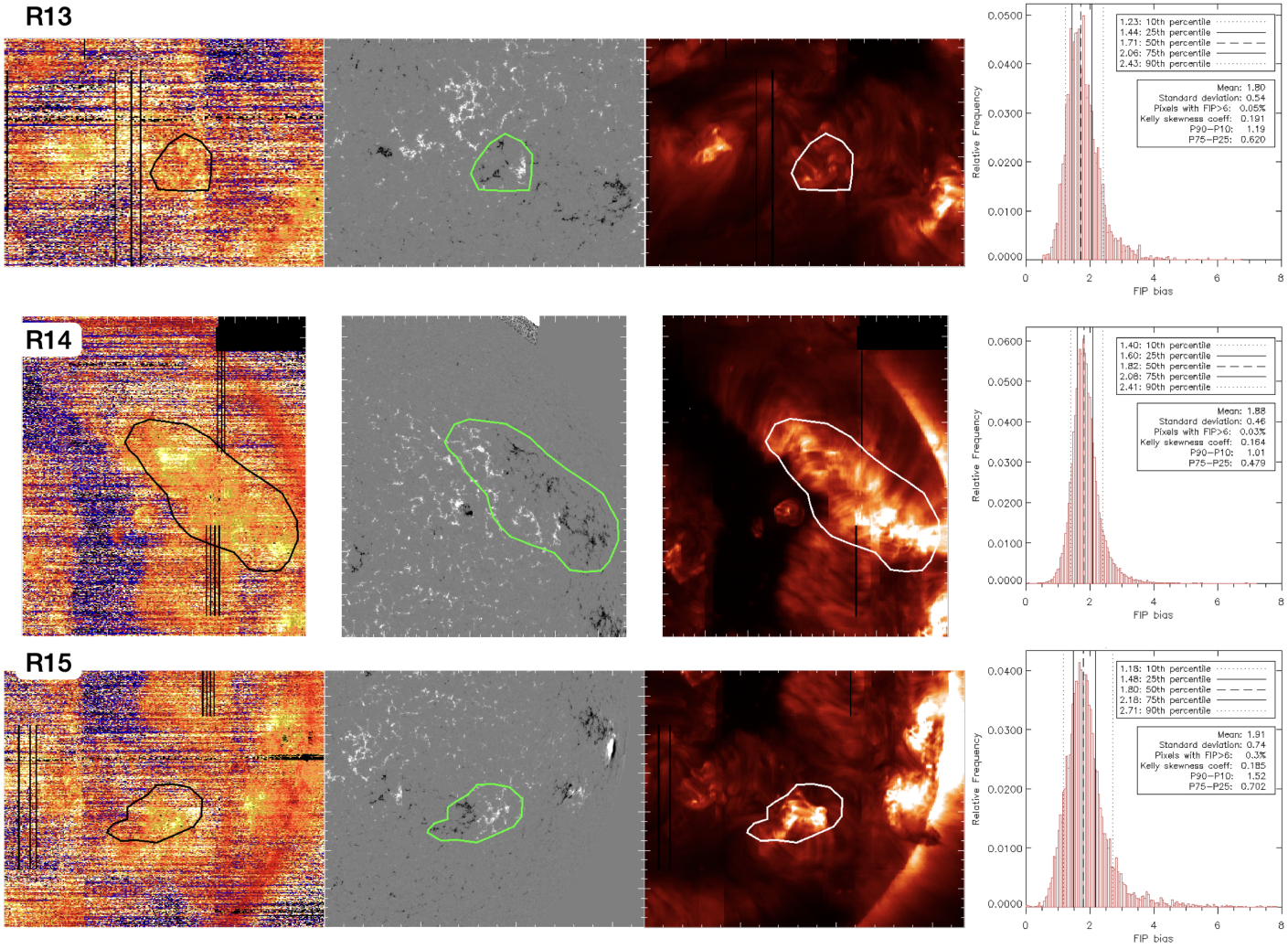

Figure 5.6: FIP bias distributions in the selected active region contours (R13-R15) indicating the magnetic field boundaries of the active regions. From left to right: *Hinode* EIS Si/S FIP bias, HMI line of sight magnetic field strength, *Hinode* EIS Fe XIII 202.04 Å intensity, and FIP bias distribution within the active region contour (shown in black, green and white, respectively).

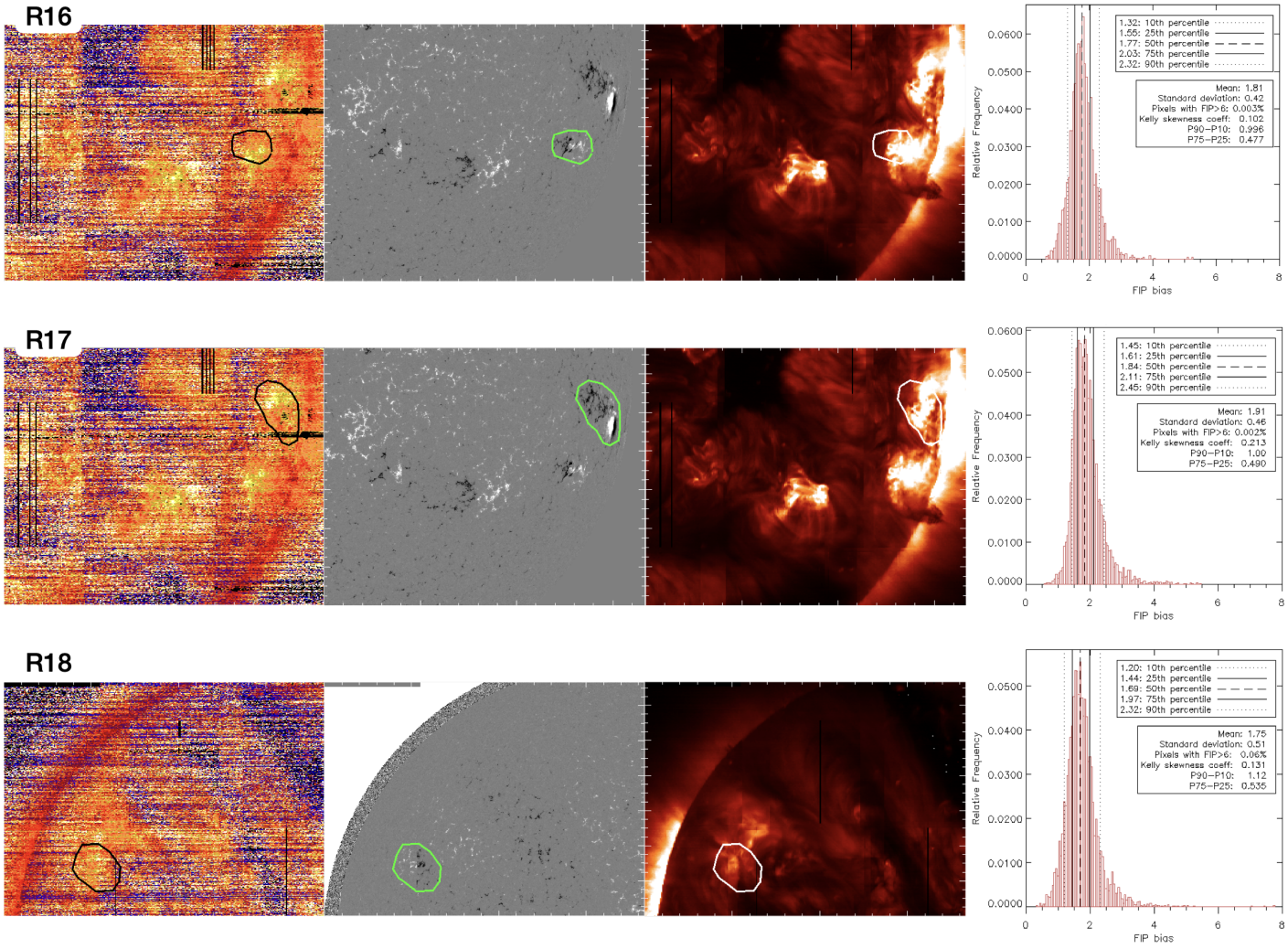

Figure 5.7: FIP bias distributions in the selected active region contours (R16-R18) indicating the magnetic field boundaries of the active regions. From left to right: *Hinode* EIS Si/S FIP bias, HMI line of sight magnetic field strength, *Hinode* EIS Fe XIII 202.04 Å intensity, and FIP bias distribution within the active region contour (shown in black, green and white, respectively).

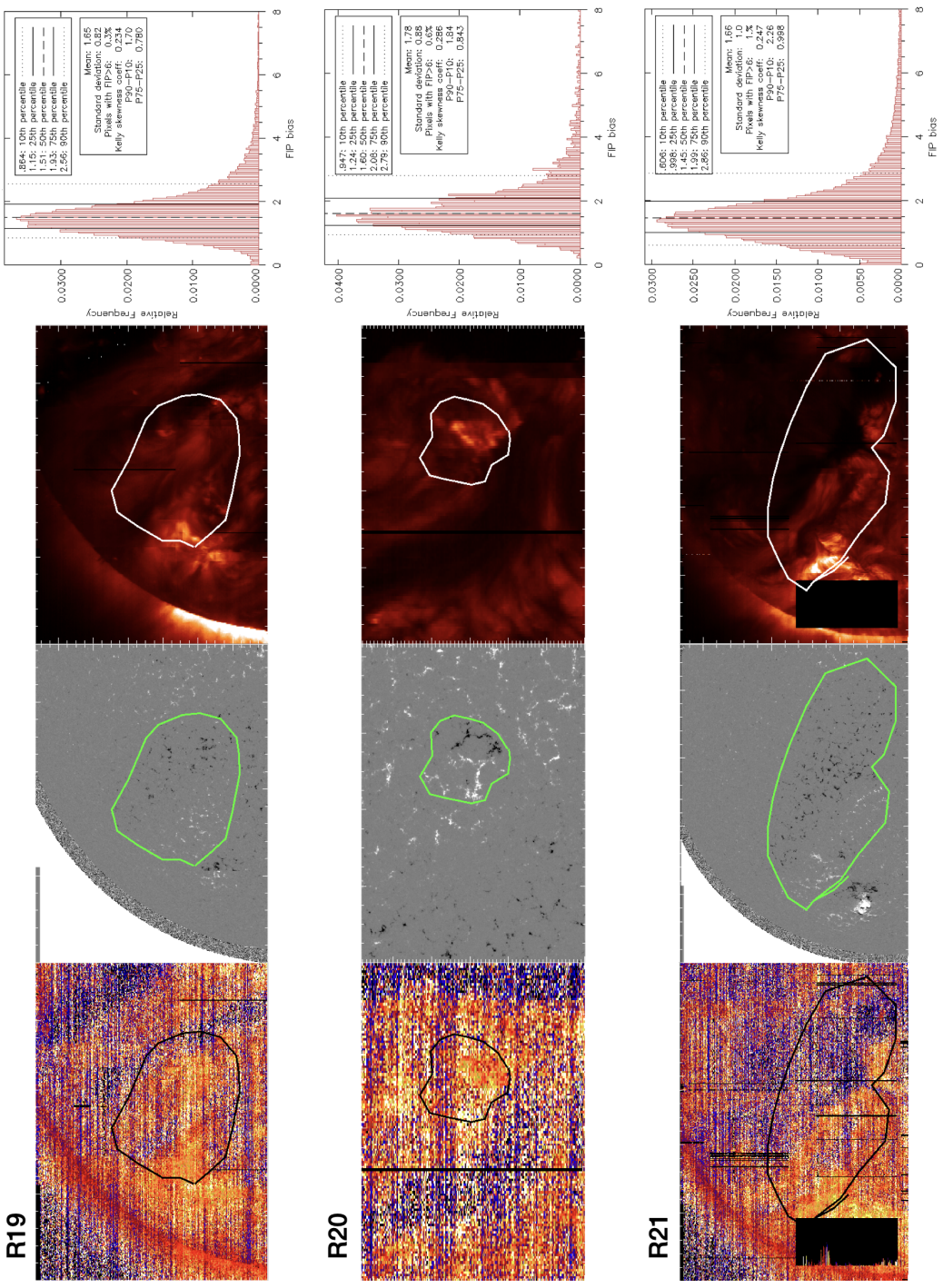

Figure 5.8: FIP bias distributions in the selected active region contours (R19-R21) indicating the magnetic field boundaries of the active regions. From left to right: *Hinode* EIS Si/S FIP bias, HMI line of sight magnetic field strength, *Hinode* EIS Fe XIII 202.04 Å intensity, and FIP bias distribution within the active region contour (shown in black, green and white, respectively).

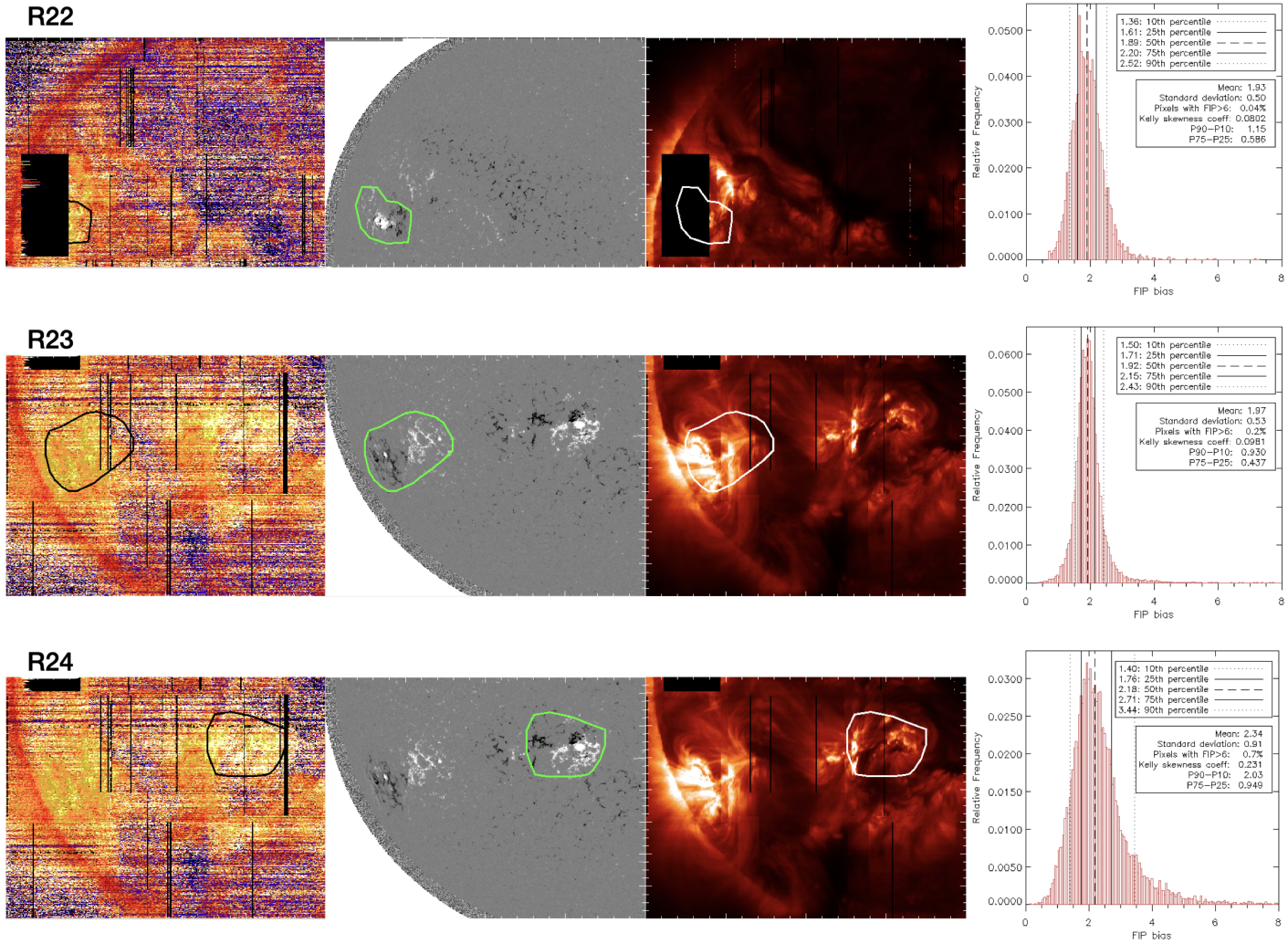

Figure 5.9: FIP bias distributions in the selected active region contours (R22-R24) indicating the magnetic field boundaries of the active regions. From left to right: *Hinode* EIS Si/S FIP bias, HMI line of sight magnetic field strength, *Hinode* EIS Fe XIII 202.04 Å intensity, and FIP bias distribution within the active region contour (shown in black, green and white, respectively).

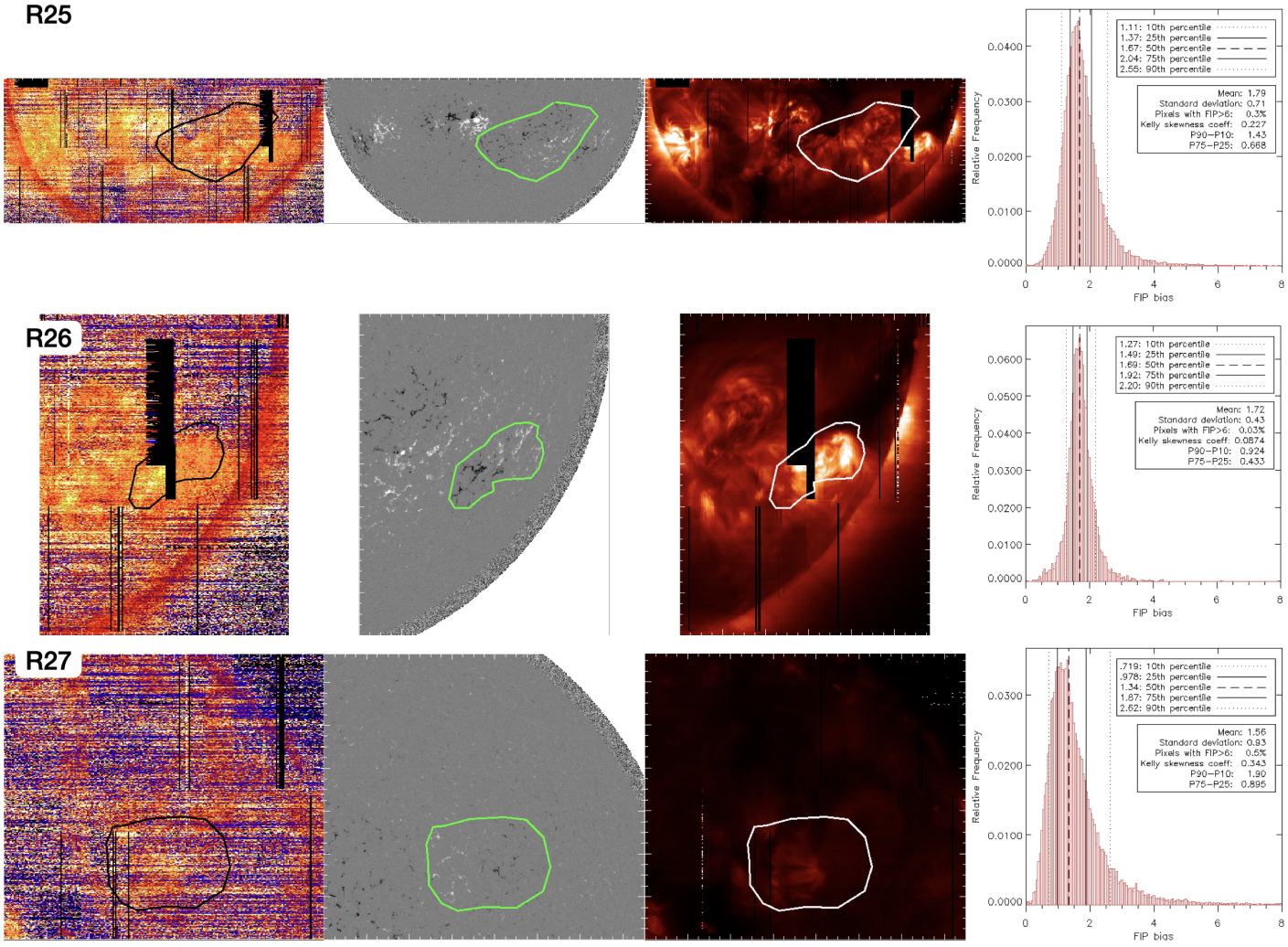

Figure 5.10: FIP bias distributions in the selected active region contours (R25-R27) indicating the magnetic field boundaries of the active regions. From left to right: *Hinode* EIS Si/S FIP bias, HMI line of sight magnetic field strength, *Hinode* EIS Fe XIII 202.04 Å intensity, and FIP bias distribution within the active region contour (shown in black, green and white, respectively).

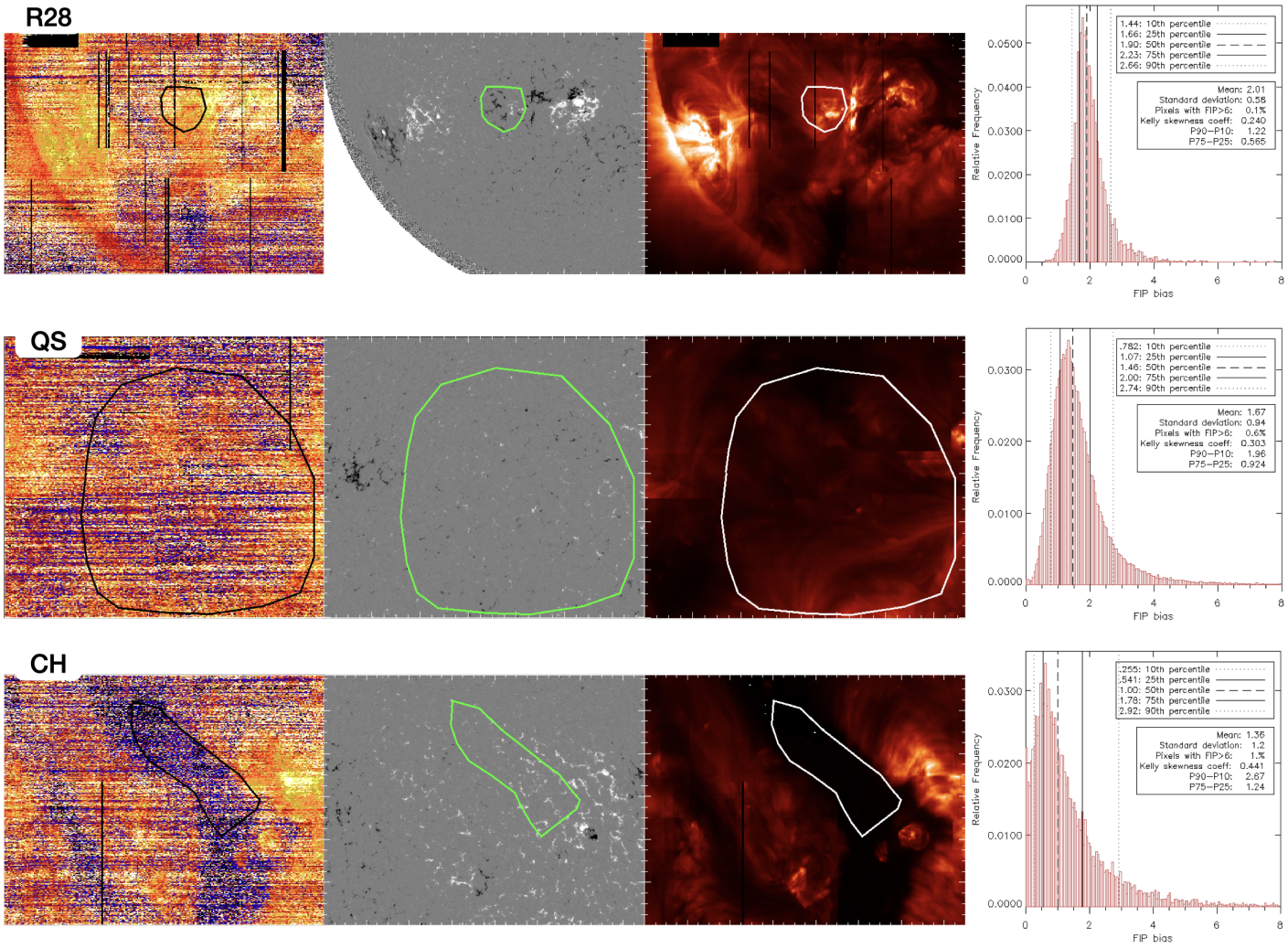

Figure 5.11: FIP bias distributions in a selected active region contour (R28) indicating the magnetic field boundaries of the active region and representative examples of quiet Sun (QS) and coronal hole (CH) regions. From left to right: *Hinode* EIS Si/S FIP bias, HMI line of sight magnetic field strength, *Hinode* EIS Fe XIII 202.04 Å intensity, and FIP bias distribution within the active region contour (shown in black, green and white, respectively).

At the time of the January 2013 scan, the SDO and STEREO spacecraft were located such that they provided full coverage of the Sun: SDO was located at Earth and STEREO-A (STEREO-B) was located approximately 120° ahead of (behind) the Earth with respect to the Sun-Earth line (see Figure 4.8). The availability of STEREO EUVI observations from the far side of the Sun enabled a better determination of the time of emergence and, therefore, a more precise age estimation for the active regions in this scan. However, STEREO data were not available for the two scans that took place in 2015. Communications with STEREO-B were lost in 2014 and, in 2015, STEREO-A was located at an angle of approximately 180° from the Earth which resulted in a data gap coinciding with the time running up to the EIS scans. As a consequence, the uncertainties on the ages of the active regions in these scans are higher.

In addition, synoptic map data from the Global Oscillations Network Group (GONG; Harvey et al., 1996) instruments were used to identify whether an active region is part of an activity nest. These are long-lived regions of magnetic activity, where repeated flux emergence takes place (van Driel-Gesztelyi and Green, 2015). Magnetic fields brought up by each flux emergence reconnect with the preexisting field, making activity nests sites of stronger magnetic reconnection and heating rates (van Driel-Gesztelyi and Green, 2015). Where an active region emerged in a region of preexisting magnetic activity, the location of that active region was tracked back in time for multiple rotations to identify whether repeated flux emergence took place at its location. If that was the case, both the age of the most recent significant flux emergence and the age of the nest were determined.

5.2.2 FIP Bias and Plasma Composition

FIP bias was calculated using the *Hinode* EIS Si X 258.38 Å (low FIP, FIP = 8.15 eV) and S X 264.23 Å (high FIP, FIP = 10.36 eV) emission lines ratio. The method for calculating the FIP bias in each pixel makes use of a DEM analysis and a density analysis, designed to remove temperature and density effects on the FIP bias calculation (see Section 3.3.7 or Brooks and Warren, 2011; Brooks et al., 2015, for additional details). Here, the Fe XIII 202.04 Å/203.82 Å ratio was used

EIS Study Details	
Study acronyms	DHB_006 (January 2013 & April 2015) DHB_007 (October 2015)
Study numbers	491 (January 2013 & April 2015) 544 (October 2015)
Emission lines used	Fe x 184.53 Å, Fe viii 185.21 Å, Fe ix 188.49 Å, Fe xi 188. 21 Å, Fe x 188.29 Å, Fe xii 195.12 Å, Fe xiii 202.04 Å, Fe xii 203.72 Å, Fe xiii 203.82 Å, Fe xvi 262.98 Å, Fe xiv 264.78 Å, Fe xv 284.16 Å, Si x 258.38 Å, S x 264.22 Å (January 2013) Fe x 184.53 Å, Fe viii 185.21 Å, Fe viii 186.60 Å, Fe ix 188.49 Å, Fe xii 192.39 Å, Fe xi 188. 21 Å, Fe x 188.29 Å, Fe xii 195.12 Å, Fe xiii 202.04 Å, Fe xiii 203.82 Å, Fe xvi 262.98 Å, Fe xiv 264.78 Å, Fe xv 284.16 Å, Si x 258.38 Å, S x 264.22 Å (April & October 2015)
Field of view	$492'' \times 512''$
Rastering	$2''$ slit, 123 positions, $4''$ coarse step
Exposure time	30s
Total raster time	1h 1m 30s
Reference spectral window	Fe xii 195.12 Å

Table 5.2: Summary of *Hinode* EIS study details and emission lines used for creating the FIP bias maps.

to estimate the electron density, and Fe lines Fe viii to xvi to derive the DEM. For the FIP bias line pair, the line formation temperatures are $\log(\mathrm{T[K]}) \approx 6.2$ for Si x 258.38 Å and $\log(\mathrm{T[K]}) \approx 6.25$ for S x 264.23 Å, while for the density line pair, the formation temperatures are $\log(\mathrm{T[K]}) \approx 6.25$ for Fe xiii 203.82 Å and $\log(\mathrm{T[K]}) \approx 6.30$ for Fe xiii 202.04 Å (Dere et al., 1997; Del Zanna et al., 2021). Therefore, these diagnostics cover the right temperature for studying the quiescent active regions presented in this work. The EIS study details and emission lines used are summarized in Table 5.2.

5.3 Method and Data Analysis

5.3.1 Full Sun Maps

Each full Sun map was created by stitching together 26 EIS observations (rasters) taken from 09:37 UT on the 16th to 07:06 UT on the 18th for the January 2013 scan, from 09:14 UT on the 1st to 01:49 UT on the 3rd for the April 2015 scan and from 10:27 UT on the 16th to 01:31 UT on the 18th for the October 2015

scan. Before creating the full Sun maps, pixels that had an associated χ^2 value (defined in Eqn 3.23) above 12 were removed from each raster. The chosen threshold of 12 corresponds to the number of Fe lines used in the DEM analysis, as detailed in Section 3.3.6 (see also Brooks and Warren, 2011; Brooks et al., 2015, for a full description of the method).

The individual EIS rasters are taken such that, together, they cover the entire Sun, which means that there are overlap regions with data from two or more rasters. The full Sun map value for these pixels is calculated after the FIP bias filtering, as the average of all the pixel values available for that location. The January 2013 full Sun FIP bias map (Figure 5.1c) shows the same data that was used by Brooks et al. (2015), but note that the display image in their Figure 3 is not directly comparable. Figure 3 in Brooks et al. (2015) shows qualitative data (a FIP bias proxy defined as the Si X 258.38 Å/S X 264.23 Å intensity ratio), while Figure 5.1c here shows the quantitative data (the FIP bias computed from the DEM calculation) - see the discussion in Brooks et al. (2015) on how their Figure 3 was constructed.

To create the corresponding full Sun magnetogram, cropped HMI images that match the start time and field of view (FOV) of each of the individual rasters are also stitched together. This is to ensure that the FIP bias of each active region is assigned to magnetic field properties calculated using the magnetogram that is closest in time for each of the EIS rasters. In the overlap regions, the most recent magnetogram data were kept.

5.3.2 Active Region Identification

Active regions were identified using HMI line of sight (LOS) magnetic field data, and their boundaries were defined by eye in the plane of the image, tracking the evolution of the active region and looking for a sharp gradient between the magnetic flux of the active region and its surroundings. Where a sharp gradient was not easily identifiable, observations of the photospheric magnetic field evolution were used to identify all the magnetic flux fragments that originate from the flux emergence (these fragments move outwards from the main PIL of the active region as the active region ages). Boundaries were defined to include all these magnetic flux fragments.

The selected contours were broad enough to include all the magnetic flux associated with the active region. This included small-scale background field between active region field fragments, but this was accounted for by filtering out pixels with an absolute magnetic flux density of less than 30 G. The same method was used for selecting the boundaries of individual polarities within an active region. In addition, when selecting the contour for one polarity, any opposite polarity field was filtered out as well.

The HMI contours were then plotted over the FIP bias map to extract the corresponding FIP bias values. The number pixels included in each contour vary depending on the size of the active region, from values of approximately 10,000 pixels for small active regions (e.g. R2, R10) to values of approximately 100,000 pixels for large active regions (e.g. R8, R21). The resulting FIP bias distributions within each selected contour are characterised by the median FIP bias value (P_{50}, i.e. the 50th percentile), the spread ($P_{25} - P_{75}$, i.e. the difference between the 25th and 75th percentiles) and Kelly's skewness coefficient (e.g. Groeneveld and Meeden, 1984):

$$S_K = \frac{P_{90} + P_{10} - 2 \times P_{50}}{P_{90} - P_{10}}. \tag{5.1}$$

Note that the spread is an indicator of the range of FIP bias values observed in the active region, rather than an error associated with the median FIP bias value.

5.4 Results

It has long been recognised that the strongest FIP effect is observed in active regions (e.g. Widing and Feldman, 2001). Active regions are sites of stronger magnetic activity, so it is likely that the magnetic field properties are linked to the FIP effect drivers. The aim of this work is to gain a better understanding of how the magnetic field and its distribution within an active region influence the observed FIP bias.

5.4.1 FIP Bias, Total Unsigned Magnetic Flux and Age

An active region's total unsigned magnetic flux varies throughout its lifetime, increasing in the emergence phase and decreasing in the decay phase. The total magnetic flux content of the active region defines its lifetime (Schrijver and Zwaan, 2000). Therefore, total unsigned magnetic flux and age must be considered together. The total unsigned magnetic flux was defined by integrating the absolute magnetic flux density (measured by SDO HMI) over all the pixels within the active region contour. Therefore, the total unsigned magnetic flux is sensitive to how the contour boundaries are defined. However, most of the flux is concentrated towards the center of the contour and the flux contribution from close to the boundaries mostly comes from small magnetic flux fragments embedded in the background quiet Sun. Including the background quiet Sun flux into the calculation would artificially increase the total unsigned flux value, particularly for active regions that cover a larger area. To account for this, all pixels with an absolute magnetic flux density lower than 30 G were excluded. This way, the contour boundaries can be extended to include all the magnetic field fragments that originate from the flux emergence. The variation of FIP bias with active region total unsigned magnetic flux and age is shown in Figures 5.12 and 5.13. In both plots, the vertical bars indicate the FIP bias spread, rather than a measurement error (see Section 5.2.1). For the active regions that emerged on a part of the Sun that was not observed by any spacecraft, the age measurement has an associated error bar that corresponds to the minimum and maximum age for that region (see Section 5.2.1). The plots in Figures 5.12 and 5.13 show no global correlation between the FIP bias of an active region and total unsigned magnetic flux or age. However, this does not mean that there is no change in the FIP bias of active regions during their lifetimes. Rather, it indicates the need to study FIP bias variation in the context of the evolution of each active region and understand their individual evolutionary paths. It is likely that a normalisation of these parameters would be needed for a better comparison between active regions, i.e. normalise the total unsigned magnetic flux by peak total unsigned magnetic flux (the magnetic flux content of the active region), and normalise the age by the total lifetime of the

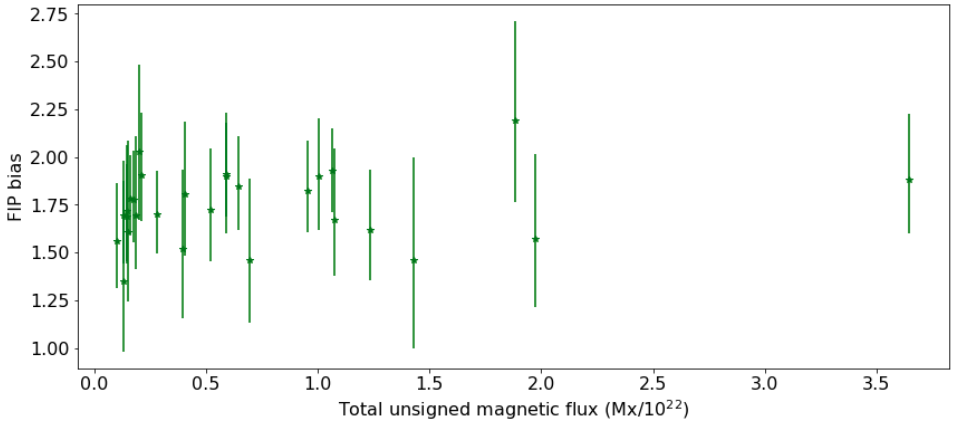

Figure 5.12: FIP bias variation with total unsigned magnetic flux of the active region. The vertical bars indicate the FIP bias spread, i.e. the 25th and 75th percentile of the distribution in each region. The 50th percentile is highlighted with a star.

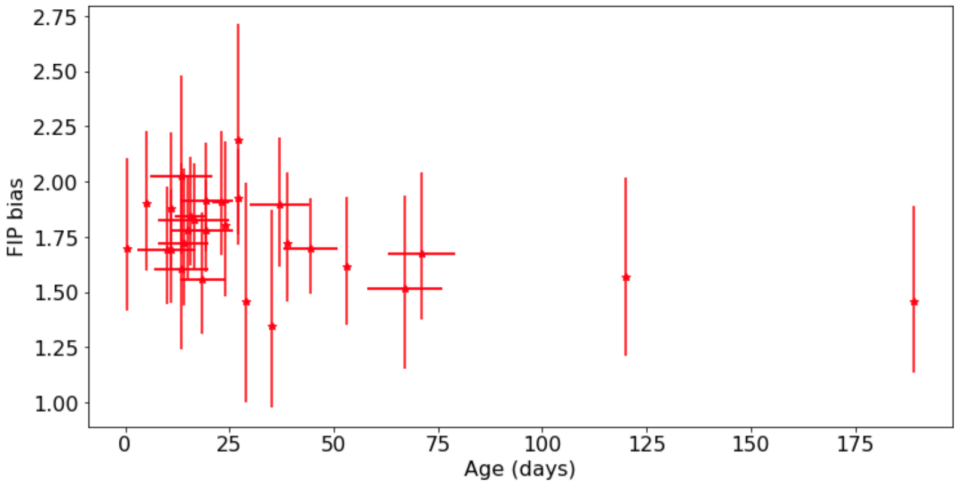

Figure 5.13: FIP bias variation with active region age. The vertical bars indicate the FIP bias spread, i.e. the 25th and 75th percentile of the distribution in each region. The 50th percentile is highlighted with a star. The error bar associated with the age measurement corresponds to the minimum and maximum age for that region, in case there was no observation available at the time and location of its emergence.

active region. This would essentially be an indicator for the evolutionary stage of each active region. However, defining the end of an active region's life is difficult, particularly in the case of very dispersed active regions like some of the examples in the dataset analysed here.

5.4.2 FIP Bias and Magnetic Flux Density

As active regions evolve from emergence through decay, there is a change in their magnetic flux density, which raises a question about whether the flux density shows any correlation with the FIP bias. The mean magnetic flux density is defined as the total unsigned flux of an active region (calculated as described in Section 5.4.1) divided by the area of the defined contour. The variation of FIP bias as a function of magnetic flux density is shown in Figure 5.14. Similar to Figures 5.12 and 5.13, the vertical bars show the spread in FIP bias within the region. For this plot, data from individual polarities of all the active regions in the dataset were used instead of overall active regions. This decision was motivated by the asymmetries in the motion and stability of the leading and following polarities, which result in the following polarity decaying faster than the leading polarity (Hale and Nicholson, 1938). In the emergence phase, the leading polarity converges more quickly into a more compact and longer lived magnetic field configuration, while the following polarity may form shorter lived spots that become dispersed faster. This results in different magnetic flux densities in opposite polarities, essentially placing them at different evolutionary stages. However, the asymmetry becomes weaker with time, so the separation into leading and following polarities is particularly important for younger active regions and less important for dispersed active regions.

The results show that FIP bias increases with mean magnetic flux density in the region ≤ 200 G. The Pearson correlation coefficient between the median FIP bias values and the magnetic flux density in this region is 0.65. This is in agreement with Baker et al. (2013) who found a moderate correlation between FIP bias and magnetic flux density. It is interesting to note that, although populated with fewer data points, the same trend does not seem to continue in the region ≥ 200 G, where all the datapoints have sunspots, supporting the findings of Doschek and Warren (2017) that the FIP effect partially shuts down in sunspot areas.

5.4.3 FIP Bias in Leading and Following Polarities

A comparison between the median FIP bias values in the leading vs. following polarities of the active regions is shown in Figure 5.15. The plot shows that 10

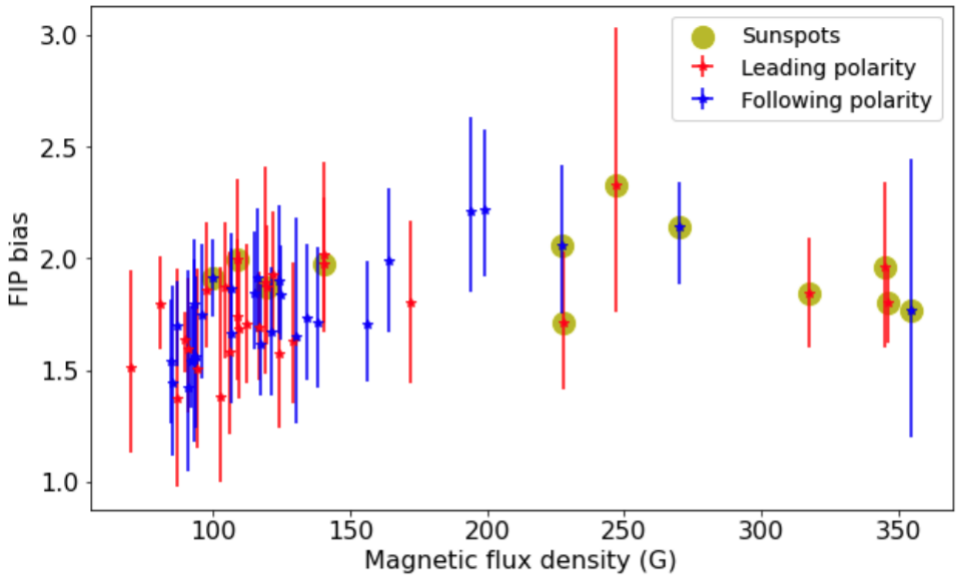

Figure 5.14: FIP bias variation with magnetic flux density for individual leading (red) and following (blue) polarities. The vertical bars indicate the FIP bias spread, i.e. the 25th and 75th percentile of the distribution in each region. The 50th percentile is highlighted with a star. Active regions that still have a sunspot are highlighted with a yellow dot. The Pearson correlation coefficient between the median FIP bias values and the magnetic flux density in the region ≤ 200 G is 0.65.

active regions (35% of the sample) have higher FIP bias in the following polarity, 8 active regions (28%) have higher FIP bias in the leading polarity and the remaining 10 active regions (35%) have approximately the same FIP bias in both polarities (difference smaller than 0.05 in FIP bias). The higher FIP bias values registered in one polarity or another are not correlated with the active region's position on the disc, indicating that this difference is due to an asymmetry between the two polarities rather than a projection effect resulting from the different angle at which the coronal loops are observed.

Across the dataset, there is a large variety of active regions at different evolutionary stages: an emerging active region (R10); very decayed active regions that have formed filament channels along their main PILs (e.g. R8, R11, R21); active regions that have compact magnetic field in both polarities (e.g. R3, R10, R24) or a single polarity (e.g. R1); active regions that have decayed far beyond having homogeneous field in either the leading or the following polarities (e.g. R7, R14, R19) and active regions that are dominated by one polarity (e.g. R8). It is likely that this

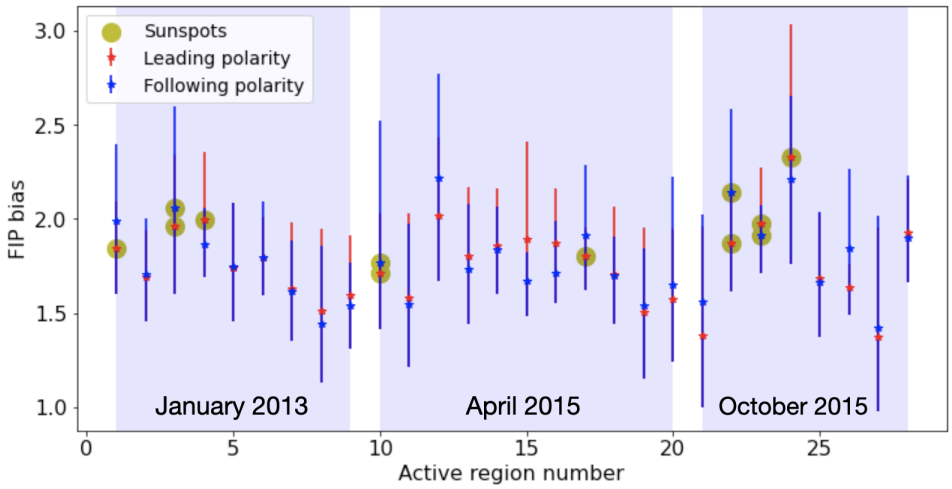

Figure 5.15: FIP bias in leading (red) vs. following (blue) polarities. The x axis indicates the active region R code (1-28) used within the dataset, as defined in Figure 5.1. The vertical bars indicate the FIP bias spread, i.e. the 25th and 75th percentile of the distribution in each region. The 50th percentile is highlighted with a star. Active regions that still have a sunspot are highlighted with a yellow dot.

very varied magnetic field configuration is the reason why no systematic trend is seen.

A case study of R1 (January 2013) is shown in Figure 5.16. The leading polarity has lower FIP bias than the following polarity. This active region is an example showing the asymmetric configuration of the magnetic field in the leading polarity as compared to the following. The leading polarity is more compact and still has a sunspot, while the following polarity is already dispersed. The asymmetry can also be found in the weakly different FIP bias values and distributions, possibly due to the fact that the higher flux density above the sunspot is actually decreasing the overall FIP bias (see Section 5.4.2). This active region is located close to disc centre, such that differences in FIP bias are likely due to asymmetries in the opposite polarities rather than projection effects.

5.4.4 FIP Bias at Different Evolutionary Stages

The active regions in the dataset are at different stages in their evolution and can therefore offer insight into FIP bias values in these different stages. For this, the active regions are categorised into 5 groups based on their evolutionary stages

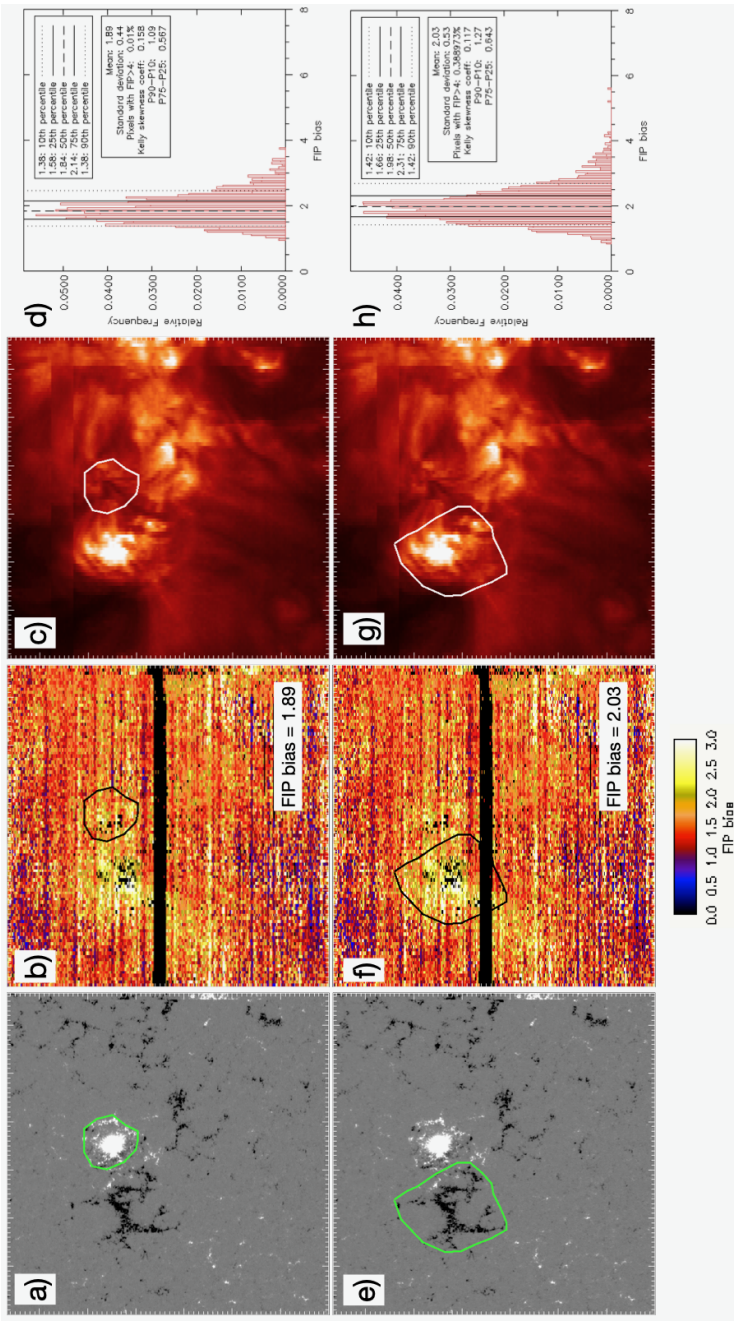

Figure 5.16: Case study of the median FIP bias in the leading (top) vs. following (bottom) polarities of R1 (January 2013). The maps show a,e) HMI LOS photospheric magnetic field strength; b, f) *Hinode* EIS FIP bias; c, g) *Hinode* EIS Fe XIII 202.04 Å intensity; d,h) histograms of the FIP bias within the contours shown in green, black, and white on the other panels. The values in the two boxes show the median FIP bias value in the defined contour. The top and bottom maps correspond to observations taken at the same time.

Evolutionary stage (no. of active regions)	Median FIP bias range	Kelly's skewness coefficient range
Emerging active regions (1)	1.7	0.16
Active regions with spots (4)	1.9 - 2.2	0.10 - 0.23
Decayed active regions (8)	1.6 - 2.0	0.13 - 0.27
Extended, very dispersed active regions (6)	1.4 - 1.8	0.09 - 0.34
Active regions with filament channels (4)	1.5 - 1.6	0.23 - 0.25

Table 5.3: Median FIP bias and Kelly's skewness coefficient ranges for the active regions in each category, excluding those active regions that are located close to the limb (outside $\pm 60^{\circ}$ longitude)

(see Table 5.3). The lifetime of an active region is typically divided into emergence phase and decay phase. The decay phase is always longer than the emergence phase, but it varies from around 70% of the total lifetime for ephemeral active regions to as much as 97% for large active regions (van Driel-Gesztelyi and Green, 2015). As the decay phase is so much longer, here it is further divided into four substages: active regions that still have sunspots (at the peak development or in their early decay phase), decayed active regions (sunspots have disappeared), extended and very dispersed active regions (field is so dispersed that it is not easily distinguished from the quiet Sun), and active regions with filament channels (while not necessarily a different evolutionary stage, these active regions are older and more dispersed than the previous category and have the distinct feature of filament channels along their main PIL).

The results shown in Table 5.3 suggest that, generally, the FIP bias of fully developed active regions is higher than that of the emerging active region and then it reduces for the progressively more dispersed groups. Baker et al. (2018) found a dependence of FIP bias on active region evolution for seven emerging flux regions. The present result indicates that the same behaviour is found in larger active regions as well.

The lowest FIP bias values are found in active regions that have formed filament channels. Such an example is active region R11 (see Figure 5.5). The filament channel is seen as the dark feature in the EUV emission, which corresponds to a cor-

ridor of low magnetic field strength along the PIL in the associated magnetogram. This is a sign of ongoing flux cancellation taking place along the PIL to form the filament channel structure. The FIP bias map indicates that the filament channel has distinctly lower FIP bias values than the rest of the active region. It is likely that this is due to flux magnetic reconnection in the lower atmosphere which brings photospheric material up into the corona, leading to lower FIP bias values as a result of plasma mixing (see Baker et al., 2022, and Section 2.4.3 in this thesis).

5.4.5 FIP Bias Distribution Within Active Regions

FIP bias within the active regions has a significant spread, which varies between 0.4 and 1.0. The spread values for all the active regions are given in Table 5.1, and individual active region contours and characteristics are shown in Figures 5.2-5.11. Reference examples for the distribution of FIP bias values in a quiet Sun and coronal hole regions are shown in Figure 5.11.

This spread is likely an indicator of different substructures within an active region having different FIP bias values. An interesting case study to turn our attention to is R11 (see Figure 5.5). This is a very decayed active region, with lower FIP bias values in the filament channel along its main PIL and higher FIP bias values in the arcade loops and hotter areas, which is likely why this active region has a relatively high FIP bias spread.

The lowest spread is seen in active regions that are located close to the limb, which is likely due to the method used for defining the active region contours. The HMI magnetic field is a photospheric measurement, while the FIP bias is a coronal observation. Magnetic field expands into the corona compared to the photosphere, so using a photospheric magnetic field contour will likely introduce a challenge in fully capturing the coronal loops. Closer to the limb, this effect is amplified by projection effects.

Additionally, all distributions were found to be right-hand skewed (see Table 5.1). The skewness coefficient has a wide range of values for all the evolutionary stages between active regions with spots and very dispersed active regions (see

Table 5.3). However, in the active regions with filament channels category, the skewness coefficient values do not exhibit this variation.

5.5 Summary and Discussion

In this study, the characteristics of coronal plasma elemental composition are investigated across 28 active regions of varying size, magnetic complexity and age. The sample of active regions includes one in its emergence phase and 27 in the decay phase, with the longest lived active region in the study being 244 days old. Plasma composition is determined through the FIP bias value, which indicates by how much low-FIP elements are enhanced in the corona relative to high-FIP elements, and the range of active regions studied enables an analysis of how plasma composition might be influenced by magnetic field strength, age, complexity and evolutionary stage.

The median FIP bias values in the studied active regions fall in the range of 1.4 to 2.2, very similar to the values found by Baker et al. (2018) which varied between 1.2 and 2.0. Baker et al. (2018) analysed emerging flux regions with a total unsigned magnetic flux of $0.13 - 38 \times 10^{20}$ Mx, while the active regions in the present study range from small to large, and have total unsigned magnetic flux values of $1 - 36.4 \times 10^{21}$ Mx. Very similar FIP bias values are observed, in spite of the significant difference in total magnetic flux, which is a further indication that FIP bias is not influenced by the total magnetic flux. For reference, the median FIP bias values for a representative example of quiet Sun was 1.5 and for coronal hole 1.0 (see Figure 5.11)

Magnetic flux density, however, appears to play a role. FIP bias increases with magnetic flux density in the region ≤ 200 G, but that trend appears to stop for regions with mean magnetic flux density ≥ 200 G, which all belong to regions with sunspots. In the region ≤ 200 G, it is possible that increased magnetic flux density drives stronger heating at the chromospheric loop footpoints, ionising higher proportion of elements and, therefore, driving a stronger fractionation process which increases the FIP bias. In contrast, in the region ≥ 200 G the strong magnetic field

concentration in the umbra of sunspots can inhibit convection and lower the temperature at chromospheric level which means a lower proportion of elements are being ionized, thus producing a lower FIP effect. These observations bring more evidence supporting Doschek and Warren (2017) who found that the plasma composition around sunspots is close to photospheric. It is also possible that the variation in magnetic flux density has a similar effect on the Alfvén waves driving the fractionation process (according to the ponderomotive force model described in Section 2.3), although this aspect was not investigated in this work.

It is also interesting to note that an active region moves from higher to lower magnetic flux density throughout its evolution (so from right to left on the plot in Figure 5.14). Most of the active regions in the dataset are in different stages of the decay phase. The ones with a flux density ≥ 200 G still have sunspots, and they are in the early decay phase, while the ones ≤ 100 G are in the late decay phase. The trend of FIP bias decreasing with decreasing magnetic flux density, is, therefore, an indirect indication that FIP bias decreases with time in the active region decay phase. This result is in agreement with the previous result of Baker et al. (2015) who found that, in the decay phase of an active region, FIP bias is decreasing and remains coronal for a longer time only in a part of the active region's high flux density core. The lowest value of 1.4 is observed in two active regions that are very dispersed to the point where they are hard to distinguish from quiet Sun. This is in line with the results of Ko et al. (2016), who found that, in a decaying active region, FIP bias decreases from 1.8 over 3 days until it settles at a value of 1.5, which they describe as a 'basal' state of the quiet Sun. The FIP bias method and line ratio used in their study is very similar to the one used in this study, which means the values can be compared directly.

The FIP bias distribution within the active regions has a significant spread, which indicates that there is a range of physical processes or a range of conditions influencing a single process in different active region substructures that influence the FIP bias in different ways. An interesting example is presented by the four regions that have formed filament channels along their main PIL. While having the lowest

overall FIP bias values, they show a high spread and percentage of high FIP bias values. The spatial distribution of the FIP bias indicates a closer to photospheric value in the filament channel with higher FIP bias values surrounding the channel in the remnant active region arcade field. Having these substructures with different plasma composition increases the spread of the FIP bias distribution.

The lack of general trends of FIP bias with total magnetic flux and age or systematic reasons for the observed differences in the FIP bias in leading and following polarities, as well as the dependence of FIP bias on the active region evolutionary stage, indicate that the processes influencing the composition of an active region are complex and specific to its evolution, history and magnetic configuration or environment.

It is interesting to compare the active region FIP bias values to in situ studies of slow solar wind composition. Although the slow solar wind is believed to originate from active regions, in situ composition measurements find higher FIP bias values than the ones observed in the presented active regions. von Steiger and Schwadron (2000) found that the average FIP bias of the slow solar wind, relative to O and averaged over three low-FIP elements (Mg, Si, Fe) is 2.6. This is quite high, compared to the median FIP bias values presented in this study (1.4 to 2.2). Among the active regions in this study, AR11654 (here R3) was identified as a potential slow solar wind source region (Brooks et al., 2015). The FIP bias values observed both in the upflow region at the edge of the active region (remotely, using EIS data) and in situ in the solar wind are generally higher than the median FIP bias for that region (Brooks et al., 2015; Stansby et al., 2020). This could suggest that the slow solar wind originates from the part of an active region that has stronger FIP bias, such as outflows from active region edges (Brooks et al., 2015) located close to the active region footpoints that were found to have higher FIP bias (Baker et al., 2013). This highlights the potential of plasma composition in identifying solar wind source regions. Of course, FIP bias measurements in the solar corona and in the solar wind use different diagnostics, so direct comparisons must be done carefully.

Chapter 6

Plasma Composition Patterns at Sub-Active Region Level: Links to Alfvén Wave Activity

This chapter contains results published in The Astrophysical Journal (Mihailescu et al., 2023). This work was carried out under the supervision of Prof. Lucie Green, Dr. Deborah Baker, Dr. David Long and Prof. Lidia van Driel-Gesztelyi. The FIP bias calculations were performed by Dr. David Brooks (George Mason University). The ponderomotive force simulations were performed by Dr. Martin Laming (US Naval Research Laboratory). The results of this work were presented in a contributed talk at the Waves and Instabilities in the Solar Atmosphere Meeting (Newcastle, UK) in June 2023 and four seminars at the NASA Goddard Space Flight Center (Greenbelt, MD, United States) in March 2023, the US Naval Research Laboratory (Washington, DC, United States) in March 2023, The National Astronomical Observatory of Japan (Mitaka, Japan) in September 2023 and the JAXA Institute of Space and Astronautical Science (Kanagawa, Japan) in September 2023.

6.1 Introduction

Plasma composition in active regions is highly variable, both spatially and in time, likely reflecting the variety of processes taking place throughout an active re-

gion's evolution and in different parts of the active region. As detailed in previous chapters, the FIP bias changes throughout the lifetime of an active region (see Sections 2.4.1, 5.4.2 and 5.4.4) and shows significant variations on sub-active region scales (see Sections 2.4.1 and 5.4.5). These variations are linked to a diverse processes including magnetic activity (see Section 2.4), wave activity (see Section 2.3), heating or magnetic topology (see Section 2.4.3).

The measured FIP bias values can also vary depending on the diagnostic used to measure it. While elements are broadly categorised into low-FIP and high-FIP, different low-FIP elements can show different levels of enhancement, and high-FIP elements can in some instances show enhancement too. The clearest example is S (FIP = 10.36 eV) which sits close to the boundary between low-FIP and high-FIP elements. In some instances it shows no or little enhancement (i.e. it behaves like a high-FIP element), while in others it shows significant enhancement (i.e. it behaves like a low-FIP element; see e.g. the coronal hole measurements of Brooks and Warren, 2011). In addition, remote sensing FIP bias diagnostics (both in the EUV and X-rays) can capture plasma populations with different temperatures depending on the formation temperature of the emission lines involved. For example, the Si x 258.38 Å/S x 264.22 Å diagnostic observes cooler coronal plasma as the formation temperature of these lines is around 1.5 MK, while the Ca xiv 193.87 Å/Ar xiv 194.40 Å diagnostic observes hotter coronal plasma since the lines form at around 4 MK. Therefore, differences in FIP bias values measured with different diagnostics can be due to either the elements themselves behaving differently or the diagnostic probing different temperature plasma populations. Ko et al. (2016) found a high correlation (correlation coefficient varying between 0.76 and 0.91 depending on the region selected) between the FIP bias measured with Si x 258.38 Å/S x 264.22 Å and Fe xii 195.12 Å/S x 264.22 Å ($\log(T_{MAX}[K]) = 6.2$) in a decaying active region. This indicates that Fe and Si show similar FIP enhancement relative to S (note that S is the high-FIP element in both diagnostics). To et al. (2021) found more significant differences between FIP bias diagnostics when analysing the Si x 258.38 Å/S x 264.22 Å compared to Ca xiv 193.87 Å/Ar xiv 194.40 Å FIP bias

values in a small flare. This study suggests that the elements considered to be high-FIP could be behaving differently, i.e. S could be acting like a low-FIP element, as previously suggested by Laming et al. (2019). The behaviour of S is a powerful tool that can be used to gain insight into the details of the fractionation process in a given location.

The work presented in this chapter explores the power of studying the plasma composition patterns using multiple FIP bias diagnostics, particularly involving variations in the behaviour of S, to obtain insight into Alfvén wave activity within an active region. The analysis is focused on active region AR12665 following an episode of new flux emergence in the preexisting magnetic field environment of the region. *Hinode* EIS spectroscopic observations of two FIP bias diagnostics (Si X 258.375 Å/S X 264.233 Å and Ca XIV 193.874 Å/Ar XIV 194.396 Å) show strikingly different fractionation patterns in different parts of the active region. This result is interpreted in the context of the ponderomotive force model, which proposes that the plasma fractionation is generally driven by the ponderomotive force that arises as a result of Alfvén wave refraction in the solar chromosphere (see Section 2.3.2). Model simulations predict that Alfvén waves with different properties deposit their energy at different heights in the chromosphere which can create different plasma composition patterns.

6.2 Evolution of AR 12665

6.2.1 Photospheric White Light and Magnetic Field Evolution

Active region AR12665 (Figure 6.1) was first observed by SDO HMI at the eastern limb on 2017 July 5, with sunspots already present in both polarities. A new episode of significant flux emergence had begun between the leading and following polarities just as the active region region rotated into Earth view. By July 8, the emerging flux formed a new positive sunspot, which started moving towards (see top panels in Figure 6.2) and then orbiting around the preexisting leading sunspot in a counterclockwise direction (see bottom panels in Figure 6.2). They eventually collided around 12:00 UT on July 9 and became one sunspot consisting of two um-

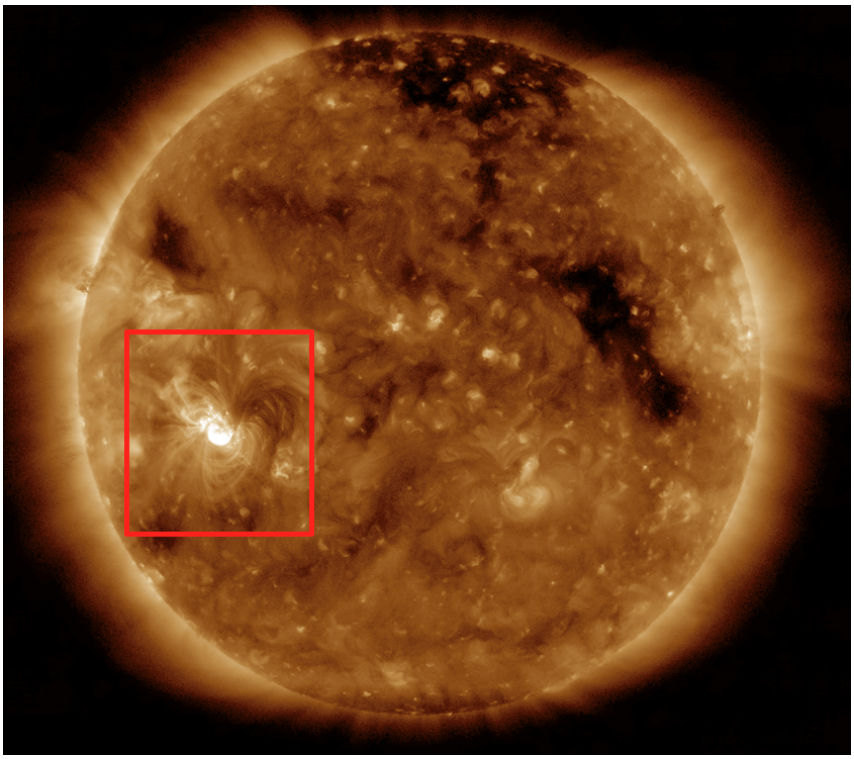

Figure 6.1: SDO AIA 193 Å context image of target AR 12665 on 2017 July 9 at 03:59 UT.

brae separated by a light bridge within one common penumbra. Approximately one day later the light bridge disappeared (not pictured). This orbiting motion lasted for multiple days and was studied in detail by James et al. (2020). For the first approximately 1.5 days, the light bridge constantly separated the new from the preexisting positive sunspot umbrae. This provides an opportunity to track the evolution of the newer and older parts of the active region separately.

6.2.2 Coronal Evolution

In the EUV, images from the SDO AIA showed two main loop populations: the new loops and the preexisting loops. White light images were used to identify the boundaries between these two populations. The new loops had been formed recently by the flux emergence and are rooted in the newly formed positive sunspot (see Figure 6.2). They are bright, relatively small hot loops in the core of the active region (see Figure 6.3). The preexisting loops had been part of the active region since before the flux emergence and are rooted in the preexisting positive sunspot

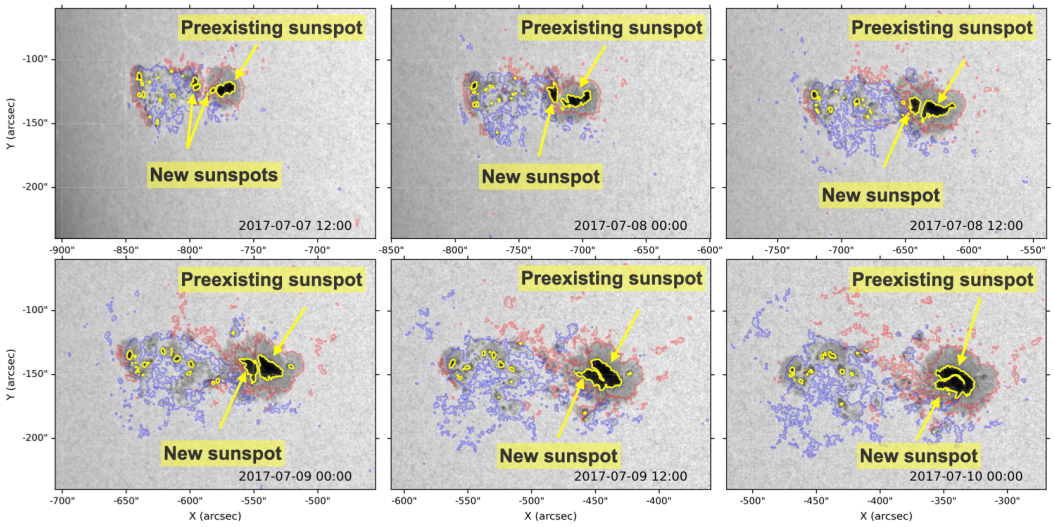

Figure 6.2: SDO HMI Continuum emission and photospheric magnetic field evolution of AR 12665, every twelve hours, prior to and during the *Hinode* EIS scans. Red (blue) contours represent areas of HMI line of sight photospheric magnetic field strength above (below) 200 G (−200 G). Yellow contours represent values below 25,000 ct/s in the continuum emission, indicating the location of the sunspot umbrae.

(see Figure 6.2). They are fainter, high-lying warm loops located in the southern part of the active region (see Figure 6.3).

In the few days running up to the EIS scans on July 9 (see Section 6.3.1), the active region showed modest activity, with only one C1.0 flare on July 7 at 13:37 UT and one C3.4 flare on July 8 at 23:50 UT. On July 9, however, the flaring activity becomes more intense, with an M1.3 flare at 03:09 UT and four C-class flares at 06:15 UT, 07:28 UT, 08:55 UT and 11:44 UT being observed at the boundary between the new and the preexisting loop populations.

6.3 Plasma Composition

6.3.1 Hinode EIS Observations

The FIP bias was calculated using spectroscopic observations from the *Hinode* EIS. The EIS dataset contains 6 scans of the active region over a period of approximately 13 hours. In this work, we analyse the first and the last scans in the series. Details of the EIS scans used are provided in Table 6.1.

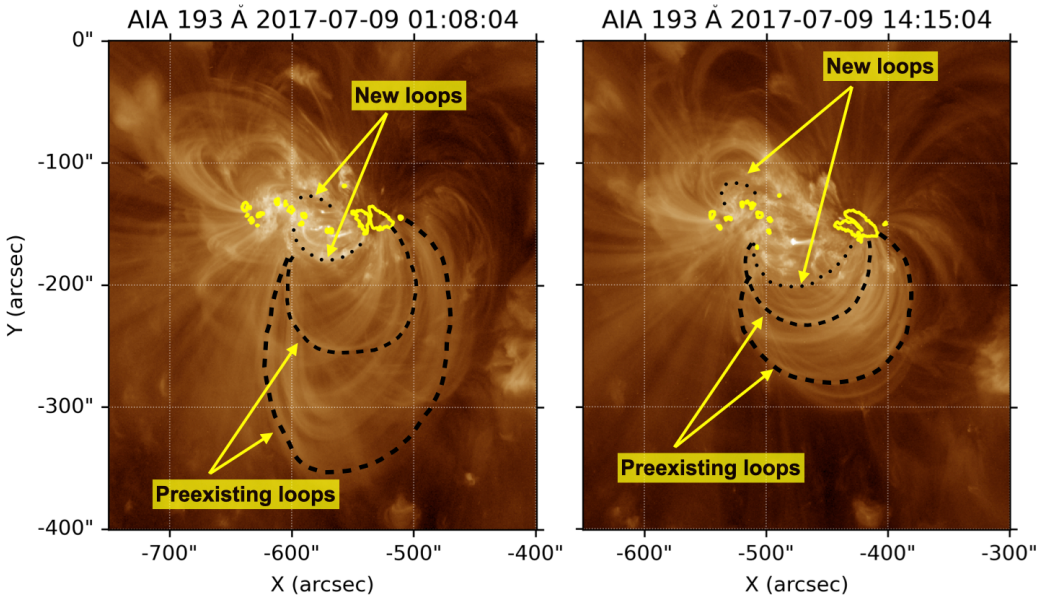

Figure 6.3: SDO AIA 193 Å passband images at the times matching the middle time of the EIS raster scans. Yellow contours represent values below 25,000 ct/s in the continuum emission, indicating the location of the sunspots. Black dotted (dashed) lines indicate representative examples of loops belonging to the new (preexisting) loop populations.

6.3.2 Method

Two line pair diagnostics are used for the plasma composition measurements: Si x 258.38 Å (low FIP, FIP = 8.25 eV) & S x 264.22 Å (high FIP, FIP = 10.36 eV) and Ca XIV 193.87 Å (low FIP, FIP = 6.11 eV) & Ar XIV 194.40 Å (high FIP, FIP = 15.76 eV). The theoretical formation temperatures for emission lines included in the two diagnostics are different: the Si x 258.38 Å and S x 264.22 Å lines form around $\log(T_{MAX}[K]) = 6.2$, while the Ca XIV 193.87 Å and Ar XIV 194.40 Å form around $\log(T_{MAX}[K]) = 6.7$ and $\log(T_{MAX}[K]) = 6.6$ respectively (from the CHIANTI database Version 10, Dere et al., 1997; Del Zanna et al., 2021). The lines involved in the two diagnostics were fitted using the Python EISPAC software (Weberg et al., 2023) and line ratios for each diagnostic were calculated in every pixel in the EIS rasters to obtain an approximation of the FIP bias (second column in Figures 6.4 and 6.5). As line ratios are sensitive to temperature variations, DEM maps (created using the regularised inversion method of Hannah and Kontar, 2012) in the temperature bins corresponding to the formation temperatures of the lines in

EIS Study Details	
Raster middle times	09/07/2017 01:08 09/07/2017 14:15
Study acronym	DHB_007
Study number	544
Field of view	$492'' \times 512''$
Rastering	$2''$ slit, 123 positions, $4''$ coarse step
Exposure time	30s
Total raster time	1h 1m 30s
Reference spectral window	Fe XII 195.12 Å
DEM lines	Fe VIII 185.213 Å, Fe VIII 186.601 Å, Fe IX 188.497 Å, Fe IX 197.862 Å, Fe X 184.536 Å, Fe XI 188.216 Å, Fe XI 188. 299 Å, Fe XII 192.394 Å, Fe XII 195.119 Å, Fe XIII 202.044 Å, Fe XIII 203.826 Å, Fe XIV 264.787 Å, Fe XIV 270.519 Å, Fe XV 284.16 Å, Fe XVI 262.984 Å, Ca XIV 193.874 Å, Ca XV 200.972 Å.
Density diagnostic lines	Fe XIII 202.04 Å, Fe XIII 203.82 Å
Line ratio lines	Si X 258.38 Å, S X 264.22 Å, Ca XIV 193.87 Å, Ar XIV 194.40 Å

Table 6.1: Summary of *Hinode* EIS study details and emission lines used for creating the FIP bias measurements.

each diagnostic are shown for context (third and fourth columns in Figures 6.4 and 6.5).

Additional FIP bias measurements, corrected for temperature and density effects, were also calculated in a few key locations. In these locations, spectra were averaged over a few tens of pixels pixels (creating a macropixel) for all the lines included in the calculation. The method used for the FIP bias calculation in each of these macropixels uses a DEM analysis to account for the temperature effects and a density analysis to account for density effects (see Section 3.3.7.3). The DEM was derived using a series of Fe lines supplemented with a couple of Ca lines for additional high temperature constraints (see Table 6.1) and the density was calculated using the Fe XIII 202.04 Å/Fe XIII 203.82 Å diagnostic. A Markov-Chain Monte Carlo (MCMC) algorithm in the PintOfAle (Kashyap and Drake, 1998, 2000) SolarSoft (Freeland and Handy, 1998) package was used to compute the DEM distri-

bution, and the CHIANTI database (Dere et al., 1997) version 10 (Del Zanna et al., 2021) to compute the contribution functions (G(T,n)) for each of the spectral lines involved in the diagnostic. Note that this method used to derive the DEM distribution for the FIP bias calculation is different from the one used for computing the DEM distribution provided in Figures 6.4 and 6.5 for context purposes only. For photospheric abundances, the values of Scott et al. (2015b,a) were used. Note that using different sets of photospheric abundances could result in slightly different FIP bias measurements. This method is described in detail by Brooks and Warren (2011); Brooks et al. (2015). This method is computationally expensive, hence it was applied to a few macropixels only, rather than everywhere in the EIS scans.

There are 8 such locations in total. For each of the 2 rasters, 4 macropixels were selected: one for each loop population and each diagnostic (see first panel of Figures 6.4 and 6.5). This was done to obtain representative FIP bias values for each of the loop populations in both diagnostics. Slightly different macropixels were chosen for the two diagnostics. This is because the formation temperatures for the lines involved in the two diagnostics are different. For each diagnostic, a few macropixels were selected along the loops of interest and the macropixel with the best signal to noise ratio was kept.

6.3.3 Results

The FIP bias values are summarised in Table 6.2. In the emerging loops, the Si/S FIP bias increases over the 12h from 2.3 to 3.0 and the Ca/Ar FIP bias from 2.6 to 3.3. This result agrees with previous studies which found increasing FIP bias in the emergence phase of an active region (Widing and Feldman, 2001; Baker et al., 2018). While the increase is observed in both diagnostics, the Ca/Ar values are slightly higher than the Si/S ones (albeit close to the 0.3 uncertainty in the measurements previously estimated by Brooks et al., 2017).

In the preexisting loops, the FIP bias behaviour is different. The Si/S FIP bias changes slightly from 1.8 to 2.0, but this is within the 0.3 error limit. The Ca/Ar FIP bias shows an increase from 4.3 to 7.8 and, more importantly, shows consistently high values. This is very interesting because these values are significantly higher

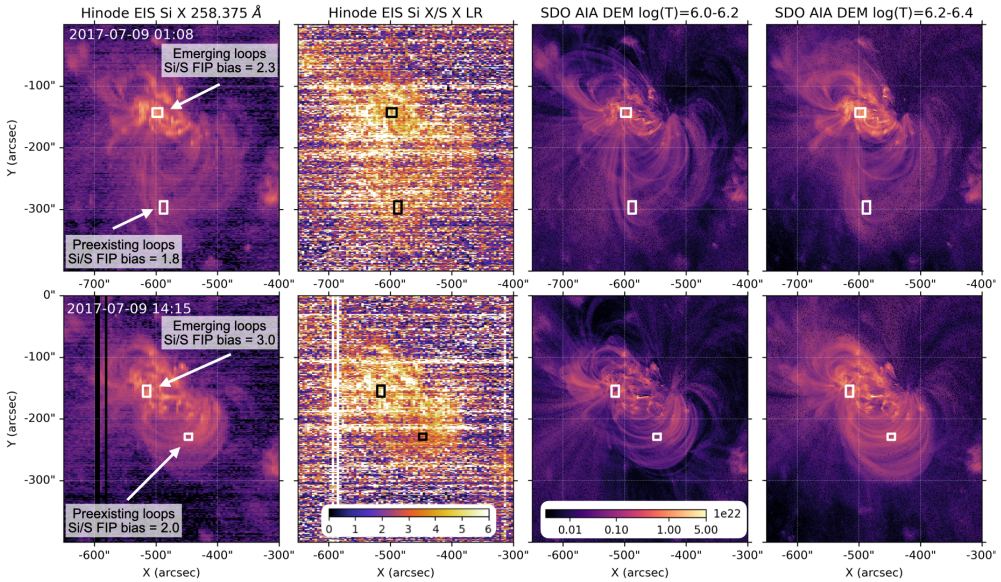

Figure 6.4: Si X/S X results. From left to right: *Hinode* EIS Si X 258.38 Å intensity, *Hinode* EIS Si X 258.38 Å/S X 264.22 Å line ratio, SDO AIA DEM in the log(T[K]) = 6.0 – 6.2 and the log(T[K]) = 6.2 – 6.4 temperature bins (computed using the method developed by Hannah and Kontar, 2012, 2013). The boxes indicate the locations of the macropixels for this diagnostic.

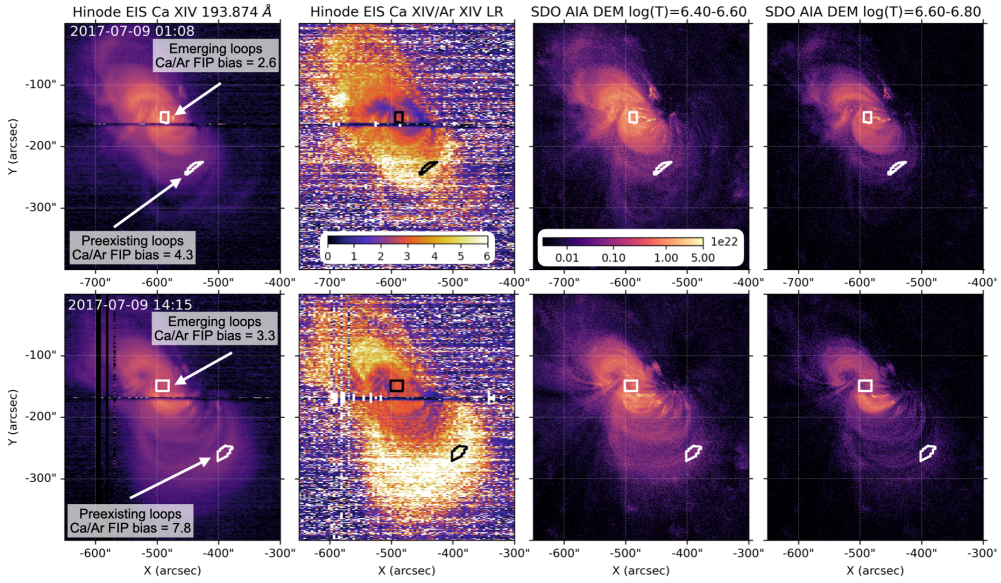

Figure 6.5: Ca XIV/Ar XIV results. From left to right: *Hinode* EIS Ca XIV 193.87 Å intensity, *Hinode* EIS Ca XIV 193.87 Å/Ar XIV 194.40 Å line ratio, SDO AIA DEM in the log(T[K]) = 6.4 – 6.6 and the log(T[K]) = 6.6 – 6.8 temperature bins (computed using the method developped by Hannah and Kontar, 2012). The boxes indicate the locations of the macropixels for this diagnostic.

than the Si/S FIP bias values in the same loop population. To check that these high values are indeed representative of the entire population of preexisting loops, one can examine the line ratio maps (see second column of Figure 6.5). The line ratio maps show high values everywhere in the population of preexisting loops, suggesting that the high FIP bias values are not isolated to the location of the macropixels that were chosen for the FIP bias calculation. Of course, one must be cautious when analysing line ratio maps as they are sensitive to temperature and density effects. In particular, for the Ca/Ar line ratio, significant temperature effects due to plasma above $\log(T[\mathrm{K}]) = 6.6$ must be considered (see e.g. Feldman et al., 2009; Doschek and Warren, 2017; To et al., 2021). This is because the presence of a significant amount of plasma above this temperature would lead to high Ca/Ar ratio that is due to the change in temperature rather than FIP bias (see Figure 7.5 showing the contribution function dependence on temperature for this line pair). The AIA DEM analysis (see third and fourth panel in Figures 6.4, 6.5) shows that the emission in these preexisting loops is mostly cooler, with most of the emission coming from the $\log(T[\mathrm{K}]) = 6.2 - 6.4$ and $\log(T[\mathrm{K}]) = 6.4 - 6.6$ temperature bins, making it unlikely that the high Ca/Ar FIP bias values observed are a result of a temperature effect.

The large Ca/Ar FIP bias values observed in the preexisting loops might appear extreme but they are not uncommon. Similarly high values have been observed before, for example, in the Ca/Ar ratio in flare loops (e.g. Doschek et al., 2015), in the Mg/Ne ratio in an emerging flux region (e.g. Young and Mason, 1997; Widing and Feldman, 2001), in the Mg/O ratio in coronal mass ejection cores (e.g. Landi et al., 2010), and in various diagnostics in post coronal mass ejection current sheets (e.g. Ko et al., 2003; Ciaravella et al., 2002). The newest aspect of the present results is the different behaviour of the two diagnostics used to probe the plasma composition in the two loop populations. While in the emerging loops, the Si/S and Ca/Ar diagnostics indicate similar FIP bias values, in the preexisting loops there is a significant difference between the lower Si/S FIP bias values and higher Ca/Ar FIP bias values. This raises the question of whether the mechanism driving the FIP

Raster Time	FIP Bias			
	Emerging Loops		Preexisting Loops	
	Si/S	Ca/Ar	Si/S	Ca/Ar
2017 July 9 01:08 UT	2.3 ± 0.3	2.6 ± 0.3	1.8 ± 0.3	4.3 ± 0.3
2017 July 9 14:15 UT	3.0 ± 0.3	3.3 ± 0.3	2.0 ± 0.3	7.8 ± 0.3

Table 6.2: *Hinode* EIS FIP bias results summary.

effect has different characteristics in the two loop populations, so this possibility was explored further using simulations from the ponderomotive force model.

It is important to bear in mind that the macropixel locations vary between the two EIS scans and, within one raster, they are also different for each diagnostic. This aspect could also be responsible for some of the differences observed. The reasoning for choosing different locations is as follows. Firstly, the loop populations evolve and also move due to solar rotation in the approximately 13 hours between the two EIS scans, so the macropixel locations are changed as well to track the loops. Secondly, for one loop population in one raster, the hotter parts have better signal to noise ratio for the Ca/Ar diagnostic, while the cooler parts have better signal to noise ratio for the Si/S diagnostic. The macropixel chosen for each diagnostic was selected such that it maximizes the signal to noise ratio for that diagnostic. Figures 6.4 and 6.5 do not show significant variations in the either the line ratio values or the DEM values within a given loop population. This suggests that the FIP bias values within a loop population are relatively constant. Therefore, the effects of varying the macropixel locations to increase the signal to noise ratio should be minimal. In addition, there is significant flaring activity that involves loops close to the boundary between the emerging and the preexisting loops. Since flaring is likely to affect the plasma composition temporarily, all macropixels were located as far away from the flaring location as possible to minimize the effects of flaring on the measurements. This results in the emerging loops macropixels being closer to the loop footpoint and the preexisting loop macropixels being closer to the loop apex. It is possible that this has an impact on the composition measurements. However, this impact is expected to be minimal since Figures 6.4 and 6.5 suggest there are no significant FIP bias variations along the loops in this case.

6.4 The Ponderomotive Force Model

The ponderomotive force model (Laming, 2004, 2015; Laming et al., 2019) is a 1D static model which proposes that the FIP effect is generated in the chromosphere by Alfvén wave activity originating in the corona (see Section 2.3.2 for a detailed description). At coronal loop footpoints, refraction of these Alfvén waves in the high density gradient of the chromosphere (see Figure 6.6a) generates a ponderomotive force. This ponderomotive force acts on the ionized material (i.e. mostly low-FIP elements since they have a much higher ionization fraction than the high-FIP elements, see Figure 6.6b,c), preferentially bringing them upwards to the top of the transition region. From the transition region, fractionated plasma is transported upwards into the corona via a steady upflow (Bray et al., 1991). Once plasma leaves the transition region and reaches the corona, two things happen. First, the temperature increases enough (typical coronal temperatures are approximately $\log(T[K]) \approx 6.0$) to ionize all elements, so low-FIP and high-FIP elements are no longer separated into ions and neutrals. Second, there is no significant density gradient anymore, so the ponderomotive force becomes very small, if at all present (see Section 2.3.2). This means that the fractionation process stops at the top of the transition region, and the plasma composition pattern is locked in. From here, the fractionated plasma is brought upwards into the corona via transport mechanisms such as diffusion or ablation. Note that the current implementation of the ponderomotive force model uses a 1D static model chromosphere, and so it does not cover this last part of the chain.

The pattern (the relative enhancement of different elements) and strength (the level of enhancement) of the fractionation process depend on the height in the chromosphere at which the ponderomotive force is generated. This, in turn, is dictated by whether the Alfvén wave driver is in resonance with the loop or not. Resonance here means that the wave travel time from one loop footpoint to the other is an integral number of wave half-periods. Resonant waves accumulate much more wave energy in the corona than in the chromospheric footpoints, and drive the ponderomotive force close to the top of the chromosphere (see Figure 6.6e). This results

in mild fractionation levels (see Figure 6.6f) because of the ionized background gas. Non-resonant waves drive the ponderomotive force at lower heights (see Figure 6.6h), which results in stronger fractionation levels (see Figure 6.6i) because the background gas is neutral.

6.4.1 Model Simulations

The ponderomotive force model was used to make predictions of the fractionation patterns in the two loop populations shown in Figures 6.4 and 6.5. Simulation predictions match best with the *Hinode* EIS observations when assuming the ponderomotive force driver is resonant waves in the emerging loops and non-resonant waves in the preexisting loops. This scenario is described in detail below.

There are two main parts that make up the simulations: setting the loop environment and selecting the properties of the waves driving the fractionation. For each loop population, the loop environment is constructed as follows. The coronal part of the loop is constructed using the parameters in Table 6.3. The chromospheric environment at the footpoint of the loop is assumed to be that given by Avrett and Loeser (2008). Chromospheric parameters that are key to the fractionation process are the temperature and density gradient in the chromosphere (see Figure 6.6a) and the ionization fractions of the low-FIP and high-FIP elements, which are calculated assuming Saha ionization (see Figure 6.6b,c). Section 2.3.2 describes in detail how the Alfvén wave propagation is treated in each part of the loop and the role of each portion of the loop plays in the fractionation process. Once the environment is set, the model simulated the propagation of an Alfvén wave of a given frequency to obtain the fractionation pattern it will produce. The main free parameters here are the wave frequency and amplitude. The chromospheric model is not changed throughout the simulations.

First, the loop length, plasma density along the loop and magnetic field strength are estimated to construct the coronal part of the loop environment. The loop lengths were estimated using a Potential Field Source Surface (PFSS) model of the active region created using the IDL *Solarsoft* package*Solarsoft* library[1] (Freeland and

[1]Details at: http://www.ascl.net/1208.013

Handy, 1998) provided by Schrijver and DeRosa (2003). In the PFSS model, a representative loop that matched the EUV observations (see Figure 6.3) was selected for each loop population and its length was calculated. The plasma density along the loop was measured in the macropixel boxes shown in Figures 6.4, 6.5 using the Fe XIII 202.04 Å/Fe XIII 203.82 Å diagnostic from *Hinode* EIS. The expansion of the magnetic field in the low corona, which also influences the fractionation process, was estimated using photospheric magnetic field strength (estimated from magnetic flux density measurements with SDO HMI) and coronal magnetic field strength (estimated using the PFSS extrapolation). All loop parameters are summarised in Table 6.3. Using these loop parameters, the resonant frequencies for each loop population are calculated using:

$$f_{\text{resonance}} = \frac{v_A}{2L}, \tag{6.1}$$

where L is the loop length and v_A is the Alfvén speed calculated as:

$$v_A = \frac{B}{\sqrt{4\pi\rho}}, \tag{6.2}$$

where B is the coronal magnetic field strength, and ρ is the loop density. The resonant frequencies and Alfvén speeds characteristic to each loop population are given in Table 6.3 are well.

Once the environment is set, the wave properties were varied to test what wave frequency and amplitude best reproduces the plasma composition patterns observed by EIS. The best agreement was found when assuming the Alfvén wave driver is resonant in the emerging loops and non-resonant in the preexisting loops. These two cases are presented below. Simulations were run assuming that the fractionation process is driven by Alfvén waves at the emerging loop resonant frequency ($\Omega_{\text{EL resonance}} = 0.351$ rad s^{-1}) in both the emerging and the preexisting loops. A discussion on why this is likely to be an appropriate choice is provided in Section 6.4.2. The wave amplitude was free to vary (see Table 6.4).

Results for the resonant case are shown in Figure 6.6d,e,f. In this case, the ponderomotive acceleration starts to increase in the middle of the chromosphere and is

highest at the top of the chromosphere and the transition region (Figure 6.6e). As a result, the abundances of Si and Ca (relative to H, i.e. absolute abundances) start increasing slightly from the middle of the chromosphere, and show the highest enhancement around the top of the chromosphere and the transition region (Figure 6.6f). The focus is on the relative abundance predictions at the top of the transition region (i.e. 2500 km above the photosphere in these simulations) since the model suggests that abundance ratios are locked in once the plasma leaves this layer and is transported into the corona (see Section 2.3.2). Hence these are the ones to be compared with coronal observations. At the top of the transition region, Ar and S are essentially not fractionated. Ca and Si are both significantly fractionated. Ca shows a stronger fractionation than Si (Figure 6.6f) which is likely because the ionization fraction of Ca is higher than the one of Si (Figure 6.6b) which means a larger fraction of the Ca atoms are affected by the ponderomotive force. While the differences in the ionization fraction of low-FIP elements are very small, i.e. approximately 0.1%, they are significant when it comes to the fractionation process. This is because of the high density gradient in the chromosphere: an additional enhancement that is very small at a given chromospheric layer will become significant when transported to the layers above since the density decreases so quickly (see Figure 6.6a). This could explain why the *Hinode* EIS observations show slightly higher Ca/Ar FIP bias values than Si/S FIP bias values in the emerging loops.

Results for the non-resonant case are shown in Figure 6.6g,h,i. In this case, fractionation happens lower down in the chromosphere and is overall stronger: the ponderomotive acceleration starts increasing at the bottom of the chromosphere, reaches a maximum at the middle of the chromosphere and then decreases (Figure 6.6h). The abundances of Si and Ca (relative to H) start increasing from the bottom of the chromosphere, which results in stronger enhancements at the top of the transition region compared to the resonant case. Interestingly, in this case S behaves similarly to Si and Ca rather than Ar: it becomes enhanced as well, but to a lower degree than Si and Ca. As in the resonant case, Ar shows no fractionation. This could explain the strong difference between the Ca/Ar FIP bias and the Si/S FIP bias in

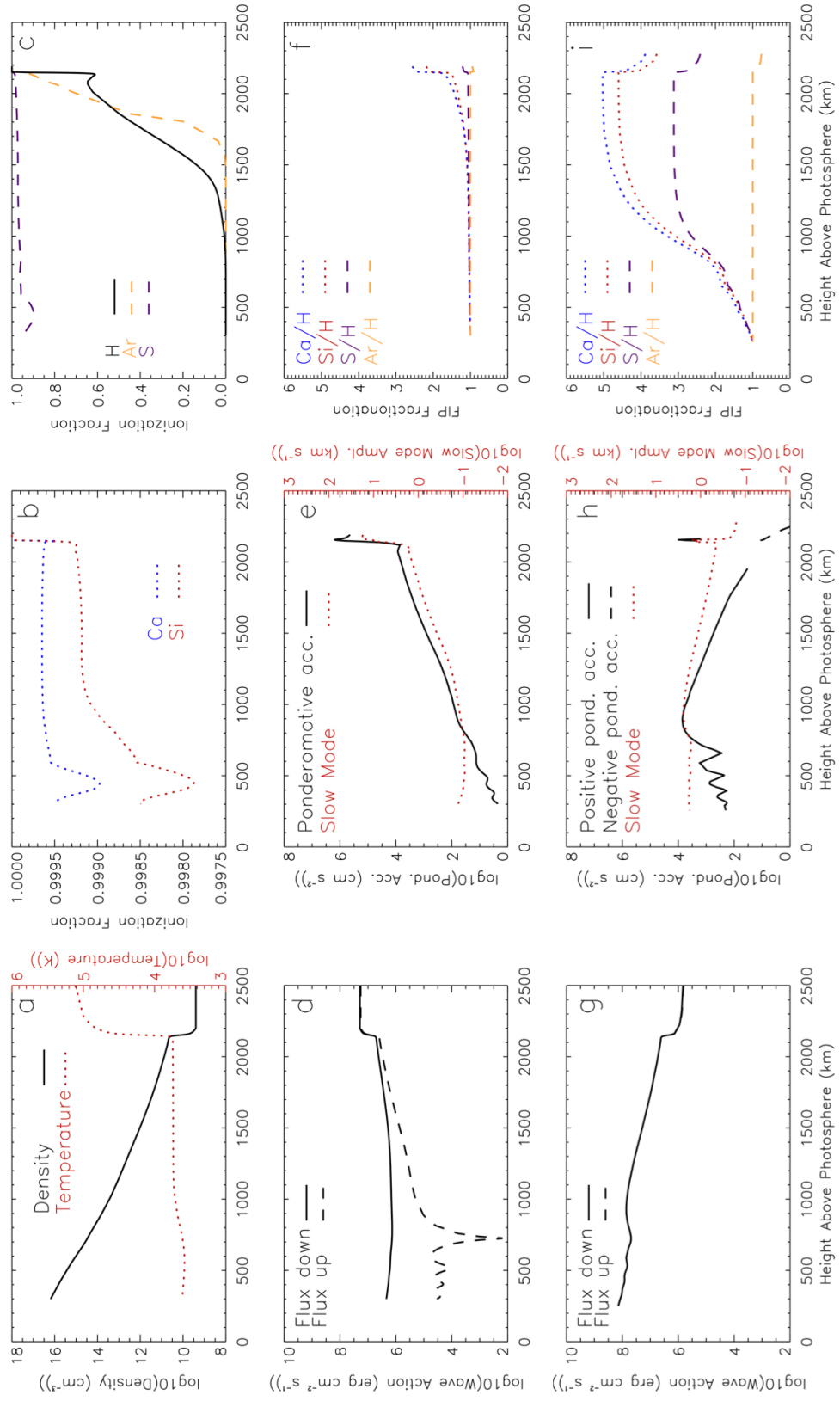

Figure 6.6: Ponderomotive force model predictions. First row shows the variation with height of: a) electron temperature and density, b) ionization fractions for low-FIP elements, c) ionization fractions for high-FIP elements. Second (third) row shows the resonant (non-resonant) fractionation case, i.e. the variation with height of: d, g) Alfvén wave energy fluxes (the downward and upward fluxes are identical in the non-resonant case) e) ponderomotive acceleration f) FIP bias relative to H.

Parameter	Emerging Loops	Preexisting Loops
L	100 Mm	510 Mm
ρ	$10^{9.5}$cm^{-3}	$10^{8.5}$cm^{-3}
Coronal B	250 G	200G
v_A	10^4 km s^{-1}	2.5×10^4 km s^{-1}
$f_{\rm resonance}$	0.05 s^{-1}	0.025 s^{-1}
$\Omega_{\rm resonance}$	0.351 rad s^{-1}	0.157 rad s^{-1}
$A_{\rm chromo}$	0.22 km s^{-1}	0.03 km s^{-1}
$A_{\rm coronal}$	44 km s^{-1}	14 km s^{-1}

Table 6.3: Parameters used for ponderomotive force model predictions. Parameters listed here follow the same notation in Equations 6.1 and 6.2. For the wave amplitudes, $A_{\rm chromo}$ is the chromospheric wave amplitude at the $\beta = 1$ layer used as input for the model simulations and $A_{\rm coronal}$ is the coronal wave amplitude predicted by the model.

the *Hinode* EIS measurements of the preexisting loops. As in the resonant case, Ca is more strongly enhanced than Si due to its higher ionization fraction. However, in the non-resonant case, the largest discrepancy between diagnostics comes from the fact that S experiences significant fractionation as well, i.e. does not behave like a high-FIP element anymore. Therefore, the enhancement of Si is underestimated when measured relative to S.

It is important to note that the main free parameter when running the model and making FIP bias predictions is the chromospheric amplitude $A_{\rm chromo}$ of the wave that drives the fractionation process. In the absence of observations that can help constrain the amplitudes of these waves at the chromospheric level, an estimate of the amplitudes was required to be able to make a FIP bias prediction. Small changes in the wave amplitudes result in large changes in the estimated fractionation strength at the top of the transition region. However, while the strength of the fractionation is strongly dependent on the amplitude, the behaviour of S is mainly determined by the chromospheric height at which the fractionation process is driven which directly depends on the frequency of the wave driver (and, more specifically, on how close the frequency of the driver is to the resonant frequency of the loop) rather than the amplitude. Therefore, model predictions can be used to obtain a qualitative understanding of the relative enhancement of different elements and, more specifically, to test the conditions when S becomes fractionated as well.

Emerging Loops			Preexisting Loops		
$A_{\rm chromo}$	Si/S	Ca/Ar	$A_{\rm chromo}$	Si/S	Ca/Ar
0.20 km s^{-1}	1.61	2.31	0.025 km s^{-1}	1.32	3.13
0.22 km s^{-1}	1.80	2.70	0.030 km s^{-1}	1.48	5.1
0.26 km s^{-1}	2.22	4.00	0.035 km s^{-1}	1.68	7.0
0.30 km s^{-1}	2.87	6.1	0.040 km s^{-1}	1.93	14.7

Table 6.4: Ponderomotive Force Model Predictions with Variable $A_{\rm chromo}$. For the wave amplitudes, $A_{\rm chromo}$ is the chromospheric wave amplitude at the $\beta = 1$ layer. $A_{\rm corona}$ changes in proportion. Parameters are chosen to span the range of Si/S and Ca/Ar in Table 6.2.

In the example described in this section and shown in Figure 6.6, the calculations are initiated with the wave amplitudes $A_{\rm chromo}$ given in Table 6.3. These are the input chromospheric wave amplitudes which resulted in fractionation patterns that best matched the *Hinode* EIS observations at 01:08 UT. The model predicts the waves to develop amplitudes $A_{\rm coronal}$ in the coronal portions of the loops. In the chromosphere, where the FIP fractionation is calculated, the resonant wave amplitude returns to $A_{\rm chromo} = 0.22$ km s^{-1}. The non-resonant wave amplitude is much larger, of order 1 km s^{-1}. This is characteristic of the non-resonant waves: they are more likely to leak into the chromosphere, so a higher fraction of the wave energy accumulates in the chromosphere than in the corona.

Using the inputs listed in Table 6.3, the model predicts the following results: in the emerging loops (resonant wave driver case), a Si/S FIP bias of 1.8 and Ca/Ar FIP bias of 2.7 and, in the preexisting loops (non-resonant wave driver case), a Si/S FIP bias of 1.5 and Ca/Ar FIP bias of 5.1. These values are directly calculated from the simulation composition patterns at transition region level shown in Figure 6.6f,i. Following the same approach, $A_{\rm chromo}$ can be changed slightly to obtain FIP bias values that match the *Hinode* EIS observations at 14:15 UT as well (see Table 6.4). The key result, however, is that while the predicted FIP bias values depend on the selected $A_{\rm chromo}$, the significant differences between the two diagnostics (given by the behaviour of S) depend on whether the wave is resonant or not.

While one could model Si/S and Ca/Ar coming from different strands with different wave populations within each loop, it is interesting that the same fraction-

ation process (i.e. one wave in each loop, of the same frequency) for both Si/S and Ca/Ar reduces the former and increases the latter in going from emerging to preexisting loops. One might achieve better agreement between model and observation with more waves, but this would be at the expense of more model parameters.

6.4.2 Alfvén Waves Origin Discussion

The ponderomotive force model simulations suggest that the fractionation pattern observed in the two loop populations could be explained if the driver is resonant waves in the emerging loops and non-resonant waves in the preexisting loops. This naturally raises a question regarding the origin of these waves. One possibility explored in this work is that the waves giving rise to the fractionation seen in the emerging loops have a coronal driver, and consider both a coronal and a photospheric driver for the waves giving rise to the fractionation observed in the preexisting loops. The emerging loops make up the hot and very active core of the active region. If we assume that the corona is heated via a nanoflare heating mechanism, then, along with heating the corona, this mechanism will also release coronal Alfvén waves, some fraction of which will potentially be at resonance with the loop and can drive the fractionation (Laming, 2017; Dahlburg et al., 2016). The preexisting loops are cooler, likely indicating that nanoflare heating is weaker in this case. This suggests that an external driver is more likely to generate the waves needed for the fractionation observed here.

The first candidate is of coronal origin. One possibility is that resonant waves in the emerging loops could be communicated to the pre-existing loops where they will be non-resonant. The equation of motion for waves on the pre-existing loops (2) with displacement x_2 forced by kink oscillations of the emerging loops (1) is given by:

$$\rho_2 \left(\ddot{x_2} + \Omega_2^2 x_2 \right) = -\frac{\partial}{\partial r} \left(\frac{\delta \mathbf{B}_{1\perp}^2}{8\pi} + \frac{B_0 \delta \mathbf{B}_{1||}}{4\pi} \right), \tag{6.3}$$

where, on the left hand side (the 'driven' side), ρ_2 and Ω_2 are the density and resonant frequency of the preexisting loops respectively and, on the right hand side (the 'driver' side), $\delta \mathbf{B}_1$ is the magnetic field perturbation in the emerging loops, with

components perpendicular and parallel to the ambient magnetic field B_0 indicated. Here, the assumption is that $\delta\mathbf{B}_1 \propto 1/r$. The notation (1) and (2) here corresponds to the loop populations indicated as emerging and preexisting loops in Figure 6.1. The first Alfvénic term on the right hand side $\delta\mathbf{B}_{1\perp}^2/8\pi = \rho_1\delta\mathbf{v}_{1\perp}^2/2$ and oscillates at $2\Omega_1$ to give:

$$\frac{x_2}{x_1} = \frac{\rho_1}{\rho_2}\frac{2\Omega_1^2}{\Omega_2^2 - 4\Omega_1^2}\frac{x_1}{R}, \tag{6.4}$$

where x_1 is the displacement of the emerging loops, ρ_1 and Ω_1 are the density and resonant frequency of the emerging loops respectively, and R is the separation between the flux tubes. With $x_1 = 44/0.351 = 125$ km, Eqn. 6.4 indicates that $x_2/x_1 = 0.3$ requires a separation between flux tubes of $2'' - 4''$, much smaller than the observed separation of order $100''$.

The effect of the second, compressive, term on the right hand side is more model dependent (e.g. Mikhalyaev and Solovév, 2005; Verwichte et al., 2006). When the plasma beta $\beta \ll 1$, the r-component of the wavevector exterior to the emerging loop can be written as:

$$k_r^2 v_{Ae}^2 = \Omega^2 - k_z^2 v_{Ae}^2 = k_z^2 \frac{v_{A1}^2 - v_{Ae}^2}{1 + \rho_e/\rho_1}, \tag{6.5}$$

where

$$\Omega^2 = k_z^2 \frac{B_e^2 + B_0^2}{4\pi(\rho_e + \rho_1)} \tag{6.6}$$

is the tube oscillation frequency in terms of exterior and interior ambient magnetic fields B_e, B_0, and densities ρ_e, ρ_1 (Mikhalyaev and Solovév, 2005). When $v_{Ae} > v_{A1}$ (the usual case), k_r is imaginary and the exterior wave is evanescent, meaning that the kink oscillations are trapped inside the loop, making transfer of wave energy from one loop to the other unlikely. Such a situation has been studied in detail for magnetosonic waves escaping from reconnection current sheets by Provornikova et al. (2018). This is the assumed scenario when running the simulations presented in this work. This scenario is certainly oversimplified, and many possibilities must exist for the excitation of wave modes as magnetic flux emerges. One difficulty with this scenario is that waves generated by nanoflares are highly localised to single

loops rather than loop populations which raises questions about whether this type of wave transfer could realistically take place.

A second candidate could be of photospheric origin, and include p- and g-mode oscillations or other perturbations of the photospheric plasma flows generated by the flux emergence happening in the close vicinity of the preexisting loops footpoints (see Figure 6.2). These can act as a driver for both resonant and non-resonant waves. Among the wide range of possible photospheric perturbations, those with long wavelengths could naturally couple and perturb the neighbouring preexisting loops population at the same time. In this regard, it is worth noting that this active region shows an interesting global rotation of the photospheric magnetic field (see James et al., 2017) which suggests there could be a photospheric or sub-photospheric wave driver on large spatial scales. Interestingly, Grant et al. (2022) have detected coherent waves across multiple pores in the photosphere suggesting a coupled wave excitation mechanism and a driver acting on scales of several tens of Mm. The rotational motion observed in the active region studied here could also drive torsional Alfvén waves. The associated spatial scales of the driver may explain coupled behaviour of different loops. The S enhancement in the preexisting loops (as suggested by the *Hinode* EIS observations) and the fact that, as suggested by the model, the fractionation process takes place lower down in the chromosphere than in the non-resonant case support the scenario of a photospheric origin for the waves driving fractionation in the preexisting loops. It is, however, important to note that the low frequencies and long wavelengths implied for 3 or 5 minutes p-modes which make them reflect more easily in the chromosphere mean that high chromospheric wave amplitudes, > 10 km s^{-1} are required. Higher frequency non-resonant waves, such as modeled in Figure 6, reduce this amplitude to ~ 1 km s^{-1}.

These are a couple of options that could explain the presence of non-resonant waves in the preexisting loop. However, understanding the exact origin of these waves is beyond the scope of this thesis and is a topic that requires in depth further investigations in the future.

6.5 Summary and Discussion

Spectral analysis of *Hinode* EIS observations of active region AR12665 show very different FIP bias values in two parts of the active region. The emerging loops, i.e. the new part of the active region, show enhanced Si/S FIP bias (2.3 to 3.0) and slightly higher Ca/Ar FIP bias (2.6 to 3.3). The preexisting loops, i.e. the old part of the active region, show more modest Si/S FIP bias (1.8 to 2.0) but very strong Ca/Ar FIP bias (4.3 to 7.8). The Ca/Ar FIP bias is slightly higher than the Si/S FIP bias in the emerging loops, but much higher than the Si/S FIP in the preexisting loops. The study suggests that the ponderomotive force model is able to predict this effect using simple assumptions about the properties of the waves driving the fractionation process in the two loop populations.

One possibility explored in this work is that the fractionation pattern observed in the emerging loops can be a result of resonant Alfvén waves of coronal origin. In this case, Ar and S show no fractionation, while Ca and Si show significant fractionation (Ca slightly higher than Si which could explain the slightly stronger Ca/Ar FIP bias compared to Si/S FIP bias). This can be explained by fractionation occurring at the top of the chromosphere (as was previously suggested for the hot core loops from measurements of significantly higher FIP bias values by Brooks and Yardley, 2021).

The fractionation pattern observed in the preexisting loops can be a result of non-resonant waves. In this case, Ca and Si show stronger fractionation than in the previous case (Ca again slightly higher than Si) and Ar again shows no fractionation. The key difference is that, in these conditions, S shows significant fractionation as well, resulting in a much lower Si/S FIP bias than Ca/Ar FIP bias. This can be explained by fractionation occurring lower down in the chromosphere (as was previously suggested by Laming et al., 2019). Note that although the two diagnostics measure different FIP bias levels, they are both detecting coronal abundances in both the hot core loops and pre-existing loops. It is the combination of Si/S and Ca/Ar FIP bias measurements that allow further probing of the model predictions,

and the development of the resonant/non-resonant wave explanation of the wider loop environment.

It is important to note that the model is only analysing the chromospheric and transition region environment, predicting abundances at the top of the transition region. Transport mechanisms from the top of the transition region to the corona must be considered to be able to make a prediction of the FIP bias in the corona. The model suggests that the abundance change at the top of the transition region can be reached within minutes (Laming, 2015). However, previous studies (Widing and Feldman, 2001; Baker et al., 2018), found that the FIP bias increases with time in the emergence phase over hours to days. This indicates that transport processes that bring the fractionated plasma into the corona are much slower than the processes that drive the fractionation, so predicted chromospheric abundances will not be reflected in the corona right away. Nevertheless, assuming that these coronal transport timescales are similar in the emerging and preexisting loops, qualitative trends predicted by the ponderomotive force model can be compared to the *Hinode* EIS observations.

There is an increase in both the Si/S FIP bias and the Ca/Ar FIP bias of the emerging loops over the 13 hour period between the two *Hinode* EIS scans. This could indicate that the fractionated plasma is slowly being transported to the corona, i.e. the fractionation pattern at the top of the transition region is slowly being reflected in the corona. The strong increase of the Ca/Ar FIP bias in the preexisting loops over the 13 hour period could be explained following the same reasoning, with the exception that the final Ca/Ar FIP bias is higher, so the increase appears to be more drastic. The steady increase assumption requires reasonably quiet coronal conditions. However, there are 1 M-class and 4 C-class flares at the boundary between these two loop populations in between the first and the second *Hinode* EIS scans. In the EUV, previous studies showed that flaring can either temporarily reduce the FIP bias to photospheric values (Warren, 2014) or increase it (To et al., 2021). While the boxes selected for the FIP bias measurements are located further

away from the flaring sites, the possibility that the flaring activity influences the coronal transport mechanisms in the loops under study cannot be excluded.

Finally, this result is particularly relevant for connection science studies. Typically the FIP bias diagnostics used in remote sensing studies (e.g. Si/S, Fe/S, Ca/Ar, Mg/Ne) are different from the ones used for in-situ measurements (e.g. Fe/O), so understanding when these diagnostics behave differently is important for connnecting the two types of measurements. According to the ponderomotive force model, resonant waves drive little fractionation in larger loops (e.g. the ones in this study) and no fractionation in open loops (although this aspect has been questioned by Réville et al., 2021). However, as this work suggests, fractionation can still be driven in these loops by non-resonant waves if an external driver is present and a similar process could happen in open field lines. In this case, the Si/S FIP bias would be very low (and this can be extended to other low-FIP elements relative to S) so the area under study could mistakenly be believed to show no/weak fractionation unless a second diagnostic (not including S) is used. Therefore, understanding what differences to expect between different FIP bias diagnostics and being able to predict in what conditions S starts experiencing significant fractionation is important for connecting in-situ plasma parcels to their origin on the Sun. This is especially important given that S is commonly used in both remote sensing and in-situ FIP bias diagnostics.

Chapter 7

Plasma Composition Variations in a Solar Flare: Links to Coronal Loop Radiative Cooling

This chapter includes results to be submitted for publication. The spectroscopic data analysis and interpretation was performed by myself in collaboration with Dr. Peter Young (NASA Goddard Space Flight Center). The EBTEL simulations were performed by Dr. David Brooks (George Mason University) using loop parameters I provided. This work was carried out under the supervision of Prof. Lucie Green, Dr. Deborah Baker, Dr. David Long and Prof. Lidia van Driel-Gesztelyi. The results of this work were presented at the *Hinode* 16/IRIS 13 Meeting (Niigata, Japan) in September 2023 as a contributed talk.

7.1 Introduction

The plasma composition in flare loops is different from that of quiescent active region loops. As discussed in detail in Section 2.4.2, unlike quiescent active region loops, where fractionated plasma is supplied to the corona via the loop footpoints, in flare loops, the corona is supplied with unfractionated plasma. Results from full-Sun spectra in the EUV (Warren, 2014) and X-rays (e.g. Mondal et al., 2021; Nama et al., 2023) found evidence that the average FIP bias, dominated by the flare emission, evolves from quiet Sun values in the preflare phase to photo-

spheric values around the peak of the GOES X-ray flux, and returns to its original value over the course of a few minutes to hours. The situation is actually more complex with the spatially resolved observations from *Hinode* EIS showing that brighter flare loop apex have coronal composition (Doschek et al., 2015, 2018), but the FIP bias values decreasing along the loop as the footpoint is approached (Doschek et al., 2018). These observations suggest that chromospheric evaporation is supplying the corona with unfractionated plasma via the chromospheric footpoints of the flare loops (Warren, 2014). The photospheric composition observed during these evaporation episodes suggests that plasma is transported from deep in the chromosphere, below the region where the fractionation process takes place.

It is known that flare dynamics affect flare loop plasma composition, but these plasma composition changes, in turn, have effects on other flare related processes such as the radiative cooling process of flare loops. Flare loops cool mainly via radiation and, in the temperature range $\log(T[\mathrm{K}]) = 5.3 - 7.0$, radiation is dominated by emission from Fe lines (Aschwanden, 2004). As Fe is a low-FIP element, the FIP effect changes the Fe abundance in the corona, which then changes the total power radiated by the plasma. Brooks (2018) showed that the the kind of abundance changes typically driven by the FIP effect in the solar corona lead to detectable differences in the cooling lifetimes of coronal loops. In their work, they used loop cooling times measured from SDO AIA observations to study the IFIP effect (for details on the IFIP effect, see Section 2.4.2). The main question regarding the IFIP effect is whether it is the result of low-FIP elements being depleted or high-FIP elements being enhanced. Brooks (2018) modelled the radiated power loss in the two potential scenarios and found that the modelled loop cooling times better matches observations in the scenario where low-FIP elements are depleted. This is an important result for understanding the IFIP effect, but it also highlights the importance of plasma composition in the radiative cooling process.

The work presented in this chapter further explores the link between plasma composition and the radiative cooling process of flare loops plasma using spectroscopic observations. The analysis focuses on high cadence *Hinode* EIS sit-and-

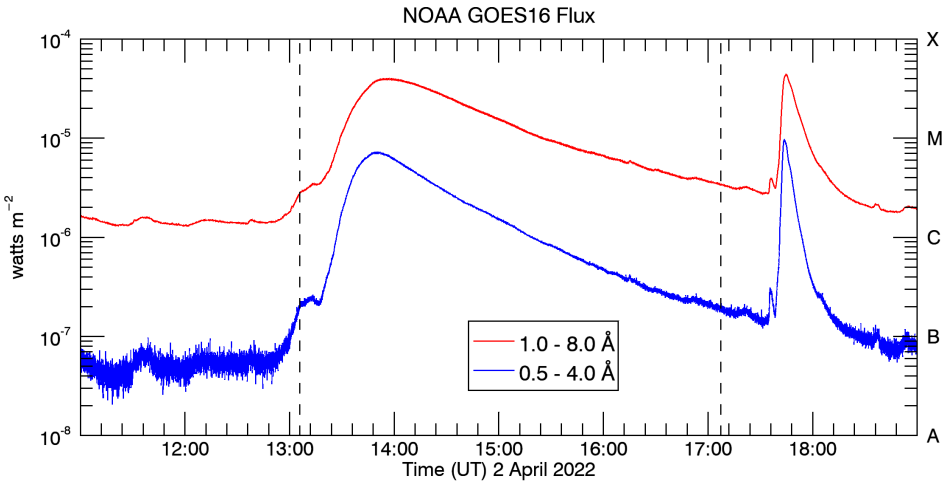

Figure 7.1: X-ray flux observed in the two GOES channels (1-8 Å and 0.5-4 Å). The vertical dashed lines indicate the start and end times of the *Hinode* EIS observations.

stare spectroscopic observations of the evolution of the flare loop plasma after the M-class flare peaking at 13:56 UT on the 2022 April 2. The flare loop's plasma composition is characterised using the Ca XIV 193.87 Å /Ar XIV 194.40 Å diagnostic, while its radiative cooling process is characterised by the time spent cooling through a range of emission lines that form at different temperatures. These observations are interpreted in the context of simulations from the EBTEL 0D hydrodynamic model which simulates the radiative cooling of flare loops following the same concept as Brooks (2018). Simulations show that photospheric composition leads to longer cooling times and weaker emission, while coronal composition leads to shorter cooling times and stronger emission. A similar trend is seen in the observations, where the loop apex shows coronal plasma composition, stronger emission and shorter cooling times for the lines included in the study, compared to the loop footpoint which shows photospheric plasma composition, weaker emission and longer cooling times. This could mean that the different plasma composition in the loop apex and loop footpoint might have significant implications for the cooling process in different parts of the loop. If this creates a strong enough temperature gradient and the density is sufficiently high, then conduction might become important and drive heat flows via along the loop which were not previously considered.

7.2 Flare Loops Evolution

The flare under study is an M3.9 long duration flare that started around 12:50 UT and peaked at 13:56 UT on the 2022 April 2 (see Figure 7.1). It accompanied the eruption of a filament that had formed in between two large active regions, AR 12976 and AR12975, and was destabilised by the emergence of a third active region, AR12977 (for a study of the filament eruption, see Janvier et al., 2023). It is the first of two M-class flares produced in this complex on this day, the second one being a short duration M4.3 flare at 17:34 (see Figure 7.1). The focus of this work is on the small flare loop arcade centered around X, Y = (910 $''$, 250 $''$), which was observed by *Hinode* EIS during the impulsive and decay phases of the flare. These flare loops start brightening in the AIA 131Å images at approximately 13:40 UT and disappear completely by 14:30 UT, suggesting the plasma has cooled below the temperature of approximately $\log(T[\mathrm{K}]) = 7.0$ imaged by the 131 Å passband (see Figure 4.7).

7.3 Hinode EIS Observations

The evolution of the flare loops was captured by *Hinode* EIS using a sit-and-stare observing study (see Table 7.1 for study details). The observation, consisting of 4 consecutive runs of the Flare_SNS_v2 study[1], started at 13:05 UT just before the beginning of the impulsive phase of the flare, and continued through most of the decay phase (see Figure 7.1). In this study, the EIS slit had a fixed position, which was ideally located to capture the flare loops cooling during the decay phase with high cadence (see Figure 7.2).

The present analysis focuses on the EIS observations taken around the peak of the flare, i.e. from approximately 13:40 UT to 14:25 UT. The level-0 data were obtained from the *Hinode* EIS archive[2] in the IDL *Solarsoft* library[3] (Freeland and Handy, 1998). The data were calibrated with the eis_prep routine from the IDL *Solarsoft* library. This routine removes the CCD dark current, cosmic ray pattern, and

[1]Details at: https://solarb.mssl.ucl.ac.uk/SolarB/estudylist.jsp
[2]Available at: https://solarb.mssl.ucl.ac.uk/SolarB/SearchArchive.jsp
[3]Details at: http://www.ascl.net/1208.013

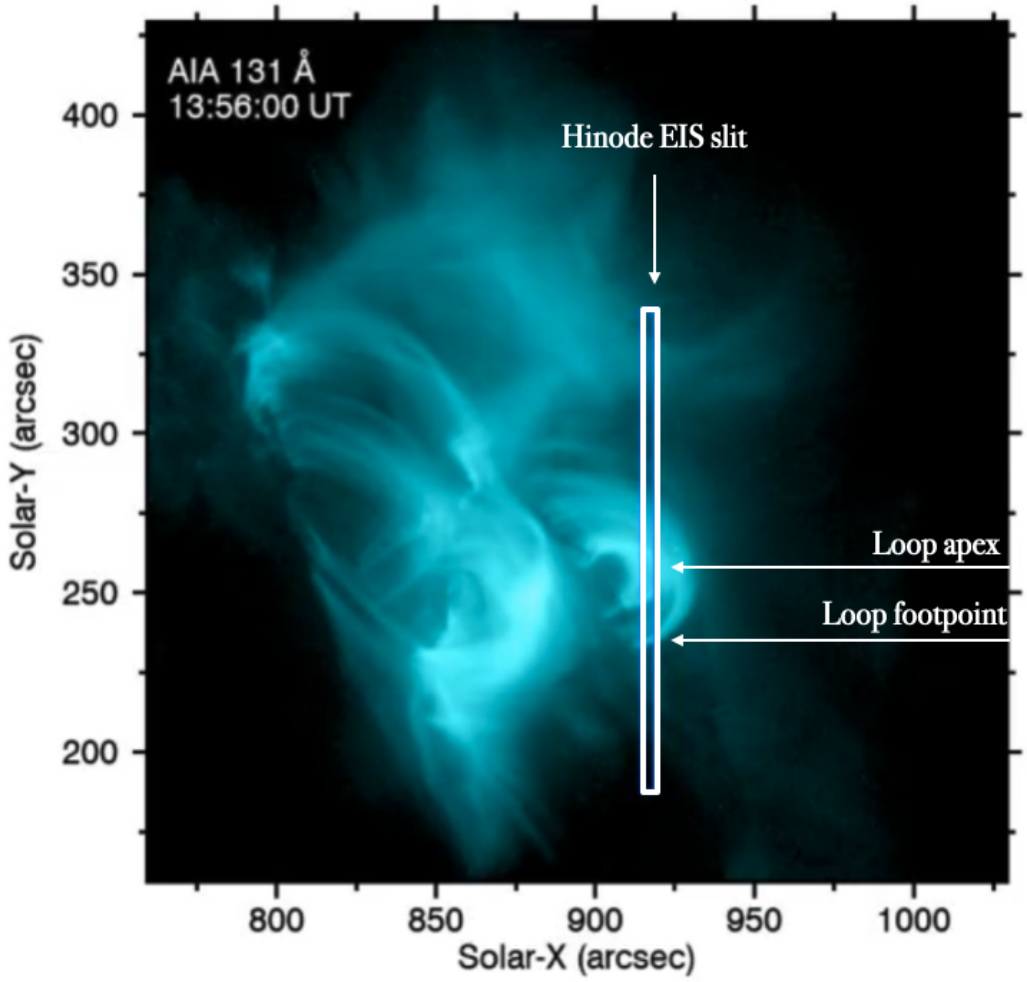

Figure 7.2: AIA 131 Å image of the flare loops at the peak of the GOES X-ray flux (13:56 UT). The blue rectangle indicates the position of the EIS slit (for Fe XII 195.119 Å).

hot and dusty pixels from detector exposures and provides the radiometric calibration to physical units (erg $cm^{-2}s^{-1}sr^{-2}Å^{-1}$).

To align the EIS rasters to AIA, the standard offset was obtained from the eis_aia_offsets routine and an additional manual correction was performed by comparing the EIS Fe XII 195.119 Å intensity map with images from the AIA 193 Å passband. For the additional correction, synthetic AIA rasters were produced from a sequence of images in the 193 Å passband using the IDL *Solarsoft* aia_make_eis_raster routine (see EIS Software Note No. 26, Young, 2023b, for more details). An offset correction of X, Y = (+8″, +15″) was found to give the best alignment.

EIS Study Details	
Raster times	02/04/2022 13:05 UT 02/04/2022 14:06 UT 02/04/2022 15:06 UT 02/04/2022 16:07 UT
Study acronym	Flare_SNS_v2 or PRY_flare_3_v2
Study number	555
Raster type	sit-and-stare (SNS)
Window height	152″
Rastering	2″ slit, 225 sets
Exposure time	10s
Exposure delay	5s
Total raster time	1h 0m 20s
Reference spectral window	Fe XII 195.119 Å

Table 7.1: Summary of *Hinode* EIS study details.

Each line used in this study (see Table 7.2) was fitted with a single Gaussian using the eis_auto_fit routine. To increase the signal to noise ratio, 2×2 binning was applied to the data before performing the fitting. This resulted in a 2″ resolution in the y direction and approximately 30 s in the x direction.

7.3.1 Flare Loop Cooling

The temperature evolution of the top of the flare loops can be followed by tracing the plasma emission in lines that cover a sequence of temperatures from $\log(T[\mathrm{K}]) = 7.2$ to $\log(T[\mathrm{K}]) = 5.7$ (see Table 7.2 and Figure 7.3). The loop top is first observed at 13:47 UT in the Fe XXIV line, between 240″ and 260″ in the Y direction. As time progresses, it becomes visible in the successively cooler lines, indicating that the loop top is cooling after the initial heating caused by the flare. After about 14:10 UT, the loop top disappears from the Fe VIII line (the coolest line analysed here), indicating that the loop top has cooled below about $\log(T[\mathrm{K}]) = 5.7$. Overall, the upper part of the flare loops cools down from $\log(T[\mathrm{K}]) = 7.2$ to $\log(T[\mathrm{K}]) = 5.7$ in approximately 23 minutes.

A second, fainter yet distinct feature that can be observed in the EIS data is the southern footpoint of the flare loops (Figure 7.2 indicates where the footpoint crosses the EIS slit). The loop footpoint is first observed at approximately 13:45 UT

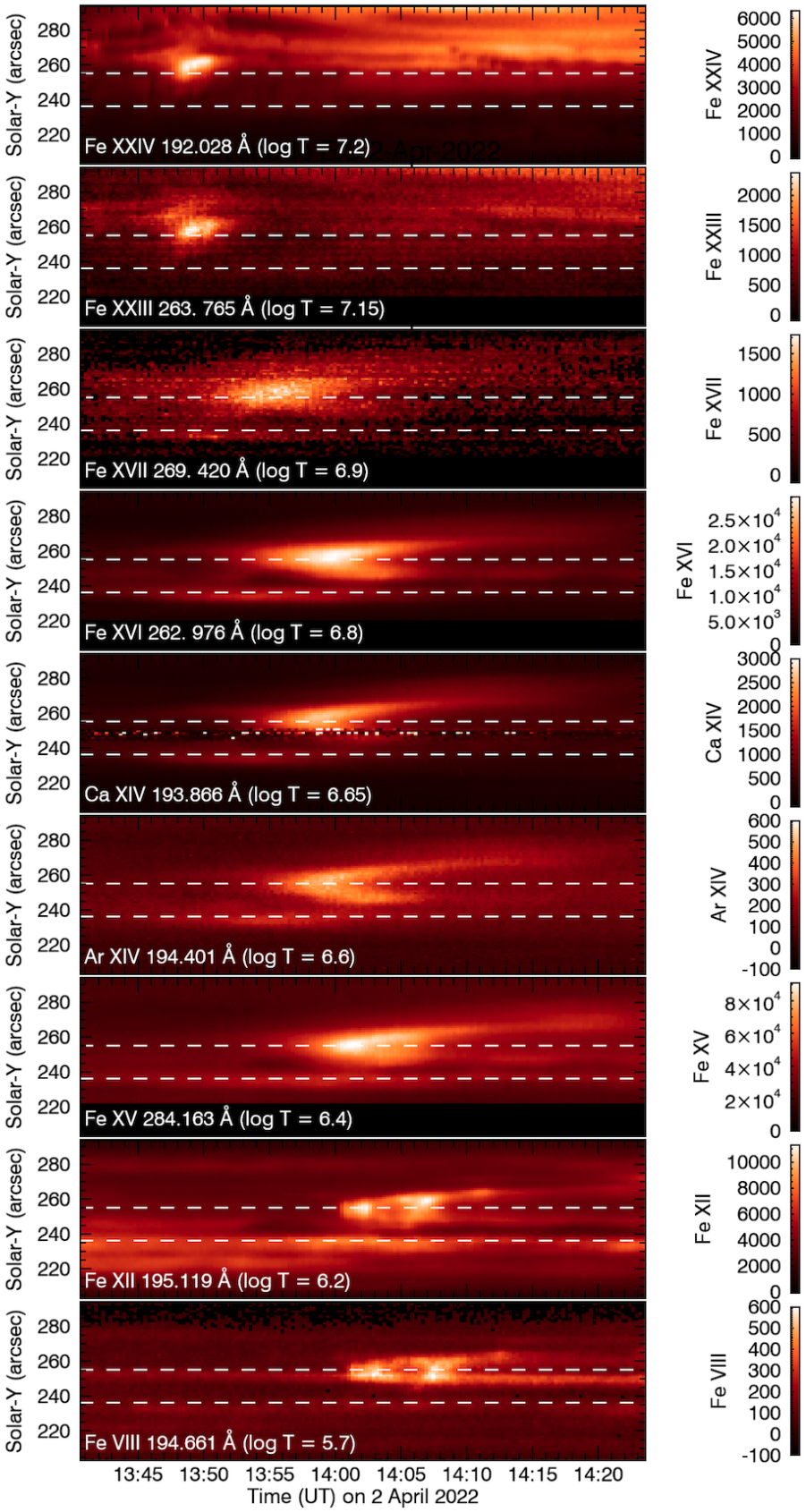

Figure 7.3: Evolution of the flare loop emission intensity (erg cm^{-1} s^{-1} sr^{-1}) for the emission lines listed in Table 7.2. Horizontal dashed lines at Y = 255″ and Y = 235″ indicate the location of the flare loop apex and footpoint respectively.

Spectral line	Wavelength	Log(T_{max}[K])
Fe VIII	194.661 Å	5.7
Fe XII	195.119 Å	6.2
Fe XV	284.163 Å	6.4
Ar XIV	194.401 Å	6.6
Ca XIV	193.866 Å	6.65
Fe XVI	262.976 Å	6.8
Fe XVII	269.420 Å	6.9
Fe XXIII	263.765 Å	7.15
Fe XXIV	192.028 Å	7.2

Table 7.2: Wavelength and formation temperature (T_{max} is the peak of the emission line contribution function; see Section 3.3) for the *Hinode* EIS spectral lines analysed in this study (CHIANTI Database Version 10.1; Dere et al., 1997; Del Zanna et al., 2021).

in the Ar XIV, Ca XIV and Fe XVI lines, between 230″ and 240″ in the y direction. It is likely not hot enough to be visible in the hotter Fe XXIII ($\log(T[\mathrm{K}]) = 7.15$) and Fe XXIV ($\log(T[\mathrm{K}]) = 7.2$) lines and, in the cooler Fe XII and Fe VIII lines the background emission is strong in the region of the footpoint throughout the scan, making it difficult to distinguish the footpoint emission from the background emission. Note that this footpoint feature is not a transition region footpoint, but rather a coronal portion of the loop that is located lower down in the corona, close to the transition region footpoint.

The lifetime of a few lines, i.e. the time their emission is maintained above a given threshold, was calculated by taking cuts through the two features identified above (see Figure 7.4). Here, the threshold is defined as 10% of the peak intensity reached in each given line. For the loop top, the cut was taken at Y = 255″ and for the loop footpoint at Y = 235″ (see dashed white lines in Figure 7.3). The loop top has a relatively short lifetime in Fe XXIV line (6 minutes), longer lifetimes in Ar XIV, Ca XIV and Fe XVI (15-18 minutes) and shorter again in Fe XII and Fe VIII (5-6 minutes). Interestingly, the emission is single peaked in the hotter lines, but double peaked for Fe XII and Fe VIII, with each peak having a lifetime of 5-6 minutes. This could potentially be indicative of two loop populations reaching this temperature at slightly different times. The loop footpoint has significantly longer lifetimes in the lines it is visible in, i.e. Ar XIV, Ca XIV and Fe XVI (32-34 minutes). It is, however,

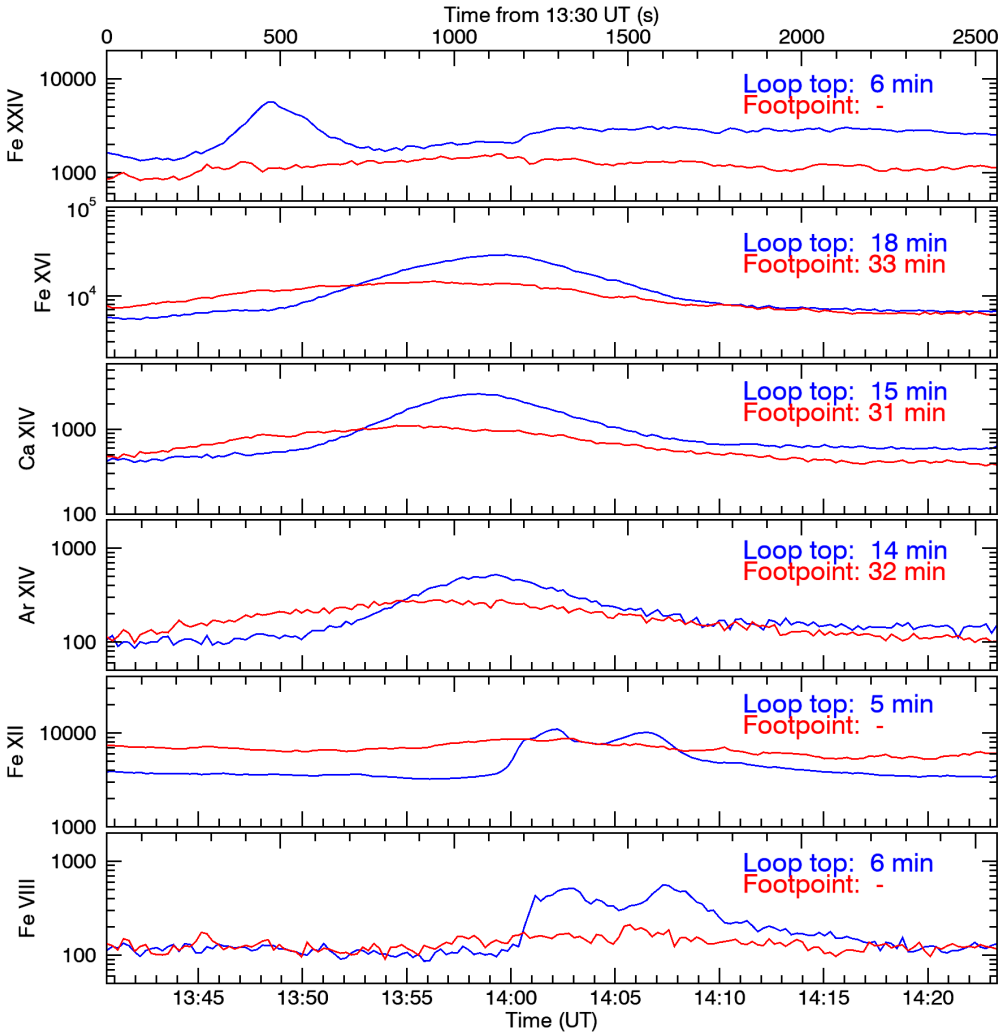

Figure 7.4: Time evolution of the main emission lines' intensity (erg cm^{-1} s^{-1} sr^{-1}) in the loop top at Y = 255″ (blue) and footpoint Y = 235″ (red). The two curves correspond to horizontal cuts at the locations of the dashed lines in Figure 7.3. The lifetime of a given line in a given feature is indicated in the top right corner of each plot, using the same colour code as for the plots.

not visible in Fe XXIV (likely it does not become hot enough), Fe XII (likely covered by the background emission level being very high at this location) or Fe VIII.

It is important to note that, while the loop apex and loop footpoint identified above both belong to the flare loop arcade, they are not part of the same loop. This is a result of the orientation of the EIS slit with respect to the flare loop arcade. The loop apex feature belongs to a smaller loop located slightly lower down, while the loop footpoint feature belongs to the larger loop located slightly higher up. In the

analysis presented here, we rely on the assumption that all loops in the flare loop arcade have a similar evolution and, therefore, the evolution of the two features can be taken to be representative of the loop arcade even if they are not part of the same individual loop. This is a reasonable assumption since all the loops in the flare loop arcade react to the same heating event.

7.3.2 Plasma Composition

To calculate the FIP bias, the Ca XIV 193.87 Å (low FIP, FIP = 6.11 eV) and Ar XIV 194.40 Å (high FIP, FIP = 15.76 eV) emission lines were used. The theoretical formation temperatures for the two lines are $\log(\mathrm{T_{MAX}[K]}) = 6.65$ for Ca XIV 193.87 Å and $\log(\mathrm{T_{MAX}[K]}) = 6.6$ for Ar XIV 194.40 Å (CHIANTI database Version 10.1; Dere et al., 1997; Del Zanna et al., 2021). As discussed in Section 3.3.7, the FIP bias in a pixel is given by:

$$\mathrm{FIP_{bias}} = \frac{I_{\mathrm{Ca\ XIV}}}{I_{\mathrm{Ar\ XIV}}} \times \frac{\int G_{\mathrm{Ar\ XIV}}(N_e,T)\mathrm{DEM}(T)dT}{\int G_{\mathrm{Ca\ XIV}}(N_e,T)\mathrm{DEM}(T)dT}, \tag{7.1}$$

where $I_{\mathrm{Ca\ XIV}}$ and $I_{\mathrm{Ar\ XIV}}$ are the measured intensities of the two spectral lines, $G_{\mathrm{Ar\ XIV}}(N_e,T)$, $G_{\mathrm{Ca\ XIV}}(N_e,T)$ are the theoretical contribution functions (as a function of electron density and temperature) and $\mathrm{DEM}(T)$ is the differential emission measure. Ideally, a DEM analysis would be used to calculate the second term in Equation 7.1. However, there are not enough Fe lines in this study to confidently constrain the DEM, particularly as the plasma goes through a wide range of temperatures as it cools down after the flare. Instead, an isothermal plasma approximation was used to estimate the second term in Equation 7.1. Assuming that, in every pixel, all emission comes from plasma at a single temperature, Equation 7.1 is reduced to:

$$\mathrm{FIP_{bias}} = \frac{I_{\mathrm{Ca\ XIV}}}{I_{\mathrm{Ar\ XIV}}} \Big/ \frac{G_{\mathrm{Ca\ XIV}}(N_e,T)}{G_{\mathrm{Ar\ XIV}}(N_e,T)}, \tag{7.2}$$

where the first term is the observed line ratio and the second term is the theoretical line ratio calculated using CHIANTI at the temperature and density measured using observations. This method is also detailed in Section 3.3.7.2. For the temperature calculation, the Fe XVI 262.984 Å / Fe XV 284.160 Å diagnostic was used. For the

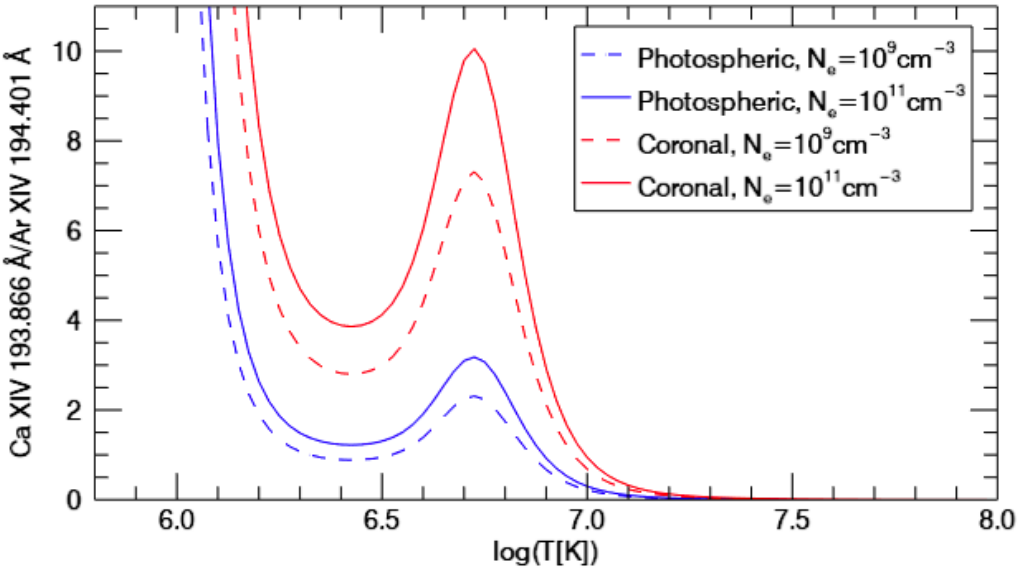

Figure 7.5: The ratio of Ca XIV 193.87 Å and Ar XIV 194.40 Å contribution functions as a function of temperature and density for photospheric (sun_photospheric_2021_asplund) and coronal (sun_coronal_2021_chianti) composition. Computed with CHIANTI (Dere et al., 1997) Version 10.1 (Del Zanna et al., 2021).

density, a constant value of 10^{10}cm^{-3} was assumed everywhere. Calculating the density in every pixel was not possible due to the high noise level for the emission lines involved in the density diagnostics available in the study. Density was calculated in a few macropixels along the loop throughout its lifetime using the Fe XII (186.85 Å + 186.89 Å)/195.12 Å, Ar XIV 187.96 Å/194.40 Å and the Ca XV 181.90 Å/182.86 Å diagnostics after spatially binning the data to reduce noise. The density does vary from one location to another and from one diagnostic to another, but it typically falls in the range of $10^{9.5}$cm^{-3} - 10^{11}cm^{-3}. Therefore, the chosen value of 10^{10}cm^{-3} was considered a reasonable approximation overall. The contribution function dependence on temperature is significantly stronger than its dependence on density (see Figure 7.5). Therefore, the error introduced by assuming a constant density is expected to have minor effects compared to errors introduced by variations in temperature, so assuming a constant density that broadly reflects the density of the structure is considered sufficient.

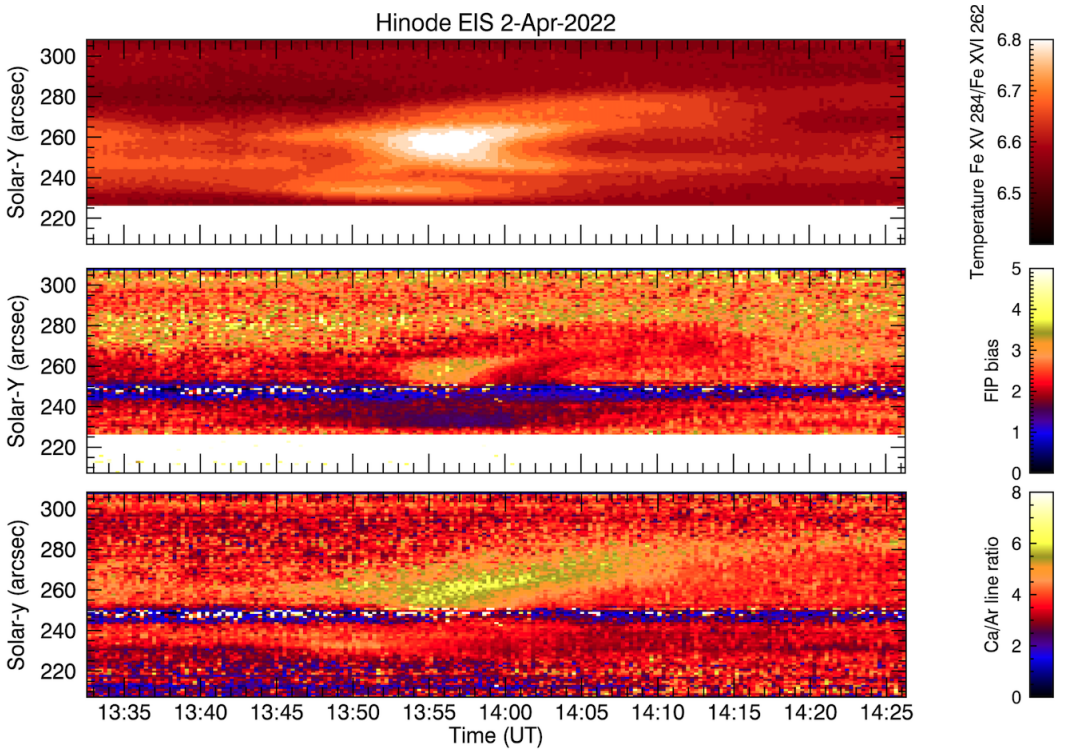

Figure 7.6: Fe XV/Fe XVI temperature (top), FIP bias corrected for temperature effects as described in Section 7.3.2 (middle) and Ca XIV 193.87 Å /Ar XIV 194.40 Å line ratio (bottom) as a function of time along a subsection of the slit focusing on the evolution of the flare loops.

While the FIP bias was calculated everywhere in the submap shown in Figure 7.6, the likely reliable values are in the region where there is enough emission from the lines used (Ca XIV, Ar XIV, Fe XV and Fe XVI), i.e. when the structure has cooled to a temperature in the range $\log(T[\mathrm{K}]) = 6.4 - 6.8$. Unfortunately, this means that we cannot make plasma composition measurements at the top of the flare loops right after the flare around 13:45 UT, when the temperature is still very high. However, after 13:51 UT, the loop top cools down enough for plasma composition measurements to be possible with this diagnostic. Fortunately, the loop footpoint is at the right temperature for composition measurements. The FIP bias map (middle panel of Figure 7.6) shows significantly different plasma composition in the loop top and the loop footpoint. While the loop top has coronal composition (in agreement with the findings of Doschek et al., 2015, 2018) with a FIP bias in the range of 3.5-4, the footpoint has much lower values of approximately 1 (in agreement with the findings

of Doschek et al., 2018, who found FIP bias decreasing from the loop apex towards the footpoint and concluded that the plasma composition at the footpoint should be photospheric or very close to photospheric). It is also interesting that the footpoint temperature increases first at approximately 13:47 UT, but its plasma composition only becomes clearly photospheric at around 13:54 UT. This could be an indication of chromospheric evaporation due to flare heating, as previously suggested by Warren (2014). The difference between both the FIP bias and line lifetimes in the loop top and footpoint naturally raise the question about links between plasma composition and radiative cooling.

7.4 Radiative Cooling Modelling

The radiative loss, i.e. total radiated power emitted from an optically thin plasma, is given by:

$$L_r = N_e N_H Q(T_e, N_e), \tag{7.3}$$

where N_e and N_H are the electron and hydrogen densities, respectively, T_e is the electron temperature and $Q(T_e, N_e)$ is the radiative loss function. The radiative loss function is essentially a sum of all the line contributions radiating at a temperature T. The main contributions are bound-bound line emission and continuum radiation, i.e. free-free emission and free-bound radiative recombination. In the temperature range $\log(T[\mathrm{K}]) = 4.5 - 7.0$, bound-bound emission from abundant elements such as C, O, Si and Fe dominates, with O having the highest contribution around $\log(T[\mathrm{K}]) \approx 5.3$ and Fe around $\log(T[\mathrm{K}]) \approx 6.0$. For $\log(T[\mathrm{K}]) \gtrsim 7.0$, however, continuum processes dominate (see e.g. Aschwanden, 2004). The radiative loss function depends on the plasma composition of the radiating plasma, particularly in the temperature range where it is dominated by emission from low-FIP elements. Figure 7.7 shows the variability of the radiative loss function with temperature for photospheric and coronal composition, as calculated by CHIANTI Version 10.1 (Dere et al., 1997; Del Zanna et al., 2021). The two functions are significantly different around $\log(T[\mathrm{K}]) \approx 6.0$, where emission from Fe (low-FIP) lines dominates

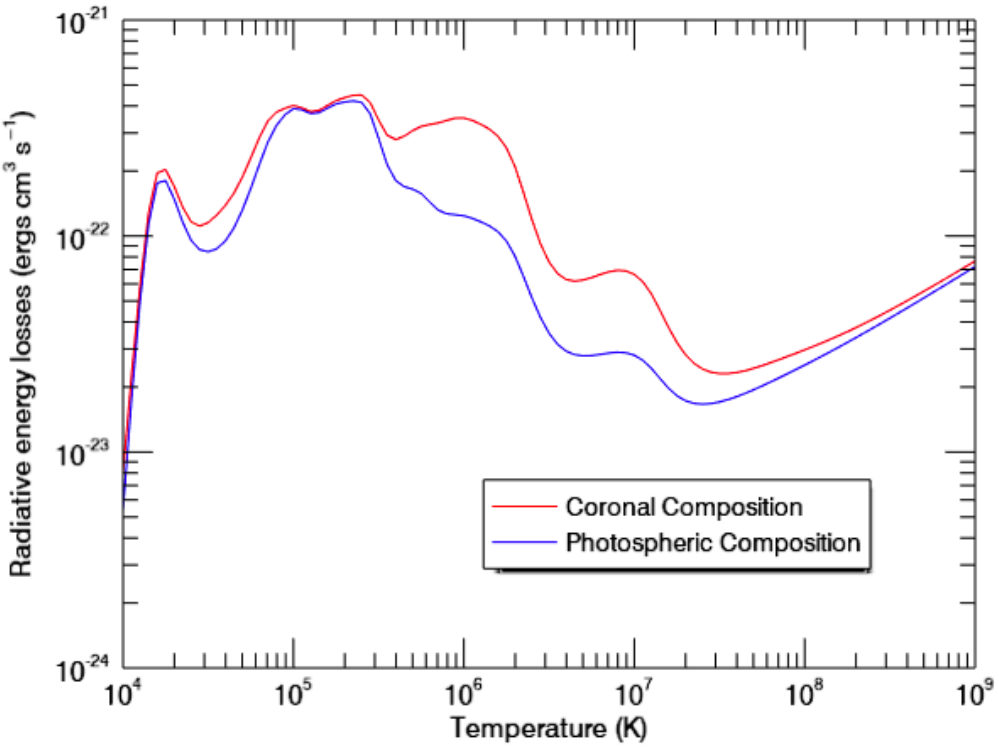

Figure 7.7: Radiative energy losses, $Q(T_e, N_e)$, as a function of electron temperature in the case of plasma with photospheric (sun_photospheric_2021_asplund) and coronal (sun_coronal_2021_chianti) composition. Computed with the CHIANTI (Dere et al., 1997) Version 10.1 (Del Zanna et al., 2021) rad_loss function for a plasma with a default density of 10^{10}cm^{-3}.

the radiative losses, but the differences are much weaker in the temperature ranges where emission from O (high-FIP) lines or continuum emission dominate.

7.4.1 The EBTEL Model

The effect of a varying radiative cooling function on flare loops can be explored using the enthalpy-based thermal evolution of loops (EBTEL) model (Klimchuk et al., 2008; Cargill et al., 2012a,b). EBTEL is a 0D hydrodynamic model which simulates the cooling process in a loop in response to a heating event, predicting the evolution of average loop parameters (e.g. temperature, density, pressure) with time. Using these loop parameters, synthetic line emission can be derived and compared to observations.

In static equilibrium conditions, the energy input brought by coronal heating must be equal to the energy losses via radiative and conductive cooling. At equilibrium, less than half of the energy losses happen via radiation to outer space (radiative cooling), and the remainder of the energy is conducted down to the transition region (conductive cooling) where it can be radiated more efficiently (Klimchuk et al., 2008). The corona, however, is not in static equilibrium as the heating rate does change in time. If the timescale of the variability is shorter than the loop lifetime, then this change in the heating rate affects the heat transfer between the coronal and the transition region parts of the loop. If the coronal heating rate increases (say as a result of a heating event), the coronal temperature increases, so the heat flux conducted down to the transition region increases as well and heats up the plasma here. This conductive cooling is particularly important right after the heating event. The transition region, however, is not able to radiate all the extra energy, so the pressure increases, creating a upwards flow of hot plasma. This process is called chromospheric evaporation. Conversely, if the coronal heating rate decreases, the coronal temperature decreases, so the downwards heat flux decreases, and the transition region plasma cools down. As a result, transition region pressure decreases and, when pressure gradients drop to sub-hydrostatic values, plasma starts to drain from the coronal part of the loop into the transition region. This process is called coronal condensation.

EBTEL models the heat transfer and plasma flows between the corona and the transition region as a result of a changing coronal heating rate function chosen by the user. The main idea behind EBTEL is to equate an enthalpy upwards flux of expanding plasma (or downwards flux of condensing plasma) with any excess or deficit in the heat flux relative to the transition region radiation loss rate (Klimchuk et al., 2008). This is done by solving simplified versions of the hydrodynamic equations that treat field-aligned average values of temperature, pressure, and density along the loop. EBTEL is necessarily a very simplified model. It is not spatially resolved, so it is not able to capture any change in the plasma parameters along the loop. The 0D aspect of the model also means that both coronal heating and radiative

losses are assumed to be spatially invariant. This is an approximation, since both of these can vary spatially which might affect the loop response to heating. The major advantage of using EBTEL, however, is that it is orders of magnitude less computationally expensive than other multi-dimensional MHD models, while still being successful at reproducing key aspects of the coronal and transition region evolution. In particular, for the aspect investigated in this work, i.e. the effect of variable plasma composition on the radiative cooling of flare loops, EBTEL is considered sufficient.

7.4.2 Model Simulations

The input parameters for the EBTEL simulations are the loop length, a radiative loss rate function and a heating function. The loop length was estimated from the SDO AIA EUV images to be in the range of $24-65$ Mm. Two radiative loss functions were considered: one assuming the loop has plasma with photospheric composition and the other with coronal composition (these two functions are shown in Figure 7.7). The heating function was chosen such that the simulated temperature and density evolution of the loop plasma matched the observations, following the method of Brooks (2018). A strong heating event of 0.023 erg $\mathrm{cm}^{-3}\mathrm{s}^{-1}$ was assumed to start 200 s and stop 450 s after the start of the simulation. The amplitude and length of this heating event were chosen such that the simulated loop reaches a temperature of $\log(\mathrm{T[K]}) \approx 7.2$ (the formation temperature of Fe XXIV) and stays at this temperature for a duration of time similar to the lifetime of the observed Fe XXIV line (see Figure 7.4). EBTEL also has an ongoing heat input, which, in these simulations, was assumed to have a rate of 5×10^{-6} erg $\mathrm{cm}^{-3}\mathrm{s}^{-1}$. This background heating rate was chosen such that, in the absence of a strong heating event, it is able to maintain the loop at a quiet Sun temperature of $\log(\mathrm{T[K]}) \approx 6.0$.

As the loop cools down, emission increases in progressively cooler lines. Figure 7.8 shows the simulated intensity evolution for the *Hinode* EIS lines listed in Table 7.2. Lifetimes for each of the lines are defined as the time spent above 10% of the maximum intensity of the line, the same as the lifetimes of the observed EIS lines to allow for comparison.

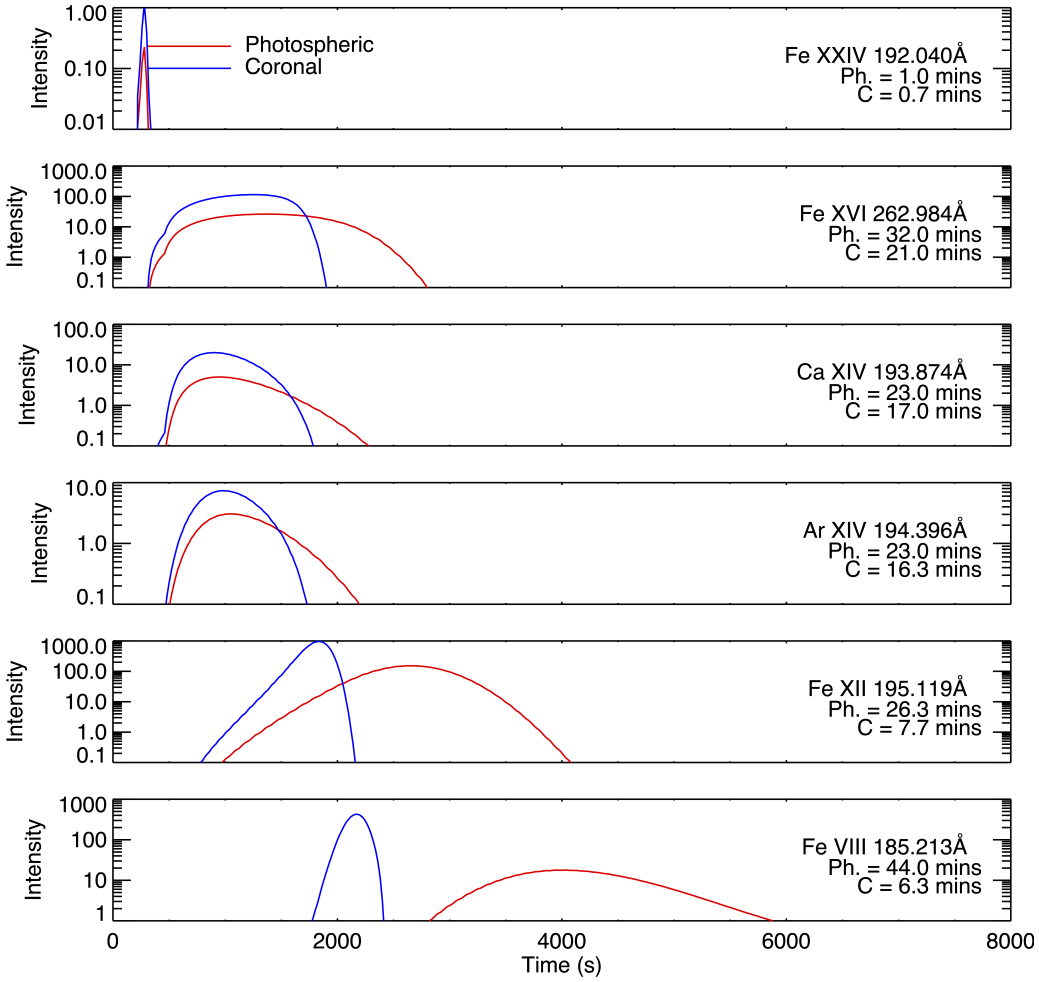

Figure 7.8: Synthetic intensity (erg cm^{-1} s^{-1} sr^{-1}) evolution of the emission lines analysed in Figure 7.4 computed using an EBTEL simulation of a heating event in a single loop strand. This is investigated in the case of coronal (blue) and photospheric (red) plasma composition along the loop, keeping all other loop parameters fixed. The lifetime of a given line in each plasma composition case is provided on the right hand side of each plot.

Simulation results presented in Figure 7.8 show that, in the coronal composition case, line intensities are higher and line lifetimes are shorter, i.e. the loop cools down faster. Conversely, in the photospheric composition case, line intensities are lower and line lifetimes are longer, i.e. the loop cools down slower. The difference in cooling times can also be observed in the time taken for the loop to emit in the Fe VIII line: the coronal composition loop brightens through Fe VIII and cools down to temperatures below $\log(T[\mathrm{K}]) = 5.7$ after approximately 2300s, while the photospheric composition one only reaches this stage after approximately 5500s. The difference in line lifetimes is barely noticeable for the very hot lines (Fe XXIV here), but progressively increases for cooler lines. This can likely be explained by the role of Fe in modulating the radiative cooling function. At higher temperatures ($\log(T[\mathrm{K}]) \gtrsim 7.0$), the continuum emission dominating the radiative cooling function is not dependent on composition (Aschwanden, 2004), so the lifetimes in the two composition cases are very similar. As the loop cools down, bound-bound emission, mainly from Fe lines, begins to dominate (Aschwanden, 2004). As Fe is a low-FIP element, it will be overabundant in the coronal composition case which increases the emission and also increases the cooling rate which speeds up the cooling process (see also Figure 7.7).

A direct comparison between the simulated and observed line lifetimes is given in Table 7.3. The pattern of the observed loop apex line lifetimes is similar to the predicted one in the coronal composition case: lifetimes are relatively short for Fe XXIV, longer for Ca XIV, Ar XIV and Fe XVI, and shorter again for Fe XII and Fe VIII. The FIP bias at the loop top is in the range 3-4, similar to the FIP bias value of 3 assumed for the EBTEL coronal composition case. Comparing the pattern in the observed loop footpoint line lifetimes and the predicted one in the photospheric composition case is more difficult since the footpoint is not visible in the very hot line (Fe XXIV) or the cool ones (Fe XII and Fe VIII). However, in the lines where it is visible (Ca XIV, Ar XIV and Fe XVI), its lifetimes are comparable to those predicted by EBTEL and consistently longer than those of the loop apex. This suggests that the different

	EIS observations		EBTEL simulations	
	Loop apex	Loop footpoint	Coronal comp.	Photospheric comp.
Fe XXIV	6 min	-	0.7 min	1 min
Fe XIV	18 min	33 min	21 min	32 min
Ca XIV	15 min	31 min	17 min	23 min
Ar XIV	14 min	32 min	16 min	23 min
Fe XII	5 min	-	8 min	26 min
Fe VIII	6 min	-	7 min	44 min

Table 7.3: Direct comparison between the line lifetimes calculated from the EIS observations (see Figure 7.4) for the loop apex (coronal composition) and footpoint (photospheric composition) and those predicted by the EBTEL simulations (see Figure 7.8) for plasma with coronal and photospheric composition.

plasma composition at the loop top and footpoint could be responsible for creating a spatially variable radiative cooling function along the flare loops.

It is important to keep in mind that conductive cooling also varies along the coronal loop, which could lead to differences in the observed cooling times of the loop apex and loop footpoint as well. Conduction is stronger at the loop footpoint than the loop apex since the temperature gradient is highest lower in the atmosphere. The effects of spatially varying conductive cooling on the cooling times measured in this work were not investigated since neither the observations, nor the simulations offered the possibility to analyse changes in temperature along the loop. However, conduction is typically significant only in the early stages of the cooling process. Right after the heating event, the coronal loop cooling is dominated by conduction to the transition region. As the loop temperature drops and the density rises (as a result of chromospheric evaporation flows), radiation becomes progressively more important and eventually takes over from conduction as the dominant cooling mechanism. The observations and simulations presented here focus on the decay phase of the flare when radiative cooling likely dominates.

Note that the IDL EBTEL implementation used here only solves the single fluid equations. The C++ implementation, ebtel++, treats the electron and ion populations separately. This might yield slightly different results for plasma above roughly $\log(T[\mathrm{K}]) = 6.7$, i.e. affecting the simulated Fe XXIV and partially Fe XVI.

Below $\log(T[\mathrm{K}]) = 6.7$, however, i.e. where the observed trends are the strongest, there is little or no difference between the two-fluid and single-fluid models.

7.5 Summary and Discussion

This work investigates the effect of plasma composition on the radiative cooling of flare loops. High-cadence *Hinode* EIS spectroscopic observations indicate coronal/photospheric composition at the loop apex/footpoint (in agreement with the findings of Doschek et al., 2018), as well as associated shorter/longer loop cooling times. This is in agreement with simulations from the EBTEL hydrodynamic model, which predicts that an increase in the FIP bias leads to faster cooling of the flare loop. EBTEL simulations of the radiative cooling of a loop following a heating event with the properties of the M-class flare observed by EIS show loop cooling times similar to those of the loop apex/footpoint observations if the assumed composition of the loop is coronal/photospheric.

Of course, direct comparisons between the EIS observations and EBTEL simulations are done under the assumption that the observed loop top and loop footpoint belong to the same loop structure. As it is clear from Figure 7.2, this flare arcade is made of multiple loops which cool down and shrink. In fact, as the loop structure is at the limb, EIS is likely looking down the loop arcade axis capturing emission from multiple loops. Since in an optically thin plasma the measured emission is an integral of the emission created by different loops along the line of sight, it is impossible to identify the exact loop that the analysed emission originates from (both for the loop apex and loop top). It is also clear that the loop apex and loop footpoint features identified in this work belong to different loops (see Figure 7.2). In addition, it is also likely that the cooling structure referred to here as the loop top might actually be a series of snapshots of consecutive loop strands that reconnect and shrink through the EIS field of view, rather than one single loop. However, the cooling time for loops with similar properties is expected to be broadly the same.

The plasma composition calculations rely on the significant assumption that the plasma observed at a particular location and given time is isothermal. This

assumption enables us to calculate the plasma temperature and use it to make an estimate of the FIP bias. Of course, in reality, there will be plasma parcels at different temperatures along the line of sight. Further work will include carrying out a DEM calculation to test and consolidate these results. However, the limited number of lines available in the EIS study makes it particularly challenging to place enough constraints on the DEM, so obtaining a reliable result is not straightforward.

In addition, some studies suggest that the plasma composition in flares changes rapidly due to chromospheric evaporation (e.g. Warren, 2014; Mondal et al., 2021; Nama et al., 2023). While it is yet unclear whether it is the composition of the whole loop that changes rapidly or just the flare loop footpoints, the upflow of evaporated photospheric plasma is likely to affect the composition of the loop apex as well. No significant changes are observed here, but this could be due to limitations in plasma composition diagnostics. The Ca XIV/Ar XIV diagnostic can be used to detect plasma composition changes in plasma at temperatures around $\log(T[\mathrm{K}]) = 6.3 - 6.8$. This means that, although the flare loops are observed with high cadence throughout the whole flare, the Ca XIV/Ar XIV diagnostic will likely not detect potential plasma composition changes due to evaporation in the impulsive phase of the flare because the plasma is simply too hot to produce enough emission in these lines.

A simple model is used here, assuming a single step function-like heating event on a single strand. In reality, the heating function is likely more similar to a succession of smaller energy releases as more and more field lines are pushed into the reconnection region. And, of course, each loop might be composed of more than one strand. In addition, the model is 0D, so it does not allow for spatially variable loop properties (composition, temperature, density, etc.). However, observations suggest that loop parameters (mainly plasma temperature and composition) are different at the apex and the footpoint, so they are likely changing along the loop.

Nevertheless, this work highlights the potentially tight link between plasma composition and the radiative cooling process of coronal loops. This is particularly important in flare loops, where chromospheric evaporation changes the composition rapidly at the loop footpoint and the time taken for the flare loop to reach a

homogenuous plasma composition appears to be similar to/shorter than the loop cooling times, so drastic changes in composition along the loop can result in different cooling speeds in different parts of the loop. Could these differences then create strong enough temperature gradients and associated heat flows along the loop? This work highlights the potential for and motivation to explore this further using spatially resolved simulations (e.g. RADYN; Carlsson and Stein, 1992; Allred et al., 2005) and observations with more available lines.

Chapter 8

General Conclusions and Future Work

8.1 General Conclusions

The work in this thesis investigates the potential drivers of plasma composition changes in the solar corona, as well as the effects these composition variations can have on other processes. In particular, I explore the impact of active region evolution, magnetic field properties and wave activity on observed plasma composition patterns, and the effects that these variations have on the radiative cooling process of flare loops. The work in this thesis uses EUV spectroscopy from *Hinode* EIS and imaging primarily from SDO AIA and HMI.

Chapter 5 explores how the evolution of active regions affects their plasma composition, particularly as a result of how their magnetic flux density changes. Results indicate that active regions that are at later stages in their decay and show lower magnetic flux density also have lower overall FIP bias values. The decayed active regions do, however, show a wider distribution of FIP bias values, which can be an indication of different processes affecting the plasma composition differently in different parts of the active region. In particular, plasma mixing as a result of active region loops reconnecting and forming connections with the surrounding solar structures is likely to dominate in this stage.

Chapter 6 explores the link between different plasma composition patterns in the solar corona and the type of wave activity that could create them according to the ponderomotive force model. According to the model, the main difference in the plasma composition patterns driven by resonant and non-resonant waves is the behaviour of S. The findings in this thesis show observational evidence in support of this idea, suggesting that resonant waves deposit their energy at the top of the chromosphere and do not drive a S enhancement in the corona. On the other hand, non-resonant waves deposit their energy lower down in the chromosphere and drive a moderate S enhancement, along with stronger enhancement of low-FIP elements than in the resonant waves' case.

Chapter 7 investigates the effects of plasma composition variations on the radiative cooling process of flare loops. Spectroscopic observations from *Hinode* EIS suggest that, after the peak of the flare, plasma at the loop apex has coronal composition and cools down faster, while plasma at the loop footpoint has photospheric composition and cools down slower. This is in agreement with predictions of the EBTEL model simulating the radiative cooling process of the plasma along a loop with coronal or photospheric composition. This is of general importance for the corona, as plasma composition variations are likely to also have effects on the radiative cooling of quiescent loops.

8.2 Future Work

The work in this thesis can naturally be extended in a few directions. These are outlined below.

8.2.1 Origin of the Plasma Composition Changes Wave Driver

Chapter 6 explores the link between plasma composition patterns in the corona and the driver of this process: wave activity and the height at which these waves deposit their energy in the chromosphere. However, the question of the origin of these waves remains. Observations suggest photospheric motions are more likely to excite non-resonant waves in the corona. However, according to the ponderomotive force model, these waves do not have high enough amplitudes to drive the

plasma composition patterns we observe. This aspect should be investigated in more detail in a separate study focusing on wave activity and constraints that wave signatures can provide for the model. This is particularly relevant for solar wind studies. In open field, it is only non-resonant waves that could drive fractionation, so understanding where they might originate from would be an important step both for better understanding the fractionation process, but also how it is linked to solar wind acceleration.

8.2.2 Plasma Composition as a Tool for Studying the Solar Wind

Connecting the Sun to the heliosphere is an area of active research. Plasma composition signatures can be a powerful tool, along with information about the magnetic configuration, for linking solar wind plasma measured in situ to its source region on the Sun (see e.g. Brooks and Warren, 2011; Stansby et al., 2020). As well as providing a tracer for the solar wind, the processes that drive changes in the elemental composition are linked to those responsible for the heating and acceleration of the solar wind and could help distinguish between different models for solar wind acceleration (see Section 2.4.4). While wave activity, turbulence and magnetic field expansion factor are key in both driving plasma composition changes and heating and accelerating the solar wind, a direct connection remains elusive.

8.2.3 Effects of Plasma Composition Variations in Solar Flares

Chapter 7 highlights the role of plasma composition variations in modelling the radiative cooling process of plasma along coronal loops. This could be particularly important in flare loops, where chromospheric evaporation brings up plasma with photospheric composition at the loop footpoints, but the loop apex maintains its coronal composition. Since this strong difference in plasma composition leads to different cooling rates at the loop apex and footpoint, this could create heat flows along the loops, in addition to those already explored in simulations and theoretical models. This is particularly important in flare loops where the cooling timescales are shorter than in quiescent conditions. This aspect should be investigated in more detail using spatially resolved simulations.

References

Abbo, L., Ofman, L., Antiochos, S. K., Hansteen, V. H., Harra, L., Ko, Y.-K., Lapenta, G., Li, B., Riley, P., Strachan, L., von Steiger, R., and Wang, Y.-M. (2016). Slow Solar Wind: Observations and Modeling. *Space Science Reviews*, 201(1):55–108.

Allred, J. C., Hawley, S. L., Abbett, W. P., and Carlsson, M. (2005). Radiative Hydrodynamic Models of the Optical and Ultraviolet Emission from Solar Flares. *The Astrophysical Journal*, 630:573–586.

Anders, E. and Grevesse, N. (1989). Abundances of the elements: Meteoritic and solar. *Geochimica et Cosmochimica Acta*, 53(1):197–214.

Antia, H. M., Bhatnagar, A., and Ulmschneider, P. (2003). *Lectures on Solar Physics*, volume 619.

Antiochos, S. K. (1994). The physics of coronal closed-filed structures. *Advances in Space Research*, 14(4):139–148.

Arge, C. and Mullan, D. (1998). Modelling of Magnetic Interactions in Partially-Ionized Gas: Application to the FIP Effect. *Solar Physics*, 182(2):293–332.

Aschwanden, M. J. (2004). *Physics of the Solar Corona. An Introduction*.

Asplund, M., Amarsi, A. M., and Grevesse, N. (2021). The Chemical Make-up of the Sun: A 2020 Vision. *Astronomy & Astrophysics*, 653:A141.

Asplund, M., Grevesse, N., Sauval, A. J., and Scott, P. (2009). The Chemical Composition of the Sun. *Annual Review of Astronomy and Astrophysics*, 47:481–522.

Avrett, E. H. and Loeser, R. (2008). Models of the Solar Chromosphere and Transition Region from SUMER and HRTS Observations: Formation of the Extreme-Ultraviolet Spectrum of Hydrogen, Carbon, and Oxygen. *The Astrophysical Journal Supplement Series*, 175(1):229.

Bahcall, J. N. and Ulrich, R. K. (1988). Solar Models, Neutrino Experiments, and Helioseismology. *Reviews of Modern Physics*, 60:297–372.

Baker, D. (2011). *Drivers of solar coronal dynamics*. Doctoral Thesis, UCL (University College London).

Baker, D., Brooks, D. H., Démoulin, P., van Driel-Gesztelyi, L., Green, L. M., Steed, K., and Carlyle, J. (2013). Plasma Composition in a Sigmoidal Anemone Active Region. *The Astrophysical Journal*, 778(1):69.

Baker, D., Brooks, D. H., Démoulin, P., Yardley, S. L., Driel-Gesztelyi, L. v., Long, D. M., and Green, L. M. (2015). FIP Bias Evolution in a Decaying Active Region. *The Astrophysical Journal*, 802(2):104.

Baker, D., Brooks, D. H., van Driel-Gesztelyi, L., James, A. W., Démoulin, P., Long, D. M., Warren, H. P., and Williams, D. R. (2018). Coronal Elemental Abundances in Solar Emerging Flux Regions. *The Astrophysical Journal*, 856(1):71.

Baker, D., Driel-Gesztelyi, L. v., Brooks, D. H., Démoulin, P., Valori, G., Long, D. M., Laming, J. M., To, A. S. H., and James, A. W. (2020). Can Subphotospheric Magnetic Reconnection Change the Elemental Composition in the Solar Corona? *The Astrophysical Journal*, 894(1):35.

Baker, D., Driel-Gesztelyi, L. v., Brooks, D. H., Valori, G., James, A. W., Martin Laming, J., Long, D. M., Démoulin, P., Green, L. M., Matthews, S. A., Oláh, K., and Kővári, Z. (2019). Transient Inverse-FIP Plasma Composition Evolution within a Solar Flare. *The Astrophysical Journal*, 875(1):35.

Baker, D., Green, L. M., Brooks, D. H., Démoulin, P., van Driel-Gesztelyi, L., Mihailescu, T., To, A. S. H., Long, D. M., Yardley, S. L., Janvier, M., and Valori, G. (2022). Evolution of Plasma Composition in an Eruptive Flux Rope. *The Astrophysical Journal*, 924(1):17.

Baker, D., Mihailescu, T., Démoulin, P., Green, L. M., van Driel-Gesztelyi, L., Valori, G., Brooks, D. H., Long, D. M., and Janvier, M. (2021a). Plasma Upflows Induced by Magnetic Reconnection Above an Eruptive Flux Rope. *Solar Physics*, 296(6):103.

Baker, D., Stangalini, M., Valori, G., Brooks, D. H., To, A. S. H., van Driel-Gesztelyi, L., Démoulin, P., Stansby, D., Jess, D. B., and Jafarzadeh, S. (2021b). Alfvénic Perturbations in a Sunspot Chromosphere Linked to Fractionated Plasma in the Corona. *The Astrophysical Journal*, 907(1):16.

Basu, S. and Antia, H. M. (2004). Constraining Solar Abundances Using Helioseismology. *The Astrophysical Journal*, 606(1):L85.

Benz, A. O. (2008). Flare Observations. *Living Reviews in Solar Physics*, 5(1):1.

Bochsler, P. (2009). Composition of matter in the heliosphere. 257:17–28. Proceedings of the International Astronomical Union, IAU Symposium.

Boerner, P., Edwards, C., Lemen, J., Rausch, A., Schrijver, C., Shine, R., Shing, L., Stern, R., Tarbell, T., Title, A., Wolfson, C. J., Soufli, R., Spiller, E., Gullikson, E., McKenzie, D., Windt, D., Golub, L., Podgorski, W., Testa, P., and Weber, M. (2012). Initial Calibration of the Atmospheric Imaging Assembly (AIA) on the Solar Dynamics Observatory (SDO). *Solar Physics*, 275(1):41–66.

Bray, R. J., Cram, L. E., Durrant, C., and Loughhead, R. E. (1991). *Plasma Loops in the Solar Corona*. Cambridge Astrophysics. Cambridge University Press.

Brooks, D. H. (2018). A Diagnostic of Coronal Elemental Behavior During the Inverse FIP Effect in Solar Flares. *The Astrophysical Journal*, 863:140.

Brooks, D. H., Baker, D., Van Driel-Gesztelyi, L., and Warren, H. P. (2017). A Solar Cycle Correlation of Coronal Element Abundances in Sun-as-a-Star Observations. *Nature Communications*, 8(1):1–7.

Brooks, D. H., Baker, D., van Driel-Gesztelyi, L., Warren, H. P., and Yardley, S. L. (2022a). Detection of Stellar-like Abundance Anomalies in the Slow Solar Wind. *The Astrophysical Journal*, 930:L10.

Brooks, D. H., Janvier, M., Baker, D., Warren, H. P., Auchère, F., Carlsson, M., Fludra, A., Hassler, D., Peter, H., Müller, D., Williams, D., Cuadrado, R. A., Barczynski, K., Buchlin, E., Caldwell, M., Fredvik, T., Giunta, A., Grundy, T., Guest, S., Haberreiter, M., Harra, L., Leeks, S., Parenti, S., Pelouze, G., Plowman, J., Schmutz, W., Schuehle, U., Sidher, S., Teriaca, L., Thompson, W. T., and Young, P. R. (2022b). Plasma Composition Measurements in an Active Region from Solar Orbiter/SPICE and Hinode/EIS. *The Astrophysical Journal*, 940(1):66.

Brooks, D. H., Ugarte-Urra, I., and Warren, H. P. (2015). Full-Sun Observations for Identifying the Source of the Slow Solar Wind. *Nature Communications*, 6(1):5947.

Brooks, D. H. and Warren, H. P. (2011). Establishing a Connection Between Active Region Outflows and the Solar Wind: Abundance Measurements with EIS/Hinode. *The Astrophysical Journal*, 727(1):L13.

Brooks, D. H. and Yardley, S. L. (2021). The Source of the Major Solar Energetic Particle Events from Super Active Region 11944. *Science Advances*, 7(10):1–11.

Brosius, J. W. (2013). Chromospheric Evaporation in Solar Flare Loop Strands Observed with the Extreme-Ultraviolet Imaging Spectrometer on Board Hinode. *The Astrophysical Journal*, 762:133.

Brown, C. M., Feldman, U., Seely, J. F., Korendyke, C. M., and Hara, H. (2008). Wavelengths and Intensities of Spectral Lines in the 171–211 and 245–291 Å Ranges from Five Solar Regions Recorded by the Extreme-Ultraviolet Imaging

Spectrometer (EIS) on Hinode. *The Astrophysical Journal Supplement Series*, 176(2):511–535.

Bø, I. M. T., Esser, R., and Lie-Svendsen, O. (2013). Effect of Coulomb Collisions on the Gravitational Settling of Low and High First Ionization Potential Elements. *The Astrophysical Journal*, 769(1):60.

Caffau, E., Ludwig, H. G., Steffen, M., Freytag, B., and Bonifacio, P. (2011). Solar Chemical Abundances Determined with a CO5BOLD 3D Model Atmosphere. *Solar Physics*, 268:255–269.

Cargill, P. J., Bradshaw, S. J., and Klimchuk, J. A. (2012a). Enthalpy-Based Thermal Evolution of Loops. II. Improvements to the Model. *The Astrophysical Journal*, 752:161.

Cargill, P. J., Bradshaw, S. J., and Klimchuk, J. A. (2012b). Enthalpy-Based Thermal Evolution of Loops. III. Comparison of Zero-dimensional Models. *The Astrophysical Journal*, 758:5.

Carlsson, M. and Stein, R. F. (1992). Non-LTE Radiating Acoustic Shocks and CA II K2V Bright Points. *The Astrophysical Journal*, 397:L59.

Choudhary, D. P., Gosain, S., Gopalswamy, N., Manoharan, P. K., Chandra, R., Uddin, W., Srivastava, A. K., Yashiro, S., Joshi, N. C., Kayshap, P., Dwivedi, V. C., Mahalakshmi, K., Elamathi, E., Norris, M., Awasthi, A. K., and Jain, R. (2013). Flux Emergence, Flux Imbalance, Magnetic Free Energy and Solar Flares. *Advances in Space Research*, 52:1561–1566.

Ciaravella, A., Raymond, J. C., Li, J., Reiser, P., Gardner, L. D., Ko, Y.-K., and Fineschi, S. (2002). Elemental Abundances and Post-Coronal Mass Ejection Current Sheet in a Very Hot Active Region. *The Astrophysical Journal*, 575(2):1116.

Culhane, J. L., Harra, L. K., James, A. M., Al-Janabi, K., Bradley, L. J., Chaudry, R. A., Rees, K., Tandy, J. A., Thomas, P., Whillock, M. C. R., Winter, B., Doschek, G. A., Korendyke, C. M., Brown, C. M., Myers, S., Mariska, J., Seely,

J., Lang, J., Kent, B. J., Shaughnessy, B. M., Young, P. R., Simnett, G. M., Castelli, C. M., Mahmoud, S., Mapson-Menard, H., Probyn, B. J., Thomas, R. J., Davila, J., Dere, K., Windt, D., Shea, J., Hagood, R., Moye, R., Hara, H., Watanabe, T., Matsuzaki, K., Kosugi, T., Hansteen, V., and Wikstol, (2007). The EUV Imaging Spectrometer for Hinode. *Solar Physics*, 243(1):19–61.

Dahlburg, R. B., Laming, J. M., Taylor, B. D., and Obenschain, K. (2016). Ponderomotive Acceleration in Coronal Loops. *The Astrophysical Journal*, 831:160.

Del Zanna, G. (2013a). The Multi-Thermal Emission in Solar Active Regions. *Astronomy & Astrophysics*, 558:A73.

Del Zanna, G. (2013b). A Revised Radiometric Calibration for the Hinode/EIS Instrument. *Astronomy & Astrophysics*, 555:A47.

Del Zanna, G., Dere, K. P., Young, P. R., and Landi, E. (2021). CHIANTI—An Atomic Database for Emission Lines. XVI. Version 10, Further Extensions. *The Astrophysical Journal*, 909(1):38.

Del Zanna, G. and Ishikawa, Y. (2009). Benchmarking Atomic Data for Astrophysics: Fe XVII EUV Lines. *Astronomy & Astrophysics*, 508(3):1517–1526.

Del Zanna, G. and Mason, H. E. (2014). Elemental Abundances and Temperatures of Quiescent Solar Active Region Cores from X-ray Observations. *Astronomy & Astrophysics*, 565:A14.

Del Zanna, G. and Mason, H. E. (2018). Solar UV and X-ray Spectral Diagnostics. *Living Reviews in Solar Physics*, 15:5.

Del Zanna, G., Weberg, M., and Warren, H. P. (2023). Hinode EIS: Updated in-Flight Radiometric Calibration. *eprint arXiv:2308.06609*.

Del Zanna, G. and Woods, T. N. (2013). Spectral Diagnostics with the SDO EVE Flare Lines. *Astronomy and Astrophysics*, 555:A59.

Dennis, B. R., Phillips, K. J. H., Schwartz, R. A., Tolbert, A. K., Starr, R. D., and Nittler, L. R. (2015). Solar Flare Element Abundances from the Solar Assembly for X-rays (SAX) on MESSENGER. *The Astrophysical Journal*, 803(2):67.

Dere, K. P., Landi, E., Mason, H. E., Monsignori Fossi, B. C., and Young, P. R. (1997). CHIANTI - an Atomic Database for Emission Lines: I. Wavelengths Greater than 50 Å. *Astronomy and Astrophysics Supplement Series*, 125(1):149–173.

Dere, K. P., Landi, E., Young, P. R., Del Zanna, G., Landini, M., and Mason, H. E. (2009). CHIANTI – an Atomic Database for Emission Lines: IX. Ionization Rates, Recombination Rates, Ionization Equilibria for the Elements Hydrogen through Zinc and Updated Atomic Data. *Astronomy & Astrophysics*, 498(3):915–929.

Diver, D. A., Fletcher, L., and Potts, H. E. (2005). FIP Enhancement by Alfvén Ionization. *Solar Physics*, 227(2):207–215.

Doschek, G. A. and Warren, H. P. (2016). The Mysterious Case of the Solar Argon Abundance near Sunspots in Flares. *The Astrophysical Journal*, 825(1):36.

Doschek, G. A. and Warren, H. P. (2017). Sunspots, Starspots, and Elemental Abundances. *The Astrophysical Journal*, 844(1):52.

Doschek, G. A., Warren, H. P., and Feldman, U. (2015). Anomalous Relative Ar/Ca Coronal Abundances Observed by the Hinode. EUV Imaging SPectrometer near Sunspots. *The Astrophysical Journal*, 808(1):L7.

Doschek, G. A., Warren, H. P., Harra, L. K., Culhane, J. L., Watanabe, T., and Hara, H. (2018). Photospheric and Coronal Abundances in an X8.3 Class Limb Flare. *The Astrophysical Journal*, 853(2):178.

Driel-Gesztelyi, L. v., Démoulin, P., Mandrini, C. H., Harra, L., and Klimchuk, J. A. (2003). The Long-Term Evolution of AR 7978: The Scalings of the Coronal

Plasma Parameters with the Mean Photospheric Magnetic Field. *The Astrophysical Journal*, 586(1):579.

Dzifčáková, E. and Dudík, J. (2017). *Kappa Distributions*. Elsevier.

Feldman, U., Mandelbaum, P., Seely, J. F., Doschek, G. A., and Gursky, H. (1992). The Potential for Plasma Diagnostics from Stellar Extreme-Ultraviolet Observations. *The Astrophysical Journal Supplement Series*, 81:387–408.

Feldman, U., Warren, H. P., Brown, C. M., and Doschek, G. A. (2009). Can the Composition of the Solar Corona be Derived from Hinode/Extreme-Ultraviolet Imageing Spectrometer Spectra? *The Astrophysical Journal*, 695(1):36–45.

Feldman, U. and Widing, K. G. (1990). Photospheric Abundances of Oxygen, Neon, and Argon Derived from the XUV Spectrum of an Impulsive Flare. *The Astrophysical Journal*, 363:292.

Feldman, U. and Widing, K. G. (1993). Elemental Abundances in the Upper Solar Atmosphere of Quiet and Coronal Hole Regions (T E 4.3 X 10 5 K). *The Astrophysical Journal*, 414:381.

Fisher, G. H., Canfield, R. C., and McClymont, A. N. (1985a). Flare Loop Radiative Hydrodynamics - Part Seven - Dynamics of the Thick Target Heated Chromosphere. *The Astrophysical Journal*, 289:434.

Fisher, G. H., Canfield, R. C., and McClymont, A. N. (1985b). Flare Loop Radiative Hydrodynamics - Part Six - Chromospheric Evaporation due to Heating by Nonthermal Electrons. *The Astrophysical Journal*, 289:425.

Fisher, G. H., Canfield, R. C., and McClymont, A. N. (1985c). Flare Loop Radiative Hydrodynamics. V - Response to Thick-Target Heating. VI - Chromospheric Evaporation due to Heating by Nonthermal Electrons. VII - Dynamics of the Thick-Target Heated Chromosphere. *The Astrophysical Journal*, 289:414–441.

Fletcher, L., Dennis, B. R., Hudson, H. S., Krucker, S., Phillips, K., Veronig, A., Battaglia, M., Bone, L., Caspi, A., Chen, Q., Gallagher, P., Grigis, P. T., Ji, H.,

Liu, W., Milligan, R. O., and Temmer, M. (2011). An Observational Overview of Solar Flares. *Space Science Reviews*, 159(1):19.

Fletcher, L., López Fuentes, M. C., Mandrini, C. H., Schmieder, B., Démoulin, P., Mason, H. E., Young, P. R., and Nitta, N. (2001). A Relationship Between Transition Region Brightenings, Abundances, and Magnetic Topology. *Solar Physics*, 203(2):255–287.

Fludra, A. and Schmelz, J. T. (1999). The Absolute Coronal Abundances of Sulfur, Calcium, and Iron from Yohkoh-BCS Flare Spectra. *Astronomy and Astrophysics*, 348:286–294.

Freeland, S. L. and Handy, B. N. (1998). Data Analysis with the SolarSoft System. *Solar Physics*, 182:497–500.

Fu, H., Madjarska, M. S., Xia, L., Li, B., Huang, Z., and Wangguan, Z. (2017). Charge States and FIP Bias of the Solar Wind from Coronal Holes, Active Regions, and Quiet Sun. *The Astrophysical Journal*, 836(2):169.

Gabriel, A. H. and Mason, H. E. (1982). Solar Physics. *Applied Atomic Collision Physics, Volume 1: Atmospheric Physics and Chemistry*, 1:346.

Gaizauskas, V., Harvey, K. L., Harvey, J. W., and Zwaan, C. (1983). Large-Scale Patterns Formed by Solar Active Regions During the Ascending Phase of Sycle 21. *The Astrophysical Journal*, 265:1056–1065.

Gallagher, P. T. (2000). *Optical and EUV Observations of the Solar Atmosphere*. PhD thesis. The Queen's University of Belfast, Belfast, N. Ireland.

Geiss, J., Gloeckler, G., and von Steiger, R. (1995). Origin of the Solar Wind From Composition Data. *Space Science Reviews*, 72:49–60.

Gloeckler, G. and Geiss, J. (1989). The Abundances of Elements and Isotopes in the Solar Wind. *AIP Conference Proceedings*, 183:49–71.

Goldschmidt, B. (1938). Fractionnement du radium dans la précipitation de l'iodate de baryum en différentes solutions de sels de baryum radifères. *Journal de Chimie Physique*, 35:407–413.

Goldschmidt, V. M. (1922). Über die Massenverteilung im Erdinneren, verglichen mit der Struktur gewisser Meteoriten. *Naturwissenschaften*, 10(42):918–920.

Golub, L., DeLuca, E., Austin, G., Bookbinder, J., Caldwell, D., Cheimets, P., Cirtain, J., Cosmo, M., Reid, P., Sette, A., Weber, M., Sakao, T., Kano, R., Shibasaki, K., Hara, H., Tsuneta, S., Kumagai, K., Tamura, T., Shimojo, M., McCracken, J., Carpenter, J., Haight, H., Siler, R., Wright, E., Tucker, J., Rutledge, H., Barbera, M., Peres, G., and Varisco, S. (2007). The X-Ray Telescope (XRT) for the Hinode Mission. *Solar Physics*, 243(1):63–86.

Grant, S. D. T., Jess, D. B., Stangalini, M., Jafarzadeh, S., Fedun, V., Verth, G., Keys, P. H., Rajaguru, S. P., Uitenbroek, H., MacBride, C. D., Bate, W., and Gilchrist-Millar, C. A. (2022). The Propagation of Coherent Waves Across Multiple Solar Magnetic Pores. *The Astrophysical Journal*, 938(2):143.

Green, L. M. and Kliem, B. (2009). Flux Rope Formation Preceding Coronal Mass Ejection Onset. *The Astrophysical Journal*, 700:L83–L87.

Grevesse, N., Asplund, M., and Sauval, A. J. (2007). The Solar Chemical Composition. *Space Science Reviews*, 130(1):105–114.

Grevesse, N. and Sauval, A. (1998). Standard Solar Composition. *Space Science Reviews*, 85(1):161–174.

Groeneveld, R. A. and Meeden, G. (1984). Measuring Skewness and Kurtosis. *Journal of the Royal Statistical Society. Series D (The Statistician)*, 33(4):391–399.

Hale, G. E., Ellerman, F., Nicholson, S. B., and Joy, A. (1919). The Magnetic Polarity of Sun-Spots. *The Astrophysical Journal*, 49:153.

Hale, G. E. and Nicholson, S. B. (1938). *Magnetic Observations of Sunspots, 1917-1924*.

Hannah, I. G. and Kontar, E. P. (2012). Differential Emission Measures from the Regularized Inversion of Hinode and SDO Data. *Astronomy & Astrophysics*, 539:A146.

Hannah, I. G. and Kontar, E. P. (2013). Multi-Thermal Dynamics and Energetics of a Coronal Mass Ejection in the Low Solar Atmosphere. *Astronomy & Astrophysics*, 553:A10.

Harra, L. K. and Mason, K. O. (2004). *Space Science*. Imperial College Press.

Harvey, J. W., Hill, F., Hubbard, R. P., Kennedy, J. R., Leibacher, J. W., Pintar, J. A., Gilman, P. A., Noyes, R. W., Title, A. M., Toomre, J., Ulrich, R. K., Bhatnagar, A., Kennewell, J. A., Marquette, W., Patron, J., Saa, O., and Yasukawa, E. (1996). The Global Oscillation Network Group (GONG) Project. *Science*, 272:1284–1286.

Harvey, K. L. (1993). *Magnetic Bipoles on the Sun*. PhD thesis.

Harvey, K. L. and Zwaan, C. (1993). Properties and Emergence Patterns of Bipolar Active Regions. *Solar Physics*, (1):85–118.

Hollweg, J. V. (1984). Resonances of coronal loops. *The Astrophysical Journal*, 277:392–403.

Howard, R. A., Moses, J. D., Vourlidas, A., Newmark, J. S., Socker, D. G., Plunkett, S. P., Korendyke, C. M., Cook, J. W., Hurley, A., Davila, J. M., Thompson, W. T., St Cyr, O. C., Mentzell, E., Mehalick, K., Lemen, J. R., Wuelser, J. P., Duncan, D. W., Tarbell, T. D., Wolfson, C. J., Moore, A., Harrison, R. A., Waltham, N. R., Lang, J., Davis, C. J., Eyles, C. J., Mapson-Menard, H., Simnett, G. M., Halain, J. P., Defise, J. M., Mazy, E., Rochus, P., Mercier, R., Ravet, M. F., Delmotte, F., Auchere, F., Delaboudiniere, J. P., Bothmer, V., Deutsch, W., Wang, D., Rich, N., Cooper, S., Stephens, V., Maahs, G., Baugh, R., McMullin, D., and

Carter, T. (2008). Sun Earth Connection Coronal and Heliospheric Investigation (SECCHI). *Space Science Reviews*, 136:67–115.

Hudson, H. S., Strong, K. T., Dennis, B. R., Zarro, D., Inda, M., Kosugi, T., and Sakao, T. (1994). Impulsive Behavior in Solar Soft X-Radiation. *The Astrophysical Journal*, 422:L25.

Imada, S. and Zweibel, E. G. (2012). SELF-ORGANIZATION OF RECONNECTING PLASMAS TO MARGINAL COLLISIONALITY IN THE SOLAR CORONA. *The Astrophysical Journal*, 755(2):93.

James, A. W., Green, L. M., Palmerio, E., Valori, G., Reid, H. A. S., Baker, D., Brooks, D. H., Van Driel-Gesztelyi, L., and Kilpua, E. K. J. (2017). On-Disc Observations of Flux Rope Formation Prior to Its Eruption. *Solar Physics*, 292(5):71.

James, A. W., Green, L. M., Van Driel-Gesztelyi, L., and Valori, G. (2020). A New Trigger Mechanism for Coronal Mass Ejections: The Role of Confined Flares and Photospheric Motions in the Formation of Hot Flux Ropes. *Astronomy & Astrophysics*, 644:A137.

Janvier, M., Mzerguat, S., Young, P. R., Buchlin, , Manou, A., Pelouze, G., Long, D. M., Green, L., Warmuth, A., Schuller, F., Démoulin, P., Calchetti, D., Kahil, F., Bellot Rubio, L., Parenti, S., Baccar, S., Barczynski, K., Harra, L. K., Hayes, L. A., Thompson, W. T., Müller, D., Baker, D., Yardley, S., Berghmans, D., Verbeeck, C., Smith, P. J., Peter, H., Aznar Cuadrado, R., Musset, S., Brooks, D. H., Rodríguez, L., Auchère, F., Carlsson, M., Fludra, A., Hassler, D., Williams, D., Caldwell, M., Fredvik, T., Giunta, A., Grundy, T., Guest, S., Kraaikamp, E., Leeks, S., Plowman, J., Schmutz, W., Schühle, U., Sidher, S. D., Teriaca, L., Solanki, S. K., Del Toro Iniesta, J. C., Woch, J., Gandorfer, A., Hirzberger, J., Orozco Suárez, D., Appourchaux, T., Valori, G., Sinjan, J., Albert, K., and Volkmer, R. (2023). A Multiple Spacecraft Detection of the 2 April 2022 M-Class

Flare and Filament eruption During the First Close Solar Orbiter Perihelion. *Astronomy & Astrophysics*, 677:A130.

Jeffrey, N. L. S., Fletcher, L., and Labrosse, N. (2016). First Evidence of Non-Gaussian Solar Flare EUV Spectral Line Profiles and Accelerated Non-Thermal Ion Motion. *Astronomy & Astrophysics*, 590:A99.

Jordan, C. and Wilson, R. (1971). The Determination of Chromospheric-Coronal Structure from Solar XUV Observations. *Physics of the Solar Corona*, 27:219.

Kaiser, M. L., Kucera, T. A., Davila, J. M., St. Cyr, O. C., Guhathakurta, M., and Christian, E. (2008). The STEREO Mission: An Introduction. *Space Science Reviews*, 136:5–16.

Kamio, S., Hara, H., Watanabe, T., Fredvik, T., and Hansteen, V. H. (2010). Modeling of EIS Spectrum Drift from Instrumental Temperatures. *Solar Physics*, 266(1):209–223.

Kashyap, V. and Drake, J. (2000). PINTofALE: Package for the Interactive Analysis of Line Emission. *Bulletin of the Astrophysical Society of India*, 28:475–476.

Kashyap, V. and Drake, J. J. (1998). Markov-Chain Monte Carlo Reconstruction of Emission Measure Distributions: Application to Solar Extreme-Ultraviolet Spectra. *The Astrophysical Journal*, 503(1):450–466.

Kato, T., Kato, M., and Shibata, K. (2000). Time Dependent Ionization Balance in Solar Flares. *Advances in Space Research*, 25(9):1781–1790.

Klimchuk, J. A. (2006). On Solving the Coronal Heating Problem. *Solar Physics*, 234(1):41–77.

Klimchuk, J. A., Patsourakos, S., and Cargill, P. J. (2008). Highly Efficient Modeling of Dynamic Coronal Loops. *The Astrophysical Journal*, 682:1351–1362.

Ko, Y.-K., Raymond, J. C., Lin, J., Lawrence, G., Li, J., and Fludra, A. (2003). Dynamical and Physical Properties of a Post-Coronal Mass Ejection Current Sheet. *The Astrophysical Journal*, 594(2):1068.

Ko, Y.-K., Young, P. R., Muglach, K., Warren, H. P., and Ugarte-Urra, I. (2016). Correlation of Coronal Plasma Properties and Solar Magnetic Field in a Decaying Active Region. *The Astrophysical Journal*, 826(2):126.

Kosugi, T., Matsuzaki, K., Sakao, T., Shimizu, T., Sone, Y., Tachikawa, S., Hashimoto, T., Minesugi, K., Ohnishi, A., Yamada, T., Tsuneta, S., Hara, H., Ichimoto, K., Suematsu, Y., Shimojo, M., Watanabe, T., Shimada, S., Davis, J. M., Hill, L. D., Owens, J. K., Title, A. M., Culhane, J. L., Harra, L. K., Doschek, G. A., and Golub, L. (2007). The Hinode (Solar-B) Mission: An Overview. *Solar Physics*, 243(1):3–17.

Kramida, A., Ralchenko, Y., Reader, J., and NIST ASD Team (2023). NIST Atomic Spectra Database (Version 5.11).

Krasnoselskikh, V., Tsurutani, B. T., Dudok de Wit, T., Walker, S., Balikhin, M., Balat-Pichelin, M., Velli, M., Bale, S. D., Maksimovic, M., Agapitov, O., Baumjohann, W., Berthomier, M., Bruno, R., Cranmer, S. R., de Pontieu, B., Meneses, D. d. S., Eastwood, J., Erdelyi, R., Ergun, R., Fedun, V., Ganushkina, N., Greco, A., Harra, L., Henri, P., Horbury, T., Hudson, H., Kasper, J., Khotyaintsev, Y., Kretzschmar, M., Krucker, S., Kucharek, H., Langevin, Y., Lavraud, B., Lebreton, J.-P., Lepri, S., Liemohn, M., Louarn, P., Moebius, E., Mozer, F., Nemecek, Z., Panasenco, O., Retino, A., Safrankova, J., Scudder, J., Servidio, S., Sorriso-Valvo, L., Souček, J., Szabo, A., Vaivads, A., Vekstein, G., Vörös, Z., Zaqarashvili, T., Zimbardo, G., and Fedorov, A. (2022). ICARUS: in-situ studies of the solar corona beyond Parker Solar Probe and Solar Orbiter. *Experimental Astronomy*, 54(2):277–315.

Krucker, S., Battaglia, M., Cargill, P. J., Fletcher, L., Hudson, H. S., MacKinnon, A. L., Masuda, S., Sui, L., Tomczak, M., Veronig, A. L., Vlahos, L., and White, S. M. (2008). Hard X-ray emission from the solar corona. *The Astronomy and Astrophysics Review*, 16(3):155–208.

Laming, J. M. (2004). A Unified Picture of the First Ionization Potential and Inverse First Ionization Potential Effects. *The Astrophysical Journal*, 614(2):1063–1072.

Laming, J. M. (2009). Non-WKB Models of the First Ionization Potential Effect: Implications for Solar Coronal Heating and the Coronal Helium and Neon Abundances. *The Astrophysical Journal*, 695(2):954.

Laming, J. M. (2015). The FIP and Inverse FIP Effects in Solar and Stellar Coronae. *Living Reviews in Solar Physics*, 12(1):2.

Laming, J. M. (2017). The First Ionization Potential Effect from the Ponderomotive Force: On the Polarization and Coronal Origin of Alfvén Waves. *The Astrophysical Journal*, 844(2):153.

Laming, J. M. (2021). The FIP and Inverse-FIP Effects in Solar Flares. *The Astrophysical Journal*, 909:17.

Laming, J. M., Vourlidas, A., Korendyke, C., Chua, D., Cranmer, S. R., Ko, Y.-K., Kuroda, N., Provornikova, E., Raymond, J. C., Raouafi, N.-E., Strachan, L., Tun-Beltran, S., Weberg, M., and Wood, B. E. (2019). Element Abundances: A New Diagnostic for the Solar Wind. *The Astrophysical Journal*, 879(2):124.

Landi, E., Raymond, J. C., Miralles, M. P., and Hara, H. (2010). Physical Conditions in a Coronal Mass Ejection from Hinode, STEREO, and SOHO Observations. *The Astrophysical Journal*, 711(1):75.

Leer, E., Holzer, T. E., and Fla, T. (1982). Acceleration of the Solar Wind. *Space Science Reviews*, 33:161–200.

Lemen, J. R., Title, A. M., Akin, D. J., Boerner, P. F., Chou, C., Drake, J. F., Duncan, D. W., Edwards, C. G., Friedlaender, F. M., Heyman, G. F., Hurlburt, N. E., Katz, N. L., Kushner, G. D., Levay, M., Lindgren, R. W., Mathur, D. P., McFeaters, E. L., Mitchell, S., Rehse, R. A., Schrijver, C. J., Springer, L. A., Stern, R. A., Tarbell, T. D., Wuelser, J.-P., Wolfson, C. J., Yanari, C., Bookbinder, J. A., Cheimets, P. N., Caldwell, D., Deluca, E. E., Gates, R., Golub, L., Park, S.,

Podgorski, W. A., Bush, R. I., Scherrer, P. H., Gummin, M. A., Smith, P., Auker, G., Jerram, P., Pool, P., Soufli, R., Windt, D. L., Beardsley, S., Clapp, M., Lang, J., and Waltham, N. (2012). The Atmospheric Imaging Assembly (AIA) on the Solar Dynamics Observatory (SDO). *Solar Physics*, 275(1-2):17–40.

Lodders, K. (2008). The Solar Argon Abundance. *The Astrophysical Journal*, 674:607–611.

Lysenko, A. L., Frederiks, D. D., Fleishman, G. D., Aptekar, R. L., Altyntsev, A. T., Golenetskii, S. V., Svinkin, D. S., Ulanov, M., Tsvetkova, A. E., and Ridnaia, A. V. (2020). X-Ray and Gamma-Ray Emission From Solar Flares. *Physics Uspekhi*, 63:818–832.

Mariska, J. T. (1992). *The Solar Transition Region*. Cambridge University Press.

Marsch, E., von Steiger, R., and Bochsler, P. (1995). Element Fractionation by Diffusion in the Solar Chromosphere. *Astronomy & Astrophysics*, 301:261–276.

Martínez-Sykora, J., Pontieu, B. D., Hansteen, V. H., Testa, P., Wargnier, Q. M., and Szydlarski, M. (2023). The Impact of Multifluid Effects in the Solar Chromosphere on the Ponderomotive Force under SE and NEQ Ionization Conditions. *The Astrophysical Journal*, 949(2):112.

Mazzotta, P., Mazzitelli, G., Colafrancesco, S., and Vittorio, N. (1998). Ionization Balance for Optically Thin Plasmas: Rate Coefficients for all Atoms and Ions of the Elements H to Ni. *Astronomy and Astrophysics Supplement Series*, 133:403–409.

McIntosh, P. S. (1981). *The birth and evolution of sunspots - Observations*. The Physics of Sunspots.

Meyer, J.-P. (1985a). The Baseline Composition of Solar Energetic Particles. *The Astrophysical Journal Supplement Series*, 57(1979):151.

Meyer, J.-P. (1985b). Solar-Stellar Outer Atmospheres and Energetic Particles, and Galactic Cosmic Rays. *The Astrophysical Journal Supplement Series*, 57:173.

Meyer, J. P. (1991). Diagnostic Methods for Coronal Abundances. *Advances in Space Research*, 11(1):269–280.

Mihailescu, T., Baker, D., Green, L. M., van Driel-Gesztelyi, L., Long, D. M., Brooks, D. H., and To, A. S. H. (2022). What Determines Active Region Coronal Plasma Composition? *The Astrophysical Journal*, 933(2):245.

Mihailescu, T., Brooks, D. H., Laming, J. M., Baker, D., Green, L. M., James, A. W., Long, D. M., Driel-Gesztelyi, L. v., and Stangalini, M. (2023). Intriguing Plasma Composition Pattern in a Solar Active Region: A Result of Nonresonant Alfvén Waves? *The Astrophysical Journal*, 959(2):72.

Mikhalyaev, B. B. and Solovév, A. A. (2005). The Oscillations of Coronal Loops Including the Shell. *Solar Physics*, 227(2):249–263.

Milligan, R. O. and Dennis, B. R. (2009). Velocity Characteristics of Evaporated Plasma Using Hinode/EUV Imaging Spectrometer. *The Astrophysical Journal*, 699(2):968.

Mondal, B., Sarkar, A., Vadawale, S. V., Mithun, N. P. S., Janardhan, P., Del Zanna, G., Mason, H. E., Mitra-Kraev, U., and Narendranath, S. (2021). Evolution of Elemental Abundances during B-Class Solar Flares: Soft X-Ray Spectral Measurements with Chandrayaan-2 XSM. *The Astrophysical Journal*, 920:4.

Murabito, M., Stangalini, M., Baker, D., Valori, G., Jess, D. B., Jafarzadeh, S., Brooks, D. H., Ermolli, I., Giorgi, F., Grant, S. D. T., Long, D. M., and Van Driel-Gesztelyi, L. (2021). Investigating the Origin of Magnetic Perturbations Associated with the FIP Effect. *Astronomy & Astrophysics*, 656:A87.

Müller, D., Nicula, B., Felix, S., Verstringe, F., Bourgoignie, B., Csillaghy, A., Berghmans, D., Jiggens, P., García-Ortiz, J. P., Ireland, J., Zahniy, S., and Fleck, B. (2017). JHelioviewer. Time-dependent 3D visualisation of solar and heliospheric data. *Astronomy and Astrophysics*, 606:A10.

Nama, L., Mondal, B., Narendranath, S., and Paul, K. T. (2023). Coronal Elemental Abundances During A-Class Solar Flares Observed by Chandrayaan-2 XSM. *Solar Physics*, 298:55.

Narendranath, S., Sreekumar, P., Alha, L., Sankarasubramanian, K., Huovelin, J., and Athiray, P. S. (2014). Elemental Abundances in the Solar Corona as Measured by the X-ray Solar Monitor Onboard Chandrayaan-1. *Solar Physics*, 289(5):1585–1595.

Payne, C. H. (1925). *Stellar Atmospheres; a Contribution to the Observational Study of High Temperature in the Reversing Layers of Stars.* PhD thesis.

Pesnell, W. D., Thompson, B. J., and Chamberlin, P. C. (2012). The Solar Dynamics Observatory (SDO). *Solar Physics*, 275(1-2):3–15.

Phillips, K. (2009). *Ultraviolet and X-ray Spectroscopy of the Solar Atmosphere*. Number 44 in Cambridge Astrophysics.

Phillips, K. J. H. (1995). *Guide to the Sun*. Cambridge University Press.

Phillips, K. J. H. and Dennis, B. R. (2012). The Solar Flare Iron Abundance. *The Astrophysical Journal*, 748:52.

Pottasch, S. R. (1963). The Lower Solar Corona: Interpretation of the Ultraviolet Spectrum. *The Astrophysical Journal*, 137:945.

Provornikova, E., Laming, J. M., and Lukin, V. S. (2018). Reflection of Fast Magnetosonic Waves near a Magnetic Reconnection Region. *The Astrophysical Journal*, 860(2):138.

Pucci, S., Lie-Svendsen, O., and Esser, R. (2010). Elemental Abundances in the Fast Solar Wind Emanating from Chromospheric Funnels. *The Astrophysical Journal*, 709(2):993.

Rakowski, C. E. and Laming, J. M. (2012). On the Origin of the Slow Speed Solar Wind: Helium Abundance Variations. *The Astrophysical Journal*, 754:65.

Reames, D. V. (2018). The "FIP Effect" and the Origins of Solar Energetic Particles and of the Solar Wind. *Solar Physics*, 293(3):47.

Reep, J. W. and Russell, A. J. B. (2016). Alfvénic Wave Heating of the Upper Chromosphere in Flares. *The Astrophysical Journal*, 818:L20.

Reep, J. W., Russell, A. J. B., Tarr, L. A., and Leake, J. E. (2018). A Hydrodynamic Model of Alfvénic Wave Heating in a Coronal Loop and Its Chromospheric Footpoints. *The Astrophysical Journal*, 853:101.

Russell, H. N. (1929). On the Composition of the Sun's Atmosphere. *The Astrophysical Journal*, 70:11.

Réville, V., Rouillard, A. P., Velli, M., Verdini, A., Buchlin, , Lavarra, M., and Poirier, N. (2021). Investigating the Origin of the First Ionization Potential Effect With a Shell Turbulence Model. *Frontiers in Astronomy and Space Sciences*, 8.

Scherrer, P. H., Schou, J., Bush, R. I., Kosovichev, A. G., Bogart, R. S., Hoeksema, J. T., Liu, Y., Duvall, T. L., Zhao, J., Title, A. M., Schrijver, C. J., Tarbell, T. D., and Tomczyk, S. (2012). The Helioseismic and Magnetic Imager (HMI) Investigation for the Solar Dynamics Observatory (SDO). *Solar Physics*, 275(1-2):207–227.

Schrijver, C. J. and DeRosa, M. L. (2003). Photospheric and Heliospheric Magnetic Fields. *Solar Physics*, 212(1):165–200.

Schrijver, C. J. and Zwaan, C. (2000). *Solar and Stellar Magnetic Activity*. Cambridge University Press.

Schwadron, N. A., Fisk, L. A., and Zurbuchen, T. H. (1999). Elemental Fractionation in the Slow Solar Wind. *The Astrophysical Journal*, 521(2):859.

Scott, P., Asplund, M., Grevesse, N., Bergemann, M., and Jacques Sauval, A. (2015a). The Elemental Composition of the Sun: II. The Iron Group Elements Sc to Ni. *Astronomy & Astrophysics*, 573:A26.

Scott, P., Grevesse, N., Asplund, M., Jacques Sauval, A., Lind, K., Takeda, Y., Collet, R., Trampedach, R., and Hayek, W. (2015b). The Elemental Composition of the Sun: I. The Intermediate Mass Elements Na to Ca. *Astronomy & Astrophysics*, 573:A25.

Shibata, K., Masuda, S., Shimojo, M., Hara, H., Yokoyama, T., Tsuneta, S., Kosugi, T., and Ogawara, Y. (1995). Hot-Plasma Ejections Associated with Compact-Loop Solar Flares. *The Astrophysical Journal*, 451:L83.

Simões, P. J. A., Reid, H. A. S., Milligan, R. O., and Fletcher, L. (2019). The Spectral Content of SDO/AIA 1600 and 1700 Å Filters from Flare and Plage Observations. *The Astrophysical Journal*, 870(2):114.

Stangalini, M., Baker, D., Valori, G., Jess, D. B., Jafarzadeh, S., Murabito, M., To, A. S. H., Brooks, D. H., Ermolli, I., Giorgi, F., and MacBride, C. D. (2021). Spectropolarimetric fluctuations in a sunspot chromosphere. *Philosophical Transactions of the Royal Society A: Mathematical, Physical and Engineering Sciences*, 379(2190).

Stansby, D., Baker, D., Brooks, D. H., and Owen, C. J. (2020). Directly Comparing Coronal and Solar Wind Elemental Fractionation. *Astronomy and Astrophysics*, 640.

Sylwester, B., Sylwester, J., Phillips, K. J. H., Kepa, A., and Mrozek, T. (2014). Solar Flare Composition and Thermodynamics from RESIK X-Ray Spectra. *The Astrophysical Journal*, 787:122.

Testa, P., Martínez-Sykora, J., and De Pontieu, B. (2023). Coronal Abundances in an Active Region: Evolution and Underlying Chromospheric and Transition Region Properties. *The Astrophysical Journal*, 944:117.

Tian, H., Tu, C., Marsch, E., He, J., and Kamio, S. (2010). The Nascent Fast Solar Wind Observed by the EUV Imaging Spectrometer on Board Hinode. *The Astrophysical Journal*, 709:L88–L93.

To, A. S. H., Long, D. M., Baker, D., Brooks, D. H., Driel-Gesztelyi, L. v., Laming, J. M., and Valori, G. (2021). The Evolution of Plasma Composition during a Solar Flare. *The Astrophysical Journal*, 911(2):86.

Tsuneta, S., Ichimoto, K., Katsukawa, Y., Nagata, S., Otsubo, M., Shimizu, T., Suematsu, Y., Nakagiri, M., Noguchi, M., Tarbell, T., Title, A., Shine, R., Rosenberg, W., Hoffmann, C., Jurcevich, B., Kushner, G., Levay, M., Lites, B., Elmore, D., Matsushita, T., Kawaguchi, N., Saito, H., Mikami, I., Hill, L. D., and Owens, J. K. (2008). The Solar Optical Telescope for the Hinode Mission: An Overview. *Solar Physics*, 249(2):167–196.

Ugarte-Urra, I., Warren, H. P., and Brooks, D. H. (2009). Active Region Transition Region Loop Populations and Their Relationship to the Corona. *The Astrophysical Journal*, 695:642–651.

van Ballegooijen, A. A. and Martens, P. C. H. (1989). Formation and Eruption of Solar Prominences. *The Astrophysical Journal*, 343(1967):971.

van Driel-Gesztelyi, L. and Green, L. M. (2015). Evolution of Active Regions. *Living Reviews in Solar Physics*, 12:1–98.

van Driel-Gesztelyi, L. and Petrovay, K. (1990). Asymmetric Flux Loops in Active Regions, I. *Solar Physics*, 126(2):285–298.

Verwichte, E., Foullon, C., and Nakariakov, V. M. (2006). Fast Magnetoacoustic Waves in Curved Coronal Loops - I. Trapped and Leaky Modes. *Astronomy & Astrophysics*, 446(3):1139–1149.

von Steiger, R. and Geiss, J. (1989). Supply of Fractionated Gases to the Corona. *Astronomy & Astrophysics*, 225(1):222–238.

von Steiger, R. and Schwadron, N. A. (2000). Solar Wind Composition. *High Energy Solar Physics*, 206.

Waldmeier, M. (1955). *Ergebnisse und Probleme der Sonnenforschung*. Leipzig, Geest & Portig.

Warren, H. P. (2014). Measurements of Absolute Abundances in Solar Flares. *The Astrophysical Journal Letters*, 786(1):L2.

Warren, H. P., Ugarte-Urra, I., and Landi, E. (2014). The Absolute Calibration of the EUV Imaging Spectrometer on Hinode. *The Astrophysical Journal Supplement Series*, 213(1):11.

Weberg, M. J., Warren, H. P., Crump, N., and Barnes, W. (2023). EISPAC - The EIS Python Analysis Code. *Journal of Open Source Software*, 8(85):4914.

Widing, K. G. and Feldman, U. (1989). Abundance Variations in the Outer Solar Atmosphere Observed in SKYLAB Spectroheliograms. *The Astrophysical Journal*, 344:1046.

Widing, K. G. and Feldman, U. (1995). Abundance Ratios of Oxygen, Neon, and Magnesium in Solar Active Regions and Flares: The FIP Effect. *The Astrophysical Journal*, 442:446.

Widing, K. G. and Feldman, U. (2001). On the Rate of Abundance Modifications versus Time in Active Region Plasmas. *The Astrophysical Journal*, 555:426–434.

Withbroe, G. L. (1978). The Thermal Phase of a Large Solar Flare. *The Astrophysical Journal*, 225:641–649.

Woods, T. N., Eparvier, F. G., Hock, R., Jones, A. R., Woodraska, D., Judge, D., Didkovsky, L., Lean, J., Mariska, J., Warren, H., McMullin, D., Chamberlin, P., Berthiaume, G., Bailey, S., Fuller-Rowell, T., Sojka, J., Tobiska, W. K., and Viereck, R. (2012). Extreme Ultraviolet Variability Experiment (EVE) on the Solar Dynamics Observatory (SDO): Overview of Science Objectives, Instrument Design, Data Products, and Model Developments. *Solar Physics*, 275(1):115–143.

Wuelser, J.-P., Lemen, J. R., Tarbell, T. D., Wolfson, C. J., Cannon, J. C., Carpenter, B. A., Duncan, D. W., Gradwohl, G. S., Meyer, S. B., Moore, A. S., Navarro, R. L., Pearson, J. D., Rossi, G. R., Springer, L. A., Howard, R. A., Moses, J. D.,

Newmark, J. S., Delaboudiniere, J.-P., Artzner, G. E., Auchere, F., Bougnet, M., Bouyries, P., Bridou, F., Clotaire, J.-Y., Colas, G., Delmotte, F., Jerome, A., Lamare, M., Mercier, R., Mullot, M., Ravet, M.-F., Song, X., Bothmer, V., and Deutsch, W. (2004). EUVI: the STEREO-SECCHI Extreme Ultraviolet Imager. *Telescopes and Instrumentation for Solar Astrophysics*, 5171:111–122.

Young, P. R. (2005). The Ne/O Abundance Ratio in the Quiet Sun. *Astronomy & Astrophysics*, 444(2):L45–L48.

Young, P. R. (2023a). CHIANTI Technical Report No. 22: CHIANTI software for interfacing with emission measure codes. Available at: https://zenodo.org/records/7504532.

Young, P. R. (2023b). Creating synthetic EIS rasters from SDO/AIA data. Available at: https://zenodo.org/records/7582257.

Young, P. R., Doschek, G. A., Warren, H. P., and Hara, H. (2013). Properties of a Solar Flare Kernel Observed by Hinode and SDO. *The Astrophysical Journal*, 766(2):127.

Young, P. R. and Mason, H. E. (1997). The Mg/Ne Abundance Ratio in a Recently Emerged Flux Region Observed by CDS. *Solar Physics*, 175(2):523–539.

Young, P. R., O'Dwyer, B., and Mason, H. E. (2012). Velocity Measurements for a Solar Active Region Fan Loop from Hinode/EIS Observations. *The Astrophysical Journal*, 744:14.

Young, P. R., Watanabe, T., Hara, H., and Mariska, J. T. (2009). High-Precision Density Measurements in the Solar Corona - I. Analysis Methods and Results for Fe XII and Fe XIII. *Astronomy & Astrophysics*, 495(2):587–606.

Young, P. R., Zanna, D. G., Mason, H. E., Dere, K. P., Landi, E., Landini, M., Doschek, G. A., Brown, C. M., Culhane, L., Harra, L. K., Watanabe, T., and Hara, H. (2007). EUV Emission Lines and Diagnostics Observed with Hinode/EIS. *Publications of the Astronomical Society of Japan*, 59(sp3):S857–S864.